DE GRUYTER

Yong-Gang Li (Ed.)

FAULT-ZONE GUIDED WAVE, GROUND MOTION, LANDSLIDE AND EARTHQUAKE FORECAST

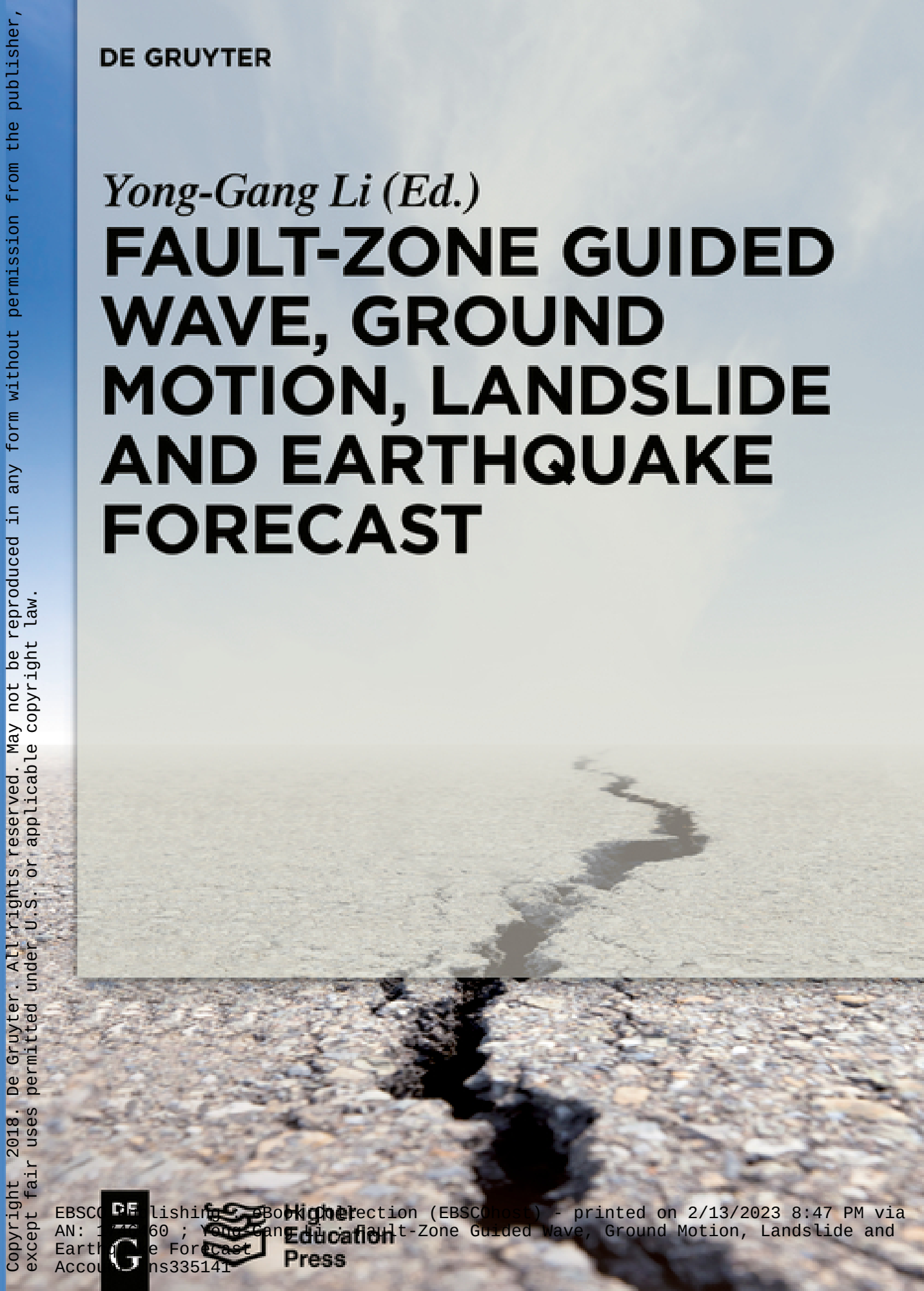

Higher Education Press

Yong-Gang Li (Ed.)

Fault-Zone Guided Wave, Ground Motion, Landslide and Earthquake Forecast

Also of Interest

Rock Anisotropy, Fracture and Earthquake Assessment
Yong-Gang Li (Ed.), 2016
ISBN 978-3-11-044070-6, e-ISBN 978-3-11-043251-0

Seismic Imaging, Fault Damage and Heal
Yong-Gang Li (Ed.), 2014
ISBN 978-3-11-032991-9, e-ISBN 978-3-11-032995-7

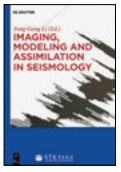

Imaging, Modeling and Assimilation in Seismology
Yong-Gang Li (Ed.), 2012
ISBN 978-3-11-025902-5, e-ISBN 978-3-11-025903-2

De Gruyter Series in Applied and Numerical Mathematics 1
Free Boundaries in Rock Mechanics
Anvarbek Meirmanov, Oleg V. Galtsev, Reshat N. Zimin, 2017
ISBN 978-3-11-054490-9, e-ISBN 978-3-11-054616-3

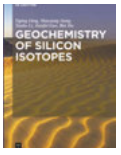

Geochemistry of Silicon Isotopes
Tiping Ding, Shaoyong Jiang, Yanhe Li, Jianfei Gao, Bin Hu, 2017
ISBN 978-3-11-040242-1, e-ISBN 978-3-11-040245-2

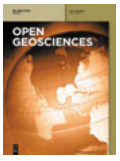

Open Geosciences
formerly Central European Journal of Geosciences
Jankowski, Piotr (Editor-in-Chief)
ISSN 2391-5447

Fault-Zone Guided Wave, Ground Motion, Landslide and Earthquake Forecast

Edited by Yong-Gang Li

DE GRUYTER

Higher Education Press

Editor
Prof. Yong-Gang Li
University of Southern California
Department of Earth Science
Zumberg Science Hall
Los Angeles, CA 90089-0740, USA
ygli@usc.edu

ISBN 978-3-11-054251-6
e-ISBN (E-BOOK) 978-3-11-054355-1
e-ISBN (EPUB) 978-3-11-054268-4

Library of Congress Control Number: 2018934506

Bibliographic information published by the Deutsche Nationalbibliothek
The Deutsche Nationalbibliothek lists this publication in the Deutsche Nationalbibliografie; detailed bibliographic data are available on the Internet at http://dnb.dnb.de.

Printing and binding: CPI books GmbH, Leck
cover image: rottadana/ iStock / Getty Images Plus
♾ Printed on acid-free paper
Printed in Germany

www.degruyter.com

Preface

This book is the fourth monograph of the earth science specializing in observational, computational, and applied geophysics. A global authorship from top institutions presents multi-disciplinary topics and current approaches in seismological research of earthquakes. This work covers: characterization of subsurface fault damage zones in California using fault-zone guided waves generated by aftershocks, explosions and teleseismic earthquakes; forwards real-time estimation of strong ground motion by the full-waveform tomography; earthquake prediction based on the ETAS model to fit seismic network catalogs of global earthquake zones; investigation of erosional agency and cascading hazards in earthquake-triggering landslides; simulation of the realistic behaviors of coal and gas outbursts; a review of international consultation on the likelihood of earthquakes after Wenchuan earthquake in China. Each chapter in this book provides the comprehensive discussion of the state-of-the-art method and technique with applications in case study. The editor approaches this as a broad interdisciplinary effort, with well-balanced observational, interpretational and numerical modeling aspects. Linked with these topics, the book highlights the importance for characterizing the earthquake rupture zone structure, ground motion estimation, landscape landslide, earthquake hazards and forecast. These contents make this book a must-read for researchers in the field of earthquake physics.

This book can be taken as an expand of previous three books in the series for researchers and graduate students to grasp the various methods and skills used in structural, geological, physical and mechanical interpretation of earthquake phenomena for solving geophysical and tectonic problems. Readers of this book can make full use of the present knowledge and techniques to understand the fault zone waveguide effect, towards real-time estimation of strong ground motion, earthquake-triggering landslides, epidemic-type aftershock sequence models and earthquake likelihood prediction to serve the reduction of earthquake disasters.

https://doi.org/10.1515/9783110543551-005

Contents

Fault-Zone Guided Wave, Ground Motion, Landslide and Earthquake Forecast

Yong-Gang Li

This book covers multi-disciplinary topics in observational, computational and applied geophysics in aspects of solid earth system. Seven chapters present recent research to: (i) image subsurface rupture zones of South Napa earthquake in California by fault-zone trapped (guided) waves, (ii) introduce fault-zone trapped waves recorded for teleseismic earthquakes to document deep fault compliant zone, (iii) towards real-time estimate strong ground motion based on full-3D waveform tomography, (iv) implement ETAS models to earthquake zones with different tectonic structures, (v) understand erosional agency and cascading hazards for earthquake-triggering landslides, (vi) simulate coal and gas outburst by discrete element and lattice Boltzmann model, and (vii) review international consultation on the likelihood of earthquakes after Wenchuan earthquake using various methods. Authors from global institutions illuminate multi-disciplinary topics with case studies. All topics in this book will be helpful for further understanding earthquake physics and hazard assessment in global seismogenic regions.

Chapter 1: "Fault-Zone Trapped Waves Generated by Aftershocks and Explosions to Characterize the Subsurface Rupture Zone of the 2014 $M_{\mathrm{w}}6.0$ South Napa Earthquake, California" by Yong-Gang Li, Rufus D. Catchings, and Mark R. Goldman.

The 2014 $M_{\mathrm{w}}6.0$ South Napa earthquake in California caused significant damage to fault rocks along the West Napa Fault Zone (WNFZ), resulting in remarkable low-velocity waveguides to trap (guide) seismic waves. Fault-zone trapped waves (FZTWs) arise from constructive interference of reflected waves from the boundaries between the low-velocity fault zone and high-velocity surrounding

https://doi.org/10.1515/9783110543551-011

rocks. Their amplitudes and dispersion characteristics of FZTWs are sensitive to the geometry and physical properties of the fault zone, and the seismic source location with respect to the fault-zone waveguide. These features of FZTWs allow us to investigate the subsurface structure and material properties of a fault zone more accurately than before. In this chapter, authors present the FZTWs generated by aftershocks of the 2014 M_w6.0 South Napa earthquake and explosions detonated within the rupture zone. The measured post-S coda durations of these FZTWs recorded at cross-fault seismic arrays and along-fault stations show that the longer coda durations generally result from the longer distances of FZTWs propagating within the fault-zone waveguide, particularly for paths in the shallower parts of the fault-zone. Previous numerical tests of waveguide trapping effects show that if there is an obvious gap (more than 3–5 times of the wavelength of the FZTWs at its dominant frequency) such as a step-over of the fault zone between the seismic source and array, FZTWs will be disrupted by this gap and not observed clearly (e.g., Li and Vidale, 1996). Our observations of FZTWs suggest the continuity of waveguide along the WNFZ that extends further southward to the Franklin Fault (FF) at seismogenic depths. This consists with results from slip models derived from teleseismic, SAR and InSAR, field mapping data (Melgar *et al.*, 2015; Brocher *et al.*, 2015; Wei *et al.*, 2015) and aftershock lineaments (Hardebeck and Shelly, 2014). 3-D finite-difference simulations of these FZTWs characterize a ∼500 m-wide fault damage zone along with the ∼14 km-long mapped surface rupture to depths in excess of 5–7 km, within which seismic wave velocities were reduced by 40%–50%. The low-velocity waveguide on the WNF extends further southward along the FF with a moderate velocity reduction of 30%–35%. On the basis of FZTWs generated by aftershocks in this study and from other geophysical data, Catchings *et al.* (2016) interpret that the overall WNF/FF is at least ∼50 km long, and is likely continuous with the Calaveras Fault.

The FZTWs generated by near-surface explosions detonated within the rupture zone and recorded at a long seismic array deployed across multiple faults in 2016 show the rupture branching structure at shallow depth during dynamic rupture of the 2014 $M6$ mainshock. Multiple rupture zones along at least three fault strands of the WNFZ, likely connecting together at 2–3 km depth and extending down to 5–7 km along the main WNF. Observations and 3-D finite-difference simulations of FZTWs generated by both aftershocks and explosions show the large amplitudes and long wavetrains at stations located within the fault zone. It infers that a great amount of seismic energy is localized within the damage zones along multiple strands of the WNFZ due to the trapping effect of low-velocity waveguides. The localization and amplification of FZTWs due to waveguide effect may have strengthened ground shaking. Therefore, the longer and more continuous WNF/FF zone is capable to pose significant regional hazards from localized amplification, extended ground shaking, and increase damage

along the fault-zone waveguide, even if the surface rupture is limited to only a portion of the overall fault zone (Catchings *et al.*, 2016).

Chapter 2: "The Calico Fault Compliant Zone at Depth Viewed by Fault-Zone Trapped Waves from Teleseismic Earthquakes" by Yong-Gang Li.

An outstanding question in study of the fault zone structure is the depth extent of the low-velocity damage zone along the fault. Some researchers argue that the low-velocity damage zone on faults is a near-surface feature that reaches only down to the top of seismogenic zone at the depth less than 2–3 km (e.g., Ben-Zion *et al.*, 2003; Lewis *et al.*, 2010). Others argue that it extends from the surface across seismogenic zone at depths to ∼10 km depth (e.g., Korneev *et al.*, 2003; Li *et al.*, 2000, 2012, 2014). Wu *et al.*, (2010) showed that the low-velocity waveguide on the San Andreas Fault (SAF) at Parkfield, California extends to the depth of 10 km or more using San Andreas Fault Observatory Drilling (SAFOD) borehole data. Ellsworth and Malin (2011) document a profound zone of rock damage on the Parkfield SAF downwards to at least half way (>5–6 km) through the seismogenic crust using both P-type and S-type of FZTWs recorded at the SAFOD borehole seismograph. FZTWs recorded at Parkfield surface and borehole stations shows that the LVZ on the Parkfield SAF extends to the depth of at least 7–8 km and the velocity reduction within the damage zone decreases with depth due to the increasing confining pressures (Li and Malin, 2008). Although FZTWs generated by explosions and local earthquakes have been used for characterization of the subsurface fault damage structure, It is hard to provide a good image of the deep fault zone due to the poor coverage of wave propagation path from these seismic sources located at shallow depths to recording stations at the surface.

In this chapter, the author introduces a new-type of FZTWs first time identified in seismograms recorded at a square seismic array consisting of 40 intermediate-period stations and 60 short-period stations deployed atop the Calico Fault (CF) in Mojave Desert, California for teleseismic earthquakes. The author examined the data from 26 $M \geqslant 6$ teleseismic earthquakes occurring in 2016 at distances of 40°–80° great circles to the seismic array site. He found prominent wavetrains characterized by large amplitudes and long durations of 3.5–4.0 s following the first P-arrival and 6–8 s after the Moho converted P-to-S waves in teleseisms recorded at stations located within the ∼1 km-wide compliant zone across the CF trace. These wavetrains with long coda durations are interpreted to be FZTWs produced within the low-velocity fault compliant zone as the Moho transmitting P wave and converted S wave of the first-arrival P-wave from the teleseismic earthquake enter the bottom of the fault compliant at a certain depth. This type of FZTWs has not been used before, but they appear to have great promise for providing unprecedented constrains of the depth

extension of fault damage zone because these FZTWs arise from seismic waves entering the bottom of fault zone at deep level.

In the previous study on the Calico Fault compliant zone (Cochran, *et al.*, 2009), the FZTWs generated by explosions and local earthquakes had been combined with travel-times inverse and InSAR observations to image the CF low-velocity compliant zone, within which seismic velocities are reduced by 40%–50%, to depths in excess of ∼5 km. In conjunction with the velocity model obtained from the previous study of the CF, current observations and simulations of the FZTWs identified in teleseisms show the Calico fault compliant zone with velocity reduction of ∼50% to depth at least 8 km beneath Mojave Desert.

Chapter 3: "Towards Real-Time Earthquake Ground-Motion Estimation Based on Full-3D Earth Structure Models" by Po Chen, En-Jui Lee and Wei Wang.

Current efforts to mitigate seismic hazards mainly focus on three areas: (i) long-term probabilistic ground-motion estimate using ground-shaking maps which plot the probability of ground motion exceeding some threshold in different areas in the next 50 years (e.g., Frankel *et al.*, 2002; Petersen *et al.*, 2008), (ii) rapid post-earthquake ground-motion notification provided by seismic networks which often consist of large numbers of telemetered seismic stations equipped with high-dynamic range broadband and strong-motion instruments (e.g., Kanamori *et al.*, 1997; Hauksson *et al.*, 2001), and (iii) earthquake early warning (EEW) which fills in the gap between long-term measures such as (i) and post-earthquake short-term measures such as (ii). EEW aims to provide an early warning few seconds to tens of seconds before strong ground shaking strikes, thus may allow implementing certain emergency mitigation efforts.

Strong ground motion during disastrous earthquakes depends upon the earthquake source that generates seismic waves and the 3D geological structure through which seismic waves propagate. Kinematic properties of the earthquake source can be estimated from seismic waveform data recorded at broadband 3-component seismic stations located in the vicinity of the earthquake source. Realistic 3D crustal structure models can be constructed beforehand through full-3D seismic waveform tomography (F3DT) using seismic waveform data from previous small to medium-sized earthquakes and ambient-noise Green's functions (e.g., Chen and Lee, 2015). Once an estimate of the seismic source and also a 3D structure model are available, synthetic seismograms and ground motion at sites of interest can be computed in real-time through the use of the reciprocity principle. In the past two decades, seismic networks have become denser and denser and also significant progresses have been made in communication technologies. On the other hand, significant progresses have been made in numerical methods for solving the elastodynamic equation in complex 3D geological media. Both of them make EEW based on full-3D seismic waveform inversion (F3DWI) an increasingly more useful option for seismic hazard mitigation.

In this chapter, authors explore the feasibility of real-time earthquake ground-motion estimation (forecast) using results from their previous studies in Southern California. They introduce in detail the state-to-art methods of numerical waver-equation solver used for solving the elastodynamic equation and receiver Green's tensor (RGT) with reciprocity for providing exact partial derivatives of the waveforms to obtain the strain fields at the receiver locations, on which the F3DWI-EEW is based. These methods include the finite-difference, finite-element, pseudo-spectral, spectral-element, discontinuous-Galerkin methods. For source inversion, the centroid moment tensor (CMT) point-source representation and the finite moment tensor (FMT) representation are developed for up to 14-parameters describing the spatial and temporal dimensions of a source and the directivity of the rupture process. Because the accuracy of the 3D seismic velocity model affects the overall performance of the EEW system, it is therefore critical to improve the accuracy of the 3D seismic velocity model. The Southern California Earthquake Center (SCEC) has been supporting the development of various velocity models in Southern California, including the latest updated model CVM-S4.26 of Thomas Jordan's research group (Lee *et al.*, 2014a). This model shows many small-scale structural features that do not exist in the previous velocity models. The authors have justified the feasibility of F3DWI-based EEW system having the potential to substantially improve the accuracy of the strong ground motion warning. For example, the synthetic peak-ground-velocity (PGV) map can then be computed using a simple kriging algorithm in less than 1 s, showing excellent agreement with the actual post-earthquake observed PGV map in Southern California.

Chapter 4: "Comparisons of ETAS Models on Global Tectonic Zones with Computing Implementation" by Annie Chu.

Branching point process models such as the Epidemic-Type Aftershock Sequence (ETAS) models are often used in modeling seismic catalogs to predict future seismicity. The ETAS model is a type of Hawkes point process model and is also called branching or self-exciting point process. In Hawkes point process, triggered events are those triggered by previous seismic activity while background events are the events treated as always existing and not being triggered by previous events. The discretion whether an event is a background event or triggered event is not observable, but is stochastically determined by model fitting. Models described for Hawkes point process are epidemic (Ogata, 1988), i.e., an earthquake can produce aftershocks like offspring, and the aftershocks produce their aftershocks, and so on. Ogata (1998) extended the temporal ETAS model to describe the space-time-magnitude distribution of earthquake occurrences by introducing circular or elliptical spatial functions into the triggering function; two forms of the conditional rate are proposed. Different triggering functions are used in Ogata's Model A and Model B.

Chu *et al.* (2011) have discovered differences in background seismicity rates, triggering behaviors, and seismicity patterns such as rate of swarming of five global earthquake zones with different tectonic structures, by fitting model parameters using Ogata's Model B. In the present Chapter, Ogata's Model A is compared with Model B in aspect of their computation and fitting-goodness. At first, the Author describes tectonic zones defined by Bird (2003) and earthquake catalogs analyzed in this study, and presents two models of Ogata (1998). The mathematical details in computational methods of expectation-maximization (EM)-type algorithm proposed by Veen and Schoenberg (2008) are then described in implementation of Model A and Model B. Finally, the computation results of catalogs in various time windows and tectonic zones as well as a comparison among them are given consequently.

In this study, different features have been revealed by data analysis using ETAS models on five global tectonic zones. Model A has a spatial response kernel scaled by the magnitude of the triggering earthquake and Model B is non-scaled. Although both models are commonly used in seismic data analysis, Model A almost always takes less computing time and iterations to reach convergence of model parameter estimation, and has a better chance for the parameters to converge to the maximum likelihood estimates (MLEs). On the other hand, Model B fits some seismic regions better than Model A, but computing time may be sacrificed for large catalogs. Catalogs from long and narrow geographical regions are harder to attain convergence for MLEs when Model B is used. In order to compare the two models in goodness-of-fit, the Akaike's information criterion and information gain (Akaike, 1974) are used. Results show that Model A fits better in some regions like Southern California while Model B fits better for other regions like Japan Honshu.

Chapter 5: "Distribution of Earthquake-Triggered Landslides across Landscapes: Towards Understanding Erosional Agency and Cascading Hazards" by Gen Li, A. Joshua West, Alexander L. Densmore, Zhangdong Jin, Fei Zhang, Jin Wang, and Robert G. Hilton.

In mountainous regions, such as the eastern margin of the Tibetan Plateau in China, earthquake-triggered landslides are a critical geo-hazard, a major agent of erosion, and a powerful driver of the carbon cycle. In order to learn how landslides distribute across landscapes provides key information for hazard management and for better understanding orogenic evolution and the cycling of carbon, authors of this chapter present the distribution of landslides caused by the 2008 $M_{\mathrm{w}}7.9$ Wenchuan earthquake at the eastern margin of the Tibetan Plateau in the context of recent advances in understanding landslide spatial patterns.

First, authors review previous studies of earthquake-triggered landslides associated with Wenchuan and other earthquakes, and conduct new analysis to

explore how the Wenchuan earthquake induced massive landslides across the steep Longmen Shan range. Many researchers have made their contributions to a Wenchuan landslide inventory in mapping landslides by various ways (Huang and Li, 2009; Dai *et al.*, 2011; Gorum *et al.*, 2011; Parker *et al.*, 2011; Xu *et al.*, 2011, 2014; Fan *et al.*, 2012; Yuan *et al.*, 2013). Li *et al.* (2014) mapped landslides using semi-automated algorithms and manual segregation of amalgamated landslide features, and examined the Wenchuan landslide inventory in the context of a generalized model of earthquake mass balance. Recently, Li *et al.* (2016) combined the landslide inventory map with analysis of digital topography, and quantified the connectivity between earthquake-triggered landslides and the regional fluvial network. Gorum and Carranza (2015) explored what mechanism controls patterns of landslides from fault-types. They suggest that for the Wenchuan case, landslides associated with thrust-slips occur over a wider zone from the fault trace than the range of landslides in the strike-slip scenario. Several studies have looked into not only the co-seismic landslides but also the post-seismic landslides caused by rainfall and reactivation of the co-seismic landslide debris in the epicentral region (e.g., Tang *et al.*, 2011; Zhang *et al.*, 2014).

Then, authors combine the landslide inventory map with analysis of digital topography, regional geology, and ground motion data to explore the controlling factors of the Wenchuan-triggered landslides concerning seismological parameters, topography, and lithology. They evaluate how and to what extent landslide debris supplies sediments to rivers based on locations of the Wenchuan landslides relative to river networks. They examine the aspects of landslides and discuss how the preferred facing directions of landslides along the Yingxiu-Beichuang fault rupture provide information about the characteristics of earthquake source, seismic ground motion, and rupture propagation. They estimate the average geometric profiles of hillslopes in the Longmen Shan region, quantify how Wenchuan landslides locate relative to hillslope ridges and river channels, and explore the implications for landslide triggers and landslide-channel connectivity. Finally, authors model the pattern of Wenchuan landslides adapting the functional form of the law of seismic wave attenuation which accounts for both geometric spreading and quality decay (Meunier *et al.*, 2007). In conjunction with models (e.g., Keefer, 1994; Malamud *et al.*, 2004; Marc *et al.*, 2016) that predict total volumes of earthquake-triggered landslides, this approach has promise for predicting the magnitude and the pattern of landslides caused by earthquakes with known characteristics of the seismogenic faults and the seismotectonic settings. This eventually leads a better hazard prediction both during earthquake events and in their aftermath.

Chapter 6: "A Review on Numerical Models for Coal and Gas Outbursts" by Yucang Wang and Sheng Xue.

An outburst of coal and gas is an event where coal or rocks together with large amount of gas are suddenly ejected from an advancing face to the excavation area. Coal and gas outbursts have resulted in major hazards in underground coal mining all over the world. Although extensive research efforts over more than 150 years, the fundamental mechanism causing coal and gas outbursts still remains unknown. There are many factors influencing the occurrence of an outburst, among which the gas content, rate of gas desorption, coal strength, stress level and some geological structures are most important. Except for in-situ investigations, the laboratory tests and analytical studies, the use of numerical simulations can provide useful insights on outbursts.

In this chapter, the most outburst models which have been proposed in the past two or three decades are reviewed. The authors find that current existing models only capture some aspects of outbursts and cannot explain all of the phenomena and process leading to an outburst. Those models are too simple to include some important mechanisms, such as the fracture and fragmentation of the solid and two-way solid-fluid coupling. Therefore, authors investigate the most important factors controlling the occurrence of outbursts, and discuss what a reliable numerical model should include in order to reproduce the realistic behaviours of outbursts. Authors finally propose a new model strategy which couples discrete element method (DEM) for fracture and Lattice Boltzmann method (LBM) for fluid flow. The new model includes more basic mechanisms and influencing factors. A completely coupled code of solid and fluid is based on the two widely used open source codes: ESyS-Particle and OpenLB (Wang *et al.*, 2012, 2014; Xue *et al.*, 2015). The two-way coupling between DEM and LBM is realized by data exchange and finally the two codes can be combined into one united code with the united input, data flow, output, MPI calls and visualization tool. The preliminary results show that the coupled model is encouraging as the entire process of an outburst is well reproduced. The discrete element model introduced in this chapter is also useful for reproducing the compressive-tensile strength ratio of rocks in earthquake study.

Chapter 7: "International Consultation on the Likelihood of Earthquakes: Two Cases in 2008 after the Wenchuan Earthquake" by Zhongliang Wu.

The author of this chapter presents documents of communications and paper reviews about the international consultation on earthquake precast after the 2008 $M8$ Wenchuan earthquake, for which he witnessed and kept all the records. After the $M8$ Wenchuan earthquake on May 12, 2008, aftershock activity became a great threat to the post-earthquake relief and reconstruction process in the earthquake hazardous region. This situation was getting worse because there

were a bunch of landside lakes caused by the mainshock in the region of Western Sichuan. Meanwhile, a paper issued by a group of Russian scientists pointed out that a magnitude $M6.5$–7.0 earthquake would occur near Beijing around August of 2008. It caused much severe concerns because the venue and time of this forecasted earthquake were tight to the 2008 Beijing Olympic Games to be held in Beijing in the summer of 2008. The estimation of Wenchuan aftershock hazard and the evaluation of a $M6.5+$ near-capital earthquake forecast requested seismologists and earth scientists to make full use of the existing means of earthquake predictability for the seismic safety of the society. In order to dealing with these earthquake forecasting issues, six experts from different countries were invited by the China Earthquake Administration (CEA) to discuss the Wenchuan aftershock sequence and review the paper published by the Russian scientists while the CEA had carried out the estimation of Wenchuan aftershock hazard domestically. Indeed, it was the first time for Chinese seismological community to organize an international consultation facing to forward forecast for a real earthquake situation.

In this chapter, the author summarizes the two real cases of earthquake forecasting: one is the Wenchuan aftershocks and another is the $M6.5$–7.0 earthquake near Beijing in 2008 via the international communication, and provides invaluable materials for study of the earthquake forecast. These materials involve with estimate based on Coulomb failure stress (CFS) changes, analysis of seismicity and estimate of aftershock probability based on the Gutenberg-Richter's Law and the Omori's Law, estimate of the duration of the strong aftershock sequence, analysis using the (SSE) algorithm based on pattern recognition as well as the ETAS model-based analysis and estimate of aftershock probabilities. From the review comments, the forecast for the near-capital earthquake was turned down eventually. In fact, there was no earthquake over magnitude $M5$ around Beijing in August, 2008. The author argued that the international collaboration would be needed in earthquake science and helpful to reduce seismic disaster risk.

The purpose of this book is to introduce the sophisticated approaches in earthquake investigation and geophysical research with case studies. In summary, the following methods and results presented in this book will be of particular interest to the readers:

- Subsurface fault damage zone continuity and rupture branching viewed by guided waves
- Fault-zone trapped waves from teleseismic earthquake for addressing the deep fault zone
- Towards real-time estimation of strong motion by F3DT tomography
- ETAS models to make future seismic predictions for global earthquake zones with different tectonic structures

- Erosional agency and cascading hazards for earthquake-triggering landslides
- Distinct element and lattice Boltzmann model for simulation of coal and gas outbursts
- International consultation for two cases in 2008 after the Wenchuan earthquake

This book is a self-contained volume which starts with an overview of the subject then explores each topic in details. Extensive reference lists and cross references with other volumes to facilitate further research. Content suited for both senior researchers and graduate students in geosciences who would broaden their horizons about observational, computational and applied seismology and geophysics. This book covers multi-disciplinary topics to allow readers to gasp the methods and techniques used in data analysis and numerical modeling for structural, physical and mechanical interpretation of geophysical and earthquake phenomena to aid the understanding of earthquake processes and hazards.

The editor of this book series wishes to thank many reviewers of multiple chapters, including Walter Money, John Evans, Brad Aagaard, Heidi Houston, En-Jui Lee, Yu-Ling Chen, Niels Hovius, Patrick Meunier, Odin Marc, Ke Li, Shi Che, Guomin Zhang, Jie Liu, Haikun Jiang and Long Jiang for providing helpful reviews on chapters of this book and for their comments and discussion on this book. We are grateful to many organizations and individuals, including HEP Director Bingxiang Li and Editor Yan Guan, who help to make our book series possible.

Key words: Fault-zone guided waves, fault damage zone continuity, rupture branching, South Napa earthquake, teleseismic earthquake, full-3D waveform tomography, ground motion real-time estimation, receiver Green's tensor, centroid moment tensor and finite moment tensor, inversions, Epidemic-Type Aftershock Sequence (ETAS) models, earthquake hazard, landslide pattern, Wenchuan earthquake, erosional agency, coal and gas outbursts, discrete element method, earthquake likelihood, international consultation, aftershock probability, Coulomb failure stress.

References

Akaike, H. (1974). A new look at the statistical model identification. IEEE Transactions on Automatic Control, AC-19, 716–723.

Baltay, A.S and J. Boatwright (2015). Ground motion observations of the 2014 South Napa earthquake. Seis. Res. Lett., 86, 355-360, doi: 10.1785/0220140232.

Ben-Zion, Y., Z. Peng, D. Okaya, L. Seeber, J.G. Armbruster, N. Ozer, A.J. Michael, S. Barris, and M. Aktar (2003). A shallow fault zone structure illuminated by trapped waves in the Karadere-Dusce branch of the North Anatolian Fault, Western Turkey. Geophys. J. Int., 152, 699–717.

Brocher, T.A., A. Baltay, J.L. Hardebeck, J. Polet, E. Langenheim, A.L. Llenos, J.J. Lienkaemper, D.P. Schwartz, J.L. Blair, T. Dawson, K.W. Hudnut, D.R. Shelly, D. Dreger, J. Boatwright, B.T. Aagaard, D. J. Wald, R.M. Allen, W.D. Barnhart, K.L. Knudsen, B.A. Brooks, K.M. Scharer (2015). The M6.0 24 August 2014 South Napa earthquake. Seism. Res. Lett. 86, 2A, doi: 10.1785/0220150004.

Catchings, R.D., M.J. Rymer, M.R. Goldman, J.A. Hole, R. Huggins, and C. Lippus (2002). High-resolution seismic velocities and shallow structure of the San Andreas Fault zone at Middle Mountain, Parkfield, California. Bull. Seis. Soc. Am., 92, 2493–2503.

Chen, P. and E.-J. Lee (2015). Full-3D Seismic Waveform Inversion—Theory, Software and Practice. Springer.

Chu, A., F.P. Scheoenberg, P. Bird, Jackson, D.D. Jackson, and Y.Y. Kagan (2011). Comparison of ETAS parameter estimates across different global tectonic zones. Bull. Seismol. Soc. Ameri., 101(5), 2323–2339.

Cochran, E.S., Y.G. Li, P.M. Shearer, S. Barbot, Y. Fialko, and J.E. Vidale (2009). Seismic and geodetic evidence for extensive, long-lived fault damage zones. Geology, 9.37(4), 315–318, doi: 10.1130/G25306A.1; Data Repository item 2009082.

Dai, F.C., C. Xu, X. Yao, L. Xu, X.B. Tu, and Q.M. Gong (2011). Spatial distribution of landslides trig-gered by the 2008 M_s8.0 Wenchuan earthquake, China. J. Asian Earth Sci., 40(4), 883–895, doi: 10.1016/j.jseaes.2010.04.010.

Ellsworth W.L. and P.E. Malin (2011). Deep rock damage in the San Andreas Fault revealed by P- and S-type fault zone guided waves, Sibson's volume. Geological Society Special Publication, New Zealand, 359, 39–53.

Fan, X.M., C.J. van Westen, O. Korup, T. Gorum, Q. Xu, F.C. Dai, R.Q. Huang, and G.H. Wang (2012). Transient water and sediment storage of the decaying landslide dams induced by the 2008 Wenchuan earthquake, China. Geomorphology, 171, 58–68.

Frankel, A.D., E.H. Field, and M.D. Petersen (2002). Documentation for the 2002 update of the national seismic hazard maps. U.S. Geological Survey Open-File Report.

Gorum, T. and E.J. M. Carranza (2015). Control of style-of-faulting on spatial pattern of earth-quake-triggered landslides. Int. J. Environ. Sci. Technol., 1–24.

Gorum, T., X.M. Fan, C.J. van Westen, R.Q. Huang, Q. Xu, C. Tang, and G.H. Wang (2011). Distribu-tion pattern of earthquake-induced landslides triggered by the 12 May 2008 Wenchuan earthquake. Geomorphology, 133(3–4), 152–167.

Hardebeck, J.L. and D.R. Shelly (2014). Aftershocks of the 2014 M6 South Napa Earthquake: Detection, Location, and Focal Mechanisms, Abs. S33F-4927, presented at 2014 Fall Meeting, AGU, San Francisco, Calif., 15–19 Dec.

Hauksson, E., P. Small, K. Hafner, R. Busby, R. Clayton, J. Goltz, and D. Given (2001). Southern California seismic network: Caltech/USGS element of TriNet 1997–2001. Seismological Research Letters, 72(6), 690–704.

Kanamori, H., E. Hauksson, and T. Heaton (1997). Real-time seismology and earthquake hazard mitigation. Nature, 390, 461–464.

Keefer, D.K. (1994). The importance of earthquake-induced landslides to long-term slope erosion and slope-failure hazards in seismically active regions. Geomorphology, 10(1–4), 265–284.

Korneev, V.A., R.M. Nadeau, and T.V. McEvilly (2003). Seismological studies at Parkfield IX: Fault-zone imaging using guided wave attenuation. Bull. Seism. Soc. Am. 80, 1245–1271.

Lee, E.-J., P. Chen, T.H. Jordan, P.B. Macchling, M.A. Denolle, and G.C. Beroza (2014). Full-3D tomography for crustal structure in Southern California based on the scattering-integral and the adjoint-wavefield methods. J. Geophys. Res., 119(8), 6421–6451.

Lewis, M. A. and Y. Ben-Zion (2010). Diversity of fault zone damage and trapping structures in the Parkfield section of the San Andreas Fault from comprehensive analysis of near fault seismograms. Geophys. J. Int., doi: 10.1111/j.1365-246X.2010.04816.x.

Li, G., A.J. West, A.L. Densmore, Z. Jin, R.N. Parker, and R.G. Hilton (2014). Seismic mountain building: Landslides associated with the 2008 Wenchuan earthquake in the context of a generalized model for earthquake volume balance. Geochemistry, Geophysics, Geosystems, 15(4), 833–844.

Li, G., A.J. West, A.L. Densmore, D.E. Hammond, Z. Jin, F. Zhang, J. Wang, and R.G. Hilton (2016). Connectivity of earthquake-triggered landslides with the fluvial network: Implications for landslide sediment transport after the 2008 Wenchuan earthquake. Journal of Geophysical Research: Earth Surface, 121(4), 703–724.

Li, Y.G. and J.E. Vidale (1996). Low-velocity fault zone guided waves; numerical investigations of trapping efficiency. Bull. Seis. Soc. Am., 86, 371–378.

Li, Y.G. and P.E. Malin (2008). San Andreas Fault damage at SAFOD viewed with fault-guided waves. Geophys. Res. Lett., 35, L08304, doi:10.1029/2007GL032924.

Li, Y.G., G. De Pascale, M. Quigley, and D. Gravely (2014). Fault damage zones of the M7.1 Darfield and M6.3 Christchurch earthquakes characterized by fault-zone trapped waves. Tectonophysics, 618, 79–101, 10.1016/j.tecto.2014.01.029.

Li, Y.G., J.E. Vidale, K. Aki, and F. Xu (2000). Depth-dependent structure of the Landers fault zone using fault zone trapped waves generated by aftershocks. J. Geophys. Res., 105, 6237–6254.

Li, Y.G., P. Malin, and E. Cochran (2012). Fault-zone trapped waves: High-resolution characterization of the damage zone on the Parkfield San Andreas Fault at depth. In: Imaging, Modeling and Assimilation in Seismology, edited by Y. G. Li. Beijing: Higher Education Press.

Malamud, B.D., D.L. Turcotte, F. Guzzetti, and P. Reichenbach (2004). Landslides, earthquakes, and erosion. Earth and Planetary Science Letters, 229(1–2), 45–59.

Marc, O., N. Hovius, P. Meunier, T. Gorum, and T. Uchida (2016). A seismologically consistent expression for the total area and volume of earthquake-triggered landsliding. Journal of Geophysical Research: Earth Surface, 121(4), 2015JF003732.

Melgar D., J. Geng, B.W. Crowell, J.S. Haas, Y. Bock, W.C. Hammond, and R.M. Allen (2015). Seismogeodesy of the 2014 M_{w}6.1 Napa earthquake, California: Rapid response and modeling of fast rupture on a dipping strike-slip fault. J. Geophys. Res., 120, doi: 10.1002/2015JB011921.

Meunier, P., N. Hovius, and A.J. Haines (2007). Regional patterns of earthquake-triggered landslides and their relation to ground motion. Geophysical Research Letters, 34(20), L20408.

Ogata, Y. (1988). Statistical models for earthquake occurrences and residual analysis for point processes. Journal of the American Statistical Association, 83, 9–27.

Ogata, Y. (1998). Space-time point process models for earthquake occurrences. Annals of the Institute of Statistical Mathematics, 50, 379–402.

Parker, R.N., A.L. Densmore, N.J. Rosser, M. de Michele, Y. Li, R.Q. Huang, S. Whadcoat, and D.N. Petley (2011). Mass wasting triggered by the 2008 Wenchuan earthquake is greater than orogenic growth. Nat. Geosci, 4(7), 449–452.

Petersen M.D., A.D. Frankel, and S.C. Harmsen (2008) Documentation for the 2008 update of the United States national seismic hazard maps. U.S. Geological Survey Open-File Report.

Tang, C., J. Zhu, X. Qi, and J. Ding (2011). Landslides induced by the Wenchuan earthquake and the subsequent strong rainfall event: A case study in the Beichuan area of China, Engineering Geology, 122(1–2), 22–33.

Veen, A. and F. Schoenberg (2008). Estimation of space-time branching process models in seismology using an EM-type algorithm. Journal of the American Statistical Association, 103(482), 614–624.

Wang, Y.C., S. Xue, S., and J. Xie (2012). A fully coupled solid and fluid model for simulating coal and gas outbursts with DEM and LBM. AGH Journal of Mining and Geoengineering, 36: 377–384.

Wang, Y.C., S. Xue, and J. Xie (2014). Two-way Coupling of solid-fluid: Discrete element model and lattice Boltzmann model. In: Seismic Imaging, Fault Damage and Heal, edited by Y.G. Li., Beijing: Higher Education Press, 143–172.

Wei, S.J., S. Barbot, R. Graves, J.J. Lienkaemper, T. Wang, K. Hudnut, Y. Fu, and D. Helmberger (2015). The 2014 $M_{\rm w}$6.1 South Napa earthquake: A unilateral rupture with shallow asperity and rapid afterslip. Seis. Res. Lett., 86, 2A.

Xue, S., L. Yuan, J.F. Wang, Y.C. Wang, and J. Xie (2015). A coupled DEM and LBM model for simulation of outbursts of coal and gas. Int. J. Coal Sci. Technol., doi: 10.1007/s40789-015-0063-4.

Xu, C., X. Xu, X. Yao, and F. Dai (2014). Three (nearly) complete inventories of landslides triggered by the May 12, 2008 Wenchuan $M_{\rm w}$7.9 earthquake of China and their spatial distribution statistical analysis. Landslides, 11(3), 441–461.

Xu, Q., S. Zhang, and W. Li (2011). Spatial distribution of large-scale landslides induced by the 5.12 Wenchuan earthquake. J. Mt. Sci., 8(2), 246.

Yuan, R.M., Q.H. Deng, D. Cunningham, C. Xu, X.W. Xu, and C.P. Chang (2013). Density distribution of landslides triggered by the 2008 Wenchuan earthquake and their relationships to peak ground acceleration. Bulletin of the Seismological Society of America, 103(4), 2344–2355.

Zhang, S., L.M. Zhang, and T. Glade (2014). Characteristics of earthquake- and rain-induced landslides near the epicenter of Wenchuan earthquake. Engineering Geology, 175, 58–73.

Author Information

Yong-Gang Li
Department of Earth Sciences, University of Southern California,
Los Angeles, CA 90089-0740, USA
E-mail: ygli@usc.edu

Chapter 1

Fault-Zone Trapped Waves Generated by Aftershocks and Explosions to Characterize the Subsurface Rupture Zone of the 2014 M_w6.0 South Napa Earthquake, California

Yong-Gang Li, Rufus D. Catchings, and Mark R. Goldman

In this chapter, authors present the fault-zone trapped waves (FZTWs) generated by aftershocks of the M_w6.0 South Napa earthquake on 24 August 2014 and explosions detonated within the rupture zone in 2016. Prominent FZTWs with large amplitudes and long wavetrains are identified in seismograms which were recorded at three ∼1-2-km long cross-fault seismic arrays (A1, A2 and A3) and four along-fault seismographs deployed in 2014 and a ∼15.5-km-long cross-fault array (W-E Line) deployed in 2016 at the West Napa Fault Zone (WNFZ) that ruptured in the 2014 M6 mainshock. We analyzed waveforms of these FZTWs from 55 aftershocks and two shots located within the rupture zone in both time and frequency to characterize the subsurface fault damage structure associated with this earthquake. Observations and 3D finite-difference simulations of these FZTWs suggest a 400–500 m wide subsurface rupture zone with the ∼14-km-long mapped surface breaks along the main fault strand of the WNFZ, within which seismic wave velocities reduced by 40%–50%. Post-S coda durations of FZTWs increase with focal depths and epicentral distances from the recording arrays, suggesting that the low-velocity waveguide along the WNFZ to depths in excess of 5–7 km extends further southward with a moderate velocity reduction of 30%–35% to Franklin Fault (FF). The combined WNF/FF zone is ∼50 km long between A1 and A3. The FZTWs generated by two shots and recorded at the 15.5 km-long W-E Line in 2016 show branching structure of the rupture zone

https://doi.org/10.1515/9783110543551-025

along multiple fault strands of the WNFZ at shallow depth, and a waveguide with moderate seismic velocity reduction along the Carneros Fault subparallel to the WNFZ and connecting the north end of FF. The localization and amplification of FZTWs due to fault-waveguide effect might have strengthened the ground shaking along the WNFZ and the faults farther to the south (Catchings *et al.*, 2016; Li *et al.*, 2016).

Key words: South Napa earthquake, multiple rupture zones, fault rock damage, fault-zone trapped waves and waveguide effect.

1.1 Introduction

Intense fracturing during earthquakes, brecciation, liquid-saturation, and possibly high pore-fluid pressure near the fault are thought to create low-velocity zones with widths ranging from a few hundred meters to a few kilometers (Mooney and Ginzburg, 1986; Catchings *et al.*, 2002, 2013, 2014a; Cochran *et al.*, 2009). These naturally formed low-velocity zones (LVZs) can efficiently trap seismic waves generated by earthquakes occurring within or close to the LVZs and active sources applied within the fault zone. Fault-zone trapped waves (FZTWs), also referred to as guided waves, arise from coherent multiple reflections and corresponding high reflection coefficients at the boundaries between the low-velocity fault zone and the surrounding higher velocity rocks (Li *et al.*, 1990, 1998). FZTWs are characterized by large amplitudes and long dispersive wavetrains) (Li and Leary, 1990; Li and Vidale, 1996; Ben-Zion, 1998; Igel *et al.*, 2002). Therefore, FZTWs can be used to evaluate intra-fault damage and the continuity and branching of rupture zones at seismogenic depths. The magnitude of fault rock damage and multiple ruptures along active faults and their temporal variations over the earthquake cycle have been observed in previous study of rupture zones of the 1994 M9.4 Landers and 1999 M7.1 Hector Mine earthquakes (Li *et al.*, 1994, 1998, 2000, 2003a, 2003b, 2014; Vidale and Li, 2003), and the rupture zone of the 2014 M6 Parkfield earthquake on the San Andreas Fault in California (Li *et al.*, 1997, 2003, 2006; Li and Malin, 2008).

In this Chapter, we use FZTWs generated by aftershocks and explosions to characterize the subsurface structure of fault rock damage along the West Napa Fault Zone (WNFZ) that ruptured in the $M_{\rm w}$6.0 South Napa earthquake occurring southwest of the city of Napa, California on 24 August, 2014, as well as the adjacent faults (Fig. 1.1). The WNFZ is located at east of the Hayward-Rodgers Creek Fault (HRCF) system and approximately 13 km west of the Concord-Green Valley Fault (CGVF) system. Both fault systems have generated historic damaging earthquakes (Bakun, 1999; Wesling and Hanson, 2008; Brocher *et al.*, 2014). However, there is evidence of two previous moderate-to-large his-

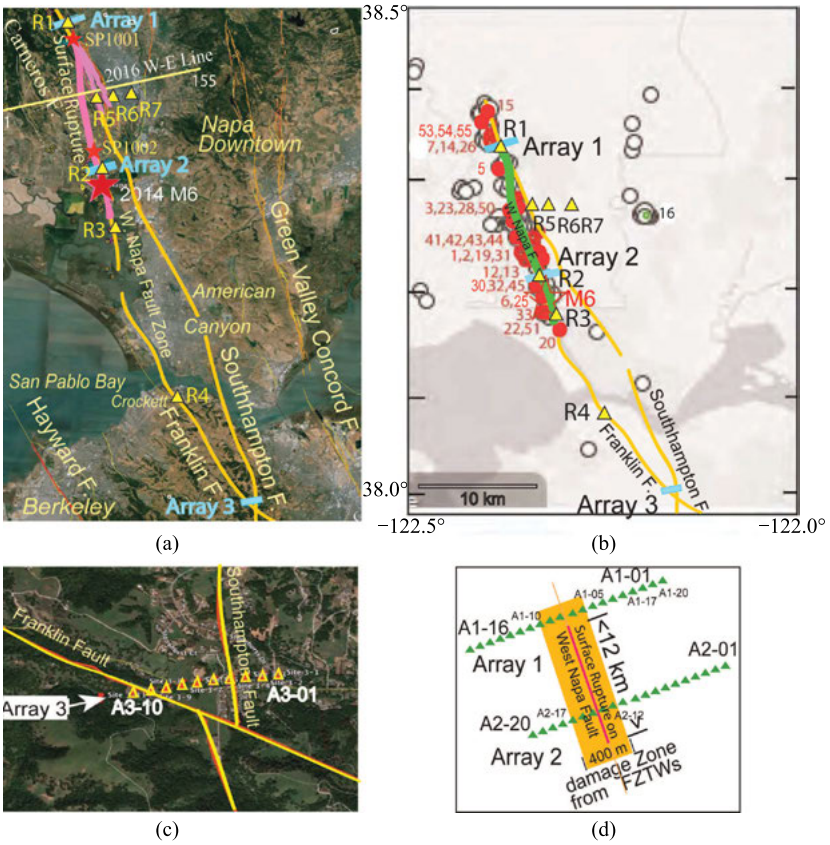

Fig. 1.1 **(a)** Map shows the 2014 M_w6.0 South Napa earthquake (star), aftershocks (dot), surface ruptures (thick line), seismic Array 1, Array 2 and Array 3 (solid bars), 7 REFTEK-130 seismographs R1–R7 (yellow triangles), and faults (thin lines) (adapted from Li *et al.*, 2016). **(b)** Map shows aftershocks (circles) recorded on the three seismic arrays between August 28 and September 9 of 2015, including 41 aftershocks (solid circles with numbers) occurring within the rupture zone along the WNF for which we observed prominent FZTWs. The thick line denotes the 2014 surface rupture zone. **(c)** Map shows the locations of 10 stations (triangles) of A3. The Franklin and Southhampton faults cross A3 and intersect just south of the recording array. **(d)** Schematic diagram showing station locations (triangles) of A1 and A2 (thick bars in Fig. 1.1a) deployed across the northern projection and the southern part of the WNF surface rupture. Thick line denotes the 14-km-long surface rupture along the WNF, consisting of a 400-m-wide rupture zone (marked by a rectangle) determined by FZTWs, within which rocks were severely damaged by the 2014 $M6$ mainshock.

toric earthquakes occurring on the WNFZ, the 31 March 1898 M5.8–6.4 Mare Island earthquake (Hough, 2014) and the 3 September 2000 M5.2 Yountville earthquake (Langenheim *et al.*, 2006).

The 2014 South Napa $M6$ mainshock occurred at a depth of 9.4-km, with aftershocks extending between 2 km and 12 km depth (Hardebeck and Shelly,

2014). The mainshock epicenter was located at ∼6 km northwest of the City of American Canyon and 1.7 km south of the southernmost mapped surface rupture. The epicenter was also close to mapped trace of the lesser known fault, the Franklin Fault (Bryant, 2005; Graymer *et al.*, 2002; Wesling and Hanson, 2008). However, the surface rupture did not fall on the main trace of any of these faults, but instead between the Carneros and West Napa faults and northwest along strike from the northern mapped end of the Franklin Fault. 3D surfaces show that the Carneros Fault is a steeply west-dipping fault that runs just west of the near-vertical 2014 rupture plane (Graymer, 2014). The Carneros Fault does not appear to have been involved in the earthquake, although relocated aftershocks suggest possible minor triggered slip on it. To south, the Franklin Fault is a steeply east-dipping fault, suggesting that the South Napa earthquake occurred on the northernmost reach of the Franklin Fault within it's 3D junction with the West Napa Fault (WNF). UAVSAR data (Donnellan *et al.*, 2014) and relocated aftershocks (Hardebeck and Shelly, 2014) suggest that the main WNF experienced triggered slip and afterslip along a length of roughly 20 km. Therefore, it is possible that the 2014 rupture took place along a largely unrecognized westerly strand of the WNF which is also steeply west-dipping based on focal mechanisms of the mainshock and connection of the surface rupture to the relocated hypocenter. Focal solutions by UC Berkeley show right-lateral motion along a plane having a similar strike (∼158°) and a rake of 172° (Brocher *et al.*, 2015).

The 2014 mainshock produced ∼14 km of surface rupture along the WNF, with maximum surface displacements of 40–45 cm (Brooks *et al.*, 2014; Hudnut *et al.*, 2014). The mapped surface rupture primarily consisted of a zone of right-lateral fractures from less than one meter to more than tens of meters wide. Although the surface rupture varied along the rupture length, it was usually observed as a zone of en echelon left-stepping fractures (Dawson *et al.*, 2014).

Combined UAVSAR and GPS Estimates of Fault Slip for the M_w6.0 South Napa earthquake, results show the slip on a single fault at the south end of the rupture near the epicenter of the event, but the rupture branches out into multiple faults further north near the Napa area (Donnellan *et al.*, 2014). The eastern two sub-parallel faults break the surface, while three faults to the west are buried at depths ranging from 2–6 km with deeper depths to the north and west. The geodetic moment release is equivalent to a M6.1 event. Additional ruptures are observed in the interferogram, but the inversions suggest that they represent a superficial slip that does not contribute to the overall moment release.

The slip patterns of the South Napa earthquake, as derived from seismology and geodesy, show that the co-seismic dislocation extended to ∼12 km depth beneath the southern portion of the epicentral region, with co-seismic slip and afterslip occurring up-dip to the north of the hypocenter (Melgar *et al.*, 2015). The peak slip was predominately right-lateral motion (up to 121 cm) with only a minor dip-slip component. Shallow slip, with the order of 60 cm, occurred at 5

km depth along a 5-km-long segment in the northern part of the surface rupture area. There was also a small 5-km-long patch with ∼15 cm of down-dip slip to the south of the hypocenter.

The rupture propagated mostly to the north and up-dip, directing the strongest shaking toward the City of Napa, where peak ground accelerations between 45% g and 61% g and MMI intensities of VII-VIII were reported (Boatwright *et al.*, 2014). The highest peak ground acceleration ($1g$) in the region was recorded near the town of Crockett, at the Carquinez Bridge probably due to local site conditions (Boatwright *et al*, 2015; Celebi *et al.*, 2015) or to an unusual path effect. However, there are strong positive residuals in strong motion records at stations to the south of the earthquake, suggesting the stronger shaking in the along-strike direction of faults in the region (Baltay and Boatwright, 2015). In particular, these positive residuals may align with the Quaternary-active Franklin or Southhampton faults. Such positive residuals are consistent with a fault-zone waveguide effect along these faults.

To investigate details of the subsurface structure (connectivity and branch) of the rupture zone along the strands of the WNFZ using fault-zone trapped waves (FZTWs), three 1–2 km long seismic recording arrays (A1, A2 and A3) were deployed across the WNFZ, and seven REFTEK-130 seismographs deployed along the WNFZ, immediately after the 2014 South Napa earthquake to recorded aftershocks (Catchings *et al.*, 2014). A part of these data recorded in the 2014 experiment have been used for analyses of peak ground velocities (PGV) and FZTWs in our published papers (Catchings *et al.*, 2016; Li *et al.* 2016). In 2016, a much longer (∼15.5 km in length) seismic array (W-E Line) was deployed across the surface rupture zones along the WNFZ and adjacent faults to record shots detonated within the rupture zone. In this Chapter, we present the FZTWs generated by both aftershocks and explosions, and recorded in the 2014 and 2016 experiments. Our observations and 3-D finite-difference simulations of these FZTWs show the continuity between the WNFZ and the Franklin Fault, and rupture branching along multiple strands of the WNFZ. The waveguide effect of low-velocity fault zones may have localized and amplified ground shaking along the WNFZ and along faults farther to the south even if the surface rupture is limited to only a portion of the WNFZ, consistent with the ground motion observations of Baltay and Boatwright (2015).

1.2 The Aftershock Data and Waveform Analyses

Four days after the $M_{\mathrm{w}}6.0$ South Napa earthquake, the USGS installed three seismic arrays Array 1, Array 2 and Array 3 (called A1, A2, and A3 for short) consisting of a total of 50 short-period (4.5 Hz) seismic stations across the West

Napa Fault (WNF) and adjacent faults for ∼2 weeks (Catchings *et al.*, 2014). 1.9-km-long A1 and A2 were deployed perpendicularly across the West Napa Fault Zone (WNFZ), at locations near the ends of the northern and southern surface ruptures, respectively (Figs.1.1a, 1.1b). A3 was deployed across the intersection of the Franklin and Southhampton faults, which could be southward continuations of the WNFZ (Fig. 1.1c). The station spacing along each array was 100 m, with vertical, fault parallel, and fault perpendicular velocity sensors (4.5 Hz) at each station. The seismometers recorded in continuous mode at 100 samples per second and were synchronized by internal GPS clocks before and after deployment. The internal clocks of the seismographs are usually accurate to within 15 ms over the 3-day deployment period, which is sufficient for our FZTW study. A1 consisted of 20 stations, referred to here as stations A1-01 to A1-20. Stations A1-20 and A1-16 of array 1 (A1) were located at the NE and SW ends of the seismic line (Fig. 1.1d) with latitude and longitude of 38.33986°N, −122.34378°W and 38.33366°N, −122.36535°W, respectively. A2 consisted of 20 stations (A2-01 to A2-20 in Fig. 1.1d), with station A2-01 on the NE end (38.23874°N, −122.30815°W) and station A2-20 on the SW end (38.23454°N, −122.32825°W). A3 consisted of 10 stations (A3-1 to A3-10 in Fig. 1c), with station A3-1 on the NE end (37.56931°N, −122.14027°W) and station A3-10 on the SW end (37.96437°N, −122.15060°W). All station locations of A1, A2 and A3 are shown in Table 1 of a companion paper (Catchings *et al.*, 2016). In the 2014 experiment, 7 REFTEK-130 three-channel seismographs (R1 to R7) with 2Hz L22 sensors were deployed around the WNFZ. 4 stations R1to R4 were located close to the main surface rupture of the $M6$ South Napa earthquake and the south part of the WNF, and stations R4, R5 and R6 were located in Napa Valley away from the surface rupture (Fig. 1.1a, 1b). Locations of stations R1 to R7 are: R1 (38.33204°N, −122.35268°W), R2 (38.23440°N, −122.31657°W), R3 (38.20700°N, −122.28872°W), R4 (38.06802°N, −122.22854°W), R5 (38.29936°N, −122.26774°W), R6 (38.29393°N, −122.24215°W), and R7 (38.29311°N, −122.22725°W).

Approximately 180 aftershocks and local earthquakes were recorded at the three seismic arrays (A1, A2 and A3) and 7 REFTEK stations between August 28 and September 9 (Julian dates 240 to 252) of 2014. We examined the waveform data from all the recorded events and selected a subset of 55 aftershocks from which seismograms show appropriate signal-to-noise ratio for further waveform analysis in this study. Seismograms from other aftershocks were evaluated either having poor signal-to-noise ration or without clear FZTWs. Locations of the 55 aftershocks are shown in Fig. 1.1b. The origin times, locations, and magnitudes of the 55 aftershocks evaluated are listed in Table 1.1. FZTWs were generated by 41 aftershocks, by which we investigate the subsurface fault-zone damage zone and the continuity between the WNRZ rupture zone and Franklin Fault.

Table 1.1 Time, location and measurements of aftershocks in this study.

No.	Date (2014) mm/dd	Julian Date	Time hh:mm:ss	Lat. (38°)	Long. (−122°)	depth (km)	M_D	Post-S Coda Duration(s)			P-to-S Time(s)			Ratio $(t_C - t_S)/(t_S - t_P)$		
								A1	A2	A3	A1	A2	A3	A1	A2	A3
1	08/28	240	22:05:16	.24483	.33317	6.57	2.23	2.4	1.6	5.0	2.0	1.2	6.0	1.2	1.3	0.8
2	08/29	241	04:16:13	.24217	.34033	7.68	2.11	2.4	1.7	4.8	2.1	1.4	5.8	1.2	1.2	0.8
3	08/29		15:39:25	.28433	.36066	6.98	1.49	1.9	1.8	5.2	1.4	1.4	6.5	1.3	1.3	0.8
4	08/29		15:53:03	.27300	.18967	5.36	1.84	1.5	1.0	2.5	3.0	2.5	6.5	0.5	0.4	0.4
5	08/29		20:24:20	.30300	.36017	6.64	1.00	1.6	3.0	–	1.2	2.3	–	1.3	1.3	–
6	08/29		22:34:40	.20550	.31150	9.56	2.37	3.0	1.8	4.2	2.5	1.5	5.0	1.2	1.2	0.8
7	08/30	242	22:21:23	.35667	.37867	4.46	1.48	1.4	3.0	5.5	0.8	2.2	6.5	1.6	1.4	0.8
8	08/31	243	02:10:43	.24400	.34233	7.57	2.04	2.4	1.6	5.0	1.9	1.3	6.0	1.3	1.2	0.8
9	08/31		02:31:14	.25083	.16267	5.51	1.51	1.5	1.0	–	3.3	2.3	–	0.5	0.4	–
10	08/31		03:56:47	.25283	.17233	8.38	2.21	1.5	1.0	2.0	3.3	2.2	6.0	0.5	0.4	0.3
11	08/31		05:14:35	.25100	.16650	7.60	1.28	1.5	1.0	2.5	3.3	2.3	5.3	0.5	0.4	0.5
12	08/31		06:25:35	.24617	.34400	7.71	2.37	2.4	1.7	4.8	2.0	1.3	5.7	1.2	1.2	0.8
13	08/31		08:56:20	.23583	.32850	9.56	3.24	2.9	1.8	5.0	2.3	1.5	5.8	1.3	1.2	0.8
14	08/31		11:12:27	.34517	.37417	2.81	1.55	1.0	2.8	6.0	0.6	2.0	6.0	1.6	1.4	1.0
15	08/31		11:19:20	.37033	.38216	4.38	1.33	1.2	3.0	6.0	0.8	2.4	6.0	1.5	1.3	1.0
16	08/31		13:37:31	.25467	.17000	9.15	2.28	1.5	1.0	2.5	3.0	1.6	6.0	0.5	0.6	0.4
17	08/31		14:23:52	.25183	.17083	7.45	1.51	1.5	1.0	2.5	1.9	1.3	5.8	0.8	0.8	0.4
18	08/31		14:34:17	.28017	.40767	4.63	1.58	1.9	1.9	5.2	1.4	1.4	6.5	1.4	1.4	0.8
19	08/31		16:12:18	.24117	.34500	6.56	1.18	2.4	1.6	–	1.9	1.2	–	1.3	1.3	–
20	09/01	244	01:14:10	.16850	.29550	8.69	2.14	3.5	2.3	3.4	3.2	1.8	4.2	1.1	1.2	0.8
21	09/01		01:40:53	.54517	.30050	2.28	1.60	1.5	1.5	–	3.3	4.5	–	0.5	0.3	–
22	09/01		01:41:14	.17717	.31017	9.15	2.47	3.3	2.2	3.5	3.0	1.8	4.5	1.1	1.2	0.8
23	09/01		11:13:55	.27783	.34500	5.38	1.44	1.9	1.8	5.2	1.4	1.2	6.2	1.4	1.5	0.9
24	09/01		15:48:21	.17300	.30383	4.58	1.22	3.4	1.7	4.0	2.8	1.3	4.5	1.3	1.3	0.8
25	09/01		20:06:36	.20000	.31133	9.00	1.53	3.1	2.0	4.2	2.7	1.6	5.3	1.2	1.3	0.8
26	09/01		20:15:00	.35983	.38800	5.06	2.42	1.5	3.0	6.5	0.9	2.3	8.0	1.6	1.3	0.8
27	09/01		20:52:45	.30150	.36083	6.09	1.14	1.8	–	–	1.2	–	–	1.5	–	–

continued

No.	Date (2014) mm/dd	Julian Date	Time hh:mm:ss	Lat. (38°)	Long. (−122°)	depth (km)	M_D	Post-S Coda Duration(s)			P-to-S Time(s)			Ratio $(t_C - t_S)/(t_S - t_P)$		
								A1	A2	A3	A1	A2	A3	A1	A2	A3
28	09/01		22:12:22	.27917	.35250	6.96	1.63	2.0	1.8	5.5	1.5	1.3	6.0	1.3	1.4	0.8
29	09/02	245	03:31:29	.22883	.33667	8.01	1.10	2.5	1.6	–	2.2	1.3	–	1.1	1.2	–
30	09/02		11:47:11	.23833	.33300	7.06	1.11	2.2	1.5	–	2.0	1.2	–	1.1	1.3	–
31	09/02		20:00:49	.24900	.36383	4.77	2.03	2.3	1.4	4.5	1.7	1.1	5.5	1.4	1.3	0.8
32	09/03	246	10:18:51	.23333	.32917	9.29	2.63	2.6	1.8	4.0	2.4	1.5	4.8	1.1	1.2	0.8
33	09/04	247	10:56:23	.18033	.30317	10.94	2.93	3.1	2.2	4.0	2.9	2.0	5.0	1.1	1.1	0.8
34	09/04		14:05:01	.35817	.38717	6.66	1.31	1.5	2.8	–	1.2	2.3	–	1.3	1.2	–
35	09/05	248	01:03:21	.20867	.32083	6.83	1.66	2.9	1.5	4.2	2.4	1.2	4.5	1.2	1.3	0.8
36	09/05		04:04:13	.19800	.31216	8.77	1.20	3.0	2.0	–	2.7	1.6		1.2	1.2	–
37	09/05		11:44:52	.21950	.32034	6.26	1.12	2.8	1.6	–	2.4	1.1	–	1.2	1.5	–
38	09/05		11:49:41	.33200	.38367	5.63	1.31	1.5	2.2	–	1.0	2.0	–	1.5	1.1	–
39	09/05		21:17:50	.14950	.30400	5.47	1.12	4.0	2.0	3.0	3.5	2.0	3.5	1.2	1.0	0.8
40	09/06	249	00:57:01	.32800	.18517	11.87	1.47	1.5	1.5	–	3.0	3.3	–	0.5	0.5	–
41	09/06		12:45:27	.24333	.36533	5.27	1.78	2.3	1.4	4.8	1.8	0.9	6.0	1.3	1.6	0.8
42	09/06		12:49:44	.24333	.37400	4.25	1.80	2.2	1.4	5.0	1.6	0.9	6.2	1.4	1.6	0.8
43	09/06		14:50:05	.24033	.34400	4.97	1.39	2.4	1.5	5.0	1.8	0.9	6.0	1.3	1.7	0.8
44	09/06		17:16:58	.23133	.32667	7.35	1.19	2.5	1.6	–	2.1	1.2	–	1.2	1.3	–
45	09/07	250	07:41:52	.22250	.31800	9.13	1.13	2.8	1.9	–	2.4	1.5	–	1.2	1.2	–
46	09/07		16:27:24	.34800	.18850	11.47	1.16	1.5	1.5	–	3.0	3.4	–	0.5	0.4	–
47	09/08	251	01:08:54	.22933	.33167	7.15	1.25	2.3	1.5	–	2.1	1.2	–	1.1	1.3	–
48	09/08		04:30:57	.40767	.47183	5.01	1.28	1.5	1.5	–	2.2	3.4	–	0.7	0.6	–
49	09/08		04:49:17	.40117	.47667	6.78	1.90	1.5	1.5	2.5	2.2	3.4	7.5	0.7	0.6	0.3
50	09/08		07:56:39	.28517	.34917	5.81	1.21	1.9	1.8	–	1.3	1.3	–	1.5	1.4	–
51	09/08		09:36:42	.17216	.29900	5.04	1.24	2.8	1.7	3.8	2.4	1.3	4.5	1.2	1.3	0.8
52	09/08		15:42:19	.33667	.37366	5.65	1.22	1.4	2.8	–	1.0	2.1	–	1.3	1.3	–
53	09/09	252	01:31:06	.36467	.38033	5.33	1.64	1.5	3.2	5.5	1.0	2.6	6.2	1.5	1.3	0.9
54	09/09		08:03:23	.35683	.37683	4.51	1.47	1.4	3.1	–	1.0	2.5	–	1.4	1.3	–
55	09/09		12:09:51	.35217	.37750	5.61	1.38	1.4	3.1	–	1.0	2.5	–	1.4	1.3	–

We identify the FZTWs on the basis of extended coda waves with large amplitudes that follow the S-arrival on seismograms recorded at stations within a fault zone (e.g., Li and Leary, 1990; Li *et al.*, 1990, 1997, 2014). Generally, the coda length of the coherent guided waves increases with increasing hypocentral distance between the earthquake source and the recording site (e.g., Li and Malin, 2008; Li *et al.*, 2000, 2012, 2003a). In addition, the difference between the P- and S-arrivals also increases with increasing hypocentral distances. Empirical studies have shown that the ratio of the post-S coda time to the time difference between the P- and S-arrivals is approximately higher than 1.2 for prominent guided waves (Li *et al.*, 2014). Thus, in this study, we use the ratio of post-S coda time to S-P arrival time difference $(t_C - t_S)/(t_S - t_P)$, to indicate prominent guided waves well generated and observed for aftershocks occurring within or close to the low-velocity fault zone when the ratio is higher than approximately 1.2. t_P and t_S are the P- and S-arrival times; $t_C - t_S$ is the post-S coda time in which the amplitudes of FZTWs are above twice those of the background signals.

1.2.1 Seismograms Recorded at the Full-Length Array A1

We first examined FZTWs for aftershocks located north of array A1. Figure 1.2a shows three-component seismograms recorded at A1 for three aftershocks (E53, E54 and E55 in Table 1.1 and Fig. 1.1; "E" means event) with hypocenters between 4.5 and 5.6 km depths. We observed prominent FZTWs with large amplitudes, long duration coda following the S-arrivals in seismograms recorded at stations between A1-05 and A1-09, which were centered on the northward projection of the surface rupture. In comparison, relatively small amplitudes and short coda are registered at stations outside of this range. We measured post-S coda durations of FZTWs to average 1.4–1.5 s (with the standard deviations of ±0.2 s) at five near-fault stations, where the amplitudes of FZTWs are above twice those of the background signal.

In the above example, the S-P times are 0.8–1.0 s for events E53, E54 and E55. Thus, the $(t_C - t_S)/(t_S - t_P)$ ratio for data recorded from these aftershocks range from 1.3 to 1.5, above the average ratio (1.2) expected for FZTWs. We interpret that the FZTWs are well excited by these aftershocks and well recorded at stations located within the low-velocity rupture zone.

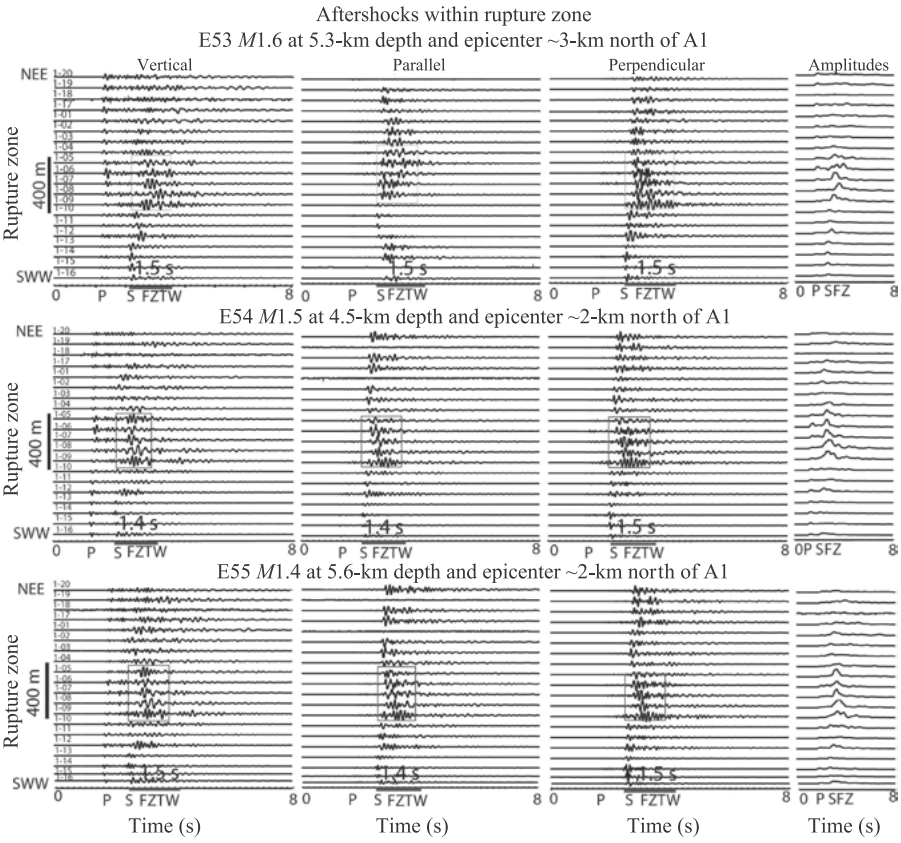

Fig. 1.2 Three-component seismograms and amplitudes recorded at 20 stations (A1-01 to A1-20) of A1 for three aftershocks E53, E54 and E5 occurring with the rupture zone at 4.5–5.6 km depth and with epicenters ∼2 to ∼3 km north of A1. Seismograms are labeled by station names (A1-01 to A1-20). NEE (northeast by east) and SWW (southwest by west) denote the ends of A1. Aftershock magnitude, focal depth, and epicentral distance from A1 are shown in the title. The origin date and time of aftershock are shown in Table 1.1. Seismograms are filtered (<8 Hz) and plotted using a fixed amplitude scale for each aftershock. Prominent FZTWs (in boxes) are observed at five stations from 1-05 to 1-09 of A1 within an apparent 400-m-wide fault zone (denoted by a vertical bar). Post-S coda durations of FZTWs average 1.4-1.5 s in length for stations within the rupture zone. Amplitudes of seismograms are smoothed and plotted in envelope using SAC (Seismic Analysis Code) program. In contrast, shorter post-S coda durations, with smaller amplitudes, are registered at stations located outside of the fault zone.

1.2.2 Seismograms Recorded within and out of the Rupture Zone

Figure 1.3 shows seismograms recorded at two arrays A1 and A2 for two aftershocks (E43 and E16 in Table 1.1 and Fig. 1.1b), occurring at 5-km depth within the southern rupture zone and at 9.1-km depth east of the WNF, respectively. Prominent FZTWs are observed at stations A1-05 to A1-09 and A2-13 to A2-17 located within a ∼400-m-wide rupture zone for the on-fault aftershock E43. Post-S coda durations of FZTWs are measured to be 2.4 s at A1 and 1.5 s at A2 within the rupture zone. The $(t_C - t_S)/(t_S - t_P)$ ratios for FZTWs are $1, 3$ and 1.7 at A1 and A2, showing that the FZTWs were well excited by aftershock E43 and well propagated along the rupture zone. In contrast, seismograms recorded at stations farther away from the rupture zone do not show clear FZTWs for the on-fault aftershock E43, and there is no obvious FZTWs observed at all stations of A1 and A2 for aftershock E16 occurring ∼15 km away from the rupture zone. The $(t_C - t_S)/(t_S - t_P)$ ratios of post-S coda durations at A1 and A2 for aftershock E16 are lower than 0.6, showing that no significant FZTWs were generated by the event and out of the fault-zone waveguide.

We then examined FZTWs recorded on A1 and A2 for two aftershocks occurring at the same depth of 6.6 km within the WNFZ rupture zone near A2. Figure 1.4a shows seismograms, amplitudes, and normalized spectral energy at A1 and A2 for aftershocks (E19 and E1 in Fig. 1.1 and Table 1.1). The epicentral distance between A1 and E19 is ∼10.5 km while the epicentral distance between A2 and E1 is ∼1 km. The amplitude envelopes of seismograms and spectral amplitude contours are computed using SAC (Seismic Analysis Code) programs. Prominent FZTWs with large amplitudes are observed at stations A1-05 to A1-09 and stations A2-12 to A2-16 due to fault-zone waveguide effect. Post-S coda durations of the high-amplitude FZTWs are 2.4 s at A1 for E19 and 1.6 s at A2 for E1. At array A1, spectral energy contours show dominant frequencies of the FZTWs at ∼5–8 Hz, with 2.3–2.5 s post-S coda durations at stations A1-05, A1-08 and A1-09 located within the rupture zone. In contrast, much shorter post-S coda durations (0.7–1.3 s) are registered at stations A1-09 and A1-13 out of the rupture zone. Similarly, at array A2, FZTWs with large spectral amplitudes and 1.5–1.6 s post-S coda durations are observed at stations A2-14, A2-15 and A2-16. In contrast, the relatively shorter post-S-wave coda durations are registered at stations A2-09 and A2-19 away from the surface rupture zone. These observations and analyses suggest that seismic energy was trapped (localized) within a low-velocity waveguide formed by the 400–500 m wide rupture zone, which likely extends to at least 6.6 km depth between A1 and A2. The $(t_C - t_S)/(t_S - t_P)$ ratio for these two on-fault aftershocks E19 and E1 ranges from 1.2 to 1.3, indicating the FZTWs well exited and propagating along the central part of the rupture zone between A1 and A2.

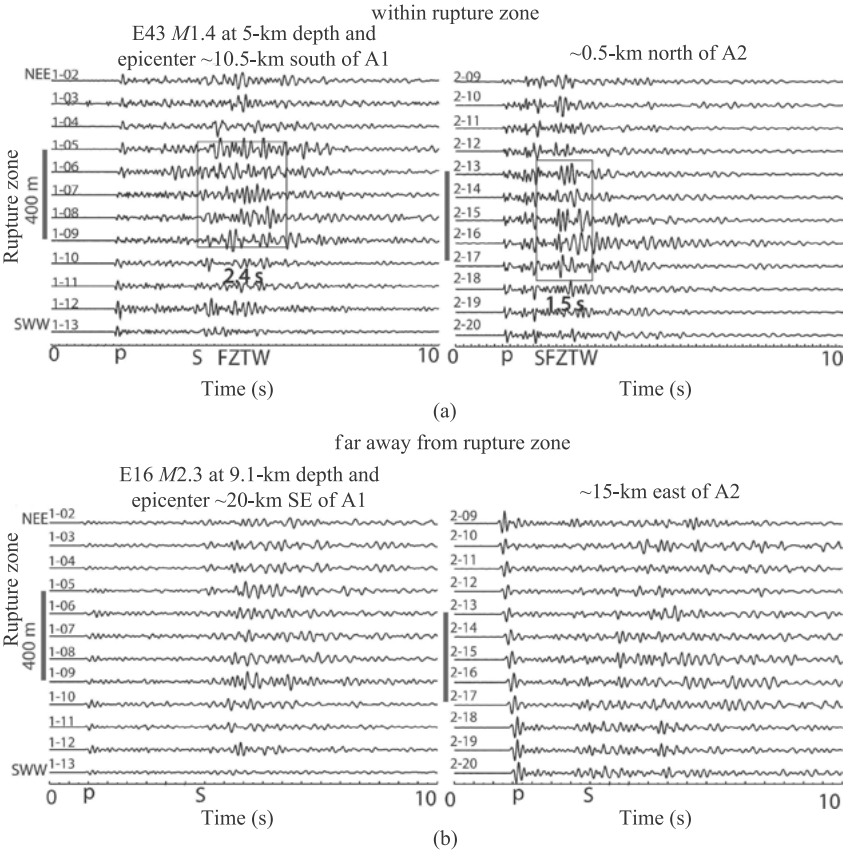

Fig. 1.3 Vertical-component seismograms recorded at array A1 and A2 for **(a)** an on-fault aftershock E43 with its epicenter near A2, and **(b)** an off-fault aftershock E16 located ∼20 km east of A1 and ∼15 km southeast of A2. Other notations are same in Figure 1.2. Prominent FZTWs (in boxes) are observed at stations 1-05 to 1-09 of A1 and 2-13 to 2-17 of A2 within an apparent 400 m-wide fault zone for the on-fault aftershock E19. Post-S coda durations of FZTWs average 2.4-s at A1 and 1.5-s in length at stations of A1 and A2 within the rupture zone for E19. Seismograms recorded at away-fault stations for E43 and at all stations for E16 do not show significant FZTW. In order to conserve space, we plot seismograms only at 12 of the 20 stations of arrays A1 and A2. Seismograms recorded at away-fault stations A1-01, A1-14 to A1-20 of A1 and A2-01 to A2-08 of A2 do not show significant FZTWs associated with the low-velocity rupture zone along the WNFZ so that they are no longer plotted.

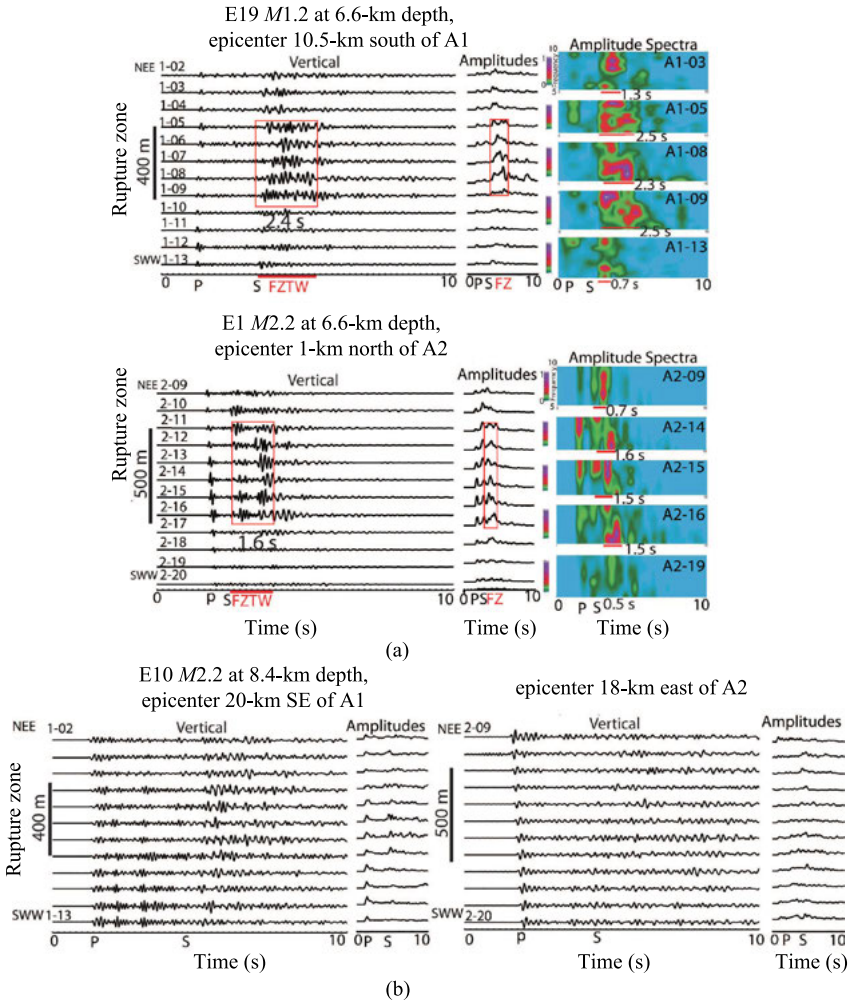

Fig. 1.4 **(a)** Vertical-component seismograms, amplitudes, and normalized spectral energy registered (top) at A1 for aftershock E19 and (bottom) at A2 for aftershocks E1 occurring within the rupture zone at ∼6.6 km depth and ∼1-km north of A2. Spectral amplitudes are normalized (0 to 1). Prominent FZTWs (in boxes) are observed at stations A1-05 to A1-09 of A1 and stations A2-11 to A2-16 of A2 located within the rupture zone. Dominant FZTWs at 5–8 Hz with 2.3–2.5 s coda duration (marked by horizontal bars) are observed at stations A1-05, A1-08 and A1-09, and 1.5–1.6 s time duration at stations A2-14, A2-15 and A2-16. In contrast, much shorter time durations of post-S coda are measured at stations A1-05, A1-13, A2-09 and A2-19. Other notations are same in Figure 1.3. **(b)** Vertical-component seismograms and amplitudes registered at A1 and A2 for aftershock E10 occurring 18–20 km east of the WNF. No clear FZTWs with large amplitude and long-duration are observed at all stations of two arrays.

However, seismograms recorded at A1 and A2 for an aftershock (E10 in Table 1.1) occurring 18–20 km east of the WNFZ do not show obvious FZTWs with large amplitudes and long post-S coda durations at all stations of A1 and A2 (Fig. 1.4b). The $(t_C - t_S)/(t_S - t_P)$ ratios of post-S coda durations registered at A1 and A2 for aftershock E10 far away from the rupture zone are less than 0.5, indicating that the source located far away from the low-velocity fault-zone could not generate significant FZTWs.

1.2.3 FZTWs Observed within the Central Rupture Zone

We evaluated FZTWs generated by aftershocks (E23, E28, E3, and E50 in Table 1.1 and Fig. 1.1b) located midway between arrays A1 and A2 at depths ranging from 5.4–7.0 km. Prominent FZTWs are observed at stations between A1-5 and A1-9 of array A1, located within the rupture zone (Fig. 1.5). FZTWs are also clearly observed at stations between A2-11 and A2-16 of array A2, located near and westward of the 2014 surface rupture. Post-S coda durations of FZTWs range in 1.8–2.0 s at these stations. The $(t_C - t_S)/(t_S - t_P)$ ratios for guided waves generated by these events range between 1.3–1.5 (*see* Table 1.1), consistent with values expected for FZTWs that are well generated and propagate along the rupture zone. Spectral amplitudes of seismograms at stations located within the rupture zone show FZTWs at 5–8 Hz, with 1.8–2.0 s post-S-wave coda durations.

Observations of FZTWs for these aftershocks indicate a prominent low-velocity waveguide between A1 and A2 above ∼7 km depth. We note that FZTW coda durations from these more centrally located events are longer than those from aftershocks located within the northern and southern portions of 2014 surface rupture zone, even though their hypocentral distances are similar, suggesting the greater magnitude of fault rock damage in the central rupture zone of the 2014 $M6$ earthquake. This observation is consistent with the greater surface slip mapped near the central part of rupture zone (Dawson *et al.*, 2014).

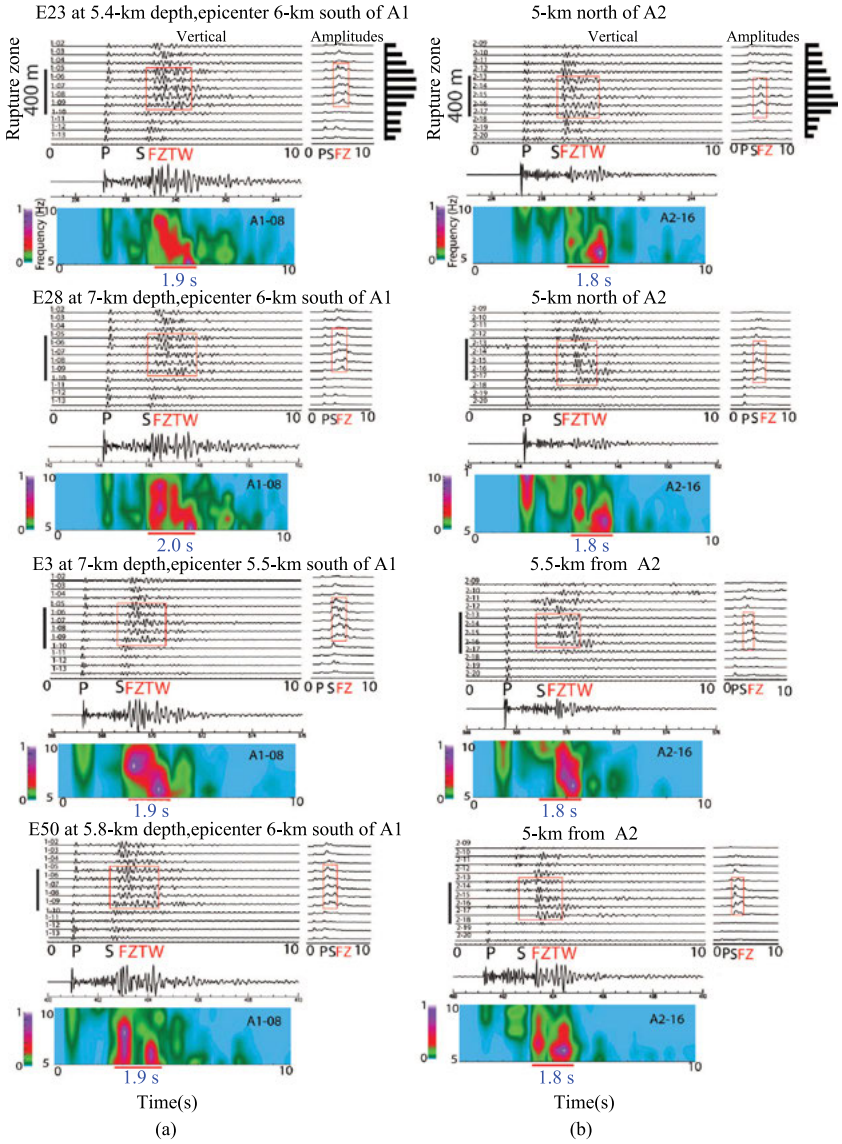

Fig. 1.5 Vertical-component seismograms, amplitudes, and normalized spectral amplitudes recorded at A1 **(a)** and A2 **(b)** for four on-fault aftershocks E23, E28, E3 and E50 that occurred at depths of 5.4–7.0 km beneath the middle of the surface rupture. Prominent FZTWs (in boxes) are observed at stations located within the rupture zone. Histograms show maximum amplitudes of post-S coda in 3 s windows for seismogram recorded at A1 and A2. Post-S coda durations of FZTWs average 1.8–2.0 s stations within the rupture zone. Spectral amplitudes of seismograms (<10 Hz) at station A1-08 of A1 and station A2-16 of A2 show FZTWs at dominant frequencies of 5–8 Hz, with coda durations marked by horizontal bars.

1.2.4 Post-S Coda Durations of FZTWs Increasing with Focal Depth

We analyzed FZTWs generated by aftershocks E14, E7, E26, and E5 (Table 1.1 and Fig. 1.1), which occurred along the northern projection of the 2014 surface rupture (Fig. 1.6) at depths increasing from 2.8 km to 6.6 km. Their epicentral distances to the center of A1 range from 2 to 3 km; therefore raypaths between these aftershocks and A1 were sub-vertical. FZTWs with relatively large amplitudes and long post-S coda durations are prominent at five stations located within the rupture zone. At array A1, post-S coda durations of FZTWs increase from 0.8 s to 1.6 s as aftershock hypocenters increase from 2.8 km to 6.6 km. The $(t_C - t_S)/(t_S - t_P)$ ratio for these on-fault aftershocks range from 1.3 to 1.6 with the maximum ration for the shallowest event E14 occurring at 2.8 km depth (*see* Table 1.1). Observations of FZTWs at arrays A1 and A2 for these aftershocks suggest that a remarkable low-velocity damage zone along the WNFZ likely extends further northward from the surface rupture of the 2014 $M6$ mainshock to depths of at least 5–6 km.

In another example, we evaluated FZTWs generated by three aftershocks (E31, E2 and E32 in Table 1.1 and Fig. 1.1) occurring at depths of 4.8, 7.7, and 9.3 km depths between A1 and A2, and recorded at the two arrays (Fig. 1.7). Prominent FZTWs are observed at stations within and near the 2014 surface rupture zone for each aftershock. The post-S coda durations of FZTWs (measured at A2) increase from 1.4 s to 1.7 s as their focal depths increase from 4.8 km to 7.7 km) but the post-S coda durations only slightly increase from 1.7 s to 1.8 s for aftershocks with focal depths between 7.7 km and 9.3 km, suggesting that a significant low-velocity waveguide likely extends to approximately 7.7 km depth at A2. Post-S coda durations (2.3 to 2.6 s) of FZTWs recorded A2 are larger than those registered at A1for the same aftershocks, suggesting a remarkable low-velocity waveguide exists along the rupture zone between A1 and A2. The $(t_C - t_S)/(t_S - t_P)$ ratio for aftershocks E31 and E2 range from 1.2 to 1.4, but the ratio for the deep aftershock E32 is 1.1 (*see* Table 1.1), indicative of weak waveguide effect below ∼7 km.

Figure 1.8 shows seismograms and amplitudes registered at A1 and A2 for four on-fault aftershocks (E41, E42, E43 and E44 in Table 1.1 and Fig. 1.1) that occurred with epicentral distances ∼0.5 to 1 km north of array A2. We observe prominent FZTWs with 1.4–1.6 s post-S coda durations at A2 and 2.2-2.5 s of post-S coda durations at A1 as aftershock focal depths increase from 4.3 km to 7.4 km. The longest coda duration (2.5 s) is for E44 occurring at the greatest along-ray distance from A2. The $(t_C - t_S)/(t_S - t_P)$ ratios measured for these aftershocks range from 1.2 to 1.7 with the maximum ratio for the shallow

aftershock E42 at 4.25-km and smallest ratio for the deep event E44 at 7.4 km depth (*see* Table 1.1), consistent with our interpretation that a remarkable low-velocity waveguide between A1 and A2 has strong trapping efficient along the rupture zone extending from the surface to depths of 5–7 km.

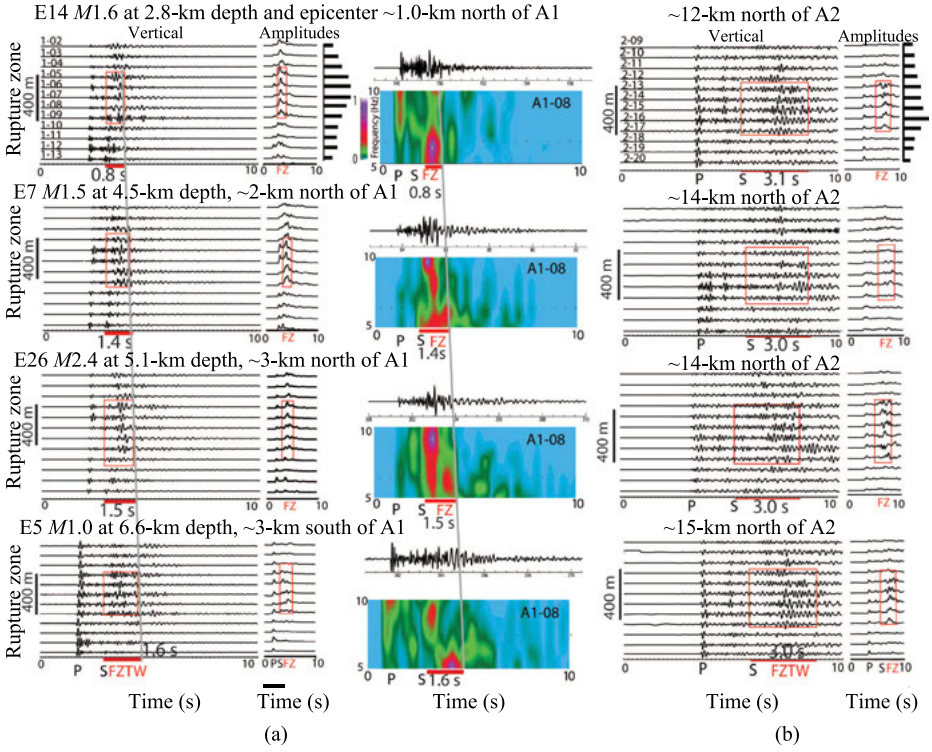

Fig. 1.6 **(a)** Seismograms and amplitudes registered at 12 stations (A1-01 to A1-16) of A1 for four on-fault aftershocks E14, E7, E26, and E5 with epicenters 1–3 km north of A1 at depths of 2.8, 4.7, 5.1, and 6.6 km. Histogram shows maximum amplitudes of post-S coda in 3 s windows for each seismogram recorded at A1. Spectral amplitudes of seismograms at station A1-08 of A1 located within the rupture zone are computed and normalized (0–1). **(b)** Same plot as shown in (a) but for data recorded at 12 stations (A2-09 to A2-20) of A2 for these aftershocks. Prominent FZTWs (in boxes) are observed at stations A1-05 to A1-09 of A1 and stations A2-13 to A2-17 of A2. Post-S coda durations of FZTWs at A1 increase from 0.8 to 1.6 s as aftershock depths increase from 2.8 to 6.6 km (the move-out denoted by the slope of a gray line). Post-S coda durations of FZTWs registered at A2 range around 3.0-3.1 s.

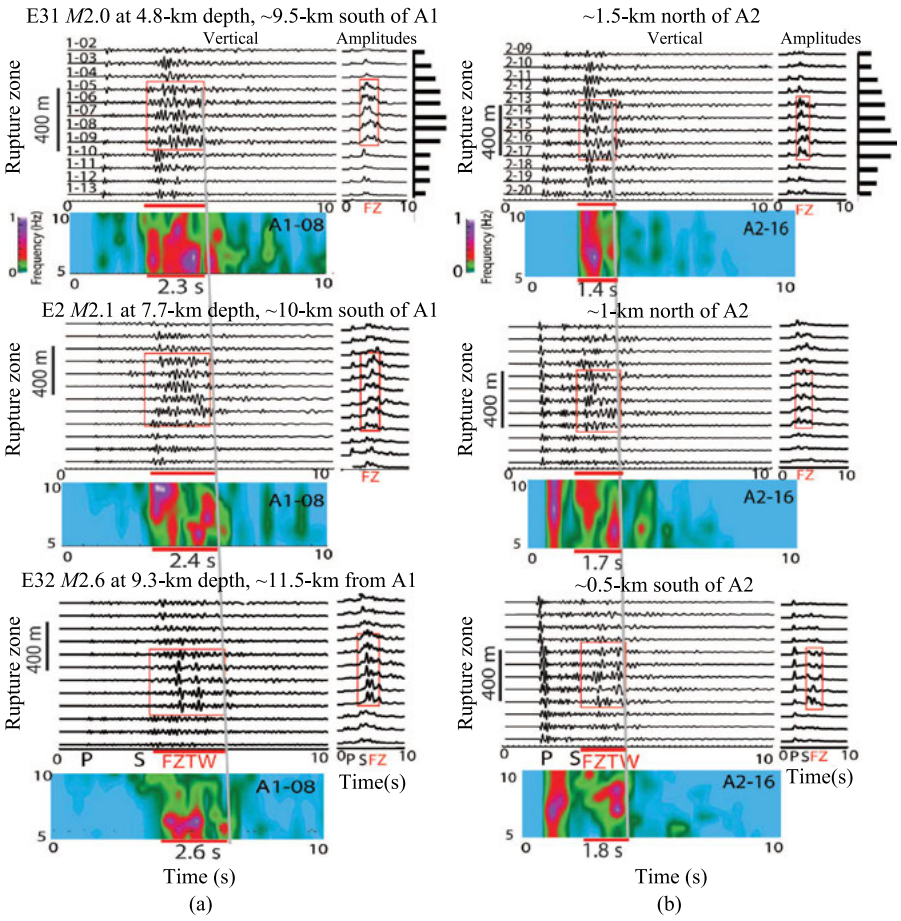

Fig. 1.7 **(a)** Seismograms, amplitudes, and normalized spectral amplitudes registered at A1 from three on-fault aftershocks E31, E2 and E32 at 4.8, 7.7 and 9.3 km depth. Post-S coda durations of FZTWs for stations of A1 within the rupture zone are 2.3–2.6 s for these aftershocks. **(b)** Same as in (a), but for A2. Prominent FZTWs (in boxes) occur at stations A1-5 to A1-9 of A1 and stations A2-12 to A2-17 of A2. Histograms show maximum amplitudes of post-S coda in 3 s windows for each seismogram recorded at A1 and A2. The post-S coda durations of the FZTWs at five fault-zone stations of A2 increase from 1.4 s to 1.7 s (denoted by a grey line) as aftershock focal depths increase from 4.8-km to 7.7 km. There is only a slight increase from 1.7 s to 1.8 s for focal depths between 7.7 km and 9.3 km. Seismograms recorded at away-fault stations do not show significant FZTWs.

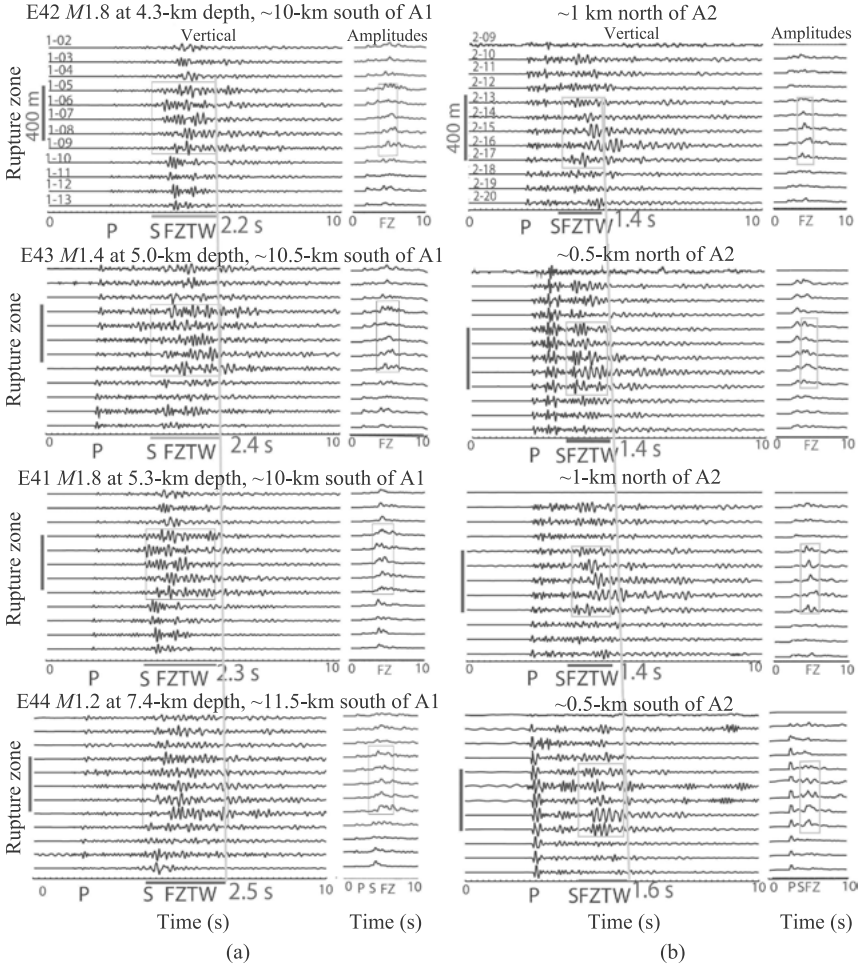

Fig. 1.8 Seismograms and amplitudes at A1 **(a)** and A2 **(b)** for a cluster of four on-fault aftershocks E41, E42, E43 and E44 with epicenters near A2 and depths ranging from 4.3 km to 7.4 km. Prominent FZTWs (in boxes) occur at stations A1-5 to A1-9 of A1 and stations A2-12 to A2-17 of A2. Post-S coda durations of FZTWs measured at A1 for stations within the rupture zone are 2.2–2.5 s for these events located 10–11.5 km south of A1; whereas post-S coda durations of FZTWs measured at A2 for stations within the rupture zone are 1.4–1.6 s. This shows that the coda duration for FZTWs increase with aftershock depth and epicentral distance.

1.2.5 Post-S Coda Durations of FZTWs Increasing with Epicentral Distance

To further examine the continuity of the rupture zone along the WNFZ at seismogenic depths, we analyzed waveforms recorded at arrays A1 and A2 for six deeper (8.7 km to 11 km depths), on-fault aftershocks (E45, E6, E25, E33, E22 and E20 in Table 1.1 and Fig. 1.1b), with epicenters 1 km to 8 km south of A2, along the southernmost 2014 rupture zone. FZTWs are observed at stations located within the WNFZ (Fig. 1.9). Post-S coda durations of FZTWs measured at A1 increase from 2.8 s to 3.2 s as epicentral distances of aftershocks increase from 12 km to 19 km. At A2, post-S coda durations of FZTWs increase from only about 1.9 s to 2.3 s with increasing epicentral distances from 1 km to 8 km. The $(t_C - t_S)/(t_S - t_P)$ ratios for FZTWs generated by these events range from 1.1–1.3 (*see* Table 1.1). In general, these ratios are smaller than those for FZTWs generated by aftershocks occurring within the central part of the rupture zone between A1 and A2 (*see* Figs. 1.3 to 1.8), indicating the low-velocity waveguide south of A2 has weaker trapping efficiency than that along the central part of the rupture zone at seismogenic depths. Alternatively, the smaller ratios may infer weaker excitation of FZTWs because they originate lower than or at the bottom of the rupture zone.

1.2.6 FZTWs Observed at Three Cross-Fault Arrays

We evaluated FZTWs across all three seismic arrays for aftershocks. Figure 1.10 shows FZTWs recorded at A1, A2, and A3 for an on-fault aftershock (E51 in Table 1.1 and Fig. 1.1b) located ∼6 km south of A2 at ∼5 km depth. FZTWs from E51 are prominent at stations of A1 and A2 located within the rupture zone. Post-S coda durations of the FZTWs average ∼2.8 s at A1 and ∼1.7 s at A2. In contrast, post-S coda durations are much shorter at stations located outside of the rupture zone.

At A3, we observe FZTWs with 3.8 s of post-S coda durations at stations A3-02 and A3-03 located near the Southhampton Fault (F1), and at stations A3-09 and A3-10 located near the Franklin Fault (F2). The FZTWs traveling ∼28 km distance from aftershock E51 to array A3 show 3.8 s post-S coda duration while the FZTWs traveling ∼18 km distance from the same aftershock to A1 show 2.8 s post-S coda duration, suggesting that either (a) rocks within the fault zone to the north from E51 along the WNFZ have been more severely damaged than those along the fault zone to south from E51 and A3 along the Franklin Fault, or (b) The deeper travel path to A3 only samples the deeper (and higher velocity) part of the waveguide. The $(t_C - t_S)/(t_S - t_P)$ ratios for FZTWs are 1.2–1.3 at

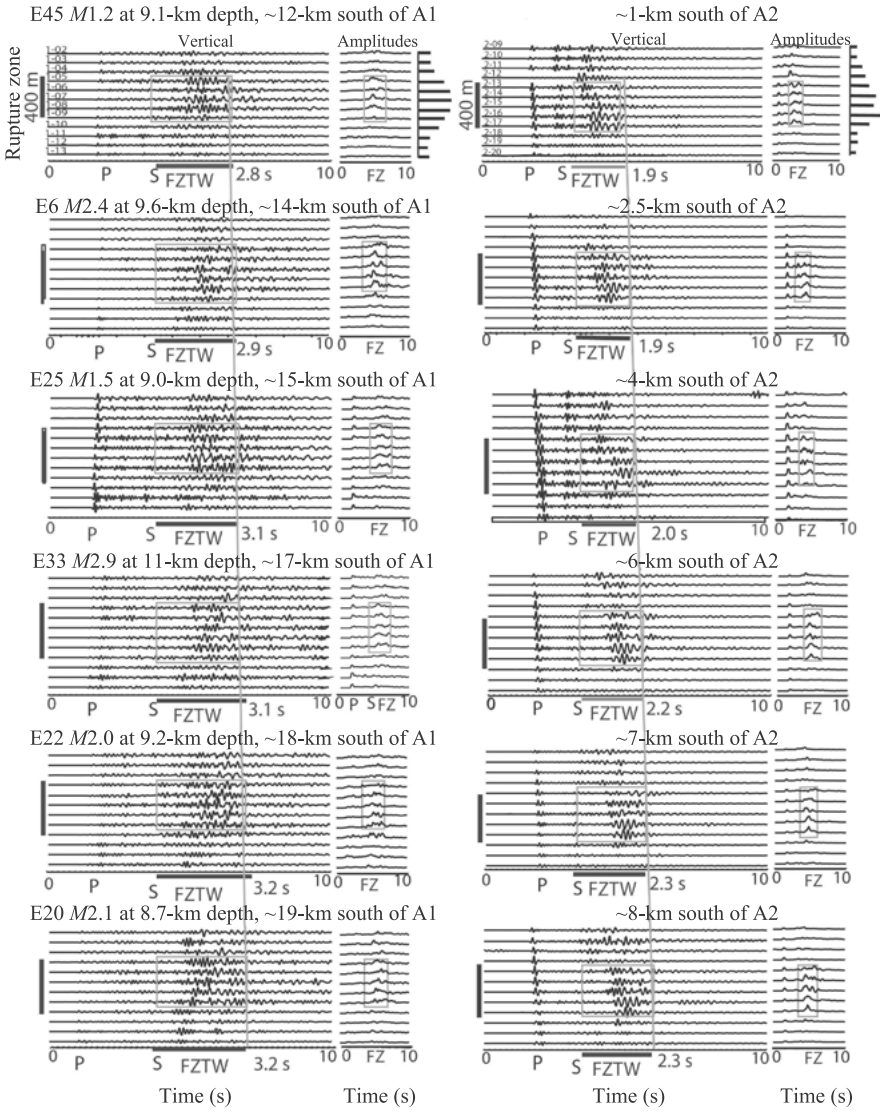

Fig. 1.9 Vertical-component seismograms and amplitudes recorded at A1 (left) and A2 (right) for six deep aftershocks E45, E6, E25, E33, E22 and E20 with epicenters 1–8 km south of A2. FZTWs (in boxes) are observed at stations A1-05 to A1-09 of A1 and stations A2-13 to A2-17 of A2. Post-S-wave coda durations of FZTWs at A1 increase from 2.8 s to 3.2 s as epicentral distances increase from 12 km to 19 km. Post-S coda durations of FZTWs at A2 increase from 1.9 s to 2.3 s as epicentral distances increase from 1 km to 8 km. Maximum amplitudes of post-S coda at 12 stations of A1 and A2 are shown in histograms.

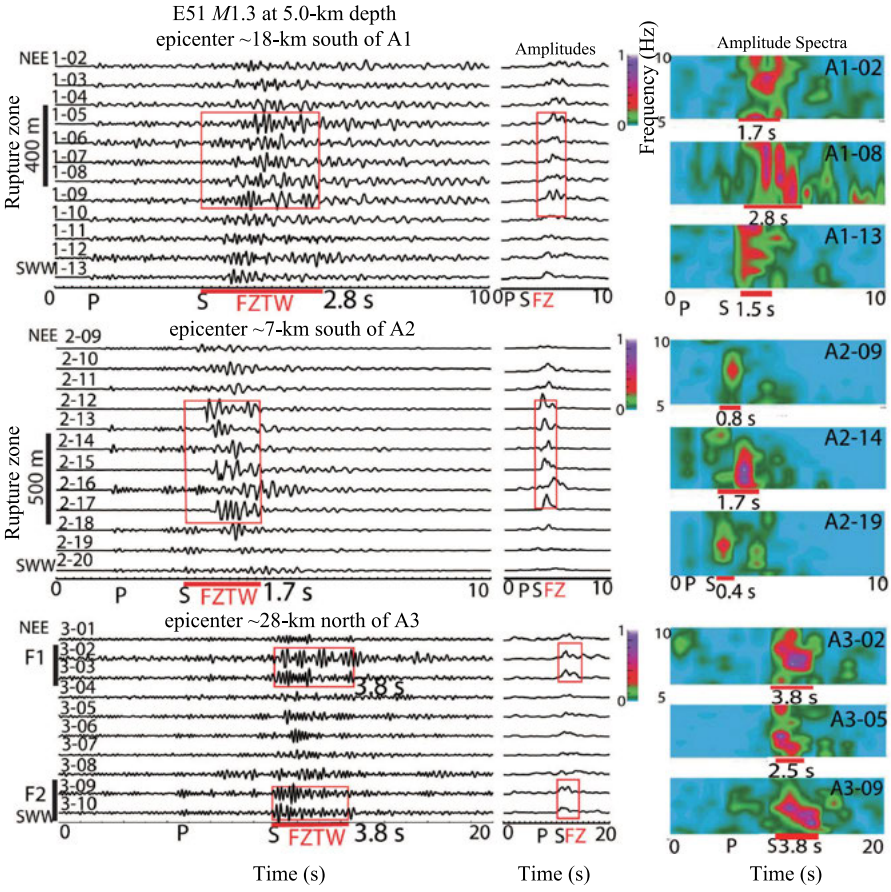

Fig. 1.10 Vertical-component seismograms, amplitudes, and normalized spectral amplitudes registered at A1 (top), A2 (Middle), and A3 (bottom) for an on-fault aftershock E51 located ∼7 km south of A2. FZTWs (in boxes) are observed at stations A1-05 to A1-09 of A1, stations A2-12 to A2-17 of A2, and stations A3-02, A3-03, A3-09, and A3-10 of A3. Post-S coda durations of FZTWs average 2.8 s at A1 and 1.7 s A2. Spectral amplitudes of seismograms show dominant FZTWs with ∼2.8 s coda duration at station A1-08 and ∼1.7 s at station A2-14; both stations are located within the rupture zone. In contrast, much shorter coda durations are observed at stations A1-02, A1-14, A2-09, and A2-19 located outside of the rupture zone. At A3, FZTWs with 3.8 s duration arrive at stations A3-02 and A3-03 located near the Franklin Fault (denoted by F1), and at stations A3-09 and A3-10 near the Southhampton Fault (F2). The time scale in plot is 0 to 20 s for A3.

A1 and A2 along the WNF but ∼0.8 for A3, showing less trapping efficiency of the waveguides south of E51 along the FF (Table 1.1).

Fig. 1.11 shows seismograms recorded at three arrays for three aftershocks E8, E6, and E4 (Table 1.1 and Fig. 1.1b) occurring within and far away from the WNFZ.

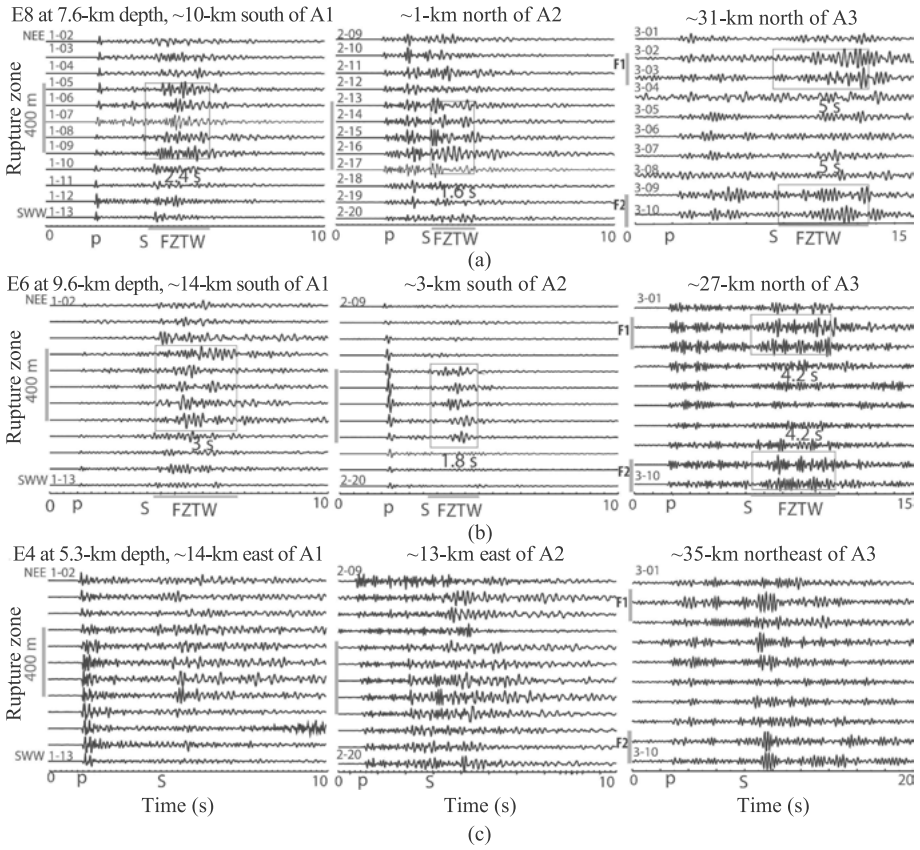

Fig. 1.11 **(a)** and **(b)** Vertical-component seismograms at A1, A2 and A3 for two aftershocks E8 and E6 that occurred within the WNF rupture zone at depths of 7.6 km and 9.6 km. Aftershock E8 located at epicentral distances of 10, 1 and 31 km from A1, A2 and A3; aftershock E6 located at 14, 3 and 27 km from A1, A2 and A3. FZTWs (in boxes) are observed at stations A1-05 to A1-09 of A1 and stations A2-12 to A2-17 of A2. Post-S coda durations of FZTWs average 2.4 s at A1 and 1.6 s at A2 for aftershock E8, and 3 s at A1 and 1.8 s at A2 for E6. At A3, FZTWs with 5-s coda (4.2-s) duration were recorded at stations A3-02, A3-03, A3-09 and A3-10 for on-fault E8 (E6). **(c)** Seismograms recorded at A1, A2 and A3 do not show significant FZTWs for aftershock E4 located ~13-km east of A2, far away from the WNF rupture zone.

Aftershock E8 and E6 are on-fault events. E8 (E6) occurred at ~10 km (14 km) south of A1, ~1 km (3 km) from A2, and ~31 km (27 km) north of A3. Aftershock E4 occurred ~14 km southeast of A1, ~12 km east of A2, and ~35 km northeast of A3. Prominent FZTWs with 2.4–3.0 s post-S coda durations and 1.6–1.8 s post-S coda durations are observed at stations of A1 and A2 within the rupture zone for aftershocks E8 and E6. The $(t_C - t_S)/(t_S - t_P)$ ratios for these FZTWs are 1.2–1.3.

At A3, we observe FZTWs with 5 s post-S coda durations at stations A3-02 and A3-03 near the Southhampton Fault and stations A3-09 and A3-10 (near the Franklin Fault) for on-fault aftershock E8, and 4.2 s post-S coda durations at these stations for E6. The $(t_C - t_S)/(t_S - t_P)$ ratios for these FZTWs recorded at A3 for events E8 and E6 are ∼0.8 (Table 1.1), suggesting that a continuous waveguide exists along the Franklin Fault and Southhampton Fault, but the waveguide trapping efficiency is weaker than that along the WNFZ.

For aftershock E4, located ∼13 km east of A2 and far away from the 2014 rupture zone, no clear FZTWs were recorded at all stations of A1, A2 and A3. Although seismograms show large-amplitudes of S-waves at stations A3-02, A3-09 and A3-10 of array A3 for E4, but with much shorter coda-durations (∼2 s) than those (∼5 s) recorded at the same stations for on-fault aftershocks E8 and E6. The $(t_C - t_S)/(t_S - t_P)$ ratio for E4 is 0.5 (*see* Table 1.1), indicating no significant guided wave energy generated by aftershock E4 occurring far away from the WNFZ.

We examined FZTWs recoded at stations A3-02 and A3-03 near the Southhampton fault (F1) and A3-09 and A3-10 near Franklin fault (F2) of array A3 for four aftershocks (E20, E22, E1 and E26 in Table 1.1 and Fig. 1.1b) occurring at depths between 5.1 km and 9.2 km along the south WNFZ. Figure 1.12 shows Post-S coda durations of FZTWs increase from ∼3.5 s to ∼6.5 s as epicentral distances increase from ∼22 km to ∼44 km, indicating that the low-velocity waveguide along the WNFZ likely extends further southward along the Franklin fault and Southhampton fault to A3. Comparing with post-S coda durations of FZTWs travelling from these aftershocks to A1 and A2 (*see* Table 1.1), the velocity reductions within the Franklin Fault and Southhampton Fault seam less than those within the WNF. The $(t_C - t_S)/(t_S - t_P)$ ratios registered at A3 for these aftershocks are ∼0.8, suggesting a weaker waveguide effect along the F1 and F2 than that along the WNFZ rupture zone. Our observations suggest that the Franklin fault and Southhampton fault experienced less damage than the WNF did in the 2014 $M6$ South Napa earthquake. They experienced significant damage in the past earthquakes, but might have been healed to base level since then.

Numerical investigations of trapping efficiency of a low-velocity waveguide for seismic waves show that if there is a discontinuity, such as a step-over between the two faults greater than several times of the fault-zone width, the propagation of FZTWs will be disrupted obviously (Li and Vidale, 1996). Therefore, if there is a fault-zone step-over between the West Napa Fault and the Franklin Fault or Southhampton Fault greater than 1–2 km, several times of the fault-zone width (∼500 m), the $(t_C - t_S)/(t_S - t_P)$ ratio for FZTWs should be much smaller than that for a continuous waveguide.

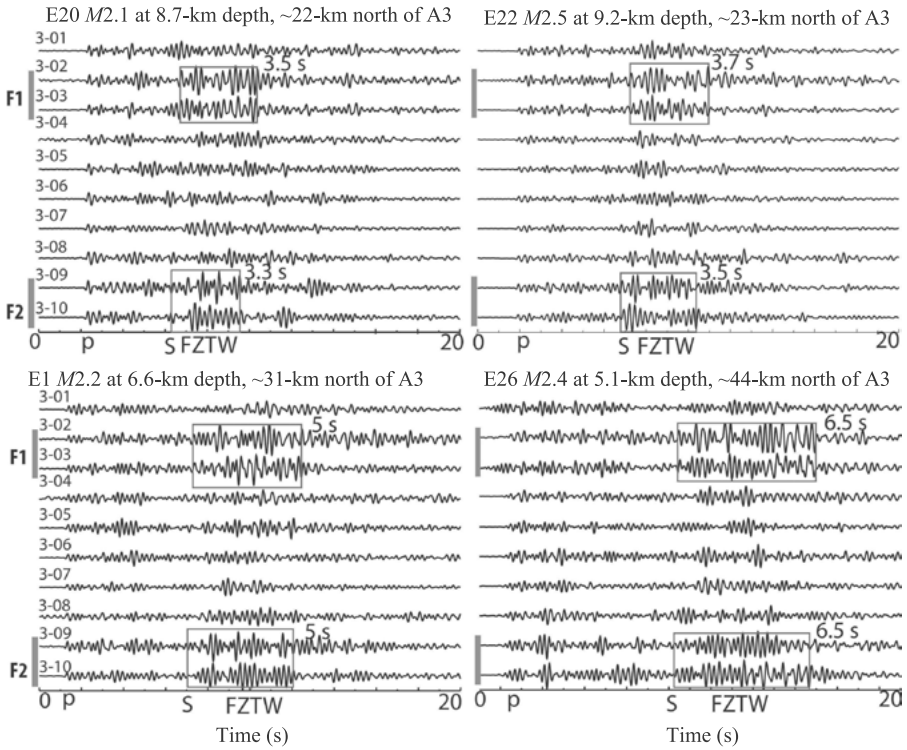

Fig. 1.12 Vertical-component seismograms at A3 for four on-fault aftershocks E20, E22, E1 and E26 that occurred at depths between 5.1 km and 9.2 km with various epicentral distances to A3. FZTWs with large amplitudes and long durations (in boxes) were recorded at stations 3-02 and 3-03 near the Southhampton fault (F1), and at stations 3-09 and 3-10 near the Franklin fault (F2). Post-S coda durations of FZTWs average from 3.5 s (3.3 s) to 6.5 s (6.5 s) as epicentral distances increase from 22 km to 44 km to F1 (F2).

1.2.7 FZTWs Observed at Cross-Fault Arrays and Along-Fault Stations

We further evaluated FZTWs recorded at three cross-fault seismic arrays with 4.5-Hz sensors together with REFTEK-130 seismographs with 2-Hz sensors for aftershocks occurring within the WNFZ at different depths and epicentral distances. Figure 1.13a shows FZTWs recorded stations of A1, A2, and A3 for two on-fault aftershocks (E13 and E18 in Table 1.1 and Fig. 1.1b) located at 9.6-km and 4.6-km depths with their epicenters right beneath A2 and middle of the surface rupture between A1 and A2, respectively. Post-S coda durations of FZTWs range from 1.8 s to 2.9 s at A1 and A2, with the longer post-S coda duration of FZTWs traveling longer hypocentral distance. The $(t_C - t_S)/(t_S - t_P)$

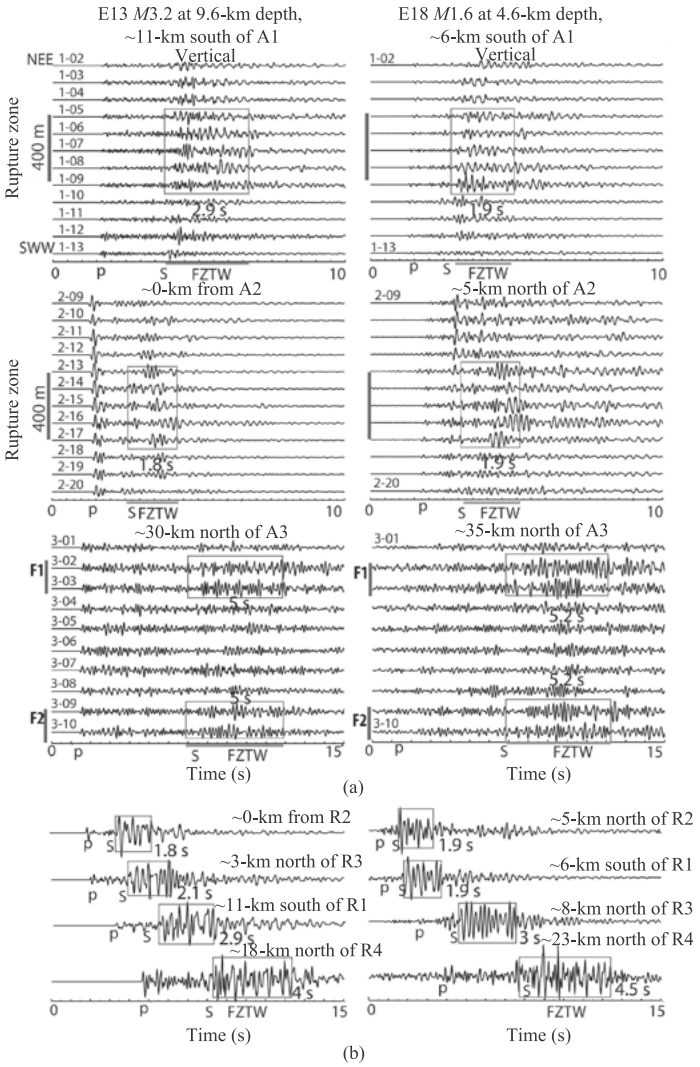

Fig. 1.13 **(a)** Seismograms at A1, A2 and A3 for aftershocks E13 and E18 occurring within the WNFZ rupture zone at depths of 9.6 and 4.6 km. E13 was located at epicentral distances of 11, 0 and 30 km from A1, A2 and A3; E18 located at 6, 5 and 35 km from A1, A2 and A3. FZTWs (in boxes) are observed at stations A1-05 to A1-09 of A1 and stations A2-12 to A2-17 of A2. Post-S coda durations of FZTWs average 2.9 s at A1 and 1.8 s at A2 for E13, and 1.9 s at A1 and A2 for E18. At A3, FZTWs (in boxes) with 5.0-s coda duration were recorded at stations A3-02, A3-03, A3-09 and A3-10 for E13 and with 5.5 s for E18. **(b)** Vertical-component seismograms (<8 Hz filtered) recorded at four REFTEK stations R1–R4 for aftershocks E13 and E18 are plotted in order of their epicentral distances between the event and stations, aligned at event origin time and with amplitudes in trace-normalized. Post-S coda durations of FZTWs (in boxes) increase from 1.8 s to 4.5 s as epicentral distances increase from 0 to 23 km.

ratios for these FZTWs recorded at A1 and A2 are 1.2–1.4, indicating that the fault-zone guided waves are well generated and propagate within the low-velocity rupture zone along the WNFZ. However, post-S coda durations of FZTWs at A3 range from 5 s to 5.5 s for E13 and E18 that occurred at 30 km to 35 km epicentral distances from A3, almost 3 times as large as the epicentral distance between E13 and A1. The $(t_C - t_S)/(t_S - t_P)$ ratios for FZTWs recorded at A3 are ∼0.8, suggesting a weaker waveguide effect along the Franklin Fault and Southhampton Fault than that along the WNFZ rupture zone.

We then examined waveform data recorded at four REFTEK seismographs R1 to R4 deployed along the WNFZ (*see* Fig. 1.1) for the same aftershocks E13 and E18. Stations R1 and R2 were co-located with the center of arrays A1 and A2; R1 and R4 were located 3 km and 18 km south of A2, respectively. Figure 1.13b show that post-S coda durations of FZTWs recorded at these stations increase from 1.8 s to 4 s as the epicentral distances increase from 0 km to 18 km along the WNFZ for E13 while post-S coda durations of FZTWs increase from 1.9 s to 4.5 s as the epicentral distances increase from 5 km to 23 km for E18. We notice that the increasing trend in coda duration of FZTWs with travel distance is not linear but is smaller for the ray-path from events to R4 that was located approximately 16 km south of the south end of the WNF surface rupture. The $(t_C - t_S)/(t_S - t_P)$ ratios at R1 to R4 for these FZTWs range from 1.1 to 1.5 (*see* Table 1.2) with the lowest ratio 1.1 for FZTWs arriving at R4. These observations suggest that a continuous waveguide extends from the WNF to the Franklin Fault, but the waveguide trapping efficiency is weaker along the Franklin Fault than that along the WNF ruptured to the surface during the 2014 $M6$ earthquake.

In the next example, Figure 1.14 shows FZTWs recorded at three arrays A1, A2, and A3, and four REFTEK seismographs R1 to R4 for two similar aftershocks (E2 and E12 in Table 1.1 and Fig. 1.1b) occurring at the same depths of 7.7-km and epicentral distance of 10-km to A1 and 1-km to A2. Post-S coda durations of FZTWs are 2.4 s at A1 and 1.7 s at A2. The $(t_C - t_S)/(t_S - t_P)$ ratios for these FZTWs recorded are 1.2–1.3. However, the post-S coda durations of FZTWs at A3 are 5 s for these two events located ∼31 km to A3, almost 3 times as long as the epicentral distance from them to A1. The $(t_C - t_S)/(t_S - t_P)$ ratios of FZTWs recorded at A3 are ∼0.8, suggesting the weaker waveguide effect along the F1 and F2 than along the WNFZ. The post-S coda durations of FZTWs recorded at four REFTEK stations increase from 1.7 s to 4 s as the epicentral distances increase from 1 km to 19 km. We notice that the increasing trend in coda duration of FZTWs with travel distance is not linear but is smaller for the ray-path from events to R4 located approximately 16 km south of the south end of the WNF surface rupture. The $(t_C - t_S)/(t_S - t_P)$ ratios for these FZTWs range from 1.0 to 1.3 (Table 1.2) with the lowest ratio 1.0 for FZTWs

Table 1.2 Time, locations and measurements of aftershocks recorded at REFTEKs.

No.	Lat. (38°)	Long. (−122°)	depth (km)	M_D	Post-S Coda Duration (s)				P-to-S Time (s)				$(t_C - t_S)/(t_S - t_P)$			
					R1	R2	R3	R4	R1	R2	R3	R4	R1	R2	R3	R4
2	0.24217	0.34033	7.68	2.11	2.5	1.8	2.0	4.0	2.1	1.4	1.7	4.5	1.2	1.3	1.2	1.0
8	0.24400	0.34233	7.57	2.04	2.4	1.6	2.0	4.0	2.0	1.3	1.8	4.0	1.2	1.2	1.1	1.0
12	0.24617	0.34400	7.71	2.37	2.6	1.7	2.0	4.0	2.0	1.3	1.8	3.6	1.3	1.3	1.1	1.1
13	0.23583	0.32850	9.56	3.24	2.9	1.8	2.1	4.0	2.3	1.5	1.7	3.7	1.3	1.2	1.2	1.1
14	0.34517	0.37417	2.81	1.55	1.0	2.8	3.2	5.2	0.6	2.1	2.3	5.0	1.6	1.4	1.4	1.1
15	0.37033	0.38216	4.38	1.33	1.2	3.0	3.3	5.5	0.9	2.3	2.5	5.2	1.4	1.3	1.3	1.1
18	0.28017	0.40767	4.63	1.58	1.9	1.9	3.0	4.5	1.3	1.3	2.4	4.2	1.5	1.5	1.2	1.1
20	0.16850	0.29550	8.69	2.14	3.5	2.2	2.0	2.8	3.2	1.8	1.7	2.8	1.1	1.2	1.2	1.0
22	0.17717	0.31017	9.15	2.47	3.3	2.0	1.7	3.3	3.0	1.8	1.5	3.5	1.1	1.1	1.1	0.9
23	0.27783	0.34500	5.38	1.44	2.0	1.7	2.2	3.3	1.5	1.3	1.8	3.3	1.3	1.3	1.2	1.0
24	0.17300	0.30383	4.58	1.22	3.5	2.0	1.8	2.3	3.0	1.6	1.5	4.5	1.3	1.3	1.2	1.0
25	0.20000	0.31133	9.00	1.53	3.1	2.0	1.7	2.7	2.7	1.6	1.3	2.7	1.2	1.3	1.3	1.0
26	0.35983	0.38800	5.06	2.42	1.5	3.0	3.5	5.3	0.9	2.4	3.0	5.3	1.6	1.3	1.2	1.0
28	0.27917	0.35250	6.96	1.63	2.0	1.7	2.3	3.5	1.5	1.3	2.0	3.5	1.3	1.3	1.2	1.0
29	0.22883	0.33667	8.01	1.10	2.5	1.8	2.1	–	2.0	1.5	1.8	–	1.2	1.2	1.2	–
30	0.23833	0.33300	7.06	1.11	2.4	1.5	1.8	–	2.0	1.2	1.5	–	1.2	1.2	1.2	–
31	0.24900	0.36383	4.77	2.03	2.3	1.4	2.5	3.5	1.8	1.1	2.2	3.5	1.3	1.3	1.1	1.0
33	0.18033	0.30317	10.94	2.93	3.0	2.3	2.8	2.7	2.8	1.8	2.8	2.7	1.1	1.2	1.0	1.0
36	0.19800	0.31216	8.77	1.20	3.2	2.2	1.8	2.8	2.7	1.8	1.4	2.8	1.2	1.2	1.3	1.0
37	0.21950	0.32034	6.26	1.12	2.8	1.8	1.4	–	2.4	1.3	1.1	–	1.2	1.4	1.2	–
39	0.14950	0.30400	5.47	1.12	4.2	2.1	1.8	2.6	3.5	2.0	1.8	3.0	1.2	1.1	1.0	0.9
42	0.24333	0.37400	4.25	1.80	2.2	1.4	2.4	4.5	1.6	0.9	2.0	4.0	1.4	1.5	1.2	1.1
43	0.24033	0.34400	4.97	1.39	2.4	1.5	1.8	3.0	1.6	1.0	1.4	3.0	1.5	1.5	1.3	1.0
47	0.22933	0.33167	7.15	1.25	2.1	1.4	1.7	2.8	1.8	1.0	1.2	2.5	1.2	1.4	1.4	1.1
50	0.28517	0.34917	5.81	1.21	2.0	1.8	2.0	3.5	1.4	1.3	1.4	3.5	1.4	1.3	1.4	1.0
51	0.17216	0.29900	5.04	1.24	3.0	1.8	1.3	2.9	2.5	1.5	1.2	2.9	1.2	1.2	1.1	1.0
52	0.33667	0.37366	5.65	1.22	1.4	2.7	3.0	–	1.0	2.1	2.4	–	1.4	1.3	1.2	–
53	0.36467	0.38033	5.33	1.64	1.6	3.3	3.5	5.8	1.2	2.5	2.8	5.8	1.3	1.4	1.3	1.0
54	0.35683	0.37683	4.51	1.47	1.7	3.2	3.5	–	1.2	2.4	2.8	–	1.4	1.4	1.3	–
55	0.35217	0.37750	5.61	1.38	1.5	3.2	3.3	–	1.1	2.4	2.6	–	1.4	1.4	1.3	–

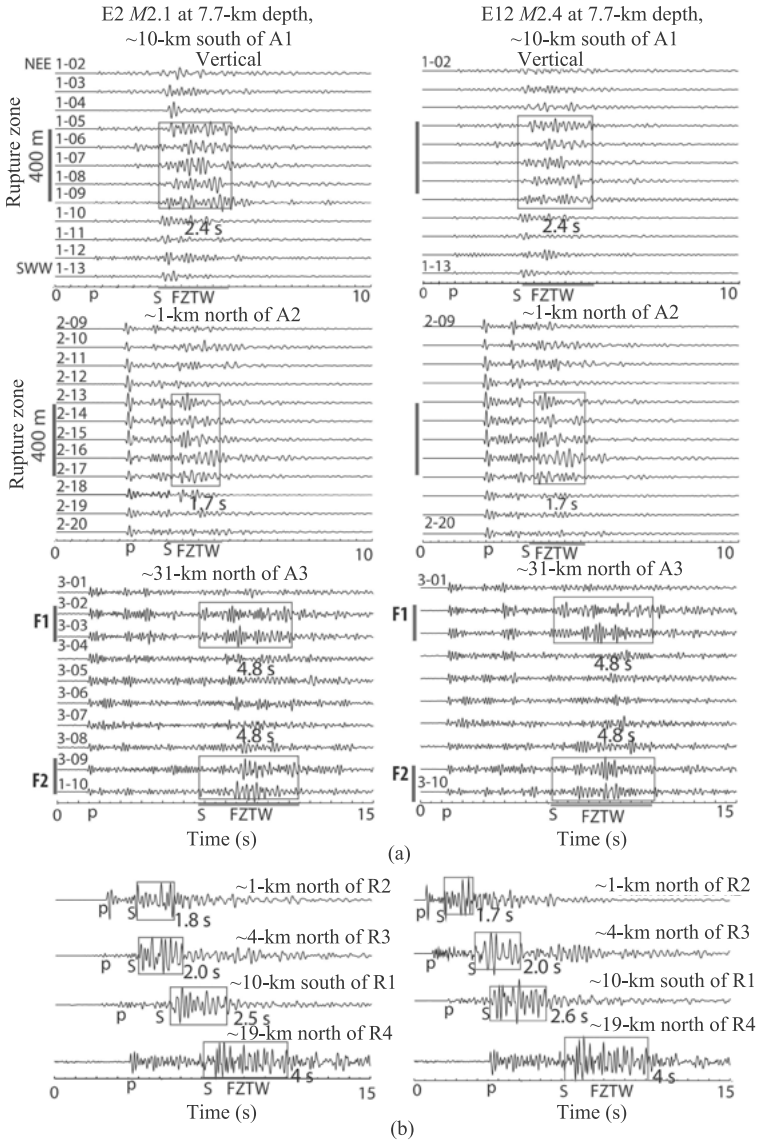

Fig. 1.14 **(a)** Seismograms at A1, A2 and A3 for two similar aftershocks E2 and E12 occurring within the WNF rupture zone at 7.7 km depth with their epicentral distances of 10, 1 and 31 km from A1, A2 and A3. FZTWs (in boxes) are observed at stations A1-05 to A1-09 of A1, stations A2-12 to A2-17 of A2, and stations A3-02, A3-03, A3-09 and A3-10 of A3. Post-S coda durations of FZTWs average 2.4 s at A1, 1.7 s at A2, and 4.8 s at A3 for E2 and E12. **(b)** Vertical-component seismograms at four REFTEK stations R1–R4 for these two similar aftershocks. Other notations are same as in Figure 1.13b. Post-S coda durations of FZTWs (in boxes) recorded at these stations increase as the epicentral distances increase but having smaller increasing rate along the F1 and F2 than along the WNF.

arriving at R4, again suggesting a continuous waveguide with weaker trapping efficiency along the south WNFZ and the Franklin Fault.

Finally, Figure 1.15 shows FZTWs recorded at three arrays A1, A2, and A3, and four REFTEK seismographs R1–R3 for two shallow aftershocks (E14 and E15 in Table 1.1 and Fig. 1.1b) occurring at 2.8-km and 4.4-km depths within the rupture zone about 1 to 4-km north of A1. Post-S coda durations of FZTWs average 1.0 s to 1.2 s at A1 and 2.8 s to 3.0 s at A2. The $(t_C - t_S)/(t_S - t_P)$ ratios for these FZTWs recorded at A1 and A2 are 1.3–1.6 for these two shallow aftershocks. The post-S coda durations of FZTWs at A3 are ∼6 s for these events located ∼42 km to ∼45 km from A3, almost 4 times as long as the epicentral distance between them and A1. The $(t_C - t_S)/(t_S - t_P)$ ratios at A3 are ∼1.0 (Table 1.2), smaller than those at A1 and A2 but larger than that at A3 for deeper aftershocks, suggesting that the waveguide along the FF has an effective trapping efficiency at shallow depth. The post-S coda durations of FZTWs recorded at these REFTEK stations increase from 1 s to 3.4 s as the epicentral distances increase from ∼1 km to ∼18 km. The $(t_C - t_S)/(t_S - t_P)$ ratios for these FZTWs at R1–R4 range from 1.1 to1.5 with the lowest ratio 1.0 for FZTWs at R4 (Table 1.2).

We analyzed waveform data recorded at REFTEK-130 seismographs located along and away from the WNFZ and Franklin Fault both in time and frequency. For example, Figure 1.16 shows prominent FZTWs recorded at four stations R1 to R4 located along with the faults, but not at station R7 located ∼2 km away from the WNF for three aftershocks E26, E13 and E20 occurring at depths of 5 km, 9.6 km and 8.7 km, respectively. We measured post-S coda durations of FZTWs increasing from 1.5 s to 5 s as the hypocentral distances between aftershock E26 and four on-fault stations R1–R4 increase from ∼6 km to ∼36 km. Similarly, we measured post-S coda durations of FZTWs increasing from 1.8 s to 3.9 s as the hypocentral distances between aftershock E13 and stations R1–R4 increase from ∼10 km to ∼23 km. We measured post-S coda durations of FZTWs increasing from 1.8 s to 3.3 s as the hypocentral distances between aftershock E20 and stations R1–R4 increase from 9 km to 20 km. In contrast, the post-S coda durations at station R7 out of the WNFZ is 1.5–1.6 s. The $(t_C - t_S)/(t_S - t_P)$ ratios for these FZTWs at R1–R4 range from 1.0 to1.6 with the larger ratio for FZTWs recorded at R1 and R2 located within the WNFZ rupture zone and smaller ratio at R4 close to the Franklin Fault (Table 1.2), indicating the stronger waveguide trapping effect along the WNFZ rupture zone than the FF.

We have observed and measured FZTWs at four REFTEK stations for 30 on-fault aftershocks (*see* Table 1.2). The measurements of FZTWs at R1 and R2 are consistent with those at co-located stations of arrays A1 and A2 (Table 1.1) within the rupture zone for the same aftershocks. We also notice the wavetrains with relative large amplitudes and long durations following the first P-arrivals at

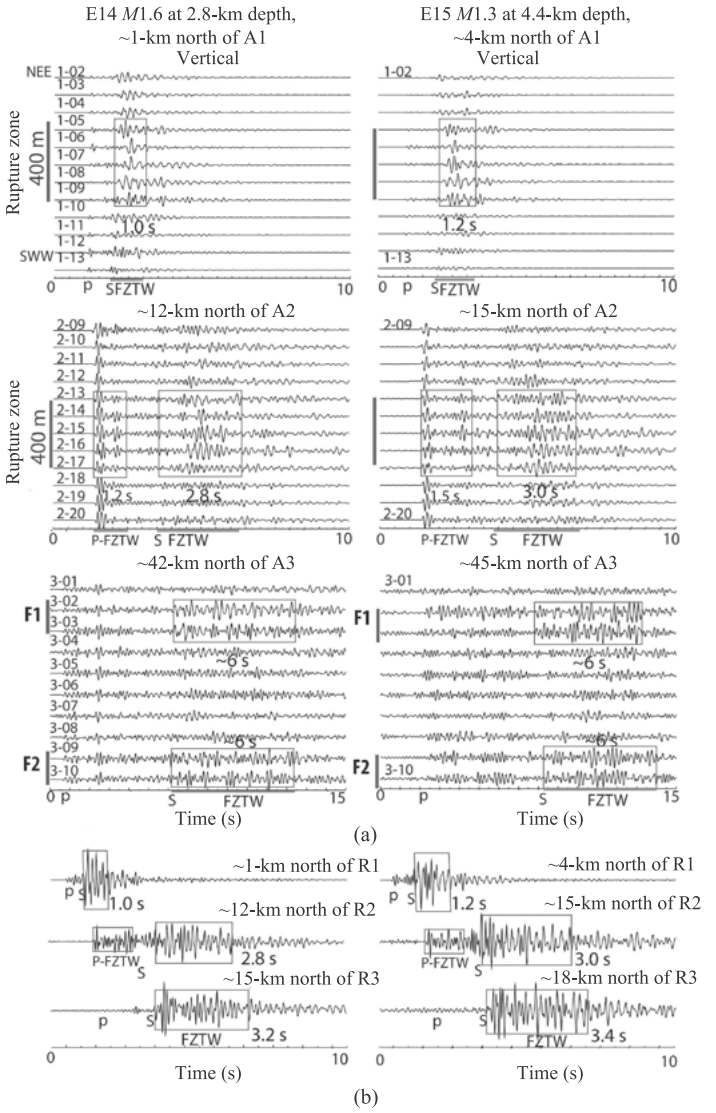

Fig. 1.15 **(a)** Seismograms at A1, A2 and A3 for two shallow aftershocks E14 and E15 occurring within the north WNF rupture zone at depths of 2.8 km and 4.4 km. Aftershock E14 was located at epicentral distances of 1, 12 and 42 km from A1, A2 and A3; aftershock E15 located at 4, 15 and 45 km from A1, A2 and A3. FZTWs (in boxes) are observed with post-S coda durations averaging 1.0–1.2 s at A1 and 2.8-3.0 s at A2. FZTWs (in boxes) with ∼6-s post-S coda duration are observed at stations A3-02, A3-03, A3-09 and A3-10. It is noted that the post P-coda durations average 1.2 to 1.5 s following the first P-arrivals at stations of A2 located within the rupture zone. **(b)** Vertical-component seismograms at four REFTEK stations R1–R3 for these two shallow on-fault aftershocks. Post-S coda durations of FZTWs (in boxes) recorded at these stations increase as the epicentral distances increase but having smaller increasing rate along the F1 and F2 than along the WNF.

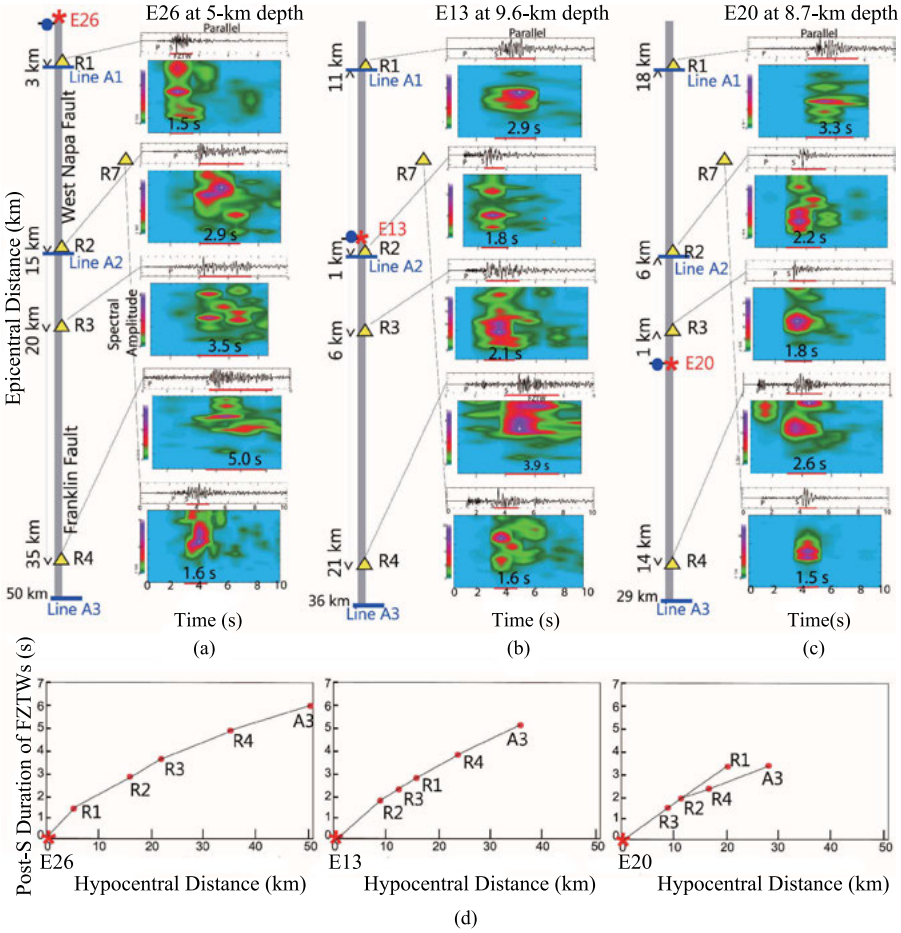

Fig. 1.16 Parallel-component seismograms and normalized spectral amplitudes at four on-fault REFTEK-130 seismometers R1 to R4 and one off-fault seismometer R7 (marked by yellow triangles) deployed along the West Napa Fault and Franklin fault (marked by gray thick lines) for 3 on-fault aftershocks E26 **(a)**, E13 **(b)** and E20 **(c)** (marked by red stars, also see Table 1.1 and Fig. 1.1) occurring at 5-km, 9.6-km and 8.7-km depths, respectively. Epicentral distances between aftershocks and seismic stations are plotted with arrows besides seismic stations in the schematic diagrams left to seismograms. The post-S coda duration of FZTWs in each plot is marked by a horizontal red bar with measured duration time. **(d)** Post-S coda durations of FZTWs (red dots) measured at four on-fault stations R1 to R4 along with WNFZ and Franklin Fault, and the cross-fault seismic array Line 3 for three on-fault aftershocks E26, E13 and E20 versus hypocentral distances between these aftershocks and seismic stations, showing that the post-S coda durations of FZTWs increase with increasing travel distances, with larger increasing rate along the WNFZ than along the Franklin Fault.

stations A2-13 to A2-16 of array A2 located within the WNFZ for two shallow aftershocks E14 and E15. We interpret these wavetrains to be as P-type FZTWs with the post-P coda durations of 1.2–1.5 s, which are shorter than the post-S coda durations of 2.8–3.0 s at the same stations for E14 and E15. We shall discuss the details of P-type FZTWs in a separate paper.

1.3 Subsurface Damage Structure Inferred from FZTWs

We have identified significant FZTWs generated by 41 Napa aftershocks and recorded on three cross-fault seismic arrays (A1, A2, and A3) and four REFTEK seismographs (R1 to R4) deployed along the WNFZ and the Franklin Fault. The $(t_C - t_S)/(t_S - t_P)$ ratios for FZTWs are equal to or larger than 1.2 on most seismograms recorded at A1, A2, and R1 to R3 for sources and receivers both located within the rupture zone of the 24 August 2014 $M6$ South Napa earthquake (refer to Table 1.1 and Table 1.2). However, the $(t_C - t_S)/(t_S - t_P)$ ratios for FZTWs on seismograms recorded at R4 and A3 located along the south WNF and Franklin fault (FF) that did not rupture in the 2014 $M6$ earthquake are 0.8–1.0 s, indicating a waveguide having moderate trapping efficiency along the south WNFZ and FF. In contrast, the $(t_C - t_S)/(t_S - t_P)$ ratios on seismograms recorded at all seismic stations for aftershocks occurring far away from the WNFZ and FF are less than 0.5, indicating no significant FZTWs were excited by these off-fault events.

Figure 1.17a shows measured post-S coda durations of FZTWs recorded at on-fault stations of arrays A1, A2, A3 and REFTEK stations R1 to R4 for the 41 aftershocks occurring within the WNFZ (*see* Table 1.1 and Table 1.2) *versus* their hypocentral distances between aftershocks and seismic stations. The measurements show that post-S coda durations of FZTWs recorded at A1, A2, R1, R2 and R3, which were located on or close to the surface rupture of the 2014 $M6$ South Napa earthquake, increase from ∼1.0 s to ∼4.0 s as hypocentral distances of these aftershocks increase from ∼3 km to ∼21 km. The longer coda durations of thee FZTWs result from their greater travel distances within the low-velocity waveguide. Although an approximately 14-km-long surface rupture was observed, the subsurface rupture likely extends beyond the northernmost and southernmost ends of the surface rupture, consistent with aftershock alignments (Hardebeck and Shelly, 2014) and afterslip observations (Hudnut *et al.*, 2014).

The post-S coda durations of FZTWs recorded at R4 and A3, which were deployed at the south West Napa fault and Franklin fault, increase from ∼2.5 s to ∼6.0 s as hypocentral distances of these aftershocks increase from ∼20 km to ∼50 km, but show a lower increasing rate than that for A1, A2, R1, R2, and R3. Our observations and measurements of post-S coda durations of FZTWs generated by these aftershocks suggest that the low-velocity waveguide along the WNFZ extends continuously to Franklin Fault, but the waveguide trapping efficiency along the south WNFZ and FF is weaker than that along the WNFZ with surface rupture during the 2014 $M6$ South Napa earthquake. Similar relationships between the waveguide trapping effect and the magnitude have been observed rupture zones of the 1992 $M7.4$ Landers and 1999 $M7.1$ Hector Mine earthquakes (Li *et al.*, 1998, 2003; Vidale and Li, 2003) and the 2004 $M6.0$ Parkfield earthquake (Li *et al.*, 2006).

Although there is an empirical relationship between coda length and seismic wave propagation distance (Fig. 1.17a), there is an amount of scatter in the data, which we suggest arises from the uncertainties of post-S coda measurements, aftershock locations, and sensitivity of the waveguide effect to the event location within the rupture zone. In general, however, the data (Fig. 1.17a) are consistent

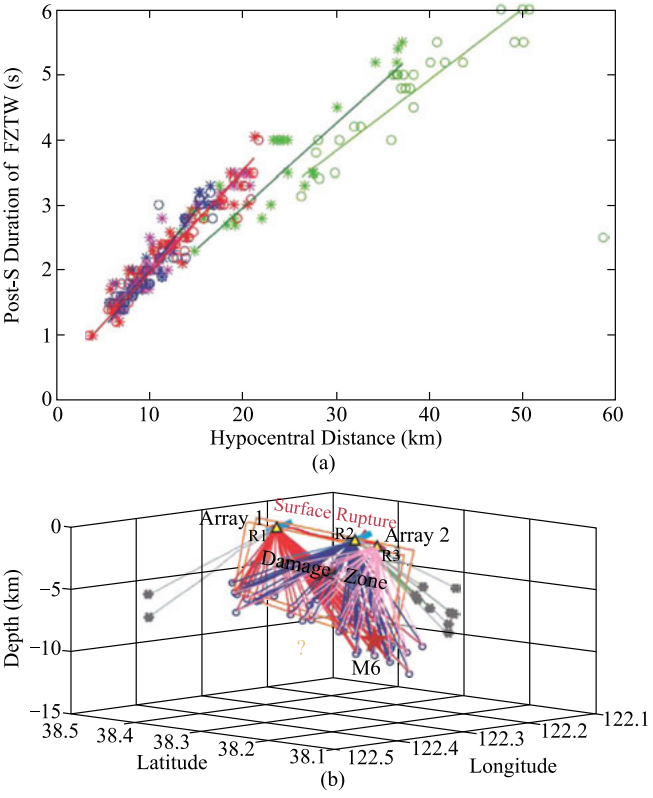

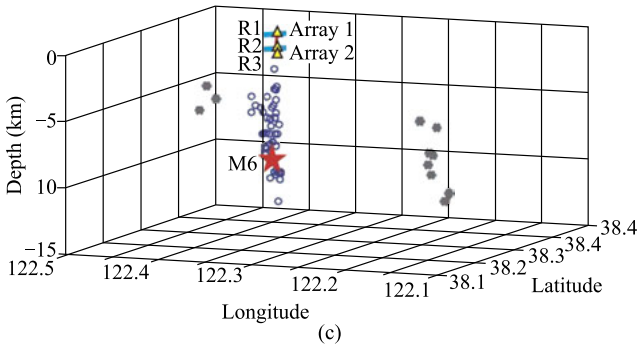

Fig. 1.17 **(a)** Measured post-S coda durations of FZTWs recorded at arrays A1 (red circles), A2 (blue circles) and A3 (green circles), and REFTEK stations R1 (red stars), R2 (blue stars), R3 (pink stars) and R4 (green stars) for 41 aftershocks that occurred at varying depths within the rupture zone along the WNFZ. Post-S coda durations are plotted versus hypocentral distances between these aftershocks and the recording stations. The solid lines (in the same color as the data points) are the least-squares fit to the measurements. Generally, for aftershocks with less ∼20 km hypocentral distances, coda duration increases more rapidly with hypocentral distance, which implies higher trapping efficiency of the waveguide (greater velocity reduction of fault rocks relative to wall rocks). This higher trapping efficiency generally occurs at the shallower depths along the rupture zone of the 2014 $M6$ south Napa earthquake. **(b)** 3D volume (viewed in the southwest direction, −135° from the north and 15° downward) showing the hypocentral locations of 55 aftershocks (Table 1.1) that were recorded at arrays A1 and A2 (marked by thick green bars), and REFTEK stations R1, R2 and R3 (yellow triangles) deployed across and along the surface rupture (thick red line) of the 2014 $M6$ South Napa earthquake and its northern projection. Straight lines are ray paths between A1 (red), A2 (blue), R1 (red), R2 (blue), R3 (pink) and the aftershocks (open circles) that generated prominent FZTWs. Straight lines (green) are the ray paths between the aftershocks (stars) and the recording stations for which we do not observe clear FZTWs. We interpret a central damage zone (bounded by the two nearly vertical rectangular planes) associated with the 2014 $M6$ mainshock, extending from the surface rupture to 5–6 km depth beneath A1 and 7–8 km depths beneath A2. The interpreted rupture zone is schematic geometry used in the model of Figure 1.18b. **(c)** 3D volume (viewed along the rupture zone, −68° from the north and 15° downward). Locations of aftershocks (open circles) generating clear FZTWs delineate the nearly vertical rupture zone (thick curve at the ground surface) crossed by array A1 and A2 (thick bars). Stars denote aftershocks which did not generate clear FZTWs.

with a continuous low-velocity waveguide at seismogenic depths along with the 2014 rupture zone. The aftershocks with shorter hypocentral distances (either at shallower depths or nearer to seismic arrays) show the greatest $(t_C - t_S)/(t_S - t_P)$ ratio for guided waves (refer to Table 1.1 and Table 1.2), implying strongest trapping efficiency of the waveguide at shallow depths between A1 and A2. We note that the two shallowest aftershocks E14 and E42 at 2.8 km and 4.25 km depth show the highest $(t_C - t_S)/(t_S - t_P)$ ratios of 1.4–1.6, implying a more prominent low-velocity waveguide at the shallow depths.

FZTWs recorded at A1, A2, A3, R1, R2, R3 and R4 (Figs. 1.13 to 1.16) show that the low-velocity waveguide along the WNFZ extends further southward to at least A3 but possibly with a more moderate fault zone velocity reduction. The existence of a relatively low-velocity waveguide to the south of the 2014 $M6$ South Napa earthquake is also consistent with the ground motion observations by Baltay and Boatwright (2015).

Empirical studies have shown that the generation of FZTWs is strongly dependent on the source location with respect to the low-velocity waveguide (e.g., Li and Leary, 1990; Li and Vidale, 1996; Ben-Zion, 1998), whereby earthquakes located within the waveguide generate stronger FZTWs than earthquakes located out of the waveguide. Thus, the relative amplitudes of the FZTWs allow us to delineate the geometry of subsurface rupture zone. Figures 1.17b, 1.17c shows the locations of 55 aftershocks (refer to Fig. 1.1) in a 3-D volume, including 41 aftershocks with prominent FZTWs recorded at A1, A2, R1, R2 and R3 that have $(t_C - t_S)/(t_S - t_P)$ ratios greater than 1.1 and 14 aftershocks without prominent FZTWs and with $(t_C - t_S)/(t_S - t_P)$ ratios less than 0.7 (refer to Table 1.1). Hypocenters of aftershocks that generated prominent FZTWs delineate a NNW-SSE-striking rupture zone that dips to the west at $> 80°$. The most recently damage zone at depth is several kilometers longer than the ∼14-km-long 2014 surface rupture and likely extends to at least 7–8 km depth near the mainshock hypocenter but only 5–6 km deep in the northern portion of rupture zone.

1.4 3-D Finite-Difference Simulations of FZTWs Generated by Aftershocks

We developed models of the WNFZ subsurface rupture zone on the basis of the hypocenters of aftershocks that generated prominent FZTWs and the measurements of FZTW coda durations and waveguide trapping efficiency (Fig. 1.17). With layer depths, fault dip, and velocities of the surrounding basement rocks based on an existing velocity model for the region (Fig. 1.18a) from Stidham *et al.* (1999) and Brocher *et al.* (2005), we constructed a velocity model (*see* Fig. 1.18b and Table 1.3) for the WNFZ and Franklin Fault. Velocities and attenuation (Q) in our model are depth dependent because increasing pressure with increasing depth influences (e.g. Suess and Shaw, 2003; McGarr *et al.*, 2009) the density and the bulk modulus of rocks as well as the healing rates of damaged rocks (e.g. Byerlee, Rice, 1992; Sibson, 1996; Marone, 1998). The depth-dependent pressure increase may also influence the development of fault gouge due to normal stress and rock strength (Scholz, 1990; Guo and Morgan,

Table 1.3 Model parameters for West Napa Rupture Zone and Franklin Fault.

Model parameters WNF (FF)	Layer 1	Layer 2	Layer 3	Layer 4	Layer 5
Depth of the layer bottom (km)	1.0	3.0	5.0	8.0	10.0
Waveguide width (m), Damage zone/core	400/200	400/200	300/150	200/100	
Waveguide S velocity (km/s)	1.0/0.75 (1.3/1.0)	1.3/1.0 (1.7/1.3)	1.8/1.25 (2.3/1.6)	2.0/1.5 (2.6/2.0)	
Waveguide P velocity (km/s)	2.0/1.5 (2.6/2.0)	2.6/2.0 (3.4/2.6)	3.5/2.5 (4.5/3.2)	4.0/3.0 (5.2/4.0)	
Waveguide Q-value	20	30	50	60	
Wall-rock S velocity (km/s)	1.5	2.0	2.5	3.0	3.5
Wall-rock P velocity (km/s)	3.0	4.0	5.0	6.0	6.5
Wall-rock Q-value	50	80	100	150	200

2007). For these reasons, we used varying velocities with depth in our model. Our 3-D model includes a 20-km-long 400-m-wide rupture zone within which velocities are reduced by 25%–50% relative to wall-rock velocities along the West Napa Fault where A1, A2, R1, R2 and R3 were located, and a 30-km-long fault zone within which velocities are reduced by 20%–35% along the Franklin Fault where R4 and A3 were located (Fig. 1.18b). We infer a maximum velocity reduction within a 200-m-wide damaged fault core at shallow depths (see model parameters in Table 1.3). The depth of the low-velocity rupture zone increases from 5 km beneath A1 to 8-km beneath A2 and A3. The damage zone diminishes below those depths.

To compute synthetic seismograms, we used a 3-D finite-difference code that fits waveforms of FZTWs recorded at A1 and A2. The finite-difference computer code is second order in time and fourth order in space (Graves, 1996; Vidale *et al.*, 1985), and it propagates the complete wave-field through an elastic media with a free surface boundary and spatially variable anelastic damping (an approximate Q). Our calculation used the maximum 90-500-90 element grids in $x - y - z$ coordinates, with a grid spacing of 100 m to simulate a volume of 9 km in width across the fault zone, 50 km in length along the fault line between A1 and A3, and 9 km in depth (*see* Fig. 1.18b). When focal depth of aftershocks are larger than 9 km, we extend the element grids in z to 120 (12 km). In order to reduce the computer memory in modeling for most aftershocks, we decrease the element grids in y and/or z to include the receiver array and hypocenter of the aftershock in study.

The low-velocity waveguide, composed of a 200-m-wide fault core zone of maximum velocity reduction sandwiched within a 400-m-wide damage jacket with milder velocity reduction, is embedded in the higher-velocity surrounding rocks with a free surface. The north portion of the waveguide with greater velocity

reductions along the WNF rupture zone is 20 km long while the southern portion of the waveguide with more moderate velocity reductions along the Franklin Fault is 30-km long (Table 1.3). The seismic array was placed across the waveguide along the fault strike. The seismic waves were derived from a double-couple source (according to the mainshock focal mechanisms) with radiation patterns included in the volume.

In the first stage of our error-and trial forward modeling approach, we used 100-m grid spacing to obtain coarse model parameters at low frequency to save computer memory space and computation time. We then used 50-m or 25-m grid spacing to increase the resolution of fault-zone structure in the model at higher frequency. When the grid spacing was 100-m and the minimum velocity was 0.75 km/s, the maximum frequency of the synthetic seismograms is 1.5 Hz. When the grid spacing was reduced to 50-m or 25-m, we increased the maximum frequency to 3-Hz or 6-Hz. When using the small grid spacing, we decreased the size of the model to an appropriate volume that included source and receivers to reduce computer memory and computation time, but to avoid losing the damping function to model edge effect.

We simulated the FZTWs recorded at A1, A2 and A3 as well as R4 for aftershocks that occurred at varying depths and epicentral distances via a trial-and-error, forward-modeling procedure to obtain the well-fit model parameters. We have used similar modeling parameters for trapped waves observed at the Parkfield San Andreas Fault zone, the Landers-Hector Mine rupture zones in California (e.g., Li *et al.*, 2000, 2004, 2008), and the 2010 Darfield and 2011 Christchurch fault zones in New Zealand (Li *et al.*, 2014). These previous studies show the sensitivity of model parameters to synthetic trapped waveforms, whereby wider fault zones produce trapped waves with lower frequencies, and lower velocity fault zones produce longer dispersive trapped waves. A lower-Q fault zone produces trapped waves with smaller amplitudes and shorter coda at lower frequencies. Variations in wall-rock velocities and layer depths affect the P- and S-arrival times, but variations in wall-rock Q produces minimal variation in modeling results. We use these results to guide the modeling and interpret features of the fault zone in the present study.

Synthetic waveforms (Fig. 1.18c) computed using our inferred velocity model (Fig. 1.18b) compare well with seismograms recorded at seismic array A1 for three on-fault aftershocks (E8, E31 and E2 in Table 1.1 and Fig. 1.1b). We use a double-couple source within the fault zone. FZTWs with large amplitudes and 2.2–2.4 s of post-S coda durations are observed at five near-fault stations A1-05 to A1-09 of A1 within the rupture zone. The consistency of the observed and computed seismograms suggests that the 2014 rupture zone consists of a remarkable low-velocity waveguide formed by severely damaged rocks. Seismic energy is trapped and best propagated with large amplitudes along the waveguide for frequencies between 1 and 6 Hz.

We compare synthetic waveforms (Fig. 1.18d) developed from our velocity model (Fig. 1.18b) with seismograms recorded at array A2 for other three on-fault aftershocks (E33, E22 and E26). The synthetic FZTW post-S-wave coda durations (2.2–3 s) compare well at five near-fault stations A2-13 to A2-17 of A2 located within the rupture zone. We then show comparisons for A3 (Fig. 1.18e) using three aftershocks (E22, E12 and E18). Post-S coda durations (3.5–5.2 s) for synthetic FZTW waveforms show large amplitudes at two stations A3-09 and A3-10 of array A3 near the Franklin Fault are consistent with the observed data recorded at A3. We also compared synthetic and observed waveforms at REFTEK station R4 for these three on-fault aftershocks showing 3.3–4.5 s coda durations of FZTWs (Fig. 1.18f).

In general, the coda duration times of FZTWs generated by these on-fault aftershocks increase as their travel (hypocentral) distances within the low-velocity fault-zone waveguide increase. However, the increasing rate of coda duration with distance for FZTWs traveling along the WNF rupture zone, within which rocks were severely damaged in the 2014 $M6$ mainshock is higher than that along the south WNF and Franklin that were unbroken at the surface in the 2014 $M6$ earthquake. We also note that the FZTW coda durations (2.2 s) for deep aftershocks E22 and E33 at 9–11 km depths is shorter than those (2.3–2.4 s) from aftershocks E2, E8 and E31 at depths of 4.8–7.7 km, although the hypocentral distances between two deep events and the recording array are greater than those between the shallower events and recording array. We suggest the shorter coda for the deeper event results from a diminished low-velocity waveguide below 7–8 km depth.

In forward modeling, the model parameters are interdependent and are not uniquely determined, as discussed in previous studies (e.g., Li and Leary, 1990; Li and Vidale, 1996; Ben-Zion, 1998; Igel *et al.*, 2002). The model parameters given in Table 1.3 are not uniquely constrained by this forward modeling because there is trade-offs among them. To obtain the best fit to observed FZTWs in

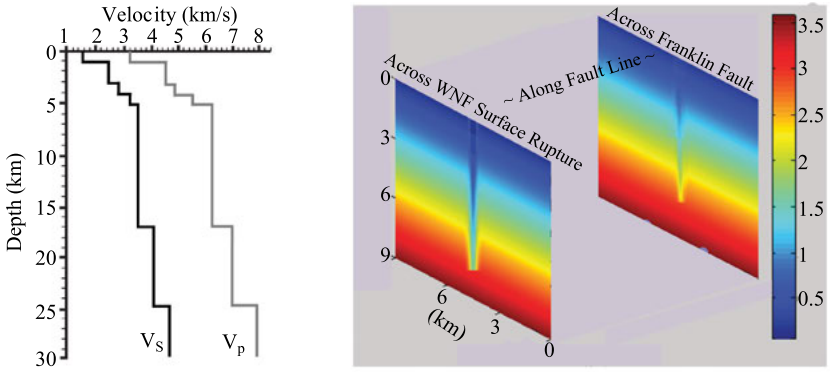

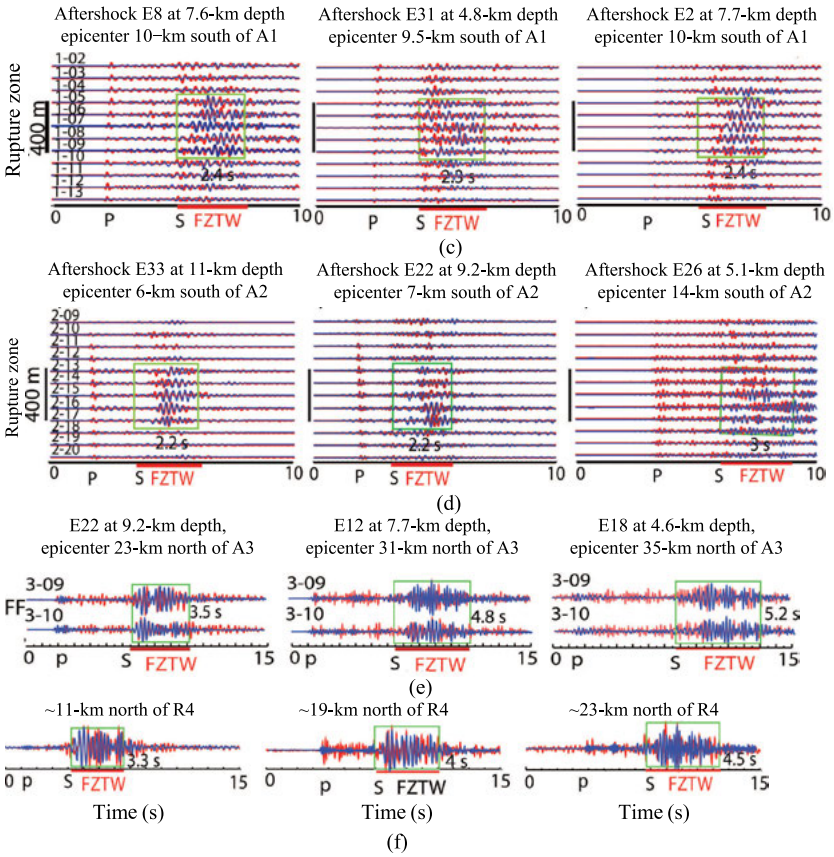

Fig. 1.18 **(a)** 1-D P- and S-velocities for the Napa region from Stidham *et al.* (1999) and Brocher *et al.* (2015) used for wall-rock velocities in our finite-difference modeling of FZTWs recorded along the West Napa Fault. **(b)** A 2-D slice of our 3-D velocity model of the WNFZ. The 400-m-wide rupture zone is exposed at the surface. Velocities within the rupture zone along the WNFZ are reduced by 40%–50% from wall-rock velocities, but reduced by 30%–35% along the Franklin Fault. **(c)** 3-D finite-difference synthetic seismograms (blue lines) using the model in (b) with observed seismograms (red lines) at array A1 for three aftershocks (E8, E31 and E2) located at depths of 7.6, 4.8 and 7.7 km, and ∼10-km epicentral distances south of A1. Seismograms were <8 Hz filtered. **(d)** Synthetic and observed seismograms at array A2 for aftershocks E33, E22 and E26 at depths of 11, 9.2 and 5.1 km, and with epicentral distances of 6, 7 and 14 km south of A2. **(e)** Synthetic and observed seismograms at stations A3-09 and A3-10 of array A3 across the Franklin Fault for aftershocks E22, E12 and E18 at depths of 9.2, 7.7 and 4.6 km, and with epicentral distances of 23, 31 and 35 km north of array A3. **(f)** Synthetic and observed seismograms at REFTEK station R4 located at the south WNF for aftershocks E22, E12 and E18 located at 11, 19 and 23 km north of R4. FZTWs (in green boxes) show large amplitudes and long post-S coda durations at stations within the rupture-zone.

modeling, we found that the S-wave velocity reduction and Q value within the damage zone are more sensitive than other model parameters to the post-S duration and amplitude of FZTWs at higher frequencies. The width of the damage zone at shallower depth is more sensitive than the width at deeper level to observations of FZTWs at stations located within the ∼400-m-wide rupture zone. Although the layer depths and velocities of surrounding rocks are constrained based on the velocity model for the Napa region (Stidham *et al.*, 1999), variations in surrounding-rock velocities and layer depths affect the arrival times of P and S waves, As a result of the limited available constraints, we permitted a 1–3 km variation in the locations of hypocenters used in our model to allow for possible lateral heterogeneity along the rupture zone and for aftershock location errors. Although our inferred velocity model resulted from 3-D finite-difference simulations of FZTWs is not well constrained by independent measurements. the finite-difference simulations provide a first-order estimate of the overall structure of the WNFZ and Franklin Fault in the subsurface.

1.5 FZTWs Generated by Explosions

1.5.1 The Explosion Data and FZTW Waveform Analysis

In September of 2016, an active seismic experiment with shots conducted in Napa Valley by Catchings et al. of the United States Geological Survey (USGS). A 15.4-km-long seismic line (called 2016 W-E Line in Fig. 1.19) consisting of 155 stations with vertical and horizontal L28 4.5-Hz sensors was deployed across the West Napa Fault Zone (WNFN) and adjacent faults. The station spacing is 100 m. The W-E seismic line nearly perpendicularly crossed multiple surface ruptures along at least three sub-parallel fault strands of the WNFZ. Another seismic array (called 2016 N-S Line) was NW-SE-oriented and 19.9-km in length, consisting of 200 vertical and horizontal sensors with 100-m station spacing 100 m, deployed across Napa Town. During the 2016 experiment, 36 shots were detonated along the two seismic lines, and two explosions (called SP1001 and SP1002 in Fig. 1.19) were detonated within the west rupture zone along the main trace of the WNFN at ∼3.5-km north and ∼5-km south of the 2016 W-E Line, respectively. Small amount of explosives set off at the bottom of 7–10 m deep drill holes allows seismic energy generated by tiny artificial sources to eliminate the near-surface soil affect and travel through the subsurface geological layers efficiently. All shots were detonated between the mid night and 5 am to avoid the day-time environmental and traffic noises. Because the length of the 2016 W-E Line is much longer than the cross-fault seismic arrays in the 2014 experiment,

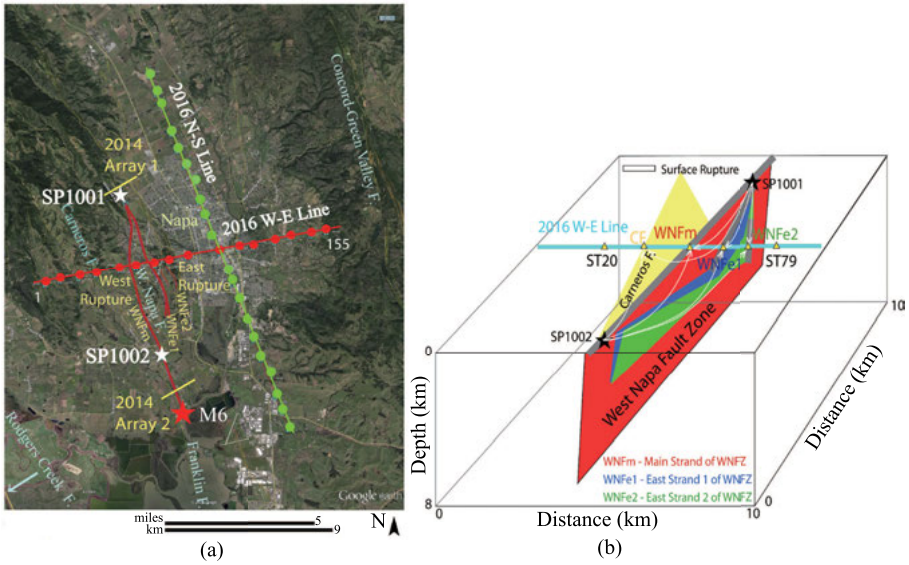

Fig. 1.19 **(a)** Map shows the 2014 M_w6.0 South Napa earthquake (red star), multiple surface ruptures (red lines) along the main and east strands (marked by WNFm, WNFe1 and WNFe2) of the West Napa Fault Zone (WNFZ), 1.9-km-long seismic Array 1 and Array 2 (yellow bars) deployed in the 2014 experiment, 15.4-km-long W-E Line (straight red line) consisting of 155 stations number by 1 to 155, and 19.9-km-long N-S Line (green line) consisting of 200 stations deployed in the 2016 experiment. 36 in-line shots (red and green circles) were detonated along the W-E and N-S seismic lines, respectively. Two explosions SP1001 and SP1002 (white stars) were detonated within the WNFm in 2016. Adjacent faults (brawn lines) with their names are shown in figure. **(b)** 3-D volume shows schematic geometry of multiple fault strands of the WNFZ and the CF, which connect at ∼3-km depth. Multiple fault strands of the WNFZ ruptured with surface breaks (marked by black rectangular bars) in the 2014 M6 mainshock. White curves with arrows denote raypaths from the explosions to stations located within the multiple strands of the WNFZ and the CF.

we expect that the FZTWs recorded in the 2016 experiment will provide more information on the rupture branching during the 2014 M_w6.0 earthquake and allow us to measure the width of multiple rupture zones more accurately.

In this section, we use FZTWs generated by two explosions and recorded at a 15.4-km long seismic array across multiple surface ruptures of the WNFZ and adjacent faults in the experiment to insight the branching structure of rupture associated with the 2014 South Napa earthquake.

Figure 1.20 shows vertical-component raw seismograms recorded at 100 stations (numbered by 1 to 100; 9.9 km in length) of the 2016 W-E Line for explosions SP1001 and SP1002. Air waves are clearly observed in seismograms because the site was very quiet during shots in experiment. The arrival times of air wave from explosion SP1001 (SP1002) to seismic stations of W-E Line are

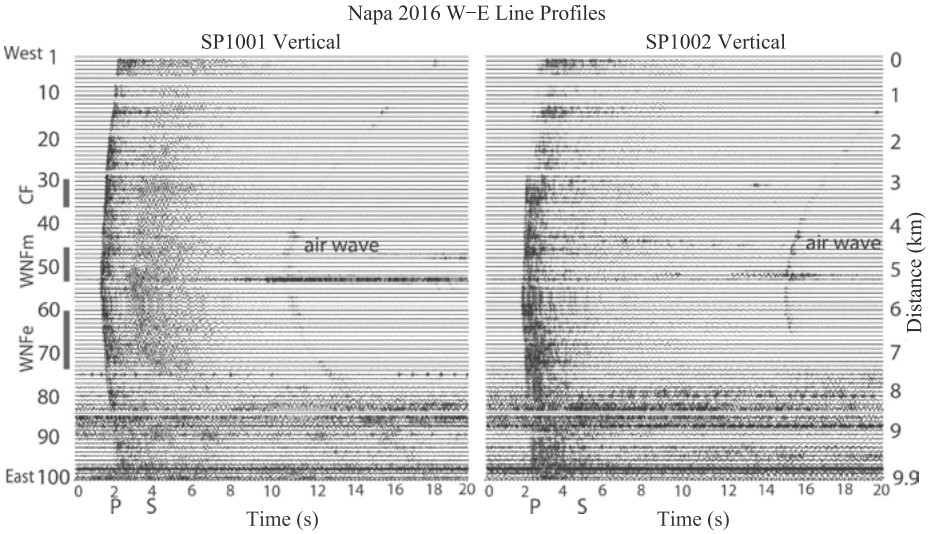

Fig. 1.20 Vertical-component raw seismograms recorded at 100 stations (numbered by 1 to 100 from west to east) of 2016 W–E Line for two shots (left) SP1001 and (right) SP1002 detonated within the rupture zone along the main strand of the WNFN at ∼3.5 km north and ∼5 km south of the center of seismic array. The station spacing is 100 m; the distance range of the seismic profile is from 0 km to 9.9 km from the west end of 2016 W-E Line. Vertical bars denote locations and widths of rupture zones including surface breaks along the main strand and east strands of the WNFZ (called WNFm and WNFe), and the width of the adjacent CF. Seismograms are plotted using a fixed amplitude scale in the profile. P, S and air waves are shown in seismograms.

consistent that it traveled over the distance of ∼3 km (∼5 km) at the sound speed of 343 m/s. We estimate Vp and Vs to be 3–4 km/s and 1.5–2 km/s along raypaths reaching 2–3 km depths, consistent with the fault wall-rock velocities in South Napa area (*see* Table 1.3).

In the same way as we identified the FZTWs generated by aftershocks. In the same way, we use the ratio of post-S coda time to S-P arrival time difference $(t_C - t_S)/(t_S - t_P)$, to indicate prominent guided waves well generated and observed for explosions detonated within the low-velocity rupture zone when the ratio is higher than 1.2.

Figure 1.21a shows band-pass (2–10 Hz) filtered seismograms recorded at 2016 W–E Line for explosion SP1001. Since we are mostly interested in the rupture branching associated with the WNFZ and nearby faults in the 2014 $M6$ mainshock, we use the data recorded at 60 stations numbered between 20 and 79 in the present study. We identify prominent FZTWs with large amplitudes and long durations (2.0–2.5 s) after S-wave at stations located within the main and branch rupture zones exposing at the surface along multiple strands of the WNFZ. The time differences between the P- and S-arrivals are approximately

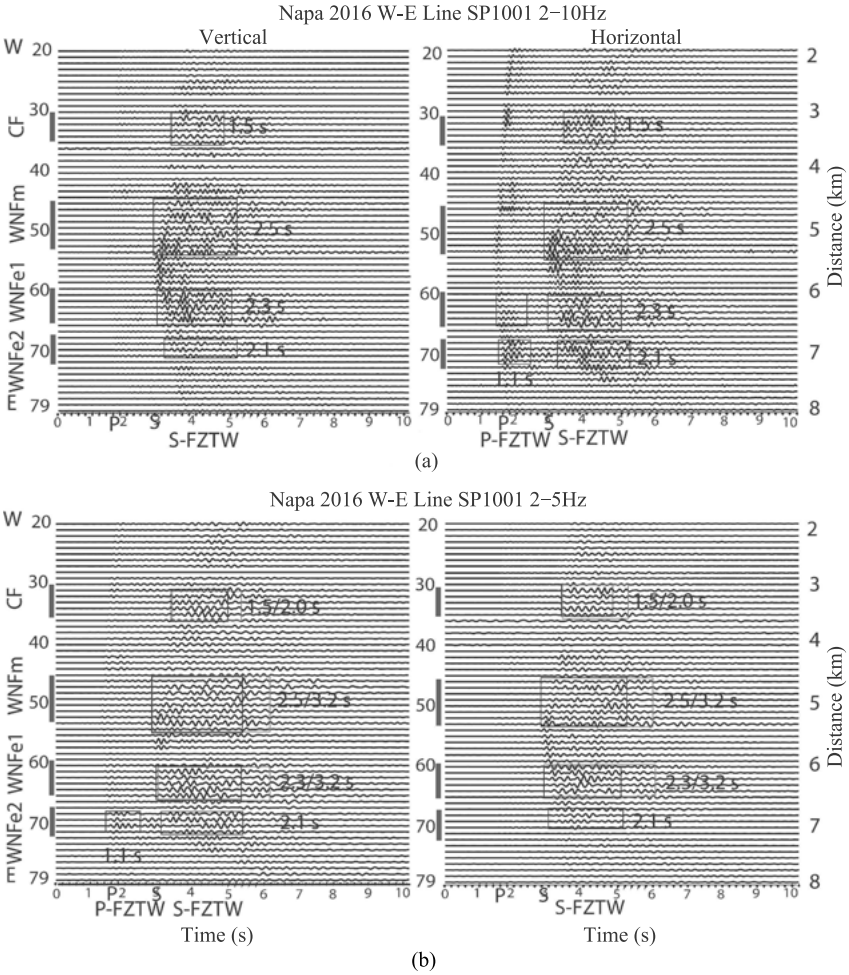

Fig. 1.21 **(a)** Vertical-component (left) and horizontal-component (right) seismograms recorded at 60 stations (numbered by 20 to 79 from west to east) of the 2016 W-E Line for explosion SP1001 detonated within the rupture zone along the WNF at ∼3.5 km north of the seismic array. The station spacing is 100 m; the distance range of the seismic profile is from 2 km to 8 km from the west end of the 2016 W–E Line. Vertical bars denote widths of rupture zones including surface breaks along the main strand and east strands of the WNFZ (called WNFm, WNFe and WNFe2), and the width of the adjacent CF. Seismograms have been band-pass (2–10 Hz) filtered, and are plotted using a fixed amplitude scale in the profile. **(b)** Same as in (a), but seismograms have been band-pass (2–5 Hz) filtered. Prominent FZTWs (in rectangular boxes) with large amplitudes and long durations following P- and S-waves (called P-FZTWs and S-FZTWs) were recorded at stations located within rupture zones of along multiple strands of the WNFZ. The duration of FZTWs shown in the box is the average value of measurements at stations located within the rupture zone width marked by a vertical bar. The leaking-mode FZTWs are recorded at the adjacent Carneros fault but with relatively short S-code duration.

1.5 s. Thus, $(t_C - t_S)/(t_S - t_P)$ ratios for these FZTWs generated by shot SP1001 range from 1.4 to 1.7, suggesting that remarkable low-velocity waveguides were formed by damaged rocks along multiple fault strands of the WNFZ at shallow depth during the 2014 $M6$ South Napa earthquake. FZTWs were well excited by the explosion and well recorded at stations as both the source and receiver located within the waveguide. The longest post-S coda (∼2.5 s) of FZTWs with largest $(t_C - t_S)/(t_S - t_P)$ ratio (∼1.7 s) are registered at stations (numbered from 48 to 54) located within the 500–600 m wide rupture zone along the main strand of the WNFZ (called WNFm), indicating that fault rocks along the WNFm experienced most severely damage during the 2014 $M6$ mainshock. Comparatively, we observe FZTWs with 2.1–2.3 s post-S coda durations and 1.4–1.5 $(t_C - t_S)/(t_S - t_P)$ ratios at stations (numbered from 61 to 65, and from 69 to 72) located within 300–400 m wide rupture zones along east strands of the WNFZ (called WNFe1 and WNFe2), suggesting that fault rocks along the east rupture zones experienced slightly less damage than those along the main rupture zone.

Figure 1.21b shows band-pass (2–5 Hz) filtered seismograms recorded at 2016 W–E line for explosion SP1001. The explosion-generating FZTWs at lower frequencies show even longer durations (∼3.2 s) with the larger $(t_C - t_S)/(t_S - t_P)$ ratio (2.1) than those at higher frequencies (2–10 Hz). The $(t_C - t_S)/(t_S - t_P)$ ratios of 1.4–2.1 for FTZWs generated by near-surface explosions are larger than the ratios of 1.2–1.5 for FZTWs generated by aftershocks occurring at seismogenic depths, suggesting that the fault rocks in the shallower portion of rupture zones had experience more severely damage during dynamic rupture in the 2014 $M6$ earthquake. We notice the wavetrains with relative large amplitudes and ∼1.1 s duration in the post-P coda at stations located within rupture zones. We call these wavetrains to be P-type FZTWs. The ratio of post-S to post-P coda durations of FZTWs is ∼0.55, consistent with the ratio of Vp to Vs for highly fractured and water-saturated rocks within the rupture zone.

We also notice wavetrains with relative large amplitudes and 1.5–2.0 s post-S coda duration in seismograms recorded at stations (numbered from 32–35) located within the ∼400-m-wide the Carneros Fault. These wavetrains are likely the FZTWs produced within the low-velocity waveguide when a seismic source is located outside the waveguide. The $(t_C - t_S)/(t_S - t_P)$ ratio of these wavetrains is 1.0–1.2, suggesting that a waveguide with more moderate velocity reduction and weak trapping effect exists along the CF than those along the WNFZ at shallow depth. The CF did not rupture in the 2014 $M6$ earthquake although minor slips might occur on it due to strong shaking by the nearby earthquake (Graymer, 2014).

Regarding to shot SP1002, we observe prominent FZTWs with large amplitudes and post-S coda durations of ∼4 s at stations located within rupture zones along multiple strands of the WNFZ and ∼3 s at stations within the Carneros

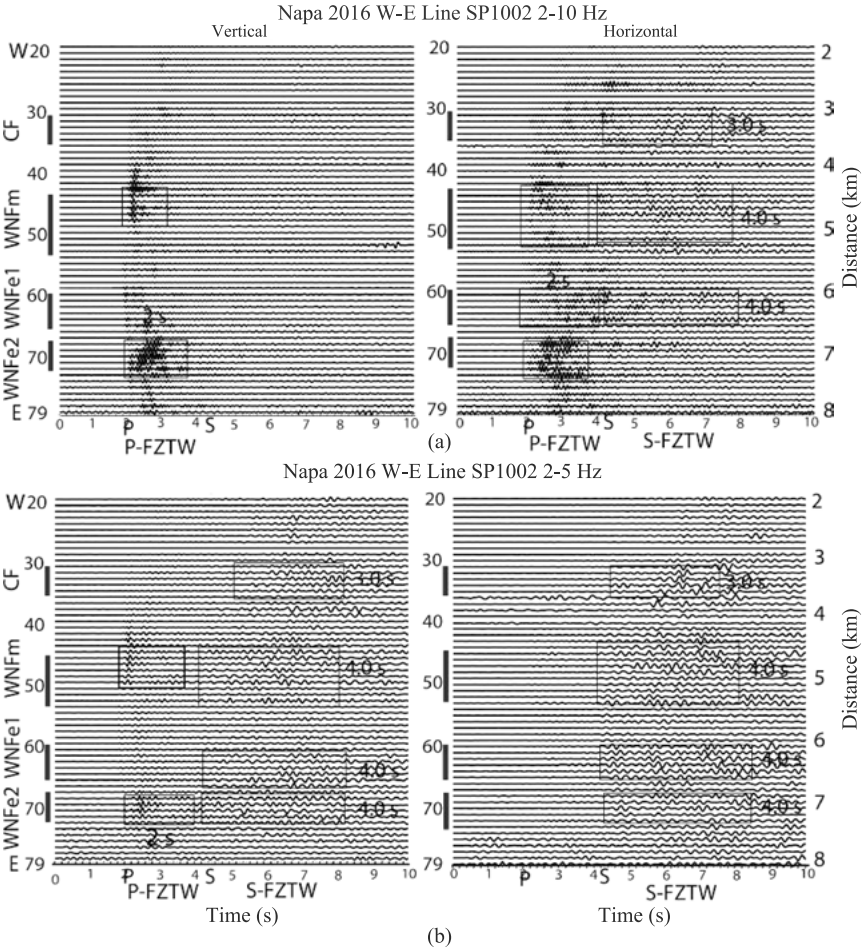

Fig. 1.22 **(a)** Vertical-component (left) and horizontal-component (right) seismograms recorded at 60 stations (numbered by 20 to 79 from west to east) of the 2016 W-E Line for explosion SP1002 detonated within the rupture zone along the WNF at ∼5 km south of the seismic array. **(b)** Same as in (a), but seismograms have been bandpass (2–5 Hz) filtered. Prominent FZTWs (in boxes) with large amplitudes and long durations following P- and S-waves (called P-FZTWs and S-FZTWs) were recorded at stations located within rupture zones of along multiple strands of the WNFZ. FZTWs are recorded at the adjacent Carneros fault but with relatively short S-code duration. Other notations are same as in Fig. 1.21.

Fault (Fig. 1.22). The time differences between the P- and S-arrivals are approximately 2.2 s at stations within the WNFZ, and 2.5 s at stations near the CF. The $(t_C - t_S)/(t_S - t_P)$ ratio for FZTWs recorded at the WNFZ is ∼1.8, showing remarkable low-velocity damage zones produced along multiple strands of the WNFZ in the 2014 $M6$ earthquake. The post-S durations and $(t_C - t_S)/(t_S - t_P)$

ratios measured at multiple strands of the WNFZ are similar suggesting that those surface rupture zones along multiple fault strands might merge at depth so that FZTWs generated by SP1002 detonated on the southern main WNF could propagate northward along multiple fault strands at the same manner. We notice P-type FZTWs with relatively large amplitudes and ∼2-s duration in the post-P coda recorded at stations located within rupture zones for explosion SP1002.

In contrast, the $(t_C - t_S)/(t_S - t_P)$ ratio for FZTWs recorded at the CF is ∼1.2, showing a low-velocity waveguide along the Carneros Fault which has less trapping effect than the waveguide along the WNF rupture zone. This ratio value (∼1.2) measured at the CF for SP1002 located on the main strand of the WNF is higher than the ratio (∼1.0) for SP1001. Combined with the surface expression and geometry of the WNF and CF, we tentatively explain that the CF runs subparallel to the north WNF, but likely connects the southern WNF-Franklin Fault at shallow depth. Fault Rocks within the CF were damaged by historical earthquakes on it and probably slightly damaged by the 2014 $M6$ mainshock.

We then compute spectral amplitudes of seismograms recorded at stations of the 2016 W-E Line located on or off multiple faults for explosions SP1001 and SP1002 detonated on the main strand of the WNFZ. Figure 1.23 shows prominent FZTWs with larger spectral amplitudes and longer post-S coda durations at stations on and close to the faults than those at stations away from the faults. Post-S coda durations of FZTWs measured from seismograms and spectral amplitudes are 2.1–2.5 s at stations (numbered by 51, 63, 66 and 69) located within rupture zones along the main and east fault strands WNFe1 and WNFe2 of the WNFZ, and 1.5–2.0 s at station 33 located at the Carneros Fault for explosion SP1001 detonated ∼3.5-km north of the seismic line. In contrast, post-S coda durations are much short (1.0–1.2 s) at stations 26 and 73 located away from faults.

For explosion SP1002 detonated ∼5-km south of the 2016 W–E Line, post-S coda durations of FZTWs measured from seismograms and spectral amplitudes are 3.8–4.0 s at stations (numbered by 51, 62, 69 and 72) located within rupture zones along the main and east fault strands WNFe1 and WNFe2 of the WNFZ, and 3.0 s at station 32 located at the CF. In contrast, Post-S coda durations are less than 1.5 s at stations 26 and 77 located away from faults. These measurements show remarkable low-velocity waveguides along multiple fault strands of the WNFZ, within which rocks were severely damaged in the 2014 $M6$ mainshock. On the other hand, there exists a low-velocity waveguide formed by moderately damaged rocks along the adjacent Carneros Fault.

In summary, Figure 1.24 shows the measured spectral amplitudes and post-S coda durations of seismograms recorded at 60 stations of the 2016 W–E Line for two shots SP1001 and SP1002. We observe largest spectral amplitudes and

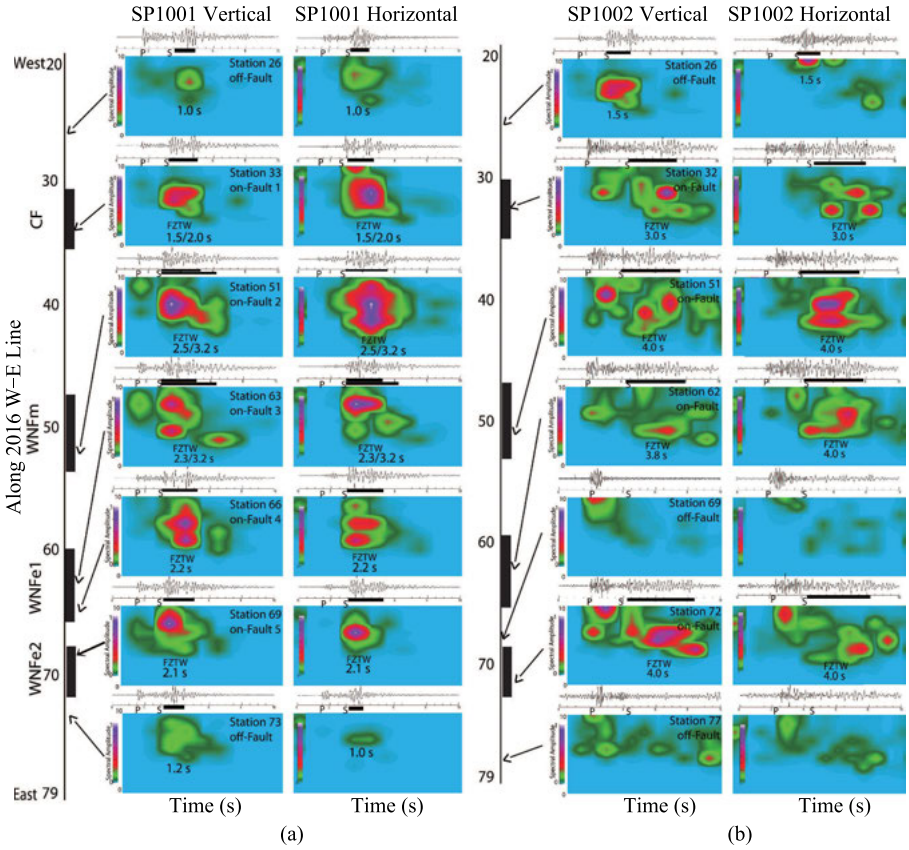

Fig. 1.23 **(a)** Spectral amplitudes of vertical- and horizontal-component seismograms recorded at seven stations (numbered by 26, 33, 51, 63, 66, 69 and 72) of the 2016 W–E Line located on or out of surface ruptures (marked by vertical black bars) along the WNFZ for shot SP1001 detonated on the main WNF at ∼3.5 km north of the seismic line. Seismograms have been low-pass (<10 Hz) filtered. Spectral contours are computed using SAC program (SPG) and normalized with respect to the maximum amplitude among them between 0 and 1 (colored from green to red). Prominent FZTWs with larger spectral amplitudes are observed at on-fault stations (33, 51, 63, 66 and 69) but smaller amplitudes at off-fault stations (26 and 72). Post-S coda durations of FZTWs measured from seismograms and spectral amplitudes show 2.5 s at station 51 located within the west rupture zone along the main WNFm, 2.1-2.3 s at stations 63, 66 and 69 within east rupture zones along strands WNFe1 and WNFe2 of the WNFZ, 1.5–2.0 s at station 33 on the Carneros Fault. In contrast, much shorter post-S coda durations (∼1.2 s) are registered at off-fault stations 26 and 72. **(b)** Same as in (a), but for explosion SP1002 located ∼5 km south of the 2016 W–E Line. Post-S coda durations of FZTWs show 3.8–4.0 s at stations 51, 62, 69 and 72 located within rupture zones along multiple strands of the WNFZ, and 3.0 s at station 32 on the CF. In contrast, less than ∼1.5 s post-S coda durations are registered at off-fault stations 26 and 77.

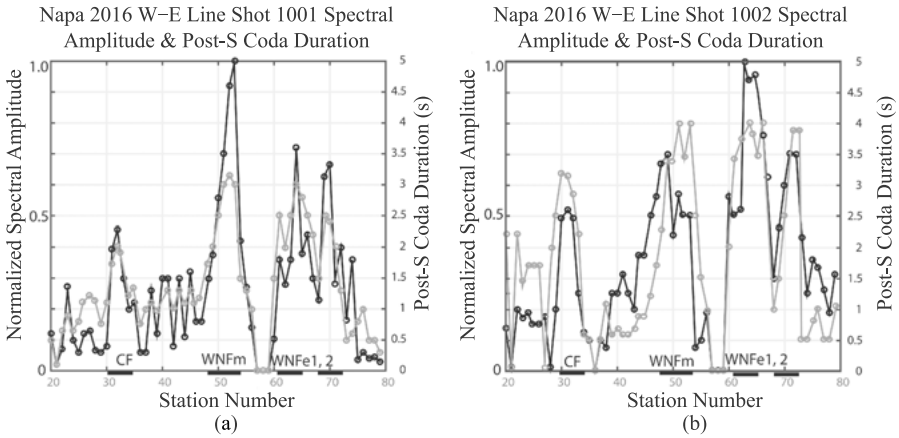

Fig. 1.24 Measured spectral amplitudes (black dots with line) and post-S coda duration (gray dots with line) of seismograms recorded at 60 stations (numbered by 20 to 79) of the 2016 W–E Line for two explosions (a) SP1001 and (b) SP1002. Seismograms have <10 Hz filtered. Spectral amplitudes have been normalized in plot. Larger spectral amplitudes and longest post-S coda durations of FZTWs are registered at stations located within rupture zones along multiple fault strands (marked by WNFm and WNFe1, 2 with black horizontal bars) of the WNFZ. Moderate spectral amplitudes and post-S coda durations of FZTWs are registered at stations located at the CF.

longest post-S coda durations of FZTWs at stations located within multiple rupture zones along the WNFZ, and moderate large spectral amplitudes and long post-S coda durations of FZTWs at stations at the Carneros Fault that had no surface breaks but might be lightly damaged due to strong shaking from the nearby 2014 $M6$ South Napa earthquake. These measurements show remarkable low-velocity waveguides formed by highly damaged rupture zones along multiple fault strands of the WNFZ. The multiple rupture zones likely connect at depth, although their surface breaks are separated from each other at surface. The CF runs sub-parallel to the north WNF and approaches the Franklin Fault so that the guided waves generated by explosion SP1002 could propagate along the waveguide with moderate velocity reduction to seismic stations located within or close to the CF.

1.5.2 3-D Finite-Difference Simulations of FZTWs Generated by Explosions

We have developed a model of the subsurface rupture zone along the main strand of the WNFZ on the basis of the hypocenters of aftershocks that generated prominent FZTWs and the measurements of FZTW coda durations and waveguide

trapping efficiency (Fig. 1.18b). In the present modeling of FZTWs generated by near-surface explosions detonated within the rupture zone, we assume that the raypaths from two explosions SP1001 and SP1002 located at ∼3.5-km north and ∼5-km south of the 2016 W–E Line may penetrate the depths above 2–3 km. Thus, we use the model parameters of two top layers in the model shown in Fig. 1.18b as the starting values of our present model.

To compute synthetic seismograms, we use a 3-D finite-difference code (Vidale *et al.*, 1985; Graves, 1996). Our calculations use the maximum 120-200-100 element grids in *x*-*y*-*z* coordinates, with a grid spacing of 50 m to simulate a volume of 6 km in width across the NWFZ and the CF, 10 km in length along the WNFZ, and 5 km in depth. This volume includes the 2016 W–E Line and two explosions SP1001 and SP1002. In order to reduce the computer memory in modeling for most aftershocks, we decrease the element grids in y to include the receiver array explosions in study.

The low-velocity waveguides along the main fault strand (WNFm) and two east strands (WNFe1 and WNFe2) of the WNFZ are 500-m (400-m) and 400-m (300-m) wide in the top layer (second top layer) of the model, within which seismic velocity reduced by 50%, 45% and 40% from surrounding rocks (Table 1.4). The Carneros Fault is 400-m (300-m) wide in the top layer (second top layer) of the model, within which seismic velocity reduced by 35% from surrounding rocks. These fault traces are separated from each other at the surface with the spans shown in the map (see Fig. 1.19). We assume the east strands WNFe1 and WNFe2 merge into the main strand WNFm of the WNFN near explosion SP1001 to north and SP1002 to south, and the CF connects the south WNF-Franklin Fault at depths above 3-km. The model parameters of deeper layers are the same as those in Table 1.3. The seismic array (2006 W-E Line) was placed across the multiple waveguides. The seismic waves were derived from an explosion source within the WNFm at ∼3.5-km (∼5-km) from the seismic array for SP1002 (SP1002).

In the first stage of our error-and trial forward modeling approach, we used 50-m grid spacing to obtain coarse model parameters at low frequency to save computer memory space and computation time. When the grid spacing was 50-m and the minimum velocity was 0.75 km/s, the maximum frequency of the synthetic seismograms is 3 Hz. We then used 25-m grid spacing to increase the resolution of fault-zone structure in the model at higher frequency. When the grid spacing was reduced to 25-m, we increased the maximum frequency to 6-Hz. When using the small grid spacing, we decreased the size of the model to an appropriate volume that included source and receivers to reduce computer memory and computation time, but to avoid losing the damping function to model edge effect.

Figure 1.25 exhibits 3-D finite-difference synthetic waveforms using model parameters in Table 1.4 for comparison with seismograms for explosion SP1001

Table 1.4 Model parameters for WNFZ rupture zones and CF at shallow depth.

Model parameters WNF (FF)	Layer 1	Layer 2	Layer 3
Depth of the layer bottom (km)	1.0	3.0	5.0
Waveguide width (m) WNFm/WNFe1/WNFe2/CF	500/400/400/400	400/300/300/300	300
Waveguide S velocity (km/s)	0.75/0.825/0.9/0.975	1.0/1.1/1.2/1.3	1.25
Waveguide P velocity (km/s)	1.5/1.65/1.8/1.95	2.0/2.2/2.4/2.6	2.5
Waveguide Q-value	20	30	50
Wall-rock S velocity (km/s)	1.5	2.0	2.5
Wall-rock P velocity (km/s)	3.0	4.0	5.0
Wall-rock Q-value	50	80	100

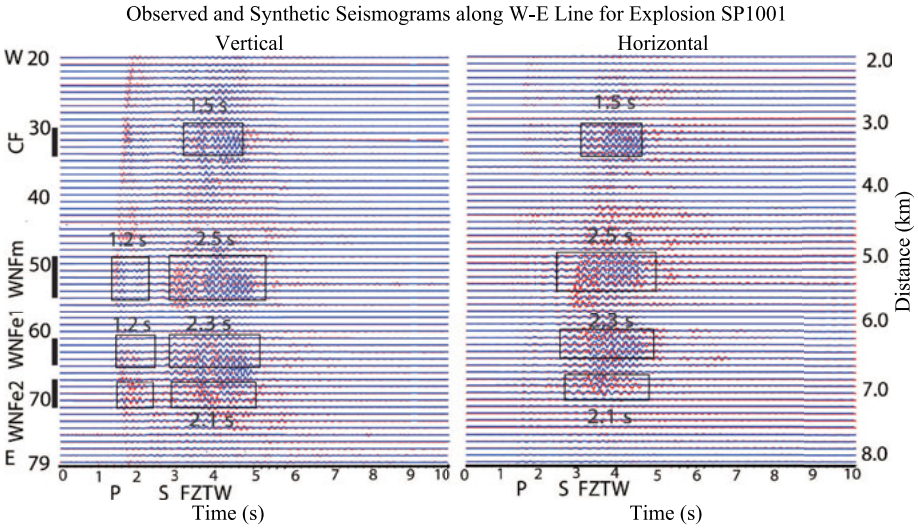

Fig. 1.25 Observed (red lines) and 3D finite-difference synthetic (blue lines) vertical- and horizontal-component seismograms at 60 stations (numbered by 20 to 79) of the 2016 W-E Line for explosion SP1001. Seismograms have been 1-6 Hz band-pass filtered and plotted using a fix amplitude scale for all traces. Prominent FZTWs with large amplitudes and 2.5-s, 2.3-s and 2.1-s post-S coda durations at stations located within the 500-m and 400-m wide rupture zones (marked by vertical bars) along the main strand (WNFm), and east strands WNFe1 and WNFe2 of the WNFZ, within which seismic velocities are reduced by 50% from those of surrounding rocks. FZTWs with 1.5 s post-S coda duration are recorded at stations within the 400-m wide Carneros Fault (CF), within which seismic velocities are reduced by 35%. The FZTWs with ∼1.2-s post-P coda durations appear in vertical-component seismograms at stations within rupture zones along multiple strands of the WNFZ.

and recorded at the 2016 W–E Line across multiple faults. An explosion source is located within the rupture zone along the main strand of the WNFZ and 3.5-km from the seismic line. Both P- and S-FZTWs generated by explosion appear at stations located within multiple rupture zones along the WNFZ and the CF, showing waveguide effect to trap seismic waves. The synthetic FZTW post-S-wave coda durations are comparable with observations at stations located within these low-velocity fault-zone waveguides. The longest post-S coda (∼2.5 s) of FZTWs are registered at stations (numbered from 48 to 54) located within the ∼500-600-m wide rupture zone along the main strand WNFm of the WNFZ, within which fault rocks experienced most severely damage in the 2014 $M6$ mainshock. Comparatively, we observe FZTWs with 2.1–2.3 s post-S coda durations at stations (numbered from 61 to 65, and from 69 to 72) located within ∼400-m wide rupture zones along east strands WNFe1 and WNFe2 of the WNFZ, within which fault rocks experienced slightly less damage than those along the main rupture zone. In contrast, ∼1.5-s post-S coda duration is at stations (numbered from 32–35) within the ∼400-m wide the Carneros Fault with more moderate velocity reduction and weak trapping effect than those along the WNFZ rupture zones at shallow depth. The synthetic P-FZTWs with ∼1.2-s coda durations are agreeable with those in vertical-component seismograms recorded at stations within WNFZ rupture zones.

In forward modeling, we used model parameters shown in Table 1.4. The P- and S-wave velocities for the rupture zone along the main strand WNFm of the WNFZ and surrounding rocks as well as layer thickness are the same as those in our previous model obtained from observations and simulations of FZTWs generated by the 2014 South Napa aftershocks (Li *et al.*, 2016). However the width of the rupture zone is 500–600 m, wider than the ∼400-m in the previous model at the top layer. The width of the low-velocity waveguide at shallower depth is more sensitive than the width at deeper level to observations of FZTWs at surface stations located within the rupture zone. The rupture zone width determined from FZTWs generated by near-surface explosions detonated within the rupture zone is likely more accurate and realistic. The widths and velocities of the east rupture zones of the WNFZ and the CF in the model come from simulations of FZTWs recorded at stations located within these multiple fault zone.

Although our inferred velocity model resulted from 3-D finite-difference simulations of FZTWs generated by aftershocks and explosions is not well constrained by independent measurements, our finite-difference simulations provide a first-order estimate of the overall structure of the WNFZ and Carneros Fault.

1.6 Discussion and Conclusion

The 2014 $M6$ South Napa earthquake sequence caused significant damage to fault rocks along the WNFZ, resulting in a remarkable low-velocity waveguide that traps seismic waves generated by earthquakes (Figs. 1.2 to 1.16) and explosions (Fig. 1.20 to Fig. 1.23). The measured post-S coda durations of FZTWs in our study show that longer coda durations generally result from longer distances of FZTWs propagating within the fault-zone waveguide (Fig. 1.17a), particularly for paths in the shallower parts of the seismogenic zone. The numerical tests of waveguide trapping effects show that if there is an obvious gap (more than 3–5 times of the wavelength of the FZTWs at its dominant frequency), such as a step-over of the fault zone between the aftershock and seismic array, FZTWs will be disrupted by this gap and not observed clearly at seismic array (Li and Vidale, 1996). Therefore, our observations of FZTW generated by 2014 Napa aftershocks occurring within the rupture zone and recorded at cross-fault seismic arrays (A1, A2 and A3) and along-fault stations (R1 to R4) in 2014 suggest that the continuity of waveguide along the WNFZ and the Franklin Fault at seismogenic depths, consistent with results from slip models derived from teleseismic, SAR and InSAR, field mapping data (Melgar *et al.*, 2015; Brocher *et al.*, 2015; Wei *et al.*, 2015) and aftershock lineaments (Hardebeck and Shelly, 2014). Combining the total length of the fault zone inferred by FZTWs, the combined WNF/Franklin Fault zone is at least 50 km long, extending from north of A1 to at least A3. On the basis of FZTW generated from more earthquakes that are north of those shown in this study and from other geophysical data, Catchings *et al.* (2016) interpret that the overall WNF/Franklin Fault is at least 74 km long, and is likely continuous with the Calaveras Fault.

Using a velocity model of the subsurface rupture zones along the main fault of the WNFZ associated with the 2014 South Napa earthquake, we have developed finite-difference simulations of FZTWs generated by aftershocks at varying depths and epicentral distances (Li *et al.*, 2016). This model (Fig. 1.18b and Table 1.3) suggests a 400–500 m wide low-velocity waveguide along the main WNF that extends to at least 5–6 km (7–8 km) depth beneath the northern (southern) portion of the rupture zone, within which velocities are reduced by 40%–50% relative to wall rock velocities with the degree of damage and velocity reduction becoming less as the depth increases. Our observations and simulations of FZTWs generated by aftershocks indicate that the south WNF and Franklin Fault are less damaged than the ruptured north WNF in the 2014 mainshock. We assume the damage zone along the WNF had been mostly healed to the background level before the 2014 $M6$ earthquake due to the long intervals between

ruptures. Thus, our current measurements provide an opportunity to characterize newly developed damage along this fault and therefore a base line for monitoring healing on active faults over time in the Napa region.

The FZTWs generated by shots detonated within the rupture zone and recorded at a long seismic array (W-E Line) across multiple faults in 2016 show the rupture branching structure on multiple fault strands of the WNFZ at shallow depth in the 2014 M_w6.0 South Napa earthquake. These rupture zones are separated at the surface but like merge at the shallow depth as shown in Figure 1.19b. The rupture bifurcation had been studied by FZTWs recorded in the 1999 M_w7.1 Hector Mine earthquake in Mojave Desert, Southern California (Li *et al.*, 2003). Eventually the dynamics of branched fault system involved in the Hector Mine earthquake has been simulated by Oglesby *et al.* (2003). On the other hand, the adjacent Carneros Fault did not rupture but possibly had minor slips due to strong shaking by the M6 South Napa mainshock occurred nearby. The FZTWs generated by explosions show a waveguide with moderate velocity reduction (by ∼35%) along the CF running subparallel to the north WNF and connects the north end of the Franklin Fault to form the Carneros-Franklin Fault (Graymer, 2014). Furthermore, our observations and simulations of FZTWs generated by explosions suggest a 1–2 km wide damage zone. An extensive (∼1.5-km-wide) and long-lived compliant zone along the Calico Fault in Mojave Desert has been evidenced by seismic and geodetic data (Cochran *et al.*, 2009). Although our inferred velocity model resulted from 3-D finite-difference simulations of FZTWs generated by aftershocks and explosions is not well constrained by independent measurements, the finite-difference simulations provide a first-order estimate of the continuity of the low-velocity damage zone along the WNFZ and the Franklin Fault as well as the branching structure of rupture zones along multiple strands of the WNFZ.

Our observations and 3-D finite-difference simulations of FZTWs generated by both aftershocks and explosions show their large amplitudes and long wavetrains at stations located within the fault zone, illuminating that a great amount of seismic energy is localized within the damage zones along multiple strands of the WNFZ due to the trapping effect of low-velocity waveguides. The results from FZTWs are consistent with the observed amplification of strong ground motion to the south in the along-strike direction of the Franklin or Southampton faults in Napa Valley (Baltay and Boatwright, 2015), potentially indicating a fault-zone guided wave. Therefore, the longer and more continuous WNF-FF zone as well as multiple rupture branching structure in a broader range may pose significant regional hazards from localized amplification, extended ground shaking, and increased damage along the fault-zone waveguides, even if the surface rupture is limited to only a portion of the overall fault zone.

Acknowledgements

This study is supported by Southern California Earthquake Center's award 15195 (contribution number 6168). Funding and support for data acquisition was provided by the U.S. Geological Survey (USGS), and we wish to thank Joanne Chan, Coyn Criley, Jemile Erdem, Gary Fuis, Uyanga Ganbaatar, Ryan Fay, Wesley Fay, Michael Rymer, George Slad, Carolyn Stieben and Joseph Svitek working in the USGS Napa experiment of 2014, and the field team working in the USGS Napa experiment of 2016. We thank Walter Money, John Evans, and Brad Aagaard of USGS for providing helpful reviews on our papers published in 2016. Seismographs and sensors used to acquire the data, which were provided by Incorporated Research Institutions for Seismology (IRIS) — Program for the Array Seismic Studies of the Continental Lithosphere. We acknowledge Steve Azevedo of the IRIS Data Management Center for his help in converting the Seismic Analysis Code (SAC)-formatted data recorded in 2014.

References

Bakun, W.H. (1999). Seismic activity of the San Francisco Bay region. Bull. Seis. Soc. Am., 89, 764–784.

Baltay, A.S and J. Boatwright (2015). Ground motion observations of the 2014 South Napa earthquake. Seis. Res. Lett., 86, 355–360, doi: 10.1785/0220140232.

Ben-Zion, Y. (1998). Properties of seismic fault zone waves and their utility for imaging low-velocity structure. J. Geophys. Res., 103, 12567–12585.

Boatwright, J., J.L. Blair, B.T. Aagaard, and K. Wallis (2015). The distribution of red and yellow tags in the City of Napa. Seism. Res. Lett., 86, 2A, doi:10.1785/0220140234.

Brocher, T.A., A. Baltay, J.L. Hardebeck, J. Polet, E. Langenheim, A.L. Llenos, J.J. Lienkaemper, D.P. Schwartz, J.L. Blair, T. Dawson, K.W. Hudnut, D.R. Shelly, D. Dreger, J. Boatwright, B.T. Aagaard, D. J. Wald, R.M. Allen, W.D. Barnhart, K.L. Knudsen, B.A. Brooks, K.M. Scharer (2015). The M6.0 24 August 2014 South Napa earthquake. Seism. Res. Lett, 86, 2A, doi: 10.1785/0220150004.

Brooks, B., K. Hudnut, C. Glennie, and T. Ericksen (2014). Near-field deformation associated with the M6.0 South Napa earthquake surface rupture, presented at 2014 Fall Meeting, AGU, San Francisco, California, 15–19 December 2014, Abstract S33F-4900.

Bryant, W.A. (2005). Digital database of quaternary and younger faults from the Fault Activity Map of California, Version 2.0. California Geological Survey.

Byerlee, J. (1990). Friction, overpressure and fault-normal compression. Geophys. Res. Lett., 17, 2109–2112.

Catchings, R.D., M.J. Rymer, M.R. Goldman, C.S. Prentice, and R.R. Sickler (2013) Fine-scale delineation of the location of and relative ground shaking within the San Andreas Fault zone at San Andreas Lake, San Mateo County, California. U.S. Geol. Surv. Open-File Report 2013–1041, 58 pp.

Catchings, R.D., M.J. Rymer, M.R. Goldman, J.A. Hole, R. Huggins, and C. Lippus (2002). High-resolution seismic velocities and shallow structure of the San Andreas Fault zone at Middle Mountain, Parkfield, California. Bull. Seis. Soc. Am., 92, 2493–2503.

Catchings, R.D., M.J. Rymer, M.R. Goldman, R.R. Sickler, and C.J. Criley (2014). A method and example of seismically imaging near-surface fault zones in geologically complex areas using Vp, Vs, and their ratios. Bull. Seismol. Soc. Am., 104, 1989–2006, doi: 10.1785/0120130294.

Catchings, R. D., M. R. Goldman, Y. G. Li, and J. H. Chan (2016). Continuity of the West Napa-Franklin fault zone inferred from guided waves generated by earthquakes following the 24 August 2014 $M_{\rm w}$6.0 South Napa earthquake. Bull. Seismol. Soc. Am., 106, 6, 2721–2746, doi: 10.1785/0120160154.

Çelebi, M., S. F. Ghahari, and E. Taciroglu (2015). Unusual downhole and surface free-field records near the Carquinez strait bridges during the 24 August 2014 $M_{\rm w}$6.0 South Napa, California, earthquake. Seis. Res. Lett., 8 (4), doi: 10.1785/0220150041.

Cochran, E.S., Y.G. Li, P. M. Shearer, S. Barbot, Y. Fialko, and J.E. Vidale (2009). Seismic and geodetic evidence for extensive, long-lived fault damage zones. Geology, 9.37 (4), 315–318, (doi:10.1130/G25306A.1; Data Repository item 2009082).

Dawson, T., K. Kelson, J. Wesling, K. Hudnut, and D. Ponti (2014). Surface fault rupture associated with the South Napa Earthquake of August 24, 2014, in Geotechnical Engineering Reconnaissance of the August 24, 2014 M6 South Napa Earthquake. Report of the NSF Sponsored GEER Association Team, California Geological Survey, Pacific Earthquake Engineering Research Center, and U.S. Geological Survey. Rep. No. GEER-037, Section 3.

Donnellan, A., J.W. Parker, B. Hawkins, S. Hensley, C.E. Jones, S.E. Owen, A.W. Moore, J. Wang, M.E. Pierce, and J.B. Rundle (2014). Combined UAVSAR and GPS estimates of fault slip for the M6.0 South Napa earthquake, Abs. S31G-04, presented at 2014 Fall Meeting, AGU, San Francisco, Calif., 15–19 Dec.

EERI (2014). M6.0 South Napa earthquake of August 24, 2014, EERI Special Earthquake Report, October 2014, 27 pp.

Graves, R.W., 1996. Simulating seismic wave propagation in 3D elastic media using staggered-grid finite differences. Bull. Seis. Soc. Am., 86, 1091–1106.

Graymer, R.W. (2014).Three-dimensional fault framework of the 2014 South Napa earthquake, San Francisco Bay region, California, Abs. S33F-4930, presented at 2014 Fall Meeting, AGU, San Francisco, Calif., 15–19 Dec.

Graymer, R.W., D.L. Jones, and E.E. Brabb (2002). Geologic map and map database of northeastern San Francisco Bay Region, California. U.S. Geol. Surv. Misc. Field Studies Map MF-2403, version 1.0, scale 1:100,000.

Graymer, R.W., E.E. Brabb, D.L. Jones, J. Barnes, R.S. Nicholson, and R.E. Stamski (2007). Geologic map and map database of Eastern Sonoma and Western Napa Counties, California. U.S. Geol. Surv. Sci. Invest. Map 2956.

Guo, Y.G. and J.K. Morgan (2007). Fault gouge evolution and its dependence on normal stress and rock strength—Results of discrete element simulations: Gouge zone properties. J. Geophys. Res., 112, B10403, doi:10.1029/2006JB004524.

Hardebeck, J.L., and D.R. Shelly (2014). Aftershocks of the 2014 $M6$ South Napa earthquake: Detection, location, and focal mechanisms, Abs. S33F-4927, presented at 2014 Fall Meeting, AGU, San Francisco, Calif., 15–19 Dec.

Hough, S.E. (2014). Where was the 1898 Mare Island earthquake? Insights from the 2014 South Napa earthquake, Abs. S44D-03, presented at 2014 Fall Meeting, AGU San Francisco, California, 15–19 December 2014.

Hudnut, K.W., T.M. Brocher, C.S. Prentice, J. Boatwright, B.A. Brooks, B.T. Aagaard, J.L. Blair, J. Fletcher, J.E. Erdem, C.W. Wicks, J.R. Murray, F.F. Pollitz, J. Langbein, J. Svarc, D.P. Schwartz, D.J. Ponti, S. Hecker, S. DeLong, C. Rosa, B. Jones, R. Lamb, A. Rosinski, T.P. McCrink, T.E. Dawson, G. Seitz, R.S. Rubin, C. Glennie, D. Hauser, T. Ericksen, D. Mardock, D.F. Hoirup, and J.D. Bray (2014). Key recovery factors for the August 24, 2014, South Napa earthquake, U.S. Geol. Surv. Open-File Rep. 2014 – 1249, 51.

Igel, H.,G. Jahnke, and Y. Ben-Zion (2002). Numerical simulation of fault zone guided waves: accuracy and 3-D effects. Pure Appl. Geophys., 159, 2067–2083.

Korneev, V.A., R.M. Nadeau, and T.V. McEvilly (2003). Seismological studies at Parkfield IX: Fault zone imaging using guided wave attenuation. Bull. Seis. Soc. Am., 93, 1415–1426.

Langenheim, V.E., R.W. Graymer, and R.C. Jachens (2006). Geophysical setting of the 2000 $M_{\mathrm{L}}5.2$ Yountville, California, earthquake: Implications for seismic hazard in NapaValley, California. Bull. Seis. Soc. Am., 96, 1192–1198.

Li, Y.G. and J.E. Vidale (1996). Low-velocity fault zone guided waves; numerical investigations of trapping efficiency. Bull. Seis. Soc. Am., 86, 371–378.

Li, Y.G. and P.C. Leary (1990). Fault-zone trapped seismic waves. Bull. Seis. Soc. Am., 80, 1245–1271.

Li, Y.G., W.L. Ellsworth, C. H. Thurber, P. E. Malin, and K. Aki (1997). Observations of fault-zone trapped waves excited by explosions at the San Andreas fault, central California. Bull. Seis. Soc. Am., 87, 210–221.

Li, Y.G. and P.E. Malin (2008). San Andreas Fault damage at SAFOD viewed with fault-guided waves, Geophys. Res. Lett., 35, L08304, doi:10.1029/2007GL032924.

Li, Y.G., G. De Pascale, M. Quigley, and D. Gravely (2014). Fault damage zones of the $M7.1$ Darfield and $M6.3$ Christchurch earthquakes characterized by fault-zone trapped waves. Tectonophysics, 618, 79–101, doi:10.1016/j.tecto.2014.01.029.

Li, Y.G., J.E. Vidale, and K. Aki (2000). Depth-dependent structure of the Landers fault zone using fault zone trapped waves generated by aftershocks. J. Geophys. Res., 105, 6237–6254.

Li, Y.G., J.E., Vidale, and S.E. Cochran (2004). Low-velocity damaged structure of the San Andreas fault at Parkfield from fault-zone trapped waves. Geophy. Res. Lett., 31, L12S06.

Li, Y.G., J.E. Vidale, D. Oglesby, S.M. Day and E. Cochran (2003a). Multiple-fault rupture of the $M7.1$ Hector Mine, California, earthquake from fault-zone trapped waves. J. Geophys. Res., 108, ESE 11, 1–25.

Li, Y.G., J.E. Vidale, K. Aki, F. Xu, and T. Burdette (1998). Evidence of shallow fault zone strengthening after the 1992 $M7.5$ Landers, California, earthquake. Science, 279, 217–219.

Li, Y.G., J.E. Vidale, S.M. Day, D.D. Oglesby, and E. Cochran (2003b). Post-seismic fault healing on the 1999 $M7.1$ Hector Mine, California earthquake. Bull. Seism. Soc. Am., 93, 854–869.

Li, Y.G., K. Aki, D. Adams, A. Hasemi, W. H. K. Lee (1994). Seismic guided waves trapped in the fault zone of the Landers, California, earthquake of 1992. J. Geophys. Res., 99, 11,705–11,722.

Li, Y.G., P. Chen, E.S. Cochran, J.E., Vidale, and T.Burdette (2006). Seismic evidence for rock damage and healing on the San Andreas fault associated with the 2004 $M6$ Parkfield earthquake, Special issue for Parkfield $M6$ earthquake. Bull. Seis. Soc. Am., 96 (4), S1–15, doi:10.1785/0120050803.

Li, Y.G., P.C. Leary, K. Aki, and P.E. Malin (1990). Seismic trapped modes in the Oroville and San Andreas fault zones. Science, 249, 763–766.

Li, Y.G., P. Malin, and E. Cochran (2012). Fault-zone trapped waves: High-Resolution Characterization of the Damage Zone on the Parkfield San Andreas Fault at Depth, Chapter 3, 107–150. In: Imaging, Modeling and Assimilation in Seismology, edited by Y. G. Li, Higher Education Press, Beijing; De Gruyter, Berlin.

Li, Y.G., R. D. Catchings, and M. R. Goldman (2016). Subsurface fault damage zone of the 2014 $M_w6.0$ South Napa, California, earthquake viewed from fault-zone trapped waves. Bull. Seismol. Soc. Am., 106, 2747–2763, doi: 10.1785/0120160039.

Marone, C. (1998). The effect of loading rate on static friction and the rate of fault healing during the earthquake cycle. Nature, 391, 69–72.

McGarr, A., M. Boettcher, J.B. Fletcher, R. Sell, M. J. S. Johnston, R. Durrheim, S. Spottiswoode, and A. Milev (2009). Broadband records of earthquakes in deep gold mine and a comparison with results from SAFOD, California. Bull. Seis. Soc. Am., 99, No.5, 2815–2824, doi: 10.1785/0120080336.

Melgar D., J. Geng, B.W. Crowell, J.S. Haas, Y. Bock, W.C. Hammond, and R.M. Allen (2015). Seismogeodesy of the 2014 $M_w6.1$ Napa earthquake, California: Rapid response and modeling of fast rupture on a dipping strike-slip fault. J. Geophys. Res., 120, doi: 10.1002/2015JB011921.

Mooney, W.D. and A. Ginzburg (1986). Seismic measurements of the internal properties of fault zones. PAGEOPH, 124, 141–157.

Rice, J.R. (1992). Fault stress states, pore pressure distributions, and the weakness of the San Andreas fault. In: Fault Mechanics and Transport Properties of Rocks, edited by B. Evans and T.-F. Wong. Academic, San Diego, Calif, 475–503.

Scholz, C.H. (1990). The Mechanics of Earthquakes and Faulting. Cambridge Univ. Press, New York.

Sibson, R.H. (1996). Structural permeability of fluid-driven fault-fracture meshes. Journal of Structural Geology, 18, 1031–1042.

Stidham C., M. Antolik, D. Dreger, S. Larsen, and B. Romanowicz (1999). Three-dimensional structure influences on the strong-motion wavefield of the Loma Prieta Earthquake, Bull. Seis. Soc. Am., 89, 1184–1202.

Suess, M. and Shaw, J.H. (2003). P wave seismic velocity structure derived from sonic logs and industry reflection data in the Los Angeles basin, California. J. Geophys. Res., 108 (B3), 2170, doi: 10.1029/2001JB001628.

Vidale, J.E. and Y.G. Li (2003). Damage to the shallow Landers fault from the nearby Hector Mine earthquake. Nature, 421, 524–526.

Vidale, J.E., D.V. Helmberger, and R.W. Clayton (1985). Finite-difference seismograms for SH waves. Bull. Seis. Soc. Am., 75, 1765–1782.

Wei Shenji, S. Barbot, R. Graves, J.J. Lienkaemper, T. Wang, K. Hudnut, Y. Fu, and D. Helmberger (2015). The 2014 M_w6.1 South Napa Earthquake: A Unilateral Rupture with Shallow Asperity and Rapid Afterslip. Seis. Res. Lett., 86, 2A.

Wesling, J.R. and K.L. Hanson (2008). Digital compilation of West Napa fault data for the Northern California Quaternary Fault Map Database. Final Technical Report submitted to the U.S. Geol. Sur., NEHRP Award 05HQAG0002.

Author Information

Yong-Gang Li
Department of Earth Sciences, University of Southern California,
Los Angeles, California 90089-0740, USA
E-mail: ygli@usc.edu

Rufus D. Catchings and Mark R. Goldman
U.S. Geological Survey
345 Middlefield Road MS 977, Menlo Park, California 94025-3591, USA

Chapter 2

The Calico Fault Compliant Zone at Depth Viewed by Fault-Zone Trapped Waves from Teleseismic Earthquakes

Yong-Gang Li

The fault-zone trapped waves (FZTWs) are first-time identified in teleseisms recorded at a square seismic array consisting of 40 intermediate-period stations and 60 short-period stations deployed atop the Calico Fault (CF) in Mojave Desert, California. We examined the data from 26 $M \geqslant 6$ teleseismic earthquakes occurring at distances of 40°–80° great circles to the Calico array site in 2006, and found FZTWs characterized by large amplitudes and long durations of 3.5–4 s following the first P-arrival and 6–8 s after the Moho converted P-to-S waves in teleseisms registered at seismic stations within the ∼1 km-wide CF compliant zone. This type of FZTWs has not been used before, but they appear to have great promise for providing unprecedented constrains of the depth extension of fault damage zone because they arise from seismic waves entering the bottom of fault zone at deep level. In the previous study on the CF (Cochran *et al.*, 2009), the FZTWs generated by explosions and local earthquakes had been combined with travel-times inverse and InSAR observations to image the CF low-velocity compliant zone, within which seismic velocities are reduced by 40%–50%, to depths in excess of 5–6 km. In order to obtain the better image of the deeper portion of the CF compliant zone, we use the FZTWs recorded for teleseismic earthquakes to document deep fault damage structure. In conjunction with the receiver function analysis and the pre-existing velocity model of the CF, our observations and simulations of the FZTWs identified in teleseisms show the Calico fault compliant zone with velocity reduction of ∼50% extending to the depth of at least ∼8 km beneath Mojave Desert.

https://doi.org/10.1515/9783110560329-084

Key words: Fault compliant zone and depth extension, teleseismic earthquake and teleseisms, fault-zone trapped waves, receiver function.

2.1 Introduction

Some geodetic estimates suggest that the Calico Fault (CF) has as much as 7 mm/yr dextral slip rates within the eastern California shear zone (Peltzer *et al.*, 2001). Recent trench data indicate that the last earthquake occurred on it at least several hundred years ago (Ganev *et al.*, 2008). Coseismic interferograms for both the Landers and Hector Mine earthquakes showed the strain localized on the CF and other nearby faults (Fialko *et al.*, 2002; Fialko, 2004). Line-of-sight displacements with amplitudes of a few centimeters and wavelengths of a few kilometers were clearly associated with the CF (Fig. 2.1a). Observed interferometric synthetic aperture radar (InSAR) anomalies for the CF are best explained with a 1–2 km wide zone around the fault with a shear modulus reduced by up to ∼60% extending to at least 5 km depth.

The CF is located midway between the 1992 M_{w}7.3 Landers and 1999 M_{w}7.1 Hector Mine ruptures along which fault-zone trapped waves (FZTWs) generated by explosions and aftershocks had observed and used to characterize the co-seismic damage and post-seismic heal of fault rocks at depth (Li *et al.*, 1994, 1998, 1999, 2000, 2001, 2002, 2003a,b; Vidale and Li, 2003). Following up these studies, a seismic investigation of the compliant zone along the CF was conducted in Mojave Desert in 2006 (Cochran *et al.*, 2009). Using seismic travel times, FZTWs generated by explosions and local earthquakes combined interferometric Synthetic Aperture Radar observations, an approximate 1–1.5 km wide CF compliant core zone was imaged to the depth of 5–6 km, within which seismic velocities are reduced by up to ∼40% compared with wall-rock (Fig. 2.1c). The observed seismic velocity (rock rigidity) reductions along the CF zone are likely due to the cumulative mechanical damage by dynamic ruptures in the past earthquakes occurring on it. This result suggests that faults can affect rock properties at substantial distances from the primary fault slip surfaces and throughout much of the seismogenic zone, implying that the portion of energy expended during rupture can drive rock cracking and develop fault systems. Permanent damage zones may, thus, play a critical role in ground motion intensity and earthquake hazard along the fault resulting from its waveguide trapping effect.

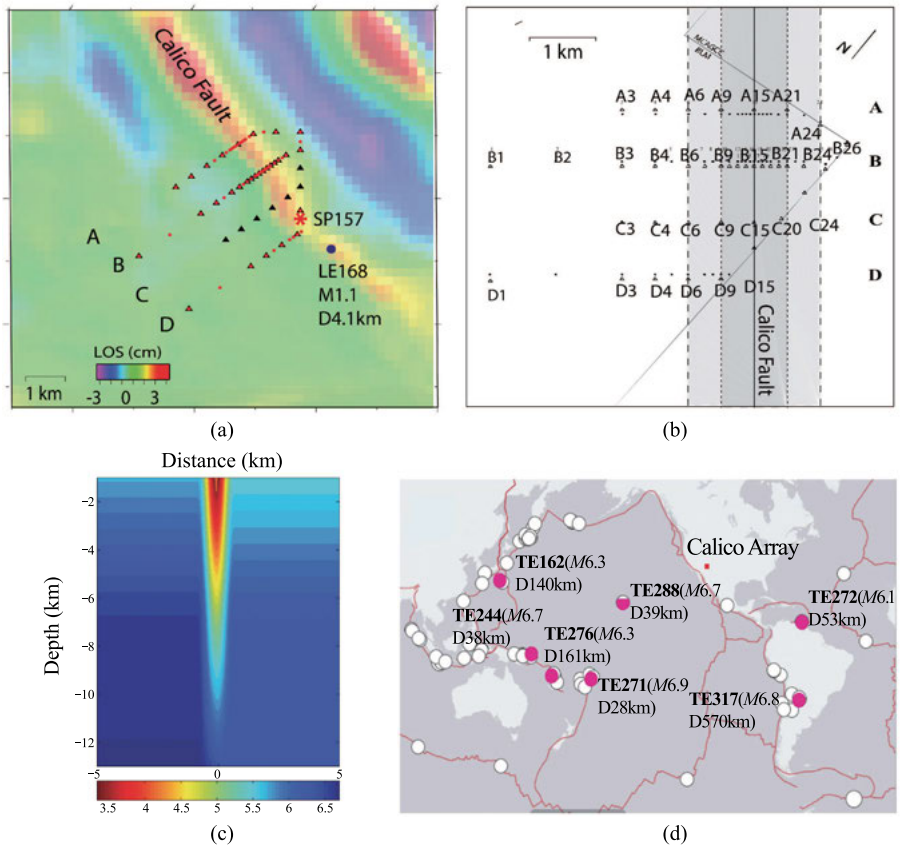

Fig. 2.1 **(a)** Map shows locations of 40 (40T, 0.025 Hz) stations (black triangles) and 60 (L22, 2 Hz) stations (red circles) along 4 seismic lines A, B, C and D deployed across the Calico Fault in 2006 (Cochran *et al.*, 2009). Colors in high-pass-filtered co-seismic interferogram from the 10/16/1999 Hector Mine earthquake during 01/13–10/20/1999 denote variations in line of sight (LOS) displacements (Fialko *et al.*, 2002). **(b)** Map shows locations of intermediate- (triangles) and short-period (dots) stations along seismic lines A, B, C and D deployed across the CF compliant zone (marked by grey color) with the 1 km-wide fault core zone (dark grey). Station spacing is not even, but with denser stations within the compliant zone. **(c)** Model of P-wave low-velocity zone along Calico fault with 40% reduction in velocity obtained by Cochran *et al.* (2009). The fault compliant zone is 1.0–1.5 km wide at the surface. The lateral velocity profile across the fault is approximated as a Hanning taper, and the velocity reduction tapers linearly to zero between 0 and 10 km depth. The damage zone is modeled to extend to 10 km depth, but with small relative velocity reductions below 5–6 km. **(d)** Map shows locations of 71 teleseismic earthquakes (white circles) with $M \geqslant 6$ recorded at 4 seismic lines in the square array atop the CF. Red circles marked by labels with TE followed by Julian date, M followed by magnitude and D followed by depth, denote seven teleseismic earthquakes for which FZTWs are identified in teleseisms and shown in this article.

However, the depth extension of the CF compliant zone is still less constrained by the FZTWs generated by near-surface explosions and local earthquakes at shallow depths because those FZTWs from these seismic sources mostly travel within the shallow portion of the fault zone. Recently, we examined the data recorded at the dense array atop the CF in the 2016 experiment for teleseismic earthquakes, and identified FZTWs in teleseisms. Because these FZTWs arise from the first-arrival P and P-to-S waves converted at the Moho discontinuity and sub-vertically enter the bottom of the Calico fault zone, they are capable to provide unprecedented constraints on the depth extension of fault compliant zone in the crust. In this chapter, we demonstrate the new type of FZTWs identified in teleseisms recorded at the CF and use them to image the deep portion of the low-velocity fault compliant zone.

2.2 The Data and Waveform Analyses

Cochran *et al.* (2009) installed a dense array of 40 intermediate-period (40T) stations and 60 short-period (L22) stations in a 1.5 km×5.5 km square adjacent to the Calico Fault (CF) to record three shots detonated within and out of the Calico Fault zone, and then to record earthquakes for six months starting from June in 2006. This square array consists of four seismic lines (Line A, Line B, Line C and Line D in Fig. 2.1a) with 1-km line spacing nearly perpendicularly across the CF. The geometry of the array and station intervals is shown in Figure 2.1b. Each station has a short-period sensor (L22 2Hz) and/or an intermediate-period sensor (40T, 0.025 Hz) buried in a 0.5–1 m deep dig hole with three components in the vertical, parallel and perpendicular to the fault strike. Seismometers worked in continuous mode at 100 samples per second, and were synchronized by internal GPS clocks. The data recorded at four cross-fault lines A, B, C and D for three explosions and five earthquakes on the CF were used for FZTWs analysis, and twenty local earthquakes and eight teleseismic earthquakes were used for travel time tomography (Cochran *et al.*, 2009).

In the present study, we examine the data recorded at four seismic lines A, B, C and D for 72 teleseismic earthquakes with magnitudes $M \geqslant 6$ occurring at distances of 40°–80° great circles (approximate 5,000–11,000 km) to the Calico seismic array site between June and November of 2006 (Fig. 2.1d). We use the data with good signal-to-noise ratio (SNR) from 26 teleseismic earthquakes occurring at depths deeper than 28 km, and identified FZTWs immediately following the first P-arrivals in teleseisms recorded at Lines A, B, C and D. These FZTWs are interpreted to arise from the first-arrival P-wave and the P-to-S wave converted at the Moho discontinuity (at ∼30 km depth beneath

Mojave Desert), which enter the bottom of the CF compliant zone. Seismograms recorded for teleseismic earthquakes occurring at depths shallower than ∼30 km are in general dominated by strong surface waves so that they are not suitable used in this study. In the present article, we show the FZTWs identified in teleseisms from 7 teleseismic earthquakes which locations and magnitudes are shown in Figure 2.1d and in Table 2.1.

Table 2.1 Teleseismic earthquakes and local earthquakes recorded at the seismic array atop the Calico fault, which waveforms are shown in this study.

Event ID	Type	Magnitude	Latitude	Longitude	Depth (km)	Distance (°)
TE162	Teleseismic	6.3	33.130	131.150	140.0	72.2
TE244	Teleseismic	6.7	−6.780	155.540	38.0	69.5
TE271	Teleseismic	6.9	−16.613	−172.035	28.0	73.5
TE272	Teleseismic	6.1	10.910	−61.650	53.0	55.0
TE276	Teleseismic	6.3	−18.860	169.090	161.0	65.7
TE288	Teleseismic	6.7	19.878	−155.935	38.9	37.8
TE317	Teleseismic	6.8	−26.038	−63.243	547.5	78.9

2.2.1 Teleseismic Earthquakes in the Southwest Direction from the Array Site

Figure 2.2a shows seismograms recorded at five 40T stations of seismic Line D across the CF for a M6.7 teleseismic earthquake (TE288 in Table 2.1 and Fig. 2.1d) occurring at 39-km depth beneath Hawaii Islands and ∼4200 km (37.8°) southwest from the CF seismic array site in Southern California. Because the array site located in Central Mojave Desert is very quiet, the primary P-wave and S-wave are visible in teleseisms while strong surface waves appear after ∼1000-s from the event origin time. We apply a band-pass filter on teleseisms to suppress the surface waves, and cut teleseisms by a 25-s time window between 435-s and 460-s, starting from ∼3 s before the first-arrival P-wave (P').

Figures 2.2b and 2.2c exhibit the band-pass (0.5–2 Hz) filtered three-component teleseisms recorded at twenty-five stations along Line B installed with 40 T and L22 sensors, respectively. We observe prominent wavetrains with large amplitudes and ∼7.5-s duration staring from ∼5-s after the first-arrival P' in two horizontal-component teleseisms at stations between B9 and B15 located within the ∼1-km-wide CF compliant core zone. However, they are not clearly observed in vertical-component teleseisms. We measure the durations of these large-amplitude wavetrains at five stations within the compliant zone where the waveform amplitudes are above twice the background signal level, and take

the average of measurements. In contrast, no such large-amplitude and long-duration wavetrains recorded at stations out of the CF compliant zone. We interpret these long-duration wavetrains with large amplitudes dominant in two horizontal-component teleseisms to be fault-zone trapped waves (FZTWs) formed by S-waves that are converted from first-arrival P waves at the Moho discontinuity (∼30-km depth beneath Mojave Desert) and sub-vertically enter the bottom of the low-velocity CF compliant zone at certain depth. We call P' for the refracted P-wave and S' for the P-to-S converted wave of the first-arrival P at the Moho discontinuity. The time difference between P' and S' is 5–5.5 s corresponding to the distance of waves traveling sub-vertically between the Moho at depth of ∼30-km and seismic array at the surface. When the P' and S' waves enter the bottom of the vertical fault zone, the P-type and S-type FZTWs are produced due to constructive interference of multiple reflected waves at the boundary between the low-velocity compliant zone and high-velocity surrounding rocks.

Both of P-type and S-type FZTWs were recorded at the stations located within the CF compliant zone at the ground surface. We observe the wavetrains with relatively large amplitudes and ∼4-s duration immediately following the P' in vertical-component teleseisms at stations located within the CF compliant zone. We call these wavetrains in P coda to be the P-type FZTWs polarized sub-vertically. They are not dominant in horizontal-component teleseisms, but visible in the perpendicular-component because the ray path from teleseismic earthquake TE288 to the seismic array is nearly perpendicular to the CF strike. We notice the multiple peaks (called P") in late coda of teleseisms, probably due to waves rebounded between the free surface and the Moho discontinuity. Figure 2.2d shows ∼7.5-s post-S' and ∼4-s post-P' coda durations of FZTWs in perpendicular-component teleseisms at stations of Lines A, C, and D located within the CF compliant zone.

We have examined seismograms recorded for other three teleseismic earthquakes occurring southwest of the CF array site. Figures 2.3a and 2.3b exhibit teleseisms recorded at Line B and Lines A, B, C and D installed with 40T sensors for a $M6.3$ teleseismic earthquake (TE276 in Table 2.1 and Fig. 2.1d) occurring at 161-km depth beneath Solomon Islands, approximately 10,000 km (65.7°) southwest of the CF seismic array. The S-type FZTWs with large-amplitudes and 7–8-s coda duration starting from 5–5.5 s after the first P-arrives are dominant in two horizontal-component teleseisms recorded at stations within the ∼1-km-wide CF compliant core zone. On the other hand, the P-type FZTWs with ∼3.5–4-s duration immediately following the P' are dominant in vertical-component teleseisms at stations within the compliant zone for this deep teleseismic earthquake from which waves propagate nearly vertically to the seismic array. Figures 2.3c and 2.3d show spectral contours at stations located within and out of the ∼1-km-wide CF compliant zone. The S-type FZTWs show large

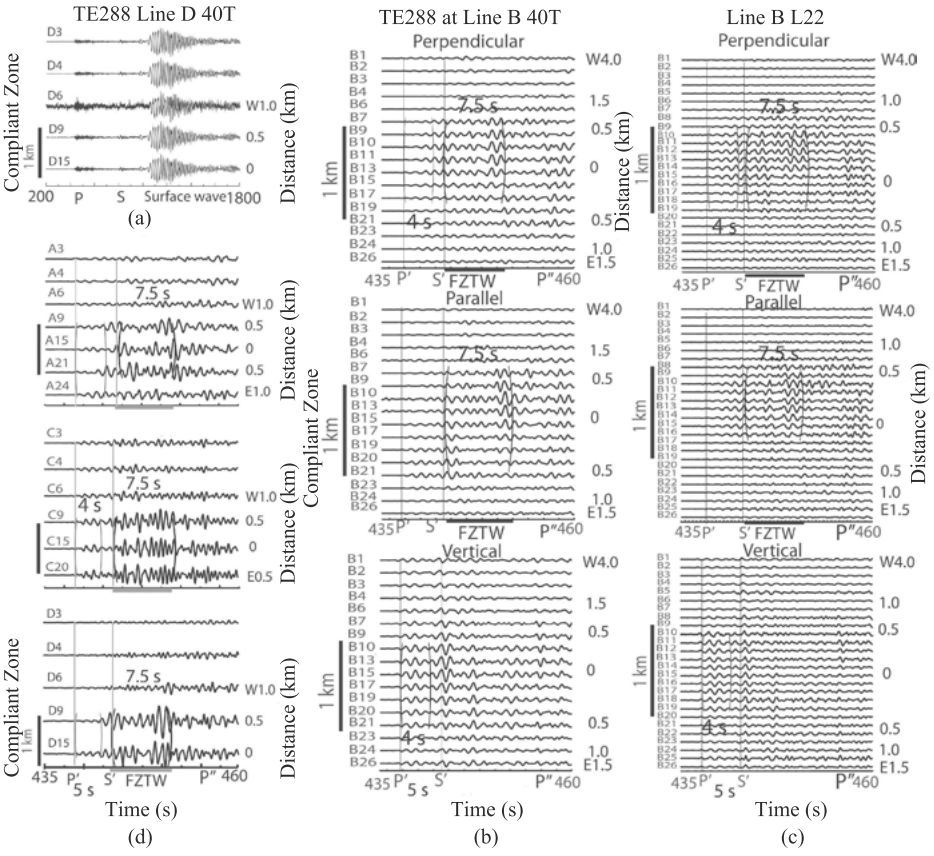

Fig. 2.2 **(a)** Seismograms in the fault-perpendicular component recorded at six 40T stations along Line D for a teleseismic earthquake TE288 which location is shown in Figure 2.1d. Station D15 is located on the fault trace. Station names and distance with respect to D15 are shown in plot. Surface waves are dominant in raw seismograms, but primary P and S waves are visible. The time scale in x-axis is 200–1800 s. **(b)** and **(c)** Three-component seismograms recorded at seventeen intermediate-period 40T stations and twenty-six L22 2-Hz stations along Line B for TE288. Station B15 is located on the fault trace. The time scale in plot is 25 s starting before the first-P arrival. P' and S' are transmitting P-wave and P-S converted wave at the Moho. P" denotes multiple waves. Seismograms have been band-pass (0.5–2 Hz) filtered and are plotted using a fixed amplitude scale for all traces in each profile, showing prominent FZTWs (in brackets) either in P-coda or S-coda at stations B9 – B19 located within a ∼1-km-wide compliant zone (marked by a vertical grey bar). **(d)** Band-pass (0.5–2.0 Hz) filtered perpendicular-component teleseisms recorded at Lines A, C and D show prominent FZTWs (in brackets) with large amplitudes and long wavetrains (marked by horizontal bars) at stations located within the ∼1-km-wide compliant core zone. Other notations are same in (a) and (b).

spectral amplitudes at 1–2 Hz and ∼7-s duration at stations A15, B15, C15 and D15 located within the CF compliant zone, but much shorter wavetrains (duration <3-s) are registered at stations B1 and B26 out of the compliant zone. The P-type FZTWs with ∼4-s duration are also visible in normalized spectral amplitude contours of teleseisms registered at stations A15, B15and D15 located within the CF compliant zone.

Figures 2.3e and 2.3f show teleseisms recorded at Line B with L22 sensors and Lines A, C and D with 40T sensors for a M6.9 teleseismic earthquake (TE271 in Table 2.1 and Fig. 2.1d) occurring at 28-km depth beneath Tonga Islands in Pacific Ocean and ∼6,200-km (55°) southeast of the CF array. We observe large-amplitude FZTWs with 7.5–8 s post-S' coda duration dominant in two horizontal-component teleseisms and 4–4.5 s duration immediately following the P' in vertical component teleseisms at stations within the ∼1-km-wide CF compliant core zone, but not at stations farther away from the zone. We notice the S-type FZTWs in vertical-component teleseisms and the P-type FZTWs in perpendicular-component teleseisms for this shallow teleseismic earthquake because the ray path from it enters the bottom of the CF compliant zone subvertically and is nearly perpendicular to the CF strike. We also notice the multiples in the later coda.

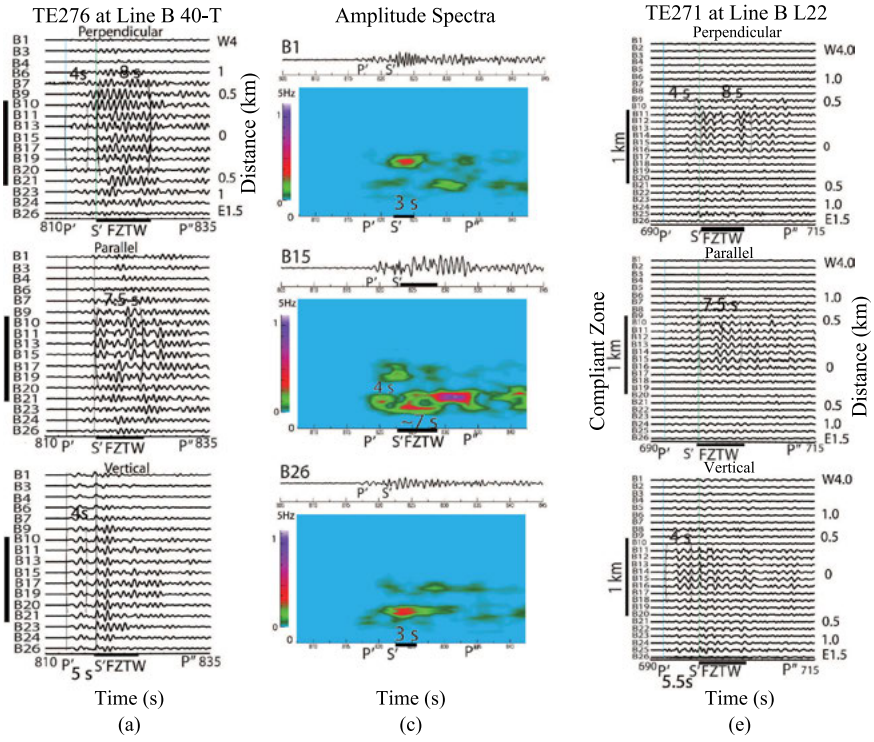

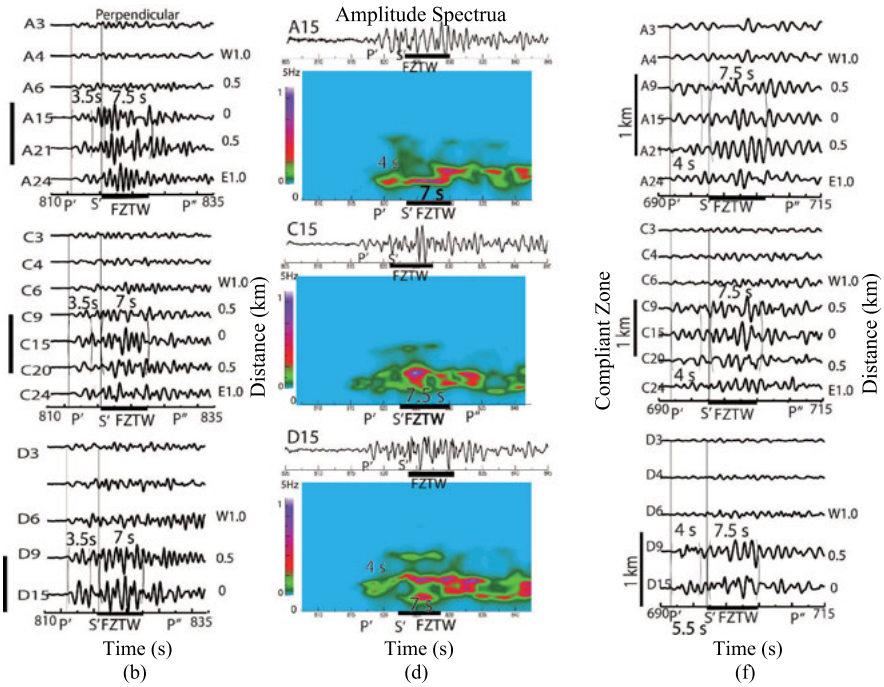

Fig. 2.3 **(a)** Three-component seismograms recorded at seventeen 40T stations along Line B for the deep teleseismic earthquake TE276 show prominent FZTWs (in brackets) with 7–8 s post-S' duration (denoted by horizontal bars) in two horizontal-component and ∼4 s post-P' duration in vertical-component teleseisms recorded at stations B9 – B21 located within the ∼1-km-wide CF compliant core zone. **(b)** Perpendicular-component teleseisms recorded at Lines A, C and D for TE276. Other notations are same as in Figure 2.2. **(c)** and **(d)** Normalized spectral amplitude contours of perpendicular-component teleseisms show large-amplitude FZTWs at 1–2 Hz with ∼7-s post-S' and ∼4-s post-P' durations at on-fault stations B15, A15, C15 and D15 but lower amplitude and shorter duration (<3-s) at stations B1 and B26 out of the compliant zone. The same amplitude scale is used for plots. **(e)** and **(f)** Same as in (a) and (b), but for teleseisms recorded at twenty-six L22 stations along Line B, and 40T stations along Lines A, C and D for the shallow teleseismic earthquake T271, showing 7.5–8 s post-S' and 4–4.5 s post-P' FZTWs at stations within the CF compliant zone.

Figures 2.4 shows teleseisms and normalized spectral amplitude contours recorded at Lines A, B, C and D for a M6.7 teleseismic earthquake (TE244 in Table 2.1 and Fig. 2.1d) occurring at 38-km depth beneath Papua New Guinea Islands ∼11,000 km (69.5°) southwest of the CF seismic array site in California. We observe large-amplitude and long-duration (∼7.5-s) wavetrains starting from ∼5.5 s after the first-P arrivals at stations between B9 and B21 located within the ∼1-km-wide CF compliant core zone but not at stations out of the zone (Figs. 2.4a and 2.4b). Consistently, these wavetrains are interpreted to be S-type FZTWs arising from the S'-wave which is converted from the P-wave

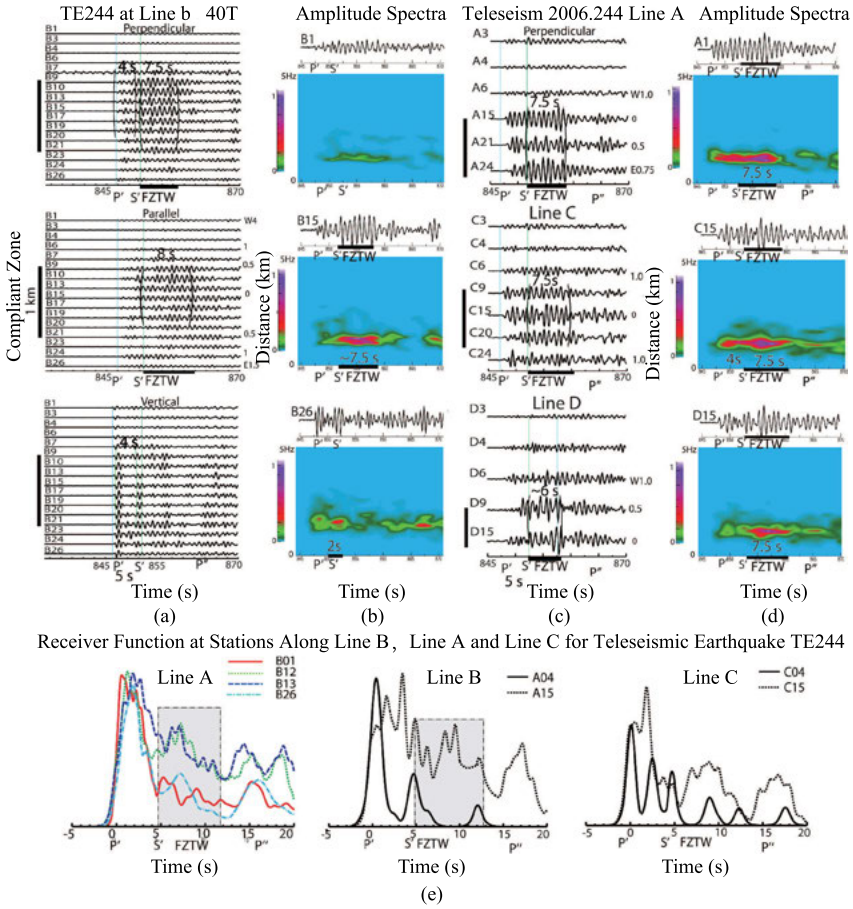

Fig. 2.4 **(a)** and **(b)** Three-component teleseisms recorded at sixteen 40T stations along Line B for a M6.7 teleseismic earthquake occurring at 38-km depth (TE244 in Table 1 and Fig. 1d), showing prominent FZTWs (in brackets) with ∼4-s post-P' and ∼7.5-s post-S durations (denoted by horizontal bars) at stations B9–B21 located within a 1-km-wide compliant zone. Normalized spectral amplitude contours of teleseisms show large-amplitude (red color) FZTWs at 1–3 Hz with ∼7.5-s duration at on-fault station B15, but lower amplitude with much shorter duration (2-s) at stations B1 and B26 out of the compliant zone. **(c)** Perpendicular-component teleseisms recorded at seismic Lines A, C and D. **(d)** Normalized spectral amplitude contours of teleseisms show large-amplitude FZTWs at 1–2 Hz with ∼7.5-s duration at stations A15, C15 and D15 located on the CF surface trace. **(e)** Receiver functions computed by deconvolution between the radial- and vertical-component teleseisms at 4 stations of Line B and 2 stations of Line A and Line C for each. P'-arrivals are aligned at time 0 s. P-to-S converted waves (S') appear at ∼5 s. The S-type FZTWs following S' show large amplitudes and ∼7.5-s duration (in grey box) at stations (B-12, B13, A15 and C15) within the CF compliant zone while lower amplitudes at stations (B01, B26, A04 and C04) outside the compliant zone. Large amplitudes following P' and P" might relate to the P-type FZTWs. The multiple P" arrives at ∼15 s.

at the Moho and sub-vertically enters the bottom of the CF compliant zone at depth. The S-type FZTWs are observed on teleseisms recorded at stations of Lines A, C and D within the CF complaint zone (Figs. 2.4c and 2.4d). We also observe the P-type FZTWs immediately following the first-arrival P' wave in vertical- and perpendicular-component teleseisms for this shallow teleseismic event, from which waves propagate almost perpendicular to the fault strike. The multiple phases of FZTWs are seen in the late coda on teleseisms.

We use the receiver function to confirm that the identified P-type and S-type FZTWs in teleseisms arise from the transmitted P-wave and P-to-S wave converted at the Moho discontinuity. In general, the receiver function analysis is helpful to equalize near-source effects in three-component seismograms and isolate the receiver effects from the observed waveforms so that we can use them to document the deep portion of the CF compliant zone. We compute receiver functions by waveform deconvolution between the radial-component and vertical-component teleseisms for isolating the local response. Figure 2.4e shows receiver functions computed for teleseisms recorded at stations of Lines A, B and C that were located within and out of the CF compliant zone for teleseismic earthquake TE244. The peak amplitudes of P' and P-to-S converted wave S' from the Moho in receiver functions arrive at 0 s and ∼5 s; the multiple-phase P" arrives at ∼15 s, corresponding to the ∼30-km Moho depth and the average ∼6 km/s P-wave speed beneath Mojave Desert. Large-amplitudes between 5 s and 12 s in receiver functions at stations B12, B13, A15 and C15 located within the CF compliant zone are likely associated with S-type FZTWs arising from S' wave. In contrast, much lower amplitudes following S' in receiver functions at stations B01, B26, A04 and C04 located outside the compliant zone. The amplitude peaks in receiver functions immediately following the firs-arrival P' wave at stations located within the CF compliant zone are likely the P-type FZTWs.

2.2.2 Teleseismic Earthquakes in the West Direction from the Array Site

We then examine teleseisms recorded for a $M6.3$ earthquake (TE162 in Table 2.1 and Fig. 2.1d) occurring at 140-km depth in Honshu Prefecture of Japan, approximately 9500-km (72.2°) west of the CF array site in California. Both of P- and S-type FZTWs are identified in teleseisms registered at Line B (Fig. 2.5a, b and c). P-type FZTWs immediate after the first-arrival P' wave show ∼4-s coda duration in vertical- and perpendicular-component teleseisms but invisible in parallel-component because the waves come from this deep teleseismic event to surface stations nearly vertically and perpendicular to the CF strike. S-type FZTWs with large-amplitude and long-duration (∼7-s) wavetrains follow-

ing the S' wave are dominant in two horizontal-component teleseisms at stations between B9 and B21 located within the ∼1-km-wide CF compliant zone. In contrast, shorter wavetrains with lower amplitudes are registered at stations out of the compliant zone, indicating abundance of seismic energy trapped within the CF compliant zone. These P- and S-type FZTWs identified in teleseisms are similar to those FZTWs generated by explosions and local earthquakes recorded at the same seismic array atop the CF (Cochran *et al.*, 2009), but they arise from the transmitting P' wave and the P-to-S converted wave (S') of the first-arrival P wave at the Moho discontinuity, which enter the bottom of CF compliant zone at depth. These FZTWs are also identified in teleseisms recorded at stations of Lines A and C located within the CF compliant zone for teleseismic earthquake TE162 (Fig. 2.5d).

The receiver functions computed by deconvolution between the radial- and vertical-component teleseisms recorded at five stations of Line B for teleseismic earthquake TE162 are shown in Figure 2.5e. The peak first-arrival P' wave and

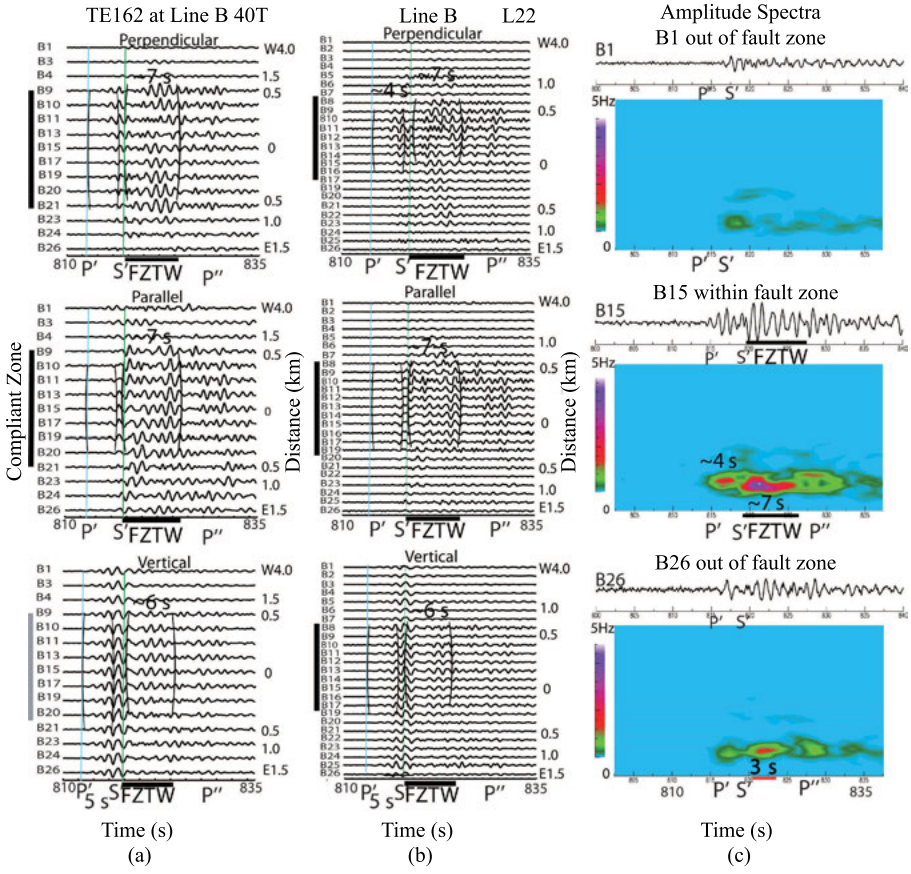

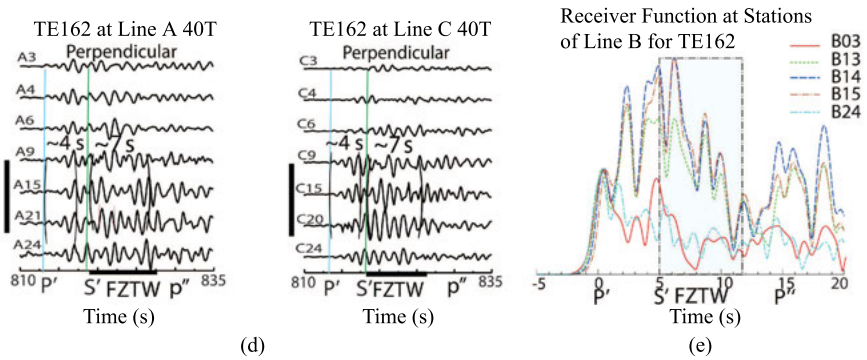

Fig. 2.5 **(a)** and **(b)** Three-component seismograms recorded at fifteen intermediate-period 40T stations and twenty-six L22 2-Hz stations along Line B for a M6.3 teleseismic earthquake TE162 show prominent FZTWs with ~7-s post-S duration (in brackets) in two horizontal seismograms and ~4-s post-P duration at stations B9 – B21 located within a ~1-km-wide compliant zone. P" denotes multiple P-waves rebounded between the surface and Moho. **(c)** Normalized spectral amplitude contours of teleseisms show large-amplitude (red color) FZTWs at 1–3 Hz with ~7-s duration after S' and ~4-s duration after P' at station B15 located on the CF trace, but lower amplitude with shorter duration (<3-s) at stations B1 and B26 out of the CF compliant zone. **(d)** Perpendicular-component teleseisms recorded at Lines A and C installed with 40-T sensors show both P- and S-type FZTWs at stations located within the CF compliant zone. **(e)** Receiver functions of teleseisms at 5 stations of Line B. The Moho converted P-to-S wave S' appear at ~5 s. The S-type FZTWs following S' show large amplitudes and ~7-s duration in S-coda (in grey box) and ~3.5–4 s duration in P-coda at stations B13, B14 and B15 located within the CF compliant zone, but lower amplitudes at stations B03 and B24 outside the compliant zone.

the Moho converted P-to-S wave (S') arrive at 0 s and ~5 s, and the multiple-phase P" arrive at 14–15 s, according to the ~30-km Moho depth and ~6 km/s P-wave speed beneath Mojave Desert. The large-amplitudes between ~5 s and 12 s in receiver functions at stations B13, B14 and B15 located within the CF compliant zone are likely associated with the S-type FZTWs arising from P-to-S converted wave S' that enters at the bottom of the CF at certain depth. In contrast, much lower amplitudes following S' in receiver functions registered at stations B03 and B24 located outside the CF compliant zone. The large amplitudes immediately following the first-arrival P' at stations B13, B14 and B15 are likely associated with the P-type FZTWs. In contrast, the amplitudes in P coda at stations B03 and B24 out of the CF compliant zone are much lower. The receiver functions of recorded teleseisms indicate that our identified FZTWs are produced by a low-velocity CF compliant zone along the CF at depth rather than a shallow anomaly structure.

2.2.3 Teleseismic Earthquakes in the Southeast Direction from the Array Site

We finally examine the teleseisms recorded at the seismic array atop the CF for teleseismic earthquakes with azimuths in the south direction from the array. Figure 2.6 shows teleseisms recorded for a $M6.8$ earthquake (TE317 in Table 2.1 and Fig. 2.1d) occurring at 548-km depth in Bolivia, approximate 7,900-km (78.9°) southeast of the CF seismic array in California. We observe both S- and P-type FZTWs at Line B installed by both intermediate (T40) and short-period (L22) sensors. Surface waves are invisible in teleseisms for this deepest earthquake recorded in the 2016 experiment. The S-type FZTWs with 6–7 s duration following the P-S converted S' waves (∼5-s after the first P-arrival) in two horizontal-component teleseisms recorded at stations within the ∼1-km-wide CF compliant zone. The S-type FZTWs are not visible in the vertical-component teleseisms because the ray path from this deep teleseismic earthquake to the CF array is almost vertical. Normalized spectral amplitude contours of teleseisms show large-amplitude FZTWs at 1–3 Hz with ∼7-s duration at on-fault station

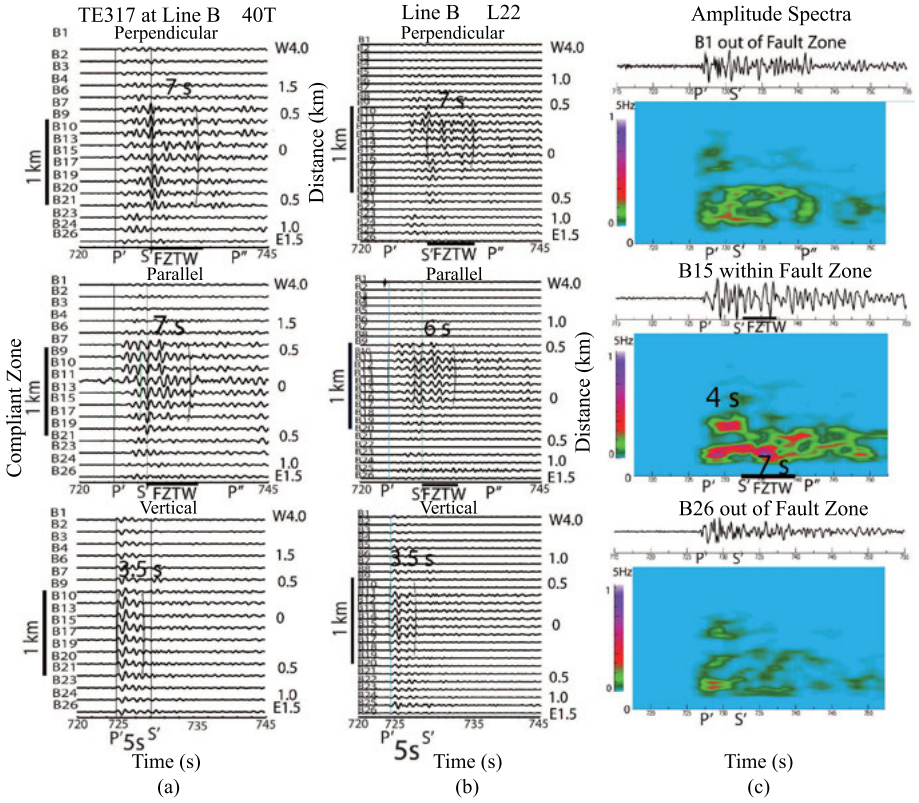

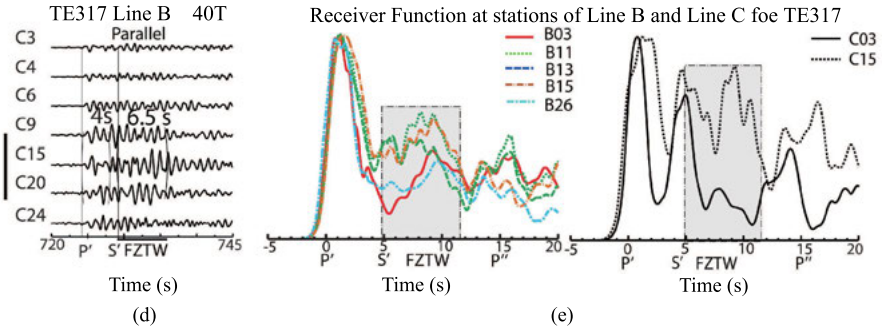

Fig. 2.6 **(a)** and **(b)** Three-component seismograms recorded at sixteen 40T stations and twenty-six L22 2-Hz stations along Line B for a M6.8 teleseismic earthquake (TE317 in Table 2.1 and Fig. 2.1d). Teleseisms show prominent FZTWs (in brackets) with ∼6-7 s post-S' duration in two horizontal teleseisms and 3.4 s post-P' duration in the vertical- and perpendicular-component teleseisms recorded at stations B9–B21 within a ∼1-km-wide compliant zone. **(c)** Normalized spectral amplitude contours of perpendicular-component teleseisms show large-amplitude FZTWs at 1–3 Hz with ∼7-s duration S-coda and ∼4-s duration in P-coda at station B15 located at the CF trace, but much lower amplitude with shorter duration at stations B1 and B26 out of the compliant zone. **(d)** Teleseisms recorded at 40-T stations of Line C, showing both P- and S-type FZTWs for teleseismic earthquake TE317. **(e)** Receiver functions computed by deconvolution between the radial- and vertical-component seismograms recorded at (left) 5 stations of Line B (left) and (right) 2 stations of Line C. P'-arrivals are aligned at time 0 s. P-to-S converted waves (S') appear at ∼5 s. The S-type FZTWs following S' show large amplitudes and ∼6.5 s duration in S-coda (in grey box) and 3.5–4 s duration in P-coda registered at stations (B11, B13, B15, and C15) within the CF compliant zone while lower amplitudes at stations (B03, B26, and C03 outside the compliant zone.

B15, but much weaker and shorter post-S' wavetrains at stations B1 and B26 out of the compliant zone (Fig. 2.6c). We also identify the P-type FZTWs with 3.5–4 s duration following the first-arrival P' dominant in vertical- and parallel-component teleseisms at stations within the CF compliant zone because waves from this deep teleseismic earthquake are nearly vertically and parallel to the CF strike from the SSE direction. We note that the P-type and S-type FZTWs for this deep event have shorter durations (∼3.5 s and 6–7 s) than those in teleseisms from shallower events because the ray paths from it enters the Moho and then the bottom of the CF compliant zone more steeply than the ray paths from the shallower events. Therefore, seismic waves travel shorter distances within the low-velocity fault zone before they arrive at the seismic array at the surface.

Figure 2.6d shows both P- and S-type FZTWs in parallel-component teleseisms recorded at Line C installed with 40T sensors for this deep event. Figure 2.6e shows receiver functions computed for teleseisms recorded at five stations of Line B and two stations of Line C, located within or out of the CF compliant

zone for teleseismic earthquake TE317. The peak amplitudes of P' and P-to-S converted wave S' from the Moho are aligned at 0 s and ∼5 s, and the multiple-phase P" arrives at ∼14–15 s in receiver functions. The large-amplitudes with durations between ∼5 s and ∼12 s in receiver functions at stations (B11, B13, B15 and C15) located within the CF compliant zone are likely associated with S-type FZTWs following the P-to-S converted S' wave while large-amplitudes with durations between 2 s and 5 s in receiver functions are likely associated with P-type FZTWs arising from the first-arrival P' wave. In contrast, the amplitudes following P' and S' in receiver functions at stations (B03, B26, and C03) located outside the compliant zone are much lower.

In Figure 2.7, we identify FZTWs in teleseisms recorded at seismic Lines A, B, C and D for a M6.1 earthquake (TE272 in Table 2.1 and Fig. 2.1d) occurring in South America, at 53-km depth and ∼6,200-km (55°) southeast of the CF array site. FZTWs with large amplitudes, ∼6-s post-S' duration and ∼4-s post-P' duration were recorded at stations located within the ∼1-km-wide CF compliant zone. P-type FZTWs following the first P-arrivals are obvious in parallel-component teleseisms for this teleseismic earthquake because the ray path to the seismic array is sub-vertical and sub-parallel to the CF strike. We notice the multiples in later coda, probably due to waves rebounded between the free surface and Moho discontinuity.

In above examples (Fig. 2.2 to Fig. 2.7), we identify the wavetrains with relatively large amplitudes and ∼4-s duration immediately following the first-arrival P' waves dominant in vertical-component teleseisms recorded at stations located within the ∼1-km-wide CF compliant zone for teleseismic earthquakes occurring in various azimuthal directions from the CF array site. We interpret them to be the P-type of FZTWs arising from the transmitted P' wave from the Moho discontinuity at ∼30-km depth and entering the bottom of the CF compliant zone at certain depth in the earth crust. We also observe consistent wavetrains having large amplitudes with 6–8 s duration starting from ∼5 s after the first-arrival P' dominant in two horizontal-component teleseisms. We tentatively interpret these large-amplitude long-duration wavetrains to be S-type FZTWs arising from cohesive interference of the P-to-S converted S' wave at the Moho and entering the bottom of the CF compliant zone. The CF compliant zone plays a low-velocity waveguide to trap/guide seismic waves within it. These FZTWs identified in teleseisms are similar to those generated by explosions and local earthquakes (Cochran *et al.*, 2009), but they are recorded for teleseismic earthquakes.

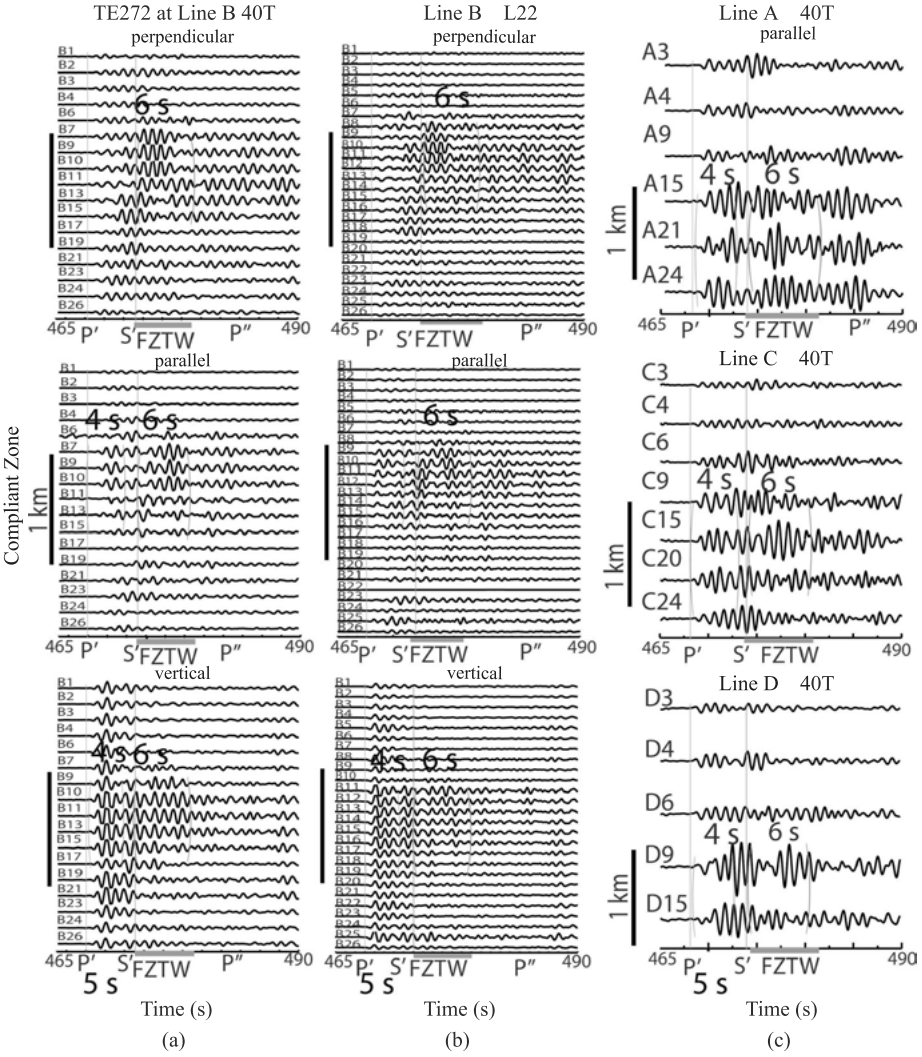

Fig. 2.7 **(a)** and **(b)** Parallel-component seismograms recorded at seventeen 40T stations and twenty-six L22 stations along Line B for a M6.1 teleseismic earthquake (TE272 in Fig. 2.1d) occurring at 53-km depth. Teleseisms have been band-pass (0.5–2 Hz) filtered, showing prominent FZTWs with ∼6-s post-S' duration in teleseisms recorded at stations located within the ∼1-km-wide CF compliant zone. **(c)** Parallel-component teleseisms recorded at Lines A, C and D for this teleseismic event, showing prominent FZTWs with ∼6-s post-S duration at stations within the compliant zone.

2.3 Simulations of FZTWs for Teleseismic Earthquakes

We construct a structural model of the Calico Fault compliant zone on the basis of the previous model shown in Fig. 2.1c (Cochran *et al.*, 2009) combined with newly observations of FZTWs for teleseismic earthquakes. Figure 2.8a shows a schematic diagram in 2-D across the fault zone to illustrate the ray path of first-arrival P wave from a teleseismic earthquake hitting the Moho discontinuity at 30-km depth, and the transmitting P (P') and converted P-to-S (S') waves that sub-vertically enter the bottom of the CF compliant zone at a certain depth in the upper crust to produce P-type and S-type FZTWs due to constructive interference of waves propagating within the low-velocity fault-zone waveguide.

We use a 3-D finite-difference code (Graves, 1996; Vidale *et al.*, 1985) to compute synthetic seismograms that fits teleseisms recorded at seismic lines across the CF. The finite-difference computer code is second order in time and fourth order in space, and it propagates the complete wave-field through an elastic media with a free surface boundary and spatially variable anelastic damping (an approximate Q). In our computation, we use a 160-160-640 element grid in $x-y-z$ coordinates with a grid spacing of 62.5 m to simulate a volume of 10 km in width, 10 km in length, and 40 km in depth. The waveguide composed of a 1-km-wide low-velocity fault zone with 50% velocity reduction embedded in the higher-velocity surrounding rocks in a half space with the free surface. The receiver array is placed at the surface and perpendicularly across the low-velocity fault-zone. We assume plane waves with P-motion come from the teleseismic earthquakes at various azimuth directions and incident angles to the Moho interface between the lower crust and the mantle.

In order to save computer memory space and computation time, we use a 125 m grid spacing in a 10 km×10 km×40 km volume (80–80–320 element grid in $x-y-z$ coordinates) to obtain coarse model parameters at low frequency in the first stage of error-and-trial forward modeling approach. When the grid spacing is 125 m and the minimum velocity within the shallow part of the fault zone was 0.75 km/s, the maximum frequency of the synthetic seismograms is 1.5 Hz. We then use 62.5-m grid spacing to increase the resolution of fault-zone structure in the model at higher frequency. When the grid spacing is reduced to 62.5-m, the maximum frequency increases to 3 Hz.

We tested a model including the 1-km-wide vertical waveguide with velocity reduction of 50% from wall-rock velocities in a layered half-space with velocity profile shown in Fig. 2.8b. The low-velocity waveguide extends from the surface to various depths of 4 km, 8 km and 12 km. Plane waves with P-motion from

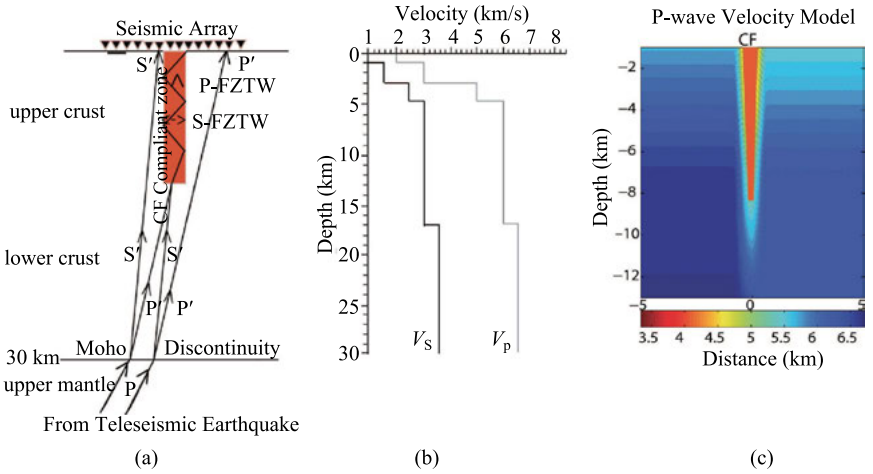

Fig. 2.8 **(a)** Schematic diagram illustrates the first-arrival P wave from a teleseismic event hitting the Moho discontinuity between the lower crust and the upper mantle and transmitting P' and S' waves, which enter the bottom of the low-velocity fault zone (marked by brawn color rectangular) to produce P-type and S-type fault-zone trapped waves (P-FZTW and S-FZTW). They are recorded at stations (triangles) atop the CF compliant zone. **(b)** 1-D P- and S-velocities beneath Mojave Desert used for surrounding-rock velocities in finite-difference modeling of FZTWs recorded at the CF seismic arrays for teleseismic earthquakes. **(c)** The model of P-wave velocities across the Calico fault with a low-velocity waveguide along the CF compliant zone is similar to the velocity model provided by Cochran *et al.* (2009), but the CF compliant core zone with the maximum velocity reduction of 50% extending to the depth of ∼8-km. The fault core zone is ∼1 km wide at the surface and diminishes at 10-km depth. Only 0–13 km depth section of the model is plotted.

a teleseismic earthquake hit the Moho at 30-km depth in the direction sub-perpendicular to the fault strike (at 75° azimuth angle) and at 45° incidence angle to the vertical waveguide.

Figure 2.9 shows 3D finite-difference synthetic teleseisms using this model. The P-type and S-type FZTWs with large amplitudes and long wavetrains are observed in both P coda and S coda in teleseisms at stations located within the low-velocity waveguide. In contrast, no such wavetrains are registered at stations out of the waveguide. While S-type FZTWs are dominant in three-component teleseisms, P-type FZTWs are observed in vertical- and perpendicular-components, but not clearly seen in parallel-component teleseisms due to the waves form the teleseismic event propagate sub-parallel to the seismic array. The coda durations of P-type and S-type FZTWs increase from 3.5 s to 4.5 s and 6 s to 9 s, respectively, as the depth extension of the fault zone increases from 4 km to 12 km because FZTWs traveling a longer distance with the low-velocity waveguide to have a longer wavetrain. The duration times of synthetic P-FZTWs (∼4 s) and S-FZTWs (∼7.5 s) produced by the 8-km-deep low-velocity waveguide are

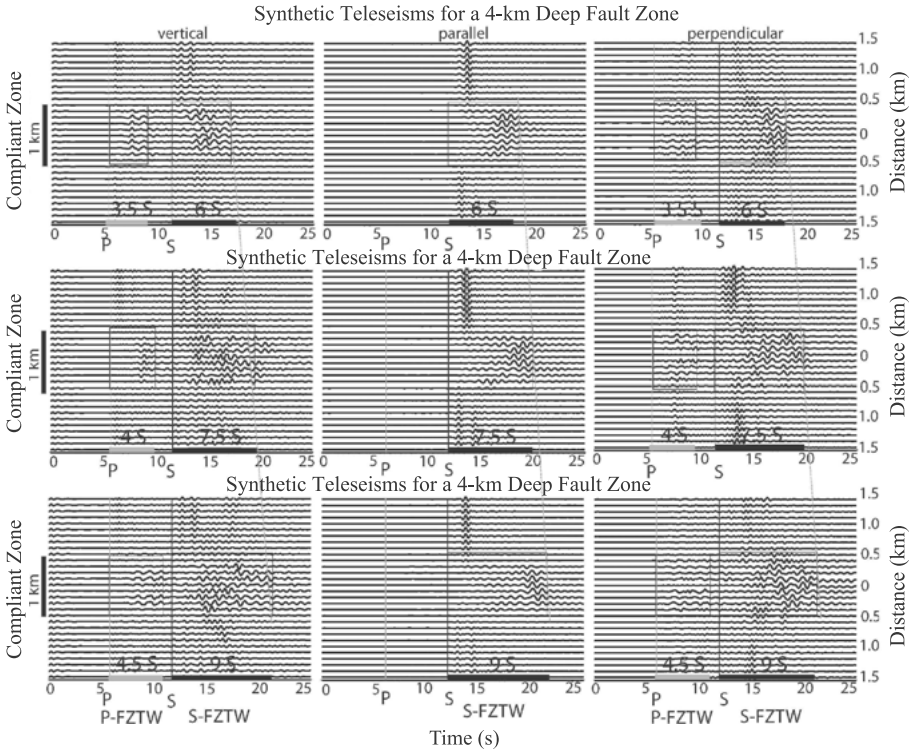

Fig. 2.9 3D Finite-difference synthetic profiles of three-component teleseisms along the cross-fault line for plane waves hitting the Moho in the direction sub-perpendicular to the fault strike and at 45° incident angle to the Moho. Seismograms have been bandpass filtered at 1–3 Hz. The P-type and S-type fault-zone trapped waves (denoted by P-FZTW and S-FZTW) with large amplitudes and long wavetrains (in rectangular boxes) are dominant in teleseisms registered at stations within a 1-km-wide low-velocity waveguide (marked by a vertical black bar). The duration times of FZTWs (denoted by horizontal black bars), within which the waveform amplitudes are above twice the background signal level, increase as the depth extension of the low-velocity waveguide increases (seen as the move-out of slop lines). Thin vertical lines aligned with the first-arrival P wave and the converted P-to-S wave in teleseisms, respectively.

mostly consistent with observations shown in Figures 2.2 to 2.7, suggesting a low-velocity compliant zone along the CF most likely to extend to a depth of approximately 8 km.

We then construct a updated velocity mode (Fig. 2.8c) for the Calico Fault compliant zone based on the previous model (Cochran *et al.*, 2009) combined with the test model used in the above example. The updated model includes a low-velocity fault core zone that is ∼1 km wide at the surface and diminishes at 8-km depth, within which seismic velocities are reduced by 50% from the wall-rock velocities. The velocities from the fault core zone are increased to background

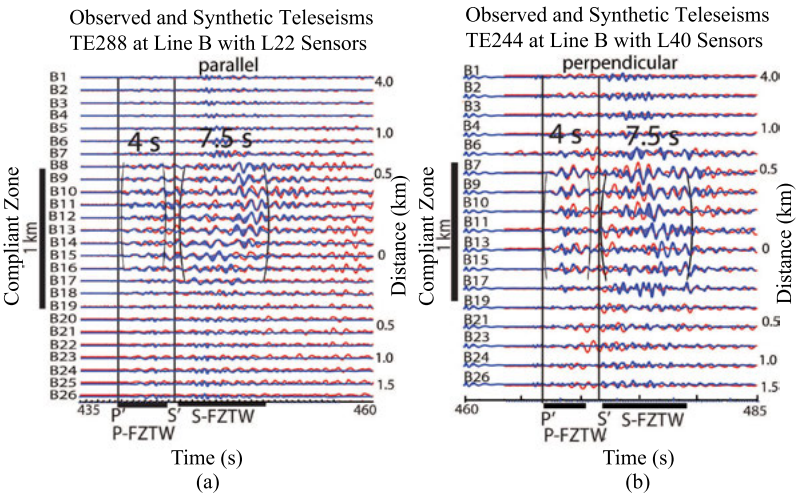

Fig. 2.10 Observed (red lines) and synthetic (blue lines) parallel- and perpendicular-component teleseisms at Line B with L22 and T40 sensors, respectively, for two teleseismic earthquakes **(a)** TE288 and **(b)** TE244 in Table 2.1. S-type FZTWs with ∼7.5-s coda duration (marked by horizontal black bar) following the S' wave are dominant in both horizontal-component teleseisms at stations between B7 and B17 located within the 1-km-wide Calico Fault compliant zone (marked by a vertical black bar). The P-type FZTWs with ∼4-s coda duration following the S' wave are prominent in perpendicular-component teleseisms. Seismograms have been 0.5–3 Hz filtered and are plotted using a fixed amplitude scale for all traces in profile.

velocity values of surrounding rocks (Fig. 2.8b) across a 1.5-km-wide sleeve zone with moderate velocity reduction 25%. The width of the fault zone decreases with a linear taper as the depth increases to 10 km.

Figure 2.10 shows 3D finite-difference synthetic seismograms using the updated structural velocity model in Figure 2.8c for comparison with teleseisms recorded for teleseismic earthquakes TE288 and TE244 occurring southwest of the CF array site. In modeling, we assume plane waves with P-motion hit the Moho at 30-km depth with the azimuth angle 75° (sub-perpendicular to the fault strike) and incidence angle 60°.

Prominent wavetrains with large amplitudes and ∼7.5-s duration staring from ∼5-s after the first-arrival P' are dominant in two horizontal-component teleseisms recorded at stations between B7 and B17 located within the ∼1-km-wide CF compliant zone for both teleseismic earthquakes. However, no such large-amplitude and long-duration wavetrains recorded at stations out of the CF compliant zone. We interpret these long-duration wavetrains with large amplitudes dominant in two horizontal-component teleseisms to be S-type fault-zone trapped waves (S-FZTWs) formed by the S' wave converted from the first-arrival P wave at the Moho discontinuity (∼30-km depth beneath Mojave Desert) and

sub-vertically entering the bottom of the low-velocity CF compliant zone at 8-km depth. The time difference between P' and S' is ∼5 s corresponding to the distance of waves traveling sub-vertically between the Moho at depth of ∼30-km and seismic array at the surface. When the S' wave enters the bottom of the vertical fault zone, S-type FZTWs are produced due to constructive interference of multiple reflected waves at the boundary between the low-velocity compliant zone and high-velocity surrounding rocks, and recorded at the stations located within the CF compliant zone at the ground surface.

The large-amplitude wavetrains with ∼4-s duration following the first-arrival P' wave are shown in perpendicular-component teleseisms recorded at stations within the CF compliant zone. We interpret these wavetrains to be P-type FZTWs arising from the P' when it sub-vertically enters the bottom of the low-velocity fault compliant zone. Because waves from the teleseismic earthquake TE288 propagate in the direction sub-vertically and sub-perpendicular to the fault strike, the P-type FZTWs are prominent in perpendicular-component teleseisms but not so obvious in parallel-component teleseisms.

Although the layer depths and velocities of surrounding rocks are constrained based on the previous velocity model (Cochran *et al.*, 2009), variations in surrounding-rock velocities and layer depths affect the arrival times of P and S waves, As a result of the limited available constraints, we permitted a ±1 s variation in the arrival times used in our model to allow for possible lateral heterogeneity along the fault zone and for different azimuth and incidence angles. Nevertheless, the finite-difference simulations of FZTWs in teleseisms provide a first-order constraint on the depth extension of the CF compliant zone beneath Mojave Desert. Also, because two key model parameters, the depth extension and the velocity reduction of the low-velocity waveguide, are negotiable in the trial-and-error forward modeling, we need to conduct a systematic simulation of teleseisms for more teleseismic earthquakes with various azimuth and incidence angles to obtain better constraints on the true depth extension of the CF compliant zone.

2.4 Discussion

An outstanding question is the depth extent of the low-velocity damage zone along the fault. Some researchers argue that the low-velocity damage zone on faults is a near-surface feature that reaches only down to the top of seismogenic zone at the depth less than 2–3 km (e.g., Ben-Zion *et al.*, 2003; Lewis *et al.*, 2010). Others argue that it extends from the surface across seismogenic zone at depths to ∼10-km depth (e.g., Korneev *et al.*, 2003; Li *et al.*, 2000, 2012, 2014;

Li and Malin, 2008). Wu *et al.* (2010) showed that the low-velocity waveguide on the San Andreas Fault (SAF) at Parkfield, California extends to the depth of 10 km or more using San Andreas Fault Observatory Drilling (SAFOD) borehole data. Ellsworth and Malin (2011) document a profound zone of rock damage on the Parkfield SAF downwards to at least half way (>5–6 km) through the seismogenic crust using both P-type and S-type of FZTWs recorded at the SAFOD mainhole seismograph. FZTWs recorded at Parkfield surface and borehole stations shows that the LVZ on the Parkfield SAF extends to the depth of at least 7–8 km although the velocity reduction within the damage zone decreases with depth due to the increasing confining pressures (Li and Malin, 2008). Although FZTWs generated by explosions and local earthquakes have been used for characterization of the subsurface fault damage structure, the wave propagation coverage is poor for the deep fault zone structure because these seismic sources are located at shallow depths.

In this chapter, the author introduces the FZTWs first time identified in seismograms recorded at the dense seismic array atop the Calico fault zone in Mojave Desert, California for teleseismic earthquakes. We interpret that the transmitting P wave and the converted S wave of the first-arrival P-wave hit at the Moho discontinuity, sub-vertically enter the bottom of compliant zone of the Calico Fault (CF) at a certain depth and produce the FZTWs at the low-velocity fault-zone waveguide. These waves are capable to provide more unprecedented constraints on the depth extension of fault damage zone beyond approach of waves generated by explosions and local earthquakes at shallower depths. Results from observations and finite-difference simulations of these FZTWs identified in teleseismic earthquakes suggest that a low-velocity waveguide on the CF has 50% velocity reduction and extends to depths in excess of ∼8 km. We shall simulate this new type of FZTWs using a full waveform modeling technique with inverse, such as the FD3D tomography method (Chen, 2012) to further confirm our results from this new type of FZTWs.

Acknowledgements

This study is supported by Southern California Earthquake Center's award 15195 and is benefited by the previous results by E.S. Cochran, Y.G. Li, P.M. Shearer, S. Barbot, Y. Fialko, and J.E. Vidale (2009). Thank Elizabeth Cochran for her work on archive of the data recorded at the seismic array deployed at the Calico Fault in 2006, and John Vidale and Heidi Houston for their reading this article. Thank En-Jui Lee for his help to download the data from IRIS DMC and Yu-Ling Chen for using his computer program to calculate receiver functions.

References

Ben-Zion, Y., Z. Peng, D. Okaya, L. Seeber, J.G. Armbruster, N. Ozer, A.J. Michael, S. Barris, and M. Aktar (2003). A shallow fault zone structure illuminated by trapped waves in the Karadere-Dusce branch of the North Anatolian Fault, Western Turkey. Geophys. J. Int., 152, 699–717.

Chen, P. (2012) Full-wave seismic data assimilation: a unified methodology for seismic waveform inversion. In: Imaging, Modeling and Assimilation in Seismology, edited by Yong-Gang Li, Higher Education Press Beijing; De Gruyer, Berlin.

Cochran, E.S., Y.G. Li, P.M. Shearer, S. Barbot, Y. Fialko, and J.E. Vidale (2009). Seismic and geodetic evidence for extensive, long-lived fault damage zones. Geology, 9.37 (4), 315–318, doi:10.1130/G25306A.1; Data Repository item 2009082.

Ellsworth, W.L. and P.E. Malin (2011). Deep rock damage in the San Andreas fault revealed by P- and S-type fault zone guided waves, Sibson's volume. Geological Society Special Publication, 359, 39–53.

Fialko, Y. (2004). Probing the mechanical properties of seismically active crust with space geodesy: Study of the coseismic deformation due to the 1992 $M_{\rm w}$7.3 Landers (Southern California) earthquake. J. Geophys. Res., 109, B03307, doi: 10.1029/2003 JB002756.

Fialko, Y., D. Sandwell, D. Agnew, M. Simons, P. Shearer, and B. Minster (2002). Deformation on nearby faults induced by the 1999 Hector Mine earthquake. Science, 297, 1858–1862, doi: 10.1126/science.1074671.

Ganev, P.N., J.F. Dolan, M.E. Oskin, L.A. Owen, and K.N. Le (2008). Paleoseismologic evidence for multiple Holocene earthquakes on the Calico fault: Implications for earthquake clustering in the eastern California shear zone. Southern California Earthquake Center Annual Meeting Proceedings and Abstracts, XVIII, 153–154.

Graves, R.W. (1996) Simulating seismic wave propagation in 3D elastic media using staggered-grid finite differences. Bull. Seis. Soc. Am., 86, 1091–1106.

Korneev, V.A., R.M. Nadeau, and T.V. McEvilly (2003). Seismological studies at Parkfield IX: Fault-zone imaging using guided wave attenuation. Bull. Seism. Soc. Am., 80, 1245–1271.

Lewis, M. A. and Y. Ben-Zion (2010). Diversity of fault zone damage and trapping structures in the Parkfield section of the San Andreas Fault from comprehensive analysis of near fault seismograms. Geophys. J. Int., doi: 10.1111/j.1365-246X.2010.04816.x.

Li, Y.G. and J.E. Vidale (1996). Low-velocity fault zone guided waves: Numerical investigations of trapping efficiency. Bull. Seis. Soc. Am., 86, 371–378.

Li, Y.G. and J.E. Vidale (2001). Healing of the shallow fault zone from 1994–1998 after the 1992 M7.5 Landers, California, earthquake. Geophy. Res. Lett., 28, 2999–3002.

Li, Y.G., and P.C. Leary (1990). Fault-zone trapped seismic waves. Bull. Seis. Soc. Am., 80, 1245–1271.

Li, Y.G. and P.E. Malin (2008). San Andreas Fault damage at SAFOD viewed with fault-guided waves. Geophys. Res. Lett., 35, L08304, doi:10.1029/2007GL032924.

Li, Y.G., G. De Pascale, M. Quigley, and D. Gravely (2014). Fault damage zones of the $M7.1$ Darfield and $M6.3$ Christchurch earthquakes characterized by fault-zone trapped waves. Tectonophysics, 618, 79–101, 10.1016/j.tecto.2014.01.029.

Li, Y.G., J.E. Vidale, and S.E. Cochran (2004). Low-velocity damaged structure of the San Andreas fault at Parkfield from fault-zone trapped waves, Geophy. Res. Lett., 31, L12S06.

Li, Y.G., J.E. Vidale, D. Oglesby, S. M. Day and E. Cochran (2003a). Multiple-fault rupture of the $M7.1$ Hector Mine, California, earthquake from fault-zone trapped waves. J. Geophys. Res., 108, ESE 11, 1–25.

Li, Y.G., J.E. Vidale, K. Aki, and F. Xu (2000). Depth-dependent structure of the Landers fault zone using fault zone trapped waves generated by aftershocks. J. Geophys. Res., 105, 6237–6254.

Li, Y.G., J.E. Vidale, K. Aki, F. Xu, and T. Burdette (1998). Evidence of shallow fault zone strengthening after the 1992 $M7.5$ Landers, California, earthquake. Science, 279, 217–219.

Li, Y.G., J.E. Vidale, S.M. Day and D. Oglesby (2002). Study of the $M7.1$ Hector Mine, California, earthquake fault plan by fault-zone trapped waves. Hector Mine Earthquake Special Issue, Bull. Seism. Soc. Am., 92, 1318–1332.

Li, Y.G., J.E. Vidale, S.M. Day, D.D. Oglesby, and E. Cochran (2003b). Post-seismic fault healing on the 1999 $M7.1$ Hector Mine, California earthquake. Bull. Seism. Soc. Am., 93, 854–869.

Li, Y.G., K. Aki, D. Adams, A. Hasemi, and W.H.K. Lee (1994). Seismic guided waves trapped in the fault zone of the Landers, California, earthquake of 1992. J. Geophys. Res., 99, 11,705–11,722.

Li, Y.G., K. Aki, J.E. Vidale, F. Xu (1999). Shallow structure of the Landers fault zone using explosion-excited trapped waves. J. Geophys. Res., 104 (B6), 20, 257–20, 275.

Li, Y.G., P.C. Leary, K. Aki, and P.E. Malin (1990). Seismic trapped modes in the Oroville and San Andreas fault zones. Science, 249, 763–766.

Li, Y.G., P. Malin, and E. Cochran (2012). Fault-zone trapped waves: High-resolution characterization of the damage zone on the parkfield San Andreas Fault at depth, In: Imaging, Modeling and Assimilation in Seismology, edited by Y. G. Li. Higher Education Press, Beijing; De Gruyter, Boston, 107–150.

Peltzer, G., Crampe, F., Hensley, S., and Rosen, P. (2001) Transient strain accumulation and fault interaction in the Eastern California shear zone. Geology, 29, 975–978, doi: 10.1130/0091 – 7613(2001)029<0975: TSAAFI>2.0.CO;2.

Vidale, J.E. and Y.G. Li (2003). Damage to the shallow Landers fault from the nearby Hector Mine earthquake. Nature. 421, 524–526.

Vidale, J.E., D.V. Helmberger, and R.W. Clayton (1985). Finite-difference seismograms for SH waves. Bull. Seis. Soc. Am., 75, 1765–1782.

Wu, J., J.A. Hole, and J.A. Snoke (2010). Fault-zone structure at depth from differential dispersion of seismic guided waves: Evidence for a deep waveguide on the San Andreas fault. Geophys. J. Int., 182, 343-354, doi: 10.111.j.1365-246X.2010.04612.x.

Author Information

Yong-Gang Li
Department of Earth Sciences, University of Southern California,
Los Angeles, California 90089-0740, USA.
E-mail: ygli@usc.edu

Chapter 3

Towards Real-Time Earthquake Ground-Motion Estimation Based on Full-3D Earth Structure Models

Po Chen, En-Jui Lee, and Wei Wang

Strong ground motion during disastrous earthquakes depends upon the earthquake source that generates seismic waves and the 3D geological structure through which seismic waves propagate. Kinematic properties of the earthquake source can be estimated, perhaps in real-time or near real-time, from seismic waveform data recorded at broadband 3-component seismic stations located in the vicinity of the earthquake source. Realistic 3D crustal structure models can be constructed beforehand through full-3D seismic waveform tomography (F3DT) using seismic waveform data from previous small to medium-sized earthquakes and ambient-noise Green's functions. Once an estimate of the seismic source and also a 3D structure model are available, synthetic seismograms at sites of interest can be computed in real-time through the use of the reciprocity principle. In this chapter, we explore the feasibility of real-time earthquake ground-motion estimation (forecast) using results from our previous studies in Southern California.

Key words: Towards real-time strong motion estimation, full-3D waveform tomography, 3D structure model, receiver Green's tensor, centroid moment tensor and finite moment tensor.

https://doi.org/10.1515/9783110560329-110

3.1 Introduction

Reliable predictions of the time, location and magnitude of an earthquake, either natural or induced, remain elusive because direct observations of the various fault-zone processes that link physical parameters, such as stress, pore pressure and slip on fault, have proven extremely difficult (e.g., Kanamori *et al.*, 1997). Current efforts to mitigate seismic hazards mainly focus on three areas: long-term (50-year) probabilistic ground-motion estimate, rapid post-earthquake ground-motion notification and earthquake early warning (EEW).

Long-term probabilistic ground-motion estimates are often presented using ground-shaking maps, which plot the probability of ground motion exceeding some threshold in different areas in the next 50 years. Such maps are used widely in the development of building codes to prevent collapses of buildings during disastrous earthquakes, determining earthquake insurance rates in earthquake-prone areas, making land-use policies and educating the public about earthquake emergency preparedness and response. In the US, the U.S. Geological Survey (USGS) periodically updates the National Seismic Hazard Maps, which show 50-year probabilistic ground-motion estimates for the US based on geological and geophysical information (e.g., Frankel *et al.*, 2002; Petersen *et al.*, 2008). In recent years, physics-based probabilistic ground-motion estimates are becoming available. Different from conventional estimates, they account for wave-propagation path effects using empirical relations (e.g., Campbell and Bozorgnia, 2008; Chiou and Youngs, 2008; Petersen *et al.*, 2008). Physics-based probabilistic ground-motion estimates account for the full-physics of 3D wave-propagation using purely numerical solutions of the elastodynamic equation, thereby improving the overall accuracy of ground-motion estimates (Graves *et al.*, 2010).

Rapid post-earthquake notifications are usually provided by seismic networks, which often consist of large numbers of telemetered seismic stations equipped with high-dynamic range broadband and strong-motion instruments (e.g., Kanamori *et al.*, 1997; Hauksson *et al.*, 2001). Seismograms recorded by the network can be used for rapid estimation of earthquake source parameters, which can be broadcast to users within minutes of a disastrous earthquake (e.g., Kanamori *et al.*, 1991). Peak ground motions recorded by the seismic network can be used to produce a map of ground motion distribution over the affected region using some interpolation techniques within 3 to 5 minutes of an earthquake (e.g., Wald *et al.*, 1999). Such a map can be distributed to emergency-response agencies for rapid dispatch of rescue missions to areas with potentially large damages.

Earthquake early warning (EEW) can fill in the gap between long-term measures such as long-term probabilistic ground-motion estimates and post-

earthquake short-term measures such as rapid post-earthquake notifications. EEW aims to provide a few seconds to tens of seconds of warning of oncoming strong ground shaking, which may allow certain emergency mitigation efforts to take place. The usefulness of EEW depends upon, to the first-order, dense seismic networks (i.e., short inter-station distances) and fast communications (i.e., the recorded ground-motion data and/or estimated parameters at different stations can be transferred across the network rapidly). In the past two decades, significant progresses have been made around the world both in seismic instrumentation (i.e., seismic networks are becoming denser and denser) and also in communication technologies, which have made EEW an increasingly more useful option for seismic hazard mitigation (e.g., Böse *et al.*, 2013). For example, even a few seconds of warning time allows the implementation of preprogrammed emergency measures, such as the deceleration of rapid-transit vehicles and high-speed trains to prevent derailment, the orderly shutdown of industrial facilities (e.g., gas pipelines, manufacturing operations, computer facilities) to minimize secondary hazards (e.g., fire hazards) and potential economic losses (e.g., Wu and Teng, 2002). EEW may also allow people to prepare for the oncoming strong shaking (e.g., getting under a sturdy table or moving away from dangerous locations), potentially saving lives.

Rapid advances in seismic instrumentation have inspired a tremendous amount of interest in the research of EEW algorithms that can effectively transform the improvements in instrumentation to shorter reporting time and lower uncertainties in the estimated ground-motion. All EEW algorithms are based on the fundamental observation that the transmission speed of electromagnetic signals is much faster than the propagation speed of seismic shear-waves and surface waves that usually generate the strongest shaking (Gasparini *et al.*, 2007). If a potentially disastrous earthquake can be detected early enough around its source region, it is possible to transmit a warning, using electromagnetic signals, to the affected sites located some distances away from the source before the damaging shear waves or surface waves propagate to those sites. Therefore, the performance of EEW algorithms is usually measured in terms of the reporting time Tr (i.e., the time needed for the EEW system to trigger and record a sufficient length of waveform data plus the time needed to process those waveform data to obtain magnitude and hypocenter), the accuracy of the estimated earthquake source parameters and the predicted ground motions at the affected sites.

Recent advances in computing technology have made full-3D seismic waveform inversion (F3DWI) a reality (e.g., Chen and Lee, 2015). F3DWI is capable of (near) real-time seismic source parameter inversions in a 3D earth structure model (Lee *et al.*, 2012). Moreover, the 3D earth structure model can be constantly improved by assimilating seismic waveform observations through full-3D tomography (F3DT) (Lee *et al.*, 2014a). In Southern California, synthetic seismograms computed using 3D structure models obtained through F3DT show a

excellent waveform agreement with observed seismograms, not only for seismograms used in the F3DT inversion, but also for seismograms from earthquakes not included in the inversion. This capability of "predicting" seismic waveforms using 3D earth structure models obtained from F3DT has been utilized in long-term physics-based probabilistic ground-motion estimates (Graves *et al.*, 2010). In this chapter, we explore the possibilities of improving EEW algorithms through F3DWI.

3.2 Methodology

Depending upon the algorithm used in issuing an alert, current EEW approaches can be roughly grouped into two categories: single-station (or onsite) approaches and network-based (or regional) approaches (e.g., Allen *et al.*, 2009; Behr *et al.*, 2015). In the single-station (onsite) approach, an alert is issued when one or more thresholds of waveform parameters measured in real-time are exceeded at one or two stations (e.g., Nakamura, 1988; Kanamori, 2005; Böse *et al.*, 2009). In the network-based approach, the first few seconds of waveforms recorded at multiple stations are used to estimate the earthquake source parameters (mainly the magnitude and hypocenter), the expected ground motions at target sites are then estimated based on the source parameters using certain empirical relations and then an alarm is issued if the expected ground motions exceed certain thresholds (e.g., Wu and Teng, 2002; Allen and Kanamori, 2003; Cua and Heaton, 2007; Cua *et al.*, 2009; Satriano *et al.*, 2011). In practice, both types of approached can be combined such as in the EEW system implemented by the Japan Meteorological Agency (JMA) (Kamigaichi *et al.*, 2009).

3.2.1 Single-Station Approach

The single-station or onsite approach is based on detecting seismic signals at one station or a few very close-by stations and issuing warning of the oncoming strong shaking at the same location of the one or a few close-by stations. This type of approaches is usually based upon detecting and analyzing P-waves. Because the strongest ground shaking usually arrives at the time of, or after, the S-wave arrival and the P-wave usually travels much faster than the S-wave, it is possible to use the information contained in the P-wave to issue a warning before the oncoming strong shaking.

Various P-wave-based observational parameters have been devised for EEW purposes. One of the widely used parameters is the dominant period of the first

few seconds of the P-wave $\tau_p^{\max}$ (Nakamura, 1988). The intuition behind this parameter is that larger earthquakes usually involve ruptures over larger asperities on faults; they therefore radiate lower frequency energy. It has been found that $\tau_p^{\max}$ scales well with earthquake magnitude for stations located within a few hundred kilometers of the epicenter (Allen and Kanamori, 2003). In practice, an initial estimate of magnitude can be obtained within about one second. As new waveform data become available, $\tau_p^{\max}$ and the magnitude estimate can be continuously updated.

A slightly modified P-wave parameter is the average period of the P-wave within a fixed time window, which is often selected to be three seconds (Kanamori, 2005). This parameter, often denoted as τ_c, also scales well with magnitude (Wu and Kanamori, 2005; Wu *et al.*, 2007). In practice, by combining τ_c and $\tau_p^{\max}$, it is possible to obtain a more robust estimate of the magnitude (e.g., Shieh *et al.*, 2008).

It has been shown that the peak displacement, velocity or acceleration of the first few seconds of the P-wave scales well with magnitude if a correction for the epicentral distance can be made (e.g., Wu and Kanamori, 2008). In practice, the peak displacement, P_d, is found to be more robust than the peak velocity or acceleration, although the peak velocity is also useful when P_d is not easily obtained (Wurman *et al.*, 2007).

In a typical onsite or single-station approach, a combination of the P-wave parameters described above is often used. Amplitude information alone may not be sufficient for issuing a warning. Small earthquakes may generate waveforms with large amplitudes and high frequency content. But if large amplitudes are associated with low frequencies, the magnitude can potentially be large and a warning should then be issued. Figure 3.1 shows a simple onsite EEW workflow based on this concept. The UrEDAS (urgent earthquake detection and alarm

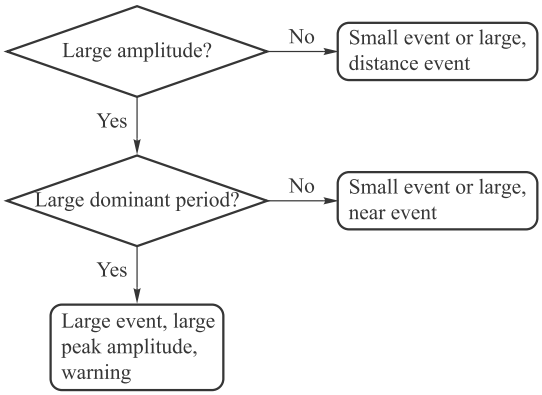

Fig. 3.1 A simple onsite early warning algorithm based on P-wave amplitude and dominant frequency (Tom Heaton's method).

system) in Japan is a good example of the onsite approach (Nakamura, 1988). In UrEDAS, the first three seconds of the P-wave waveform is used to estimate source parameters. The dominant period is used to estimate the magnitude. Once the magnitude is estimated, the amplitude can be used to estimate the epicentral distance based on a certain attenuation model. Because UrEDAS uses three-component instruments, the particle motion can be used to estimate the event azimuth and depth. A single three-component station can therefore provide estimates of all those source parameters with quite remarkable accuracy.

3.2.2 Network-Based Approach

Most of the seismic networks today are equipped with fast communication networks, which allow fast streaming of seismic waveform data recorded by individual stations inside the network to a data processing center, where new processing modules aimed at EEW can be deployed and tested. In the network-based or regional approach, seismic data from multiple stations are combined at the processing center to derive more accurate estimation of earthquake source parameters and ground motion across the affected region. Onsite or single-station algorithms can still be used inside the network setting. Parameters estimated at individual stations can also be transmitted to the processing center and integrated into the processing and assessment workflow. Different from the onsite approach, which usually detects seismic signals and provides warnings for the same location, the network-based approach aims at detecting earthquakes using stations close to the hypocenter and provides warnings to users at greater distances.

One typical example of the network-based approach is also known as the "front detection" method, which was initially proposed for San Francisco following the 1868 Hayward fault earthquake (Cooper, 1868). The fundamental concept of the front-detection method is to install seismic sensors between hypocenters of potentially disastrous earthquakes and population centers that will likely experience damaging ground motion. One example of EEW systems based on the front-detection method is the SAS (seismic alert system) implemented in Mexico for Mexico City. The SAS seismic network is composed of 12 accelerometers distributed along the coast of Guerrero above the subduction zone, where potentially damaging earthquakes may occur, and provides warning to Mexico City, which is about 320 km to the north (Espinosa-Aranda *et al.*, 1995; Espinosa-Aranda *et al.*, 2009). In general, at such a large epicentral distance, the ground-motion should be quite weak due to geometrical spreading and attenuation. But because Mexico City was built on thick basin sediments, the ground-motion can still be very strong due to the basin amplification effect, which was estimated to

increase the ground-motion amplitude by a factor of 100 to 500 (Suárez *et al.*, 2009). The system uses recorded waveform data from the first-arriving P-wave to well after the arrival of the S-wave to determine if an alert should be issued, but because of the large epicentral distance, it can still provide about 60 s of warning time for Mexico City.

The virtual subnetwork (VSN) approach adopted by the "Central Weather Bureau" (CWB) of Taiwan, China is also a variation of the front-detection method (Wu and Teng, 2002). The seismic network is composed of 79 real-time, telemetered three-component accelerometers distributed throughout Taiwan, an area of about 100 km by 300 km. As soon as the network is triggered by an event, stations located within about 60-km epicentral distance are automatically selected to form a VSN and seismic waveform data from the VSN are extracted from the large number of input channels of the entire seismic network for further processing to estimate the magnitude and the hypocenter. On average, about 22 s are required for event triggering and VSN data processing, which allows the CWB to provide warning for areas lying at distances greater than about 75 km from the epicenter.

The disadvantage of the network-based approach is that there will likely be a "blind zone" around the epicenter where no warning is possible. This is due to the fact that it takes time to transmit the seismic data from the stations near the epicenter to the processing center, to analyze those data and to issue a warning. In practice, the network-based or regional approach can be combined with the single-station or onsite approach to reduce the reporting time.

3.2.3 EEW Based on F3DWI

The strong ground motion experienced at a target site is the joint result of the earthquake source that generates seismic energy and the subsurface structure through which the seismic wave propagates. In principal, the subsurface structure can be imaged through full-3D tomography (F3DT) using seismic waveform data from previous small- to medium-sized earthquakes and/or ambient-noise Green's functions. And the seismic source parameters can be estimated, perhaps in real-time, using the waveform data recorded at stations surrounding the epicenter and also the 3D subsurface structure model determined beforehand through F3DT. As soon as an estimated earthquake source model is available, synthetic seismograms and the estimated ground motion at the target site can be computed in real-time by applying the reciprocity principle. As more waveform data become available at the processing center, the earthquake source model can be updated and the synthetic seismograms at the target site can be re-computed accordingly. It is therefore feasible, at least in principle, to implement the EEW

system based on F3DWI. The difficulty lies in the efficient implementation of the entire workflow and the availability of sufficient computational resources for carrying out the entire workflow in a sufficiently short amount of time.

With the rapid advances in computing technology and the wide availability of commodity high-performance computing hardware (e.g., multi-/many-core CPUs, graphic processing units) in the past decade, the cost of computational resources has reduced dramatically. On the other hand, significant progresses have been made in numerical methods for solving the elastodynamic equation (i.e., elastic seismic wave equation) in complex 3D geological media. Using today's computing technology, it is already feasible to build an EEW system based on F3DWI. Take for example the EEW system in Taiwan, the average reporting time is around 22 s and only the first 10 s of the waveforms after the first P arrival for a VSN network are used in data processing. In Southern California, we can obtain a relatively robust centroid moment tensor (CMT) solution using 10 s of waveforms after the first P arrival on the closest 5 stations around the epicenter. The entire calculation can be carried out on a small computer cluster with about two dozen nodes or on a couple of graphic processing units (GPUs) within about 5 s. Synthetic seismograms that account for the full physics of 3D wave propagation can be computed for all target sites within about 1 s. The synthetic peak-ground-velocity (PGV) map can then be computed using a simple kriging algorithm in less than 1 s and our synthetic PGV map shows excellent agreement with the actual post-earthquake observed PGV map for the example shown in Figure 3.2. With the continued advancement in computing technology, our processing time can be reduced even further, potentially providing even more warning time.

3.2.3.1 Numerical waver-equation solver

F3DWI-based EEW is based on the capability to solve the elastodynamic equation using a purely numerical method. In the past few decades seismologists have developed various numerical algorithms to solve the elastodynamic equation. Those numerical algorithms include the finite-difference, finite-element, pseudo-spectral, spectral-element, discontinuous-Galerkin methods. Compared with the seismic ray method, these numerical solutions can provide complete representations of the seismic wavefields in highly complex 3D geological structure models. Of course, these numerical solutions are limited by the accuracy of the underlying numerical algorithms used for solving the elastodynamic equation. Nevertheless, they should contain all possible waves propagating in a given geological structure model and there is no inherent limit in improving the accuracy of the numerical solutions in any frequency range or time window in those numerical algorithms,

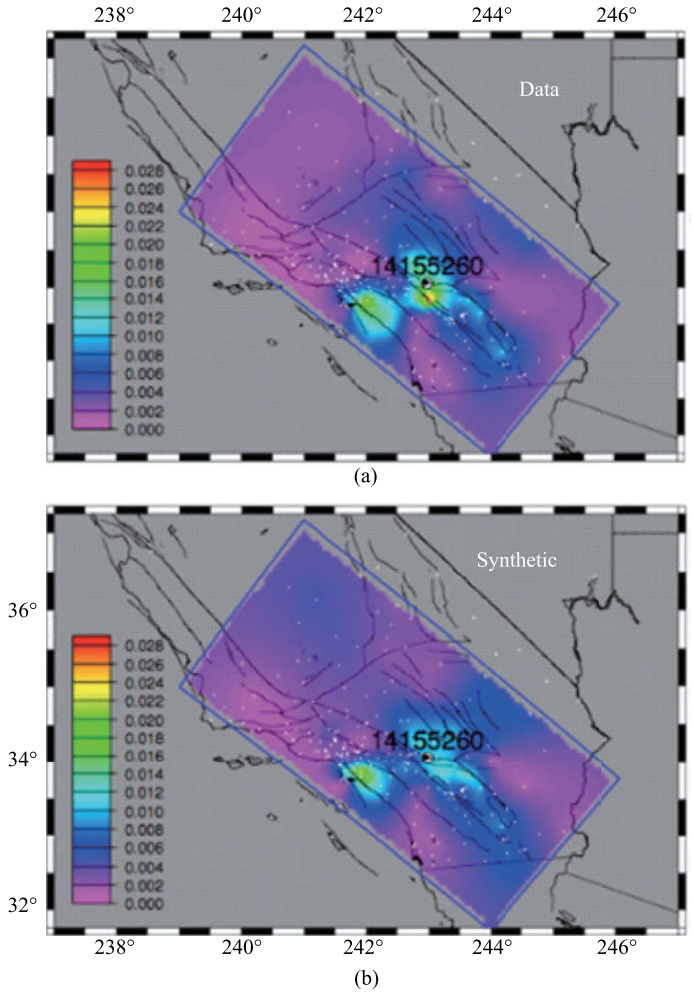

Fig. 3.2 Observed **(a)** and synthetic **(b)** peak ground velocity map for the 16 Jun 2005, M_{L}4.9 Yucaipa earthquake. White dots: locations of seismic stations, black solid lines: major faults in Southern California.

given sufficient computational resources. The computational cost for obtaining numerical solutions is significantly higher than that for obtaining ray-theoretic solutions, especially for large models at high frequencies. However, our computing capability has been increasing exponentially, more than doubling every two years in the past 20 years. The computing industry marched from the first teraflop machine to the first petaflop machine in just 12 years and it is anticipated that the fastest computer will have a peak performance of about 1 EFLOP in around 2020. The progress in the computing technology has opened up the possibilities for solving seismic inverse problems using numerical solutions of the three-dimensional elastodynamic equation.

Among all the numerical algorithms that have been adopted to solve the seismic wave equation, several algorithms have been developed more substantially than others. In the 1970s and 1980s the finite-difference (FD) method was introduced to simulate SH and P-SV waves on regular, staggered-grid, two-dimensional meshes. Extensions of the FD method to three spatial dimensions and other curvilinear coordinates and to account for anisotropic, visco-elastic material properties were carried out subsequently. The spatial derivatives in the FD method is approximated through differencing schemes and their accuracy is mainly controlled by the number of grid points required to accurately sample the wavelength. The pseudo-spectral (PS) method with Chebychev or Legendre polynomials partially overcomes some limitations of the FD method and can substantially improve the accuracy of spatial derivatives. The PS method also has its drawbacks, mainly due to the global character of its spatial derivative operator, which makes it relatively cumbersome to account for irregular modeling geometries. And parallelizing the PS method on modern distributed-memory computer clusters in an efficient and scalable way is not as straightforward as parallelizing the FD method.

There are also numerical algorithms based on the weak (i.e., variational) form of the elastodynamic equation. The finite-element (FE) method and the spectral-element (SE) method have received wide attention in the seismic modeling community. An important advantage of the weak form representation is that the free-surface boundary condition is naturally accounted for even for highly irregular surface topography. In the SE method, each element is mapped to a reference cube using the Jacobian matrix. High-order Lagrange polynomial interpolants are used to represent functions on the reference cube. The control points needed in defining the Lagrange polynomials are chosen to be the classical Gauss-Lobatto-Legendre (GLL) quadrature points. Any smooth 3D function can then be interpolated in a 3D hexahedral element by triple products of Lagrange polynomials at the GLL points. The spatial derivatives of any functions can be obtained by computing the derivatives of the Lagrange polynomials and the integrals of any functions can be approximated using the GLL integration quadrature. A direct consequence of using Lagrange interpolants and GLL quadrature is that the resulting mass matrix of the system is diagonal and a fully explicit time-marching scheme can be adopted.

The discontinuous-Galerkin (DG) method was adopted to solve the elastodynamic equation very recently. The advantages of the DG method can be summarized as follows.

- In three spatial dimensions, the DG method can achieve high-order accuracy on fully unstructured tetrahedral meshes, which are substantially easier to generate than hexahedral meshes, especially for geological structure models with complex geometries associated with topography, faults and other types of structural discontinuities.

- Unlike conventional numerical schemes, which often adopt a relatively low-order time-stepping method such as the Newmark scheme or a high-order, multi-stage method that requires storing intermediate fields such as the Runge-Kutta method, the DG method uses a high-order, single-step, explicit time integration scheme, the Arbitrary high-order DERivatives (ADER) method. The DG method allows for different polynomial degrees inside different elements (i.e., p-adaptivity) and also different time-step lengths for different elements (i.e., local time stepping). In conventional global time-stepping schemes, the element with the smallest time step length dictates its own time step length to all other elements. In the local time-stepping scheme, each element can use a different time-step length that is optimal according to its own local stability condition. This is particularly advantageous for meshes with strongly degenerate elements (i.e., slivers), as the time-step lengths for other elements are not restricted in any way by the small time-step lengths of the badly-shaped elements.
- The DG method is particularly suitable for modeling wave propagation in heterogeneous fluid-solid environment. The Riemann solver used for computing the numerical flux across element interfaces can automatically recognize discontinuities in material properties across highly irregular fluid-solid interfaces. The acoustic fluid is characterized by simply setting the shear modulus to zero. The DG method also accounts for the convection of the fluid, which allows us to correctly model the effects of ocean currents on wave propagation in complex acoustic environment.
- The majority of the operators in the DG method are applied in an element-local way, with weak nearest-neighbor coupling between elements through numerical flux functions. The resulting locality allows the DG method to achieve very high parallel efficiency on single-instruction-multiple-data (SIMD) distributed-memory parallel computers.

The primary disadvantage of the DG method is its high computational cost. Preliminary results have shown that it is about 50–60 times more expensive than the SE method. However, some recent results have shown that the DG method for solving the elastodynamic equation can be effectively accelerated using graphic processing units. Compared with the CPU implementation, the GPU-CPU hybrid implementation can achieve a speedup of about 28 times with a moderate-level optimization of the GPU memory access pattern. This is highly encouraging because with the current computing capability, the GPU-accelerated DG algorithm can already be used for solving F3DWI problems of moderate size. With the continued development of the computing technology, the DG method will be applicable to much larger problems in the near future.

Numerical algorithms for solving the elastodynamic equation are not limited to those discussed above. We also mention the boundary-element method (BEM),

the finite-volume method, the variable- and discontinuous-grid finite-difference method, the hybrid finite-difference-finite-element method. Different numerical algorithms have different advantages and drawbacks.

3.2.3.2 Receiver Green's tensor (RGT) and reciprocity

The RGTs are the strain fields, as functions of both space and time, generated by three orthogonal unit impulsive point forces acting at the receiver locations. By applying the reciprocity principle, it can be shown that the RGTs provide exact partial derivatives of the waveforms at the receiver locations with respect to the moment tensor at any point in the modeling volume. The RGTs can be calculated with high accuracy in a 3D earth structure model by solving the elastodynamic equation using numerical methods, such as the finite-difference, finite-element and spectral-element methods, and stored on disk. Since the synthetic seismograms and their partial derivatives can be retrieved from the database very rapidly, the RGT-based approach is better suited for real-time source parameter inversions. The disadvantage of this approach is that since the RGTs have to be constantly on-line for rapid access, the disk storage cost could be quite high.

Following Zhao *et al.* (2006), the displacement field from a point source located at $\mathbf{r}'$ with moment tensor M_{ij} can be expressed as (e.g. Aki and Richards 2000)

$$u_k(\mathbf{r}, t; \mathbf{r}') = M_{ij}\partial'_j G_{ki}(\mathbf{r}, t; \mathbf{r}'), \tag{3.1}$$

where ∂'_j denotes the source-coordinate gradient with respect to $\mathbf{r}'$ and the Green's tensor $G_{ki}(\mathbf{r}, t; \mathbf{r}')$ relates a unit impulsive force acting at location $\mathbf{r}'$ in direction $\hat{\mathbf{e}}_i$ to the displacement response at location $\mathbf{r}$ in direction $\hat{\mathbf{e}}_k$. Taking into account the symmetry of the moment tensor, we also have

$$u_k(\mathbf{r}, t; \mathbf{r}') = \frac{1}{2}[\partial'_j G_{ki}(\mathbf{r}, t; \mathbf{r}') + \partial'_i G_{kj}(\mathbf{r}, t; \mathbf{r}')]M_{ij}. \tag{3.2}$$

Applying reciprocity of the Green's tensor

$$G_{ki}(\mathbf{r}, t; \mathbf{r}') = G_{ik}(\mathbf{r}', t; \mathbf{r}), \tag{3.3}$$

equation (3.2) can be written as

$$u_k(\mathbf{r}, t; \mathbf{r}') = \frac{1}{2}[\partial'_j G_{ik}(\mathbf{r}', t; \mathbf{r}) + \partial'_i G_{jk}(\mathbf{r}', t; \mathbf{r})]M_{ij}. \tag{3.4}$$

For a given receiver location $\mathbf{r} = \mathbf{r}_{\mathrm{R}}$, the receiver Green tensor (RGT) is a 3^{rd}-order tensor defined as the spatial-temporal strain field

$$H_{jik}(\mathbf{r}', t; \mathbf{r}_{\mathrm{R}}) = \frac{1}{2}[\partial'_j G_{ik}(\mathbf{r}', t; \mathbf{r}_{\mathrm{R}}) + \partial'_i G_{jk}(\mathbf{r}', t; \mathbf{r}_{\mathrm{R}})]. \tag{3.5}$$

Using this definition, the displacement recorded at receiver location $\mathbf{r}_\mathrm{R}$ due to a source at $\mathbf{r}_\mathrm{S}$ with moment tensor $\mathbf{M}$ can be expressed as

$$u_k(\mathbf{r}_\mathrm{R}, t; \mathbf{r}_\mathrm{S}) = M_{ij} H_{jik}(\mathbf{r}_\mathrm{S}, t; \mathbf{r}_\mathrm{R})$$

or

$$\mathbf{u}(\mathbf{r}_\mathrm{R}, t; \mathbf{r}_\mathrm{S}) = \mathbf{M} : \mathbf{H}(\mathbf{r}_\mathrm{S}, t; \mathbf{r}_\mathrm{R}), \tag{3.6}$$

and the synthetic seismogram due to a source at $\mathbf{r}_\mathrm{S}$ with the basis moment tensor $\mathbf{M}_m$ can be expressed as

$$\mathbf{g}_m(\mathbf{r}_\mathrm{R}, t; \mathbf{r}_\mathrm{S}) = \mathbf{M}_m : \mathbf{H}(\mathbf{r}_\mathrm{S}, t; \mathbf{r}_\mathrm{R}). \tag{3.7}$$

Most of the numerical algorithms for solving the seismic wave equation, such as finite-difference, finite-element, spectral-element and discontinuous Galerkin methods, explicitly use the spatial gradients of the displacement (or velocity) and the stress (or stress rate) in their calculations. For a given receiver, the RGT can therefore be computed through three wave-propagation simulations with a unit impulsive force acting at the receiver location $\mathbf{r}_\mathrm{R}$ and pointing in the direction $\hat{\mathbf{e}}_k (k = 1, 2, 3)$ in each simulation and store the strain fields at all spatial grid points $\mathbf{r}'$ and all time sample t. The synthetic seismogram at the receiver due to any point source located within the modeling domain can be obtained by retrieving the strain Green's tensor at the source location from the RGT volume and then applying equation (3.6). For large earthquakes, the point-source representation may not be adequate. But we can always approximate a finite source through superposition of multiple point sources and the linear equation (3.6) can be easily generalized to account for a finite source model.

3.2.3.3 General concept

The conceptual diagram for the F3DWI-based EEW is shown in Figure 3.3. We adopt the network-based approach in this diagram. Observed waveforms recorded at stations close to the epicenter are being streamed to the processing center, where we can invert for a source model using equation (3.6). Because the RGTs for all receivers in a seismic network (including those close to the epicenter) were pre-computed and stored on disk, the source model can be inverted in real-time and constantly updated as new waveform data become available. When using equation (3.6) for the source inversion, the left-hand-side is the observed waveform data, the RGTs on the right-hand-side can be retrieved from disk and we can therefore invert for a source model through simple least-square or other numerical optimization algorithms depending upon the amount of usable waveform data and the computational resources available.

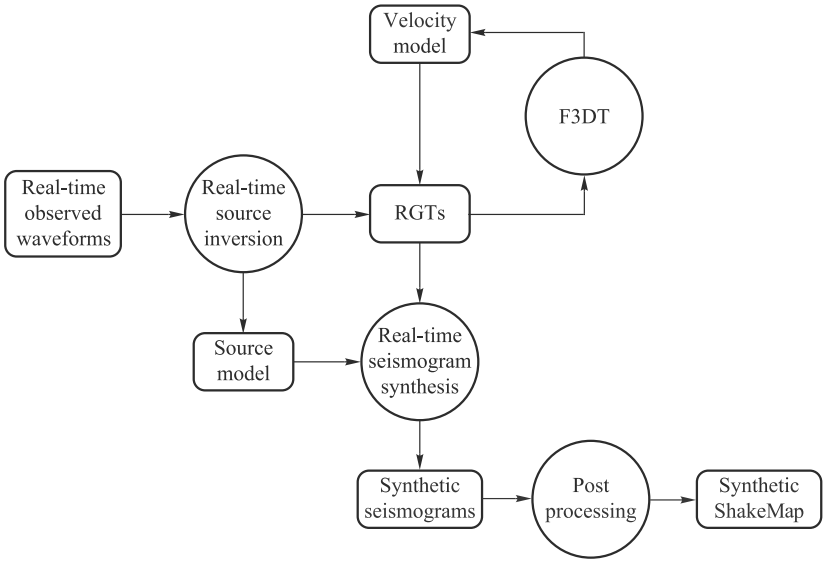

Fig. 3.3 A conceptual diagram of a F3DWI-based EEW system.

As soon as a source model is obtained, equation (3.6) is used again to estimate synthetic seismograms (ground motion parameters) at all target sites. Because the RGTs for all target sites (e.g., population centers, locations of important infrastructures) are also pre-computed and stored on disk, the calculation of equation (3.6) only involves retrieving from those RGTs at the inverted source location inside the modeling volume and applying the right-hand-side of equation (3.6). Once the synthetic seismograms are obtained, ground-motion parameters such as PGV, PGA can be easily extracted and interpolated to generate a synthetic "ShakeMap" (Fig. 3.2). As new observed waveform data becoming available, the source model can be re-inverted and updated and the synthetic seismograms and the synthetic ShakeMap can also be updated accordingly.

The accuracy of the inverted source model, as well as the accuracy of the synthetic seismograms and the synthetic ShakeMap, depends upon the accuracy of the RGTs. The most important factor that determines the accuracy of the RGTs is the accuracy of the 3D seismic velocity model used for computing the RGTs. The seismic velocity model can be determined and refined by assimilating waveform data from previous small- to medium-sized earthquakes and/or ambient-noise Green's functions through F3DT.

The appropriate choice of an earthquake source model is another important factor that can greatly affect the accuracy of ground-motion predictions. In the majority of previous EEW studies, only the magnitude and hypocenter are estimated. These two parameters, although highly important in estimating ground-motion based on empirical scaling laws, are not sufficient for computing synthetic

seismograms using equation (3.6). For a point-source representation, we require at least a moment tensor solution in order to compute synthetic seismograms. For EEW purposes, the amount of waveform data that can be used for real-time source parameter inversion is very low (e.g., ∼10 s after first P-wave arrival). It is therefore important to choose a source model with few parameters and can also be used for computing synthetic seismograms.

3.3 Source Inversion

For EEW purposes, we propose a two-stage source inversion process. In the first stage, we invert for the centroid moment tensor (CMT) point-source representation. If the estimated moment magnitude exceeds a certain threshold (e.g., $M_{\mathrm{w}} > 5$), we switch to the second stage and invert for the finite moment tensor (FMT) representation. The CMT representation has 8 independent parameters for purely double-couple earthquake source. Provided a good station azimuthal coverage, a few seconds of waveform data after the first P-wave arrival may allow us to constrain these 8 parameters with some level of confidence. The FMT representation is the lowest-order finite-source representation. For a planar rupture, the FMT parameters include the 8 independent CMT parameters and 6 additional parameters that characterize the spatial and temporal dimensions of the source and also the directivity of the rupture process. As waveform data are being streamed into the processing center, we invert for and update the 8-parameter CMT solution first. As soon as the estimated moment magnitude exceeds a pre-specified threshold, we automatically transition to the second stage and invert for and update the 14-parameter FMT representation. It is also possible to introduce a third stage for very large earthquakes (e.g., $M_{\mathrm{w}} > 6.5$), in which we invert for a detailed fault slip distribution (FSD). The number of parameters in the FSD representation can easily exceed hundreds and will require a lot more waveform data to obtain a reliable solution. For EEW purposes, it may not be worthwhile to introduce the third stage into the workflow.

3.3.1 CMT Inversion

For the CMT inversion in the first stage, the rapid full-wave CMT inversion algorithm developed and demonstrated in Lee *et al.* (2011) can be easily adapted for EEW purposes, if real-time telemetered seismic waveform data access is provided. In Lee *et al.* (2011), we developed a multi-scale grid-search algorithm based on Bayesian inference to obtain not only an optimal set of CMT param-

eters but also estimates of the uncertainties associated with each optimal CMT parameter.

In our multi-scale grid-search scheme, the model space for the 8 CMT parameters (i.e., the longitude, latitude and depth of the centroid location, the centroid time, the moment magnitude, the strike, dip and rake of the focal mechanism) is uniformly discretized and successively refined in 3 steps. In the first step, we use the normalized cross-correlation coefficient (NCC) between synthetic and corresponding observed waveforms as a criterion for selecting acceptable CMT solutions in the model space. If the synthetic waveforms computed using a CMT solution provides acceptable NCC values for all observed waveforms, that CMT solution is accepted for further analysis. In the second step, the model space is refined surrounding all the CMT solutions accepted in the first step. We use the time shift between the synthetic and the corresponding observed waveforms as the criterion to select CMT solutions in the refined model space. If the synthetic waveforms computed using a CMT solution have sufficiently small time shifts (measured using cross-correlation delay time) with respect to their corresponding observed waveforms, that CMT solution is accepted for further processing. In the third step, the model space is refined again surrounding all the CMT solutions selected in the second step. We use the amplitude ratio between the synthetic and the corresponding observed waveforms as the criterion for selecting CMT solutions. If the ratios between the amplitudes of the synthetic waveforms computed using a CMT solution and the corresponding observed waveforms are sufficiently close to unity, that CMT solution is accepted with a posterior probability computed based on the NCC, time shift and amplitude ratio values for that solution.

To adapt this multi-scale grid-search scheme to EEW, we propose to combine the three steps into a single step and instead of using three different criteria (NCC, time-shift and amplitude ratio) we will use a single criterion based on the relative waveform misfit (RWM),

$$\mathrm{RWM} = \frac{\int_{t_0}^{t_1} [s(t) - \bar{s}(t)]^2 \mathrm{d}t}{\sqrt{\int_{t_0}^{t_1} [s(t)]^2 \mathrm{d}t \int_{t_0}^{t_1} [\bar{s}(t)]^2 \mathrm{d}t}}, \tag{3.8}$$

where $s(t)$ is the synthetic waveform computed using different trial CMT solutions and $\bar{s}(t)$ is the corresponding observed waveform. To account for possible errors in the seismic velocity model, we allow a small time shift when computing the RWM. If the RWM of the synthetic waveforms computed using a CMT solution is above a prespecified threshold, that CMT solution is accepted with a certain probability based on the RWM values.

The entire calculation can be easily parallelized. There are two levels of parallelism can be exploited in the algorithm. First, the calculations of the RWMs for different trial CMT solutions are completely independent of one another,

therefore we can parallelize over different trial CMT solutions. Second, the calculations of the RWMs for different observed waveforms (i.e., different stations or channels) for the same trial CMT solution are also completely independent of each other, therefore we can parallelize over observed waveforms. This parallel algorithm can be easily implemented on parallel CPU clusters or on GPUs and we expect a nearly linear strong and weak scaling.

3.3.2 FMT Inversion

If the moment magnitude estimated in the first-stage CMT inversion exceeds a pre-specified threshold, the second-stage inversion for FMT parameters can be automatically triggered. The total number of FMT parameters is not much larger than CMT parameters and the increasing amount of observed waveform data may warrant a robust inversion of the FMT.

If we assume that the moment density $m_{jk}(\boldsymbol{x}, t)$ is everywhere proportional to a constant seismic moment tensor M_{jk}, i.e.,

$$m_{jk}(\boldsymbol{x}, t) = M_{jk} \int_{-\infty}^{t} f(\boldsymbol{x}, t')\mathrm{d}t', \tag{3.9}$$

where $f(\boldsymbol{x}, t)$ is the source-space-time function and M_{jk} is independent of space and time. We can then define the spatial and temporal polynomial moments of $f(\boldsymbol{x}, t)$ as

$$\mu^{(0,0)} = \int \mathrm{d}V(\boldsymbol{x}) \int \mathrm{d}t f(\boldsymbol{x}, t) \equiv M_0, \tag{3.10}$$

$$\mu^{(0,1)} = \int \mathrm{d}V(\boldsymbol{x}) \int \mathrm{d}t f(\boldsymbol{x}, t)(t - t_0) \equiv t_1, \tag{3.11}$$

$$\mu^{(1,0)} = \int \mathrm{d}V(\boldsymbol{x}) \int \mathrm{d}t f(\boldsymbol{x}, t)(\boldsymbol{x} - \boldsymbol{x}_0) \equiv \boldsymbol{x}_1, \tag{3.12}$$

$$\mu^{(0,2)} = \int \mathrm{d}V(\boldsymbol{x}) \int \mathrm{d}t f(\boldsymbol{x}, t)(t - t_0)^2, \tag{3.13}$$

$$\mu^{(1,1)} = \int \mathrm{d}V(\boldsymbol{x}) \int \mathrm{d}t f(\boldsymbol{x}, t)(t - t_0)(\boldsymbol{x} - \boldsymbol{x}_0), \tag{3.14}$$

$$\mu^{(2,0)} = \int \mathrm{d}V(\boldsymbol{x}) \int \mathrm{d}t f(\boldsymbol{x}, t)(\boldsymbol{x} - \boldsymbol{x}_0)(\boldsymbol{x} - \boldsymbol{x}_0)^{\mathrm{T}}, \tag{3.15}$$

where t_0 is the reference time and $\boldsymbol{x}_0$ is the reference location. Note that the source-space-time function defined in equation (3.9) is the moment-rate function in time, therefore it is compactly supported in time and the second moment should exist. Equation (3.11) defines the centroid time with respect to the reference time and equation (3.12) defines the centroid location with respect to

the reference location. If we replace t_0 and $\boldsymbol{x}_0$ in equations with t_1 and $\boldsymbol{x}_1$, respectively, we obtain

$$\hat{\mu}^{(0,2)} = \int \mathrm{d}V(\boldsymbol{x}) \int \mathrm{d}t f(\boldsymbol{x},t)(t-t_1)^2 \equiv \left(\frac{T_c}{2}\right)^2, \tag{3.16}$$

$$\hat{\mu}^{(1,1)} = \int \mathrm{d}V(\boldsymbol{x}) \int \mathrm{d}t f(\boldsymbol{x},t)(t-t_1)(\boldsymbol{x}-\boldsymbol{x}_1) \equiv \hat{\mu}^{(0,2)} \boldsymbol{v}_d, \tag{3.17}$$

$$\hat{\mu}^{(2,0)} = \int \mathrm{d}V(\boldsymbol{x}) \int \mathrm{d}t f(\boldsymbol{x},t)(\boldsymbol{x}-\boldsymbol{x}_1)(\boldsymbol{x}-\boldsymbol{x}_1)^{\mathrm{T}} \equiv \boldsymbol{U}\Lambda\boldsymbol{U}^{\mathrm{T}}, \tag{3.18}$$

where T_c is the characteristic duration, $\boldsymbol{v}_d$ is the directivity velocity vector, the 3-by-3 diagonal matrix Λ is contains the eigenvalues of the second-order spatial moment $\hat{\mu}^{(2,0)}$ and $\boldsymbol{U}$ is an orthogonal matrix of eigenvectors. For a planar rectangular rupture, the eigenvalue matrix Λ can be expressed as

$$\Lambda = \begin{bmatrix} L_c/2 & 0 & 0 \\ 0 & W_c/2 & 0 \\ 0 & 0 & 0 \end{bmatrix},$$

where L_c is the characteristic length and W_c is the characteristic width of the finite rupture. The directivity velocity vector $\boldsymbol{v}_d$ should lie on the plane of a simple planar rupture. We can define a dimensionless directivity parameter

$$D \equiv |\boldsymbol{v}_d| \frac{T_c}{L_c}, \tag{3.19}$$

to measure the magnitude of the directivity effect. For a perfectly symmetric rupture (e.g., a bilateral rupture) we have $D = 0$ and for a perfectly unilateral rupture we have $D = 1$.

Once a CMT solution is obtained, we can invert for the FMT using a gradient-based iterative optimization algorithm, which usually converges very quickly. The partial derivatives of the waveform misfit measurements with respect to the FMT parameters can be derived analytically. Figure 3.4 shows examples of the partial derivatives computed in the uniform whole-space structure model. For example, a perturbation in $\mu_1^{(1,0)}$ produces an infinitesimal shift of the centroid location along the x-axis towards east, which reduces the travel-time (hence a decrease in phase-delay time) and increases the amplitude (hence a decrease in amplitude-reduction time) for receivers on the east side of the reference point source. The decrease in travel-time on receivers to the east is caused by reduced source-receiver distances and the increase in amplitude on those receivers is due to the geometric spreading effect. A perturbation in $\mu_1^{(1,1)}$ is linked to the effect of source directivity along the x-axis.

Suppose we have an infinitesimal-length unilateral line source lying along the x-axis, centered at the origin and propagating from west to east. The travel-time is reduced (hence a decrease in phase-delay time) on receivers to the west and

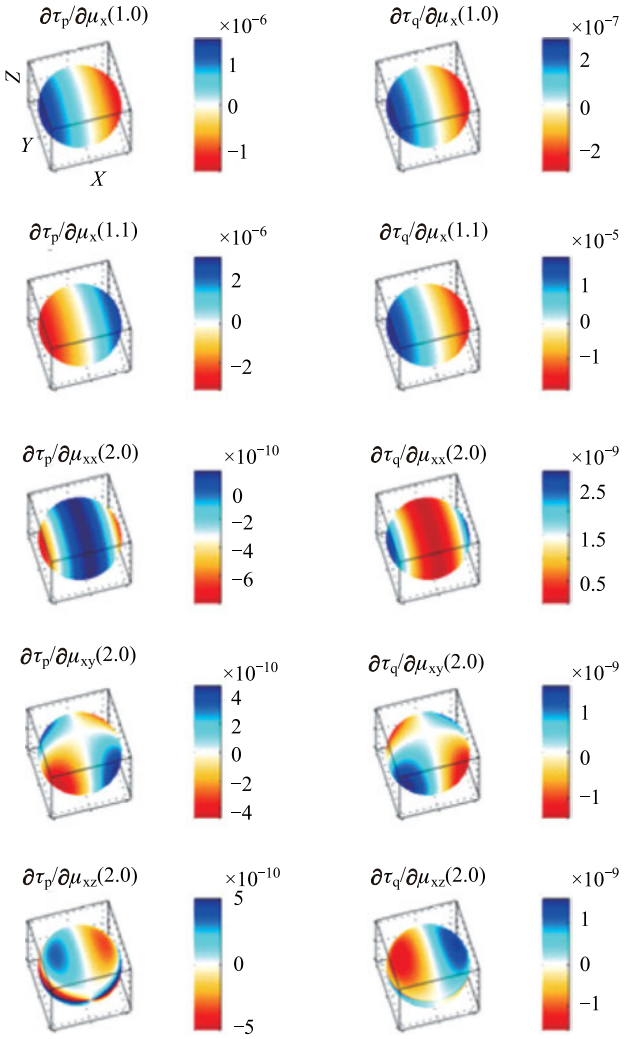

Fig. 3.4 Spatial variations of the partial derivatives of the frequency-dependent phase-delay time (left column) and amplitude-reduction time (right column) with respect to $\mu_1^{(1,0)}$ (top row), $\mu_1^{(1,1)}$ (second row), $\mu_{11}^{(2,0)}$ (third row), $\mu_{12}^{(2,0)}$ (fourth row), $\mu_{13}^{(2,0)}$ (bottom row).

increased (hence an increase in phase-delay time) because the rupture initiates from the west and propagates to the east. The amplitude is increased (hence a decrease in amplitude-reduction time) on receivers to the east because of the constructive interference effect in the direction of rupture propagation. The spatial variations in the partial derivatives with respect to components of $\mu^{(2,0)}$ can be explained by the constructive and destructive interference effect. The partial

derivatives shown in Figure 3.4 are for phase-delay and amplitude misfits and those partial derivatives have more intuitive explanations. The partial derivatives for waveform differences can also be computed without any difficulty by using the RGTs.

3.4 F3DT for EEW

The accuracy of the 3D seismic velocity model affects the overall performance of the EEW system through the RGTs at two places: the inversion of the earthquake source model and the estimation of the ground motion at target sites (Fig. 3.3). It is therefore critical to improve the accuracy of the 3D seismic velocity model.

3.4.1 Crustal Structure

For regions such as Southern California, the most important 3D crustal structure features that have significant effects on ground motion are sedimentary basins. In Southern California, many at-risk urban areas are situated on deep basins. Past wave-propagation simulations have demonstrated the importance of detailed 3D basin structures (e.g., the thickness of the sediments, 3D basin boundaries, velocity contrasts with basement rocks) and the coupling between earthquake ruptures and 3D basin structures in controlling the propagation and amplification of seismic waves (Graves *et al.*, 1998; Olsen *et al.*, 2006, 2008; Day *et al.*, 2012). In the past, basin structures in Southern California were calibrated using various techniques. Passive-source ray travel-time tomography (RTT) has been used to provide crustal-scale images of large basins (e.g., Hauksson, 2000; Lin *et al.*, 2010). Controlled-source seismic surveys were able to provide high-resolution basin images, but the results are usually confined to a few 2D profiles (e.g., Lutter *et al.*, 1999; 2004; Shaw *et al.*, 2015). Geological studies of the age and depths of sediments combined with sonic log data have been used to construct rule-based basin velocity models at locations where such data are available (e.g., Magistrale, 1996; Magistrale *et al.*, 2000). Geostatistical methods have also been applied to direct velocity measurements to construct basin models (e.g., Süss and Shaw, 2003; Shaw *et al.*, 2015).

The techniques for seismic tomography have been rapidly evolving in the past decade, partly driven by rapid advances in computing technology (e.g., Graves, 1996; Komatitsch and Tromp, 2002; Käser and Dumbser, 2006; Cui *et al.*, 2010; Komatitsch *et al.*, 2010; Mu *et al.*, 2013). The latest seismic tomography tech-

nique is full-3D seismic waveform tomography (F3DT), which uses fully numerical solutions of the 3D (visco) elastic wave equation to construct Frechet kernels and is able to iteratively update the 3D velocity model by minimizing waveform misfits (e.g., Chen, 2011; Liu and Gu, 2012; Fichtner, 2012; Chen and Lee, 2015). Its application in Southern California has shown that F3DT is now capable of providing high-resolution, high-accuracy 3D basin velocity models (Lee *et al.*, 2014; Chen and Lee, 2015).

The Southern California Earthquake Center (SCEC) has been supporting the development of Community Velocity Models (CVMs) and there are currently two major braches of 3D CVMs for Southern California: CVM-S and CVM-H. CVM-S was constructed by embedding rule-based seismic velocity models of major basins in Los Angeles and Salton Trough areas within a background seismic velocity model determined from regional seismic travel-time tomography (Magistrale *et al.*, 2000). It was later improved by adding geotechnical layers on top of the basins, a laterally varying Moho interface determined from receiver function studies (Zhu and Kanamori, 2000) and an upper-mantle model obtained from teleseismic RTT (Kohler *et al.*, 2003). The 4th version of this model is referred to as CVM-S4. A recent update has incorporated the perturbations obtained by applying 26 iterations of F3DT on CVM-S4 and the updated 3D model is referred to as CVM-S4.26 (Lee *et al.*, 2014).

CVM-H was also constructed by embedding high-resolution basin structure models within the regional seismic tomography model (Süss and Shaw, 2003; Shaw *et al.*, 2015). In the latest version, CVM-H15.1, the basin models were mainly determined using a large number of borehole data, sonic logs, 2D seismic reflection profiles, and a few 3D reflection surveys from various sources (Süss and Shaw, 2003; Shaw *et al.*, 2015); the Moho interface was obtained from receiver functions and wide-angle reflection results (Yan and Clayton, 2007; Gilbert, 2012; Tape *et al.*, 2012); the background crustal model was obtained through 16 iterations of F3DT based on the adjoin-wavefield method (Tape *et al.*, 2009, 2010); the upper-mantle structure was determined through finite-frequency teleseismic surface wave tomography (Prindle and Tanimoto, 2006).

Figure 3.5 shows the comparison of the isostatic gravity anomaly (Phillips *et al.*, 1993) (Fig. 3.5b) with the $Z_{2.5}$ map for CVM-S4 (Fig. 3.5c), CVM-S4.26 (Fig. 3.5d), and CVM-H15.1 (Fig. 3.5e). The $Z_{2.5}$ refers to the depth of $V_s = 2.5$ km/s and has been used to estimate the depth of sediments for GMPEs (Campbell and Bozorgnia, 2008). Sediment depths in the three CVMs are significantly different. Some basins that are well imaged in CVM-S4.26 are completely missing or not as well imaged in CVM-S4 and CVM-H15.1, such as the Santa Maria Basin (SMB), Cuyama Basin, Southern San Joaquin Basin (SSJB), Owens Valley, Indian Wells Valley, Santa Barbara Channel, Antelope Valley, Santa Monica Bay, and San Bernardino Basin (SBB). These low-velocity sedimentary regions in CVM-S4.26 are fairly consistent with topography (Fig. 3.5a) and also the low-value areas in

the isostatic gravity anomaly map (Fig. 3.5b). For many sedimentary regions in CVM-S4.26 the locations of maximum depths in the $Z_{2.5}$ map (Fig. 3.5d) coincide with local minima in the isostatic gravity anomaly map, such as the SMB, SSJB, Owens Valley, Antelope Valley and SBB. Note that different CVMs use different types of data to constrain basin structures. For example, the basins in Inner California Borderland in CVM-H15.1 were constructed by kriging direct velocity measurements (Shaw *et al.*, 2015). However, those basins in CVM-S4.26 were imaged purely from F3DT.

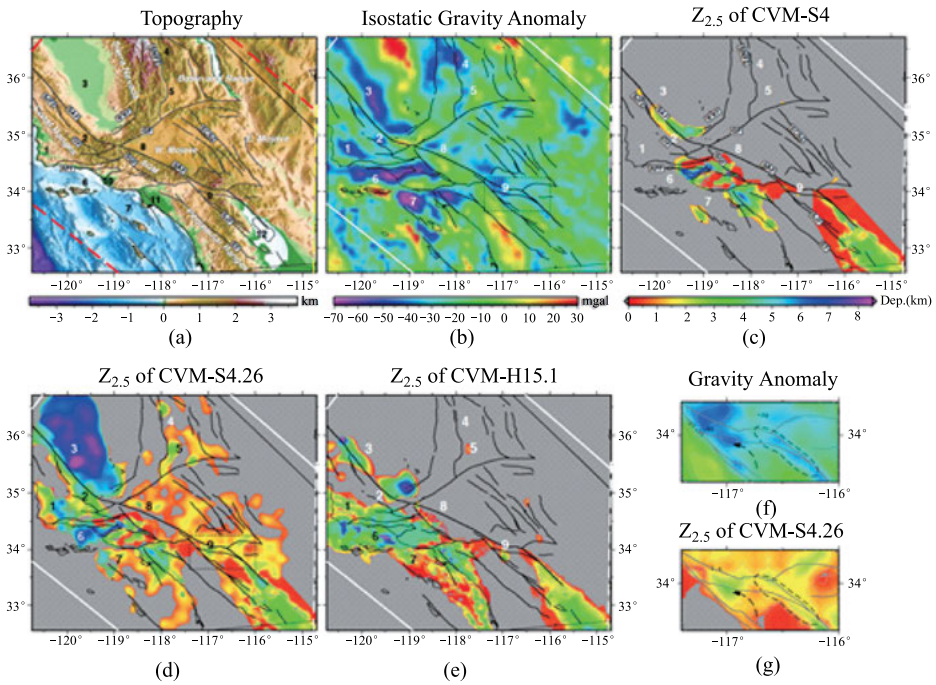

Fig. 3.5 **(a)** Map shows topography, bathymetry, major geological provinces and active faults in Southern California. Major faults are drawn in bold black: SAF-San Andreas Fault, SJFZ-San Juan Fault Zone, OF-Ozena Fault, SNFZ-Sierra Nevada Fault Zone, WWT-White Wolf Fault, GF-Garlock Fault, APF-Arroyo Parida Fault, SGF-San Gabriel Fault, EF-Elsinore Fault, SJF-San Jacinto Fault, and ECSZ-Eastern California Shear Zone. Basins mentioned in the text are labeled 1–12: 1-Santa Maria Basin (SMB), 2-Cuyama Basin, 3-Southern San Joaquin Basin (SSJB), 4-Owens Valley, 5-Indian Wells Valley, 6-Santa Barbara Channel, 7-Santa Monica Bay, 8-Antelope Valley, 9-San Bernardino Basin, 10-Ventura Basin, 11-Los Angeles Basin, 12-Salton Trough. The red and yellow dash boxes indicate Lee *et al.*'s (2014a). **(b)** Maps of isostatic gravity anomaly, **(c–e)** $Z_{2.5}$ maps for 3 CVMs in Southern California, and **(f–g)** enlarged isostatic gravity anomaly and $Z_{2.5}$ map of CVM-S4.26 in the San Bernardino Basin region. Some sedimentary basins absent in our initial model are numbered.

The depths for some well-constrained large basins in CVM-S4 have been modified in CVM-S4.26. For instance, the Los Angeles Basin (LAB) is shallower and wider in CVM-S4.26 than it was in CVM-S4 (Figs. 3.5c, d). The depths of some offshore basins in CVM-S4.26 are increased substantially compared with those in CVM-S4. These results are corroborated by the offshore basin models in CVM-H11.5, which used controlled-source surveys to constrain offshore basin structures (Shaw *et al.*, 2015). In spite of the fact that the offshore data coverage is relatively poor due to the limited number of stations on offshore islands (Lee *et al.*, 2014a), we were still able to construct many of the offshore basins that are mostly missing in our starting model CVM-S4. For instance, in CVM-S4.26, the sediments in the Santa Barbara Channel area (Fig. 3.5d), which is in the structural down-warp of a fold-and-thrust belt, is much deeper than that in CVM-S4. This feature agrees well with geology and also gravity anomalies (Fig. 3.5). Another example is the Santa Monica Bay area in CVM-S4.26, which is highly consistent with that in CVM-H15.1 and also the gravity observations (Fig. 3.5).

3.4.2 Geotechnical Layer

In addition to crustal structures, such as sedimentary basins, ground motion is also strongly influenced by shallow material properties, S-velocity in particular, of the regolith in the upper few tens to hundreds of meters below surface. This regolith layer is sometimes called the "geotechnical layer" in the engineering community. When modeling ground motion at a target site at high frequencies (> 0.5 Hz), the crustal structure model may need to be supplemented with a velocity model for the geotechnical layer at target sites. A standard approach for mapping seismic site conditions is measuring V_s^{30}, which is the average S-velocity between 0 and 30-meter depth. Many of the ground-motion prediction equations (GMPE) used in EEW systems are calibrated against site conditions described using V_s^{30} values. Maps of seismic site conditions at a regional scale are not always available due to the fact that it takes a significant amount of resources to gather the geological and geotechnical data needed to estimate the site conditions. For some seismically active urban areas, such as areas in California, site conditions can be estimated based on geologic information (e.g., Wills and Clahan, 2006). For other areas, site conditions can be estimated from topographic elevation data (Wald and Allen, 2007).

The geotechnical layer is actually part of the "critical zone", a general concept used to define the outermost layer of the solid earth that extends from the deepest reach of the groundwater chemical reactions to the top of the vegetation canopy (Anderson *et al.*, 2007; Brantley *et al.*, 2007). It is a highly dynamic

layer that hosts a wide variety of physical, chemical, hydrological and biological processes. These processes and the interactions among them create and transform the environment that sustains agriculture and most terrestrial life. In the past few years, we have started to apply F3DT to image the critical zone and have obtained very promising results.

Our initial experiments were conducted in the Blair-Wallis Watershed (BWW) in Laramie Range, Wyoming (Fig. 3.6). Seismic refraction data along all the lines shown in Figure 3.6 were acquired using 4–6 interconnected 24-channel Geometrics Geode systems and 40 Hz vertical-component geophones spaced at 1 m (for lines passing boreholes) and 2.5 m (for other lines). A 12-pound steel sledgehammer produced the seismic source by striking a 20-cm-long, 20-cm-wide and 2-cm thick stainless steel plate on the ground. Shot spacing was 10 m. When recording, eight shots were summed at each shot location to reduce uncorrelated noise and increase SNR. A straightened tape was used to ensure that all the geophones were in-line. Topographic relief along the lines was measured using a tape measure and inclinometer. The estimated accuracy of the surveyed positions was within ± 0.2 m, which is sufficiently accurate for F3DT and other geophysical imaging techniques.

Over the last two summers, we have deployed 400 vertical component seismic 10 Hz Zland nodes nine times in 200 by 200 meter sized squares. Each deployment recorded the ambient wavefield at a 500 Hz sampling rate for 3–4 days. Three different critical zone environments are sampled by the three array deployments in each of these critical zone study sites: the southern Sierra batholith, the Laramie Range (Fig. 3.7), and the Medicine Bow Mountains. The total size of these seismic recordings is 2.7 Tb and currently resides on our disk storage.

We use the seismic refraction data from Line 17 (Fig. 3.6) as an example. Our V_{p} starting model (Fig. 3.8a) was constructed using first-arrival ray-theoretic travel-time tomography (RTT). The observed travel-time was picked manually. The velocity inversion grid comprised 241×181 grid points covering the 240 m $\times$ 90 m modeling region with horizontal and vertical grid spacing of 1 m and 0.5 m, respectively. We used the ray bending implementation of Koulakov *et al.* (2010). The misfits between model-predicted and observed first-arrival travel-time were minimized using the LSQR algorithm (Paige and Saunders, 1982). After 10 iterations, the RMS travel-time misfit reduced to about 1.6 milliseconds. In our preliminary F3DT inversion, our V_{s} starting model was obtained by scaling our V_{p} starting model using a constant factor.

In our preliminary study, we have adopted the discontinuous Galerkin method as our wave-equation solver. For our preliminary F3DT inversion of Line 17, we constructed a 3D tetrahedral mesh with element sizes adapting to both spatial variations of seismic velocities and also the desired resolution (Fig. 3.9). The 2D starting model obtained from refraction tomography (Fig. 3.8a) was extended in the other horizontal dimension and interpolated onto our 3D tetrahedral mesh.

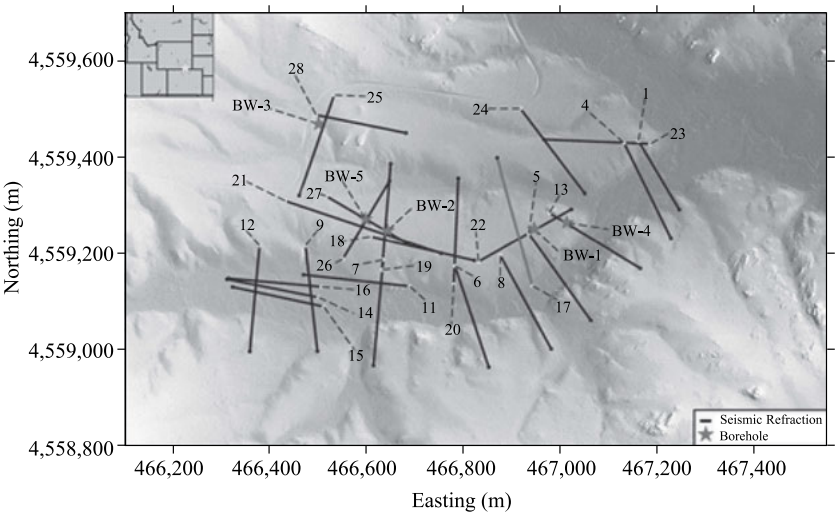

Fig. 3.6 Geophysical survey lines across the Blair-Wallis Watershed in Laramie Range, Wyoming. Black lines: survey lines with both seismic refraction and electrical resistivity data; gray line: Line 17 used in our preliminary F3DT inversion; gray stars: locations of borehole data. Background gray-scale shows local topography.

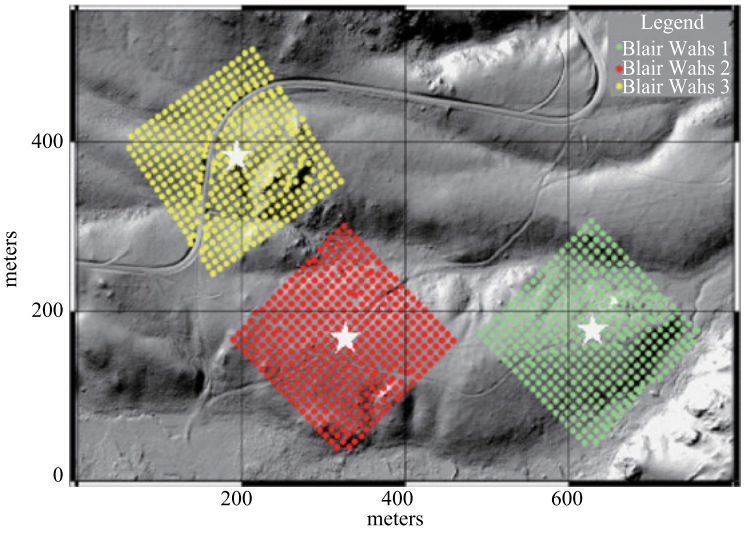

Fig. 3.7 The three arrays deployed in the Blair-Wallis Watershed during the summer of 2015. Green, red, and yellow dots show locations of the Blair Wallis 1, 2, and 3 nodal arrays, respectively. Stars indicate the locations of borehole wells, of which the three arrays were centered for ground truthing. Each array is roughly 200 m by 200 m. Each receiver recorded the ambient-noise field continuously for 3–4 days.

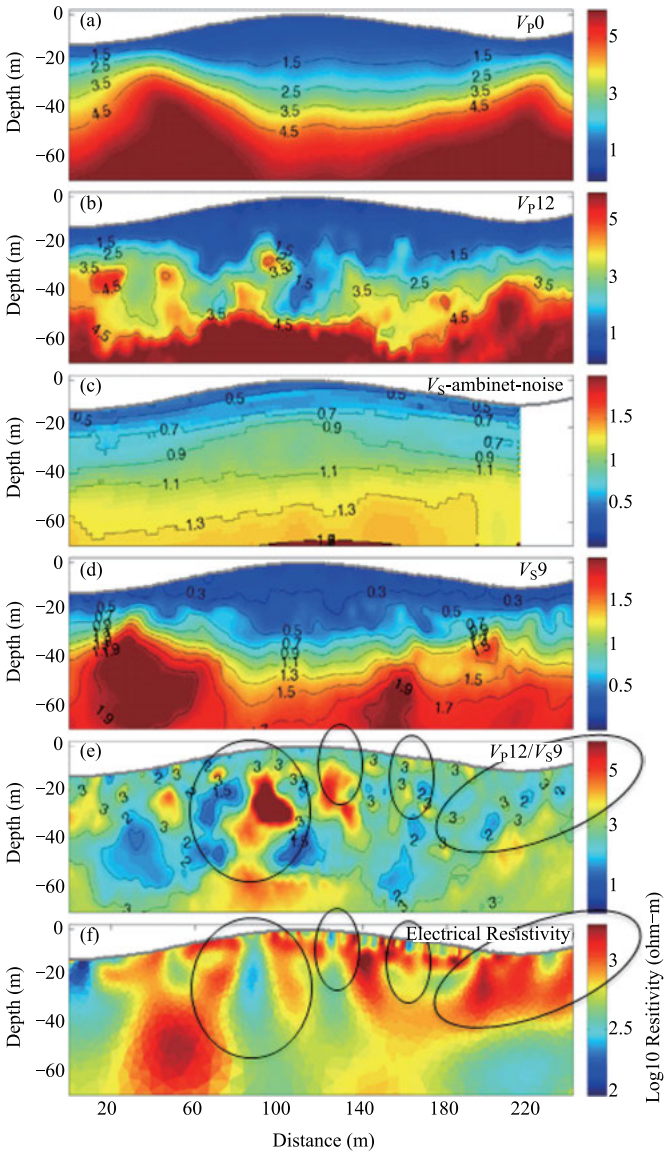

Fig. 3.8 Seismic velocity and electrical resistivity models for Line 17 (Fig. 6). **(a)** V_P model from first-arrival RTT; **(b)** V_P model from our preliminary F3DT using P/P-coda waves after 12 iterations; **(c)** V_s model from ambient noise simple-imaging; **(d)** V_s model from our F3DT using surface waves after 9 iterations; **(e)** V_P/V_s ratio model computed from (b) and (d); **(f)** electrical resistivity model. Black circles on (e) and (f) indicate major structural features that are anti-correlated (*see* text). For seismic velocity models, cool colors represent lower velocity values and warm colors represent higher velocity values, which is different from the convention used in large-scale seismic tomography but consistent with past critical-zone seismic tomography studies. For the electrical resistivity image, cool colors represent low resistivity and warm colors represent high resistivity and color scale is in log10.

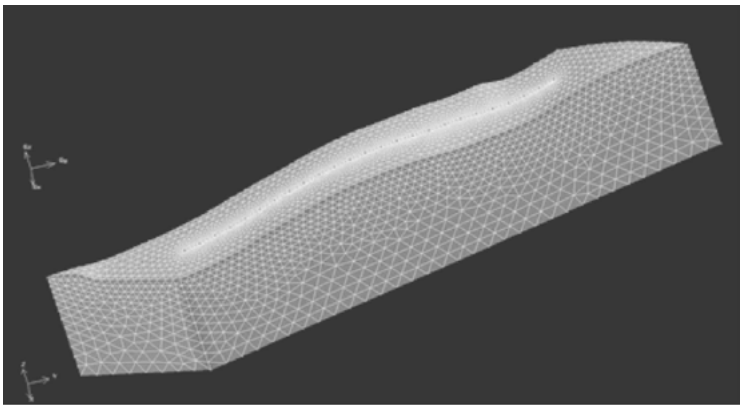

Fig. 3.9 A perspective view of the tetrahedral mesh used in our DG simulations. The top surface of the mesh conforms to local topography derived from DEM data. Locations of the seismic shots and geophones are indicated using black dots and gray dots, respectively. Element size increases gradually with both depth and the distance from the survey line.

The seismic velocities at shallower depths are much lower than those at larger depths (Fig. 8a–d) and the wavelengths at shallower depths are therefore much shorter. So at shallower depths, we used tetrahedral elements with much smaller sizes (∼0.75 m at the ground surface) than those at larger depths (∼10 m at about 150 m depth) (Fig. 3.9). To improve the resolution of the seismic velocity model just below the refraction survey line, the tetrahedral mesh was further refined on and around the vertical plane containing the survey line. As the seismic velocity model was updated from iteration to iteration, the tetrahedral mesh can be updated accordingly to adapt to the changing velocity model. If any sharp geological interfaces, e.g., the sharp boundary at the base of the weathering interface (Fig. 3.8b), spontaneously emerge during the iterative F3DT inversion, the tetrahedral mesh can be easily modified to adapt to such changes in the structure model.

Our waveform misfit quantification technique can be applied to any segment of the seismogram. Figure 3.10 shows an example of a surface wave from Line 17. For this particular example, the Rayleigh wave on the synthetic and observed seismograms can be isolated in the time domain through windowing operations using a cosine-taper window. The frequency-dependent phase and amplitude differences can be represented as weighted summations of B-spline functions and the optimal weights can be found by minimizing the energy of waveform differences in the time domain using the Levenberg-Marquardt algorithm. Figure 3.10d shows the frequency-normalized optimized phase difference as a function of frequency, which is called the “frequency-dependent phase-delay time” and can be roughly considered as frequency-dependent “travel-time” differences between

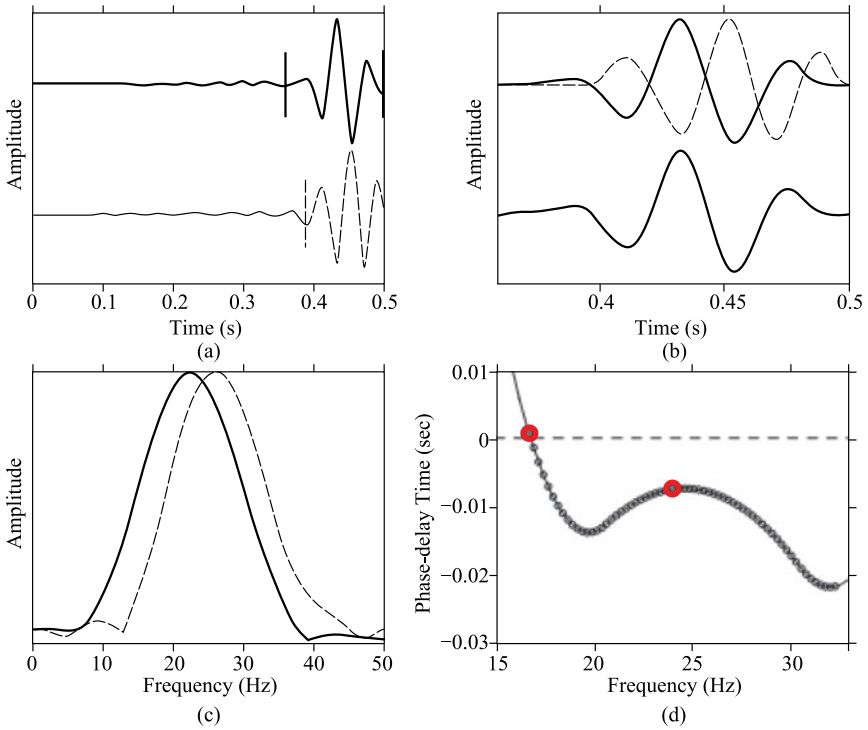

Fig. 3.10 **(a)** Observed (solid line) and synthetic (dashed) seismograms; **(b)** The top traces show the observed waveform (solid line) and the synthetic waveform (dashed); the bottom traces show the perfect fit between the observed and synthetic waveforms after correcting the synthetic waveform with the frequency-dependent phase and amplitude misfit measurements; **(c)** The amplitude spectrums of the observed (solid line) and synthetic (dashed) waveforms; **(d)** Frequency-dependent phase-delay time misfits between observed and synthetic waveforms. Kernels for the two black dots are shown in Figure 3.12.

the windowed synthetic and observed waveforms. In our preliminary F3DT inversion, this technique was applied on a hand-selected waveform subset mainly composed of P/P-coda waves (i.e., each time window is around the first-break on a seismogram) and surface waves (i.e., each time window is around the wave with the largest amplitude on a seismogram). And the frequency-dependent phase-delay time measurements were used to compute the perturbations (corrections) to the seismic velocity models.

Examples of the adjoint kernels for frequency-dependent phase-delay time measured on P/P-coda waves and surface waves used in our preliminary F3DT inversion are shown in Figure 3.11 and Figure 3.12. We have examined many kernels computed in our preliminary F3DT inversion and in the following we summarize major features of those kernels, which are also consistent with what

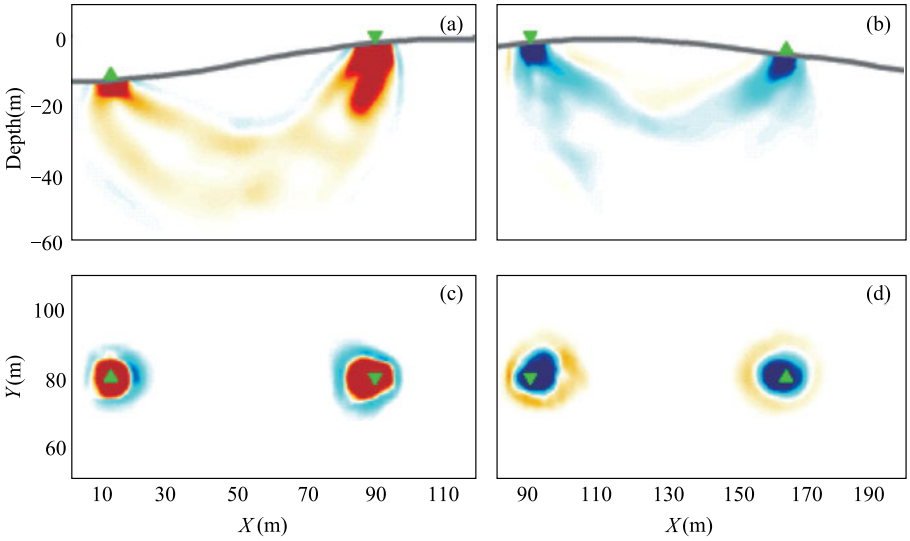

Fig. 3.11 Example adjoint kernels for P/P-coda waves for two source-receiver paths on opposite sides of the ridge top. **(a)**, **(b)**: cross-section views perpendicular to the vertical plane containing the source and receiver; **(c)**, **(d)**: map views at 15 m depth below the topography. Warm and cool colors are negative and positive perturbation to P-velocity. Green reverse triangle: source location; green triangle: receiver location; thick gray line: topography. Note that these are misfit-weighted Frechet kernels and the sign of the kernel depends upon the sign of the misfit measurement.

we expect from 3D wave physics. (i) The spatial sampling patterns of P/P-coda wave kernels are highly different from those of surface wave kernels. The cross-section views of P/P-coda kernels show the typical "banana-doughnut" shape with diminishing sensitivities along the ray-paths as discussed in Marquering *et al.* (1999) and Dahlen (2000). (ii) The sensitivities of surface wave kernels are concentrated close to the ground surface. At lower frequencies, the kernel has a wider Fresnel zone and higher sensitivities at larger depths than the kernel at higher frequencies. (iii) These two types of waves are sensitivity to different structure parameters. The kernels for P/P-coda waves show much stronger sensitivities to P-velocity (V_p) than to S-velocity (V_s). In general the sensitivities to V_s (not plotted in Fig. 3.11) is less than one tenth of their sensitivities to V_p. The surface wave kernels show stronger sensitivities to V_s than to V_p in general. (iv) The intensity of the sensitivity kernels is highly variable through space (Fig. 3.11 and Fig. 3.12). For P/P-coda wave kernels, the amplitudes of the sensitivities at source and receiver locations are much larger than those between the source and receiver locations. For surface waves, the kernel intensity decreases rapidly with depth. The intensity of both types of kernels shows significant spatial variations caused by 3D heterogeneities.

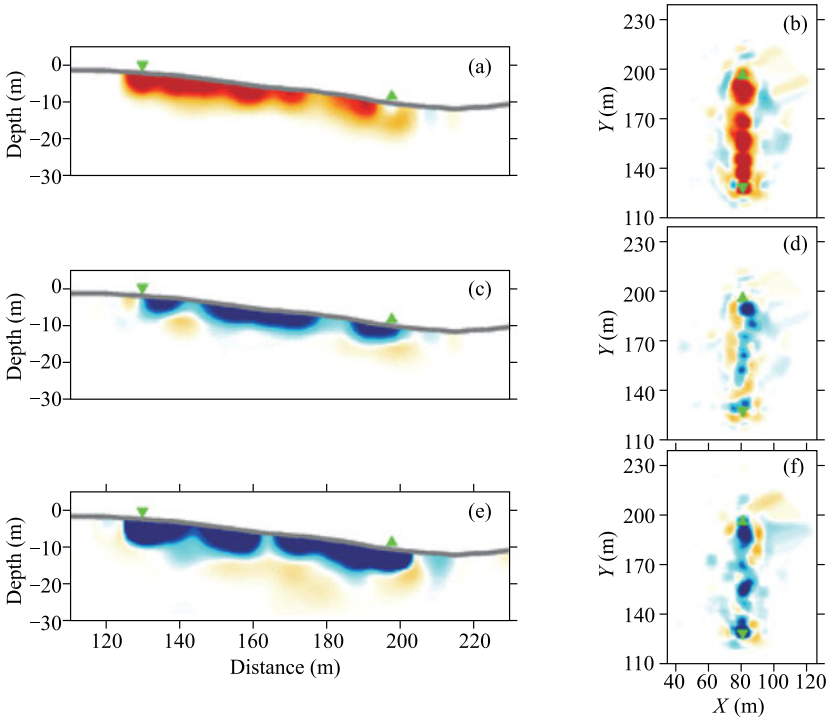

Fig. 3.12 Examples of adjoint kernels for a surface wave along the hill slope. (a), (c), (e): cross-section views perpendicular to the source-receiver plane; (b), (d), (f) map views at 2 m below topography. **(a)**, **(b)** kernel for phase-delay time measured at 16 Hz; **(c)**, **(d)** kernel for phase-delay time measured at 24 Hz; **(e)**, **(f)** misfit-weighted summation of adjoint kernels for phase-delay time measured at multiple frequencies. Warm and cool colors are negative and positive perturbation to S-velocity. Note that these are misfit-weighted Frechet kernels and the sign of the kernel depends upon the sign of the misfit measurement. For the kernel at 16 Hz in (a), (b), the misfit is positive (Fig. 10d) and the kernel is mostly red. For the kernel at 24 Hz in (c), (d), the misfit is negative (Fig. 10d) and the kernel is mostly blue.

At the current stage, we have carried out carried out 12 adjoint iterations using P/P-coda waves and 9 adjoint iterations using surface waves. Our current P- and S-velocity models for Line 17 are shown in Figure 3.8. The velocity images constructed using F3DT (Fig. 3.8b) show many small-scale structural features that do not exist in the image obtained from RTT (Fig. 3.8a). Our image of the V_p/V_s ratio (Fig. 3.8e) shows a truly remarkable anti-correlation (i.e., a high V_p/V_s value corresponds to high saturation and a low resistivity value) with the electrical resistivity image (ERI) (Fig. 3.8f), which is highly sensitive to water saturation. (i) There exist two low-resistivity (blue) zones on both sides of the ridge top in the ERI (Fig. 3.8f), which might indicate the existence of two potential water channels. The low-resistivity zone on the left side of the ridge top has even lower resistivity than the one on the right. We observe a

similar pattern in our V_p/V_s image (Fig. 3.8e) and there exist two zones with high V_p/V_s values on both sides of the ridge top at about the same horizontal distances and depths as the two low-resistivity zones in Figure 8f. The high V_p/V_s zone on the left side of the ridge top has higher V_p/V_s value than the one on the right. (ii) At a larger scale, the high-resistivity zone from horizontal distance of ∼20 m to ∼70 m on the x-axis in Figure 3.8f is anti-correlated with the low V_p/V_s zone at about the same horizontal distance and depth ranges in our V_p/V_s image in Figure 8e. (iii) The high-resistivity zone extending from horizontal distance of ∼140 m to ∼230 m on the x-axis in Figure 3.8f anti-correlates with the low V_p/V_s zone with a similar shape in our V_p/V_s image (Fig. 3.8e).

3.5 Summary and Discussion

In this chapter, we have developed a conceptual outline of an F3DWI-based EEW system and we have justified the feasibility of such a system. Compared with conventional EEW systems based mainly on scaling relations and empirical rules for seismic source parameter and ground motion estimations, the F3DWI-based EEW system has the potential to substantially improve the accuracy of the warning. It replaces scaling relations with a more robust real-time seismic source inversion based on a 3D seismic velocity model. It also replaces mostly empirical ground-motion prediction equations with a more accurate real-time synthetic seismogram generator that incorporates the full physics of elastic wave propagation in a 3D seismic velocity model. Moreover, the 3D seismic velocity model used in the EEW system can be iteratively improved through F3DT as new waveform data become available.

The central component of the F3DWI-based EEW system is the RGTs. Their efficient storage and query are of paramount importance to the feasibility of the F3DWI-based EEW system. Destructive earthquakes tend to occur on existing faults. Rather than store and query the RGTs on all grid points in our modeling volume, we can store the RGTs only on grid points that are located on faults and their proximities. It is therefore highly important to gather accurate information about the fault system, including incipient faults, for a region. The scaling of the seismic source inversion algorithm and the synthetic seismogram generation algorithm is nearly linear, which means the overall computing time needed to obtain a source model and all synthetic seismograms decreases almost linearly with increasing amount of computing resources. Even on today's commodity computing hardware, F3DWI-based EEW system should already be feasible. With the continued development of computing technologies, F3DWI-based EEW may become a routine practice for earthquake hazard mitigation.

References

Aki, K. and P.G. Richards (2000). Quantitative Seismology, Theory and Methods, vol. 2. W.H. Freeman and Company, San Francisco.

Allen, R.M. and H. Kanamori (2003). The potential for earthquake early warning in southern California. Science, 300, 786–789.

Allen, R.M., P. Gasparini, O. Kamigaichi, and M. Böse (2009). The status of earthquake early warning around the world: An introductory overview. Seismological Research Letters, 80(5), 682–693.

Behr, Y., J. Clinton, P. Kastli, C. Cauzzi, R. Racine, and M.A. Meier (2015). Anatomy of an earthquake early warning (EEW) alert: Predicting time delays for an end-to-end EEW system. Seismological Research Letters, 86(3), 830–840.

Böse, M., R. Allen, H. Brown, G. Cua, M. Fischer, E. Hauksson, T. Heaton, M. Hellweg, M. Liukis, D. Neuhauser, and P. Maechling (2013). CISN ShakeAlert—An earthquake early warning demonstration system for California. In: Early Warning for Geological Disasters—Scientific Methods and Current Practice, edited by F. Wenzel and J. Zschau, Springer, Berlin, Germany.

Böse, M., E. Hauksson, K. Solanki, H. Kanamori, Y.-M. Wu, and T.H. Heaton (2009). A new trigger criterion for improved real-time performance of onsite earthquake early warning in southern California. Bull. Seismol. Soc. Am., 99(2A), 897–905, doi: 10.1785/0120080034.

Campbell, K.W. and Y. Bozorgnia (2008). NGA ground motion model for the geometric mean horizontal component of PGA, PGV, PGD and 5% damped linear elastic response spectra for periods ranging from 0.01 to 10 s. Earthquake Spectra, 24(1), 139–171.

Chen P. (2011). Full-wave seismic data assimilation: Theoretical background and recent advances. Pure and Applied Geophysics, 168(10), 1527–1552.

Chen, P. and E.-J. Lee (2015). Full-3D Seismic Waveform Inversion—Theory, Software and Practice. Springer.

Chiou, B.S.-J., R.R. Youngs (2008) An NGA model for the average horizontal component of peak ground motion and response spectra. Earthquake Spectra, 24: 173–215.

Cooper, J.D. (1868). Earthquake indicator. San Francisco Bulletin, November 3.

Cua, G.B. and T.H. Heaton (2007). The Virtual Seismologist (VS) method: A Bayesian approach to earthquake early warning. Earthquake Early Warning Systems, 2007, 97–132.

Cua, G.B., M. Fischer, T.H. Heaton, and S. Wiemer (2009). Real-time performance of the Virtual Seismologist earthquake early warning algorithm in southern California. Seismol. Res. Lett., 80(5), 740–747, doi: 10.1785/gssrl.80.5.740.

Cui X., S. Bray, and A.L. Reiss (2010). Functional near infrared spectroscopy (NIRS) signal improvement based on negative correlation between oxygenated and deoxygenated hemoglobin dynamics. Neuroimage, 49, 3039–3046.

Dahlen, F.A., S.H. Huang, and G. Nolet (2000). Frechet kernels for finite-frequency traveltimes—I. Theory. Geophys. J. Int., 141, 157–174.

Day, S.M., D. Roten, and K.B. Olsen (2012). Adjoint analysis of the source and path sensitivites of basin-guided waves. Geophys. J. Int., 189, 1103–1124.

Espinosa-Aranda, J.M., A. Jimenez, G. Ibarrola, F. Alcantar, A. Aguilar, M. Inostroza, and S. Maldonado (1995). Mexico City Seismic Alert System. Seismological Research Letters, 66, 42–52.

Espinosa-Aranda, J.M., A. Cuellar, A. Garcia, G. Ibarrola, R. Islas, S. Maldonado, and F.H. Rodriguez (2009). Evolution of the Mexican Seismic Alert System (SASMEX). Seismological Research Letters, 80(5), 694–706.

Fichtner, A., S. Fishwick, K. Yoshizawa, and B.L.N. Kennett (2012). Optimal spherical spline filters for the analysis and comparison of regional-scale tomographic models. Physics of the Earth and Planetary Interiors, 190–191, 44–50.

Frankel, A.D., E.H. Field, M.D. Petersen, *et al.* (2002) Documentation for the 2002 update of the national seismic hazard maps. U.S. Geological Survey Open-File Report.

Gasparini, P., G. Manfredi, J. Zschau (2007) Earthquake early warning systems. Springer, Berlin.

Gilbert, H. (2012). Crustal structure and signatures of recent tectonism as influenced by ancient terranes in the western United States. Geosphere, 8, doi: 10.1130/GES00720.1.

Graves, R.W. (1996). Simulating seismic wave propagation in elastic media using staggered-grid finite differences. Bull. Seis. Soc. Am., 86, 1091–1106.

Graves R.W., A. Pitarka, and P.G. Somerville (1998). Ground-motion amplification in the Santa Monica area: Effects of shallow basin-edge structure. Bull. Seismol. Soc. Am., 88: 1224–1242.

Graves, R., T. Jordan, S. Callaghan, E. Deelman (2010) CyberShake: A physics-based seismic hazard model for Southern California. Pure Appl Geophys, 168, 367–381.

Hauksson, E. (2000). Crustal structure and seismicity distribution adjacent to the Pacific and North America plate boundary in southern California. J. Geophys. Res., 105, 13,875–13,903.

Hauksson, E., P. Small, K. Hafner, R. Busby, R. Clayton, J. Goltz, T. Heaton, K. Hutton, H. Kanamori, and J. Polet (2001). Southern California seismic network: Caltech/USGS element of TriNet 1997–2001. Seismological Research Letters, 72(6), 690–704.

Kamigaichi, O., M. Saito, K. Doi, T. Matsumori, S. Tsukada, K. Takeda, T. Shimoyama, K. Nakamura, M. Kiyomoto, and Y. Watanabe (2009). Earthquake early warning in Japan: Warning the general public and future prospects. Seismological Research Letters, 80(5), 717–726.

Kanamori, H., Hauksson E., and T. Heaton (1991). TERRAscope and CUBE project at Caltech. EOS, 72(50), 564.

Kanamori, H., E. Hauksson, and T. Heaton (1997). Real-time seismology and earthquake hazard mitigation. Nature, 390, 461–464.

Kanamori, H. (2005). Real-time seismology and earthquake damage mitigation, Annu. Rev. Earth Planet. Sci., 33(1), 195–214, doi: 10.1146/annurev.earth.33.092203.122626.

Käser M. and M. Dumbser (2006). An arbitrary high order discontinuous galerkin method for elastic waves on unstructured meshes I: the two-dimensional isotropic case with external source terms. Geophys. J. Int., 166, 855–877.

Koulakov I, D. Bindi, S. Parolai, H. Grosser, and C. Milkereit (2010). Distribution of seismic velocities and attenuation in the crust beneath the North Anatolian Fault (Turkey) from local earthquake tomography. Bull. Seism. Soc. Am., 100(1): 207–224.

Komatitsch, D. and J. Tromp (2002a). Spectral-element simulations of global seismic wave propagation—I. Validation. Geophys. J. Int., 149, 390–412.

Komatitsch, D. and J. Tromp (2002b). Spectral-element simulations of global seismic wave propagation—II. 3-D models, oceans, rotation, and self-gravitation. Geophys. J. Int., 150, 303–318.

Komatitsch, D., G. Erlebacher, D. Göddeke, and D. Michéa (2010). High-order finite-element seismic wave propagation modeling with MPI on a large GPU cluster. J. Comput. Phys., 229, 7692–7714.

Lee, E., P. Chen, T. Jordan, L. Wang (2011). Rapid full-wave centroid moment tensor (CMT) inversion in a three-dimensional earth structure model for earthquakes in Southern California. Geophysical Journal International, 186, 311–330.

Lee, E.-J., P. Chen, T.H. Jordan, P.B. Macchling, M.A. Denolle, and G.C. Beroza (2014). Full-3D tomography for crustal structure in Southern California based on the scattering-integral and the adjoint-wavefield methods. J. Geophys. Res., 119(8), 6421–6451.

Lin, C.H., H. Kumagai, M. Ando, and T.C. Shin (2010). Detection of landslides and submarine slumps using broadband seismic networks. Geophys. Res. Lett., 37, L22309, doi: 10.1029/2010GL044685.

Liu, Q. and Y.J. Gu (2012). Seismic imaging: From classical to adjoint tomography. Tectonophysics, 566/567, 31–66.

Lutter, W.J., G.S. Fuis, C.H. Thurber, and J.M. Murphy (1999). Tomographic images of the upper crust from the Los Angeles Basin to the Mojave Desert, California: Results from the Los Angeles region seismic experiment. J. Geophys. Res., 104, B11, 25,543–25,565.

Lutter, W.J., G.S. Fuis, T. Ryberg, D. Okaya, R.W. Clayton, P.M. Davis, C.Prodehl, J.M. Murphy, V.E. Langenheim, M.L. Benthien, N.J. Godfrey, N.I. Christensen, K. Thygesen, C.H. Thurber G. Simila, and G.R. Keller (2004). Upper crustal structure from the Santa Monica Mountains to the Sierra Nevada, Southern California: Tomographic results from the Los Angeles Region Seismic Experiment, Phase II (LARSE II). Bull. Seismol. Soc. Am., 94, 619–632.

Magistrale, H., S. Day, R.W. Clayton, and R. Graves (2000). The SCEC Southern California Reference Three-dimensional Seismic Velocity Model Version 2. Bull. Seismol. Soc. Am., 90, S65–S76.

Marquering, H., F.A. Dahlen, and G. Nolet (1999). Three-dimensional sensitivity kernels for nite-frequency traveltimes: the banana-doughnut paradox. Geophys. J. Int., 137, 805–815.

Mu D., P. Chen, and L. Wang (2013). Accelerating the discontinuous Galerkin method for seismic wave propagation simulations using multiple GPUs with CUDA and MPI. Earthquake Science, 26(6), 377–393.

Nakamura, Y. (1988). On the urgent earthquake detection and alarm system (UrEDAS). In: Proc. Ninth World Conference on Earthquake Engineering, Tokyo-Kyoto, Japan, 2–9 August.

Olsen K.B., S.M. Day, J.B. Minster, Y. Cui, A. Chourasia, M. Faerman, R. Moore, P. Maechling, and T. Jordan (2006). Strong shaking in Los Angeles expected from southern San Andreas earthquake. Geophys Res. Lett., 33: L07305.

Olsen K.B., S.M. Day, J.B. Minster, Y. Cui, A. Chourasia,D. Okaya, P. Maechling, and T. Jordan (2008). TeraShake2: Simulation of $M_{\rm w}$7.7 earthquakes on the southern San Andreas fault with spontaneous rupture description. Bull. Seismol. Soc. Am., 98(3): 1162–1185.

Paige, C.C. and M.A. Saunders (1982). LSQR: An algorithm for sparse linear equations and sparse least squares. ACM Trans. Math. Softw., 8(1), 43–71.

Petersen, M.D., A.D. Frankel, S.C. Harmsen, *et al.* (2008) Documentation for the 2008 update of the United States national seismic hazard maps. U.S. Geological Survey Open-File Report.

Prindle, K. and T. Tanimoto (2006). Teleseismic surface wave study for S-wave velocity structure under an array: Southern California. Geophys. J. Int., 166(2), 601–621.

Satriano, C., L. Elia, C. Martino, M. Lancieri, A. Zollo, and G. Iannaccone (2011). PRESTo, the earthquake early warning system for southern Italy: Concepts, capabilities and future perspectives. Soil Dyn. Earthq. Eng., 31(2), 137–153, doi: 10.1016/j.soildyn.2010.06.008.

Shaw B.E., K. Richards-Dinger, and J.H. Dieterich (2015). Deterministic model of earthquake clustering shows reduced stress drops for nearby aftershocks. Geophys. Res. Lett., 42, 9231, doi: 10.1002/2015GL066082.

Shieh, J. T., Y.-M. Wu, and R. M. Allen (2008). A comparison of tau-c and tau-p-max for magnitude estimation in earthquake early warning. Geophysical Research Letters, 35, L20301.

Suárez, G., D. Novelo, and E. Mansilla (2009). Performance evaluation of the seismic alert system (SAS) in Mexico City: A seismological and a social perspective. Seismological Research Letters, 80(5), 707–714.

Süss, M.P. and J.H. Shaw (2003). P-wave seismic velocity structure derived from sonic logs and industry reection data in the Los Angeles basin. California. J. Geophys. Res., 108, 1–18.

Tape, W. and C. Tape (2012). Angle between principal axes triples. Geophys. J. Int., 191, 813–831.

Tape, C., Q. Liu, A. Maggi, and J. Tromp (2009) Adjoint tomography of the southern California crust. Science, 325, 988–992.

Tape, C., Q. Liu, A. Maggi, and J. Tromp (2010). Seismic tomography of the southern California crust based on spectral-element and adjoint methods. Geophys. J. Int., 180, 433–462.

Wald, D. J. and Allen, T. I. (2007). Topographic slope as a proxy for seismic site conditions and amplification. Bulletin of the Seismological Society of America, 97(5), 1379–1395.

Wald, D.J., Quitoriano, V., Heaton, T.H., Kanamori, H., Scrivner, C.W., and Worden, C.B. (1999). TriNet "ShakeMaps": Rapid generation of peak ground motion and intensity maps for earthquakes in southern California. Earthquake Spectra, 15(3), 537–555.

Wills, C.J. and K.B. Clahan (2006). Developing a map of geologically defined site-condition categories for California. Bulletin of the Seismological Society of America, 96(4A), 1483–1501.

Wu, Y.-M. and H. Kanamori (2005). Experiment on an onsite early warning method for the Taiwan early warning system. Bulletin of the Seismological Society of America, 95, 347–353.

Wu, Y.-M. and H. Kanamori (2008). Development of an earthquake early warning system using real-time strong motion signals. Sensors, 8, 1–9.

Wu, Y.-M. and T.L. Teng (2002). A virtual subnetwork approach to earthquake early warning. Bulletin of the Seismological Society of America, 92(5), 2008–2018.

Wu, Y.-M., H. Kanamori, R. M. Allen, and E. Hauksson (2007). Experiment using the tau-c and Pd method for earthquake early warning in southern California. Geophysical Journal International, 170, 711–717.

Wurman, G., R. M. Allen, and P. Lombard (2007). Toward earthquake early warning in northern California. Journal of Geophysical Research, 112, B08311, doi: 10.1029/2006JB004830.

Yan, Z. and R.W. Clayton (2007). Regional mapping of the crustal structure in southern California from receiver functions. J. Geophys. Res., 112, B05311, doi: 10.1029/2006JB004622.

Zhao, L., P. Chen, and T. Jordan (2006). Strain Green's tensors, reciprocity, and their applications to seismic source and structure studies. Bull. Seism. Soc. Am., 106(6), 2066–2080.

Authors Information

Po Chen, Wei Wang
Department of Geology and Geophysics, University of Wyoming,
Laramie, WY 82071, USA
E-mail: pochengeophysics@gmail.com

En-Jui Lee
Department of Earth Sciences, Cheng Kung University, Taiwan, China

Chapter 4

Comparisons of ETAS Models on Global Tectonic Zones with Computing Implementation

Annie Chu

Branching point process models such as the ETAS (Epidemic-Type Aftershock Sequence) models are often used in modeling seismic catalogs to predict future seismicity. Different features have been revealed by data analysis using ETAS models on five global tectonic zones. In this chapter, global analysis will be expanded by using two types of ETAS models to fit global catalogs of the major tectonic zones. Model (A) implemented in this chapter has a spatial response kernel scaled by the magnitude of the triggering earthquake and Model (B) is non-scaled. This chapter investigates the differences between the two models in computation and seismic interpretation across the tectonic zones. An EM-type algorithm is implemented for model fitting. Although both models are commonly used in seismic data analysis, computationally Model (A) almost always takes less computing time and iterations to reach convergence of model parameter estimation, and has a better chance for the parameters to converge to maximum likelihood estimates (MLEs). Model (B) fits some seismic regions better than Model (A), such as Japan Honshu region, but computing time may be sacrificed for large catalogs. While their difference in computing may appear negligible for smaller datasets or regions that are easier to converge, Models (A) and (B) show a pronounced difference in computing time for large datasets. Catalogs from long and narrow geographical regions are harder to attain convergence for MLEs when Model (B) is used. In order to compare the two models in goodness-of-fit, the Akaike's Information Criterion and Information Gain are used. Computation is emphasized with details throughout the chapter.

https://doi.org/10.1515/9783110560329-146

Key words: Branching point processes, earthquake forecasting, epidemic type aftershock sequence model, global seismicity, space-time point process models, maximum likelihood estimation, EM algorithm, Java programming.

4.1 Introduction

Researchers have recently defined global tectonic zones according to geophysical characteristics such as crust types and relative plate velocities using plate boundary models (Bird, 2003; Bird and Kagan, 2004; Kagan *et al.*, 2010). Chu *et al.* (2011) have fitted the five global tectonic zones based on the plate boundary model of Bird (2003) using Ogata's model (2.4) (Ogata, 1998) and have discovered differences of tectonic zones in their background seismicity rates, triggering behaviors and seismicity patterns such as rate of swarming, implicated by model parameters. This chapter take a further step to include Ogata's (2.3) (1998), another commonly employed seismic model. In this chapter, Ogata's models (2.3) and (2.4) are called Models (A) and (B), respectively. While Model (B) fits better for some regions like Japan Honshu (Ogata, 1998), Model (A) fits better in some other regions like Southern California. We use the zone partition of Chu *et al.* (2011) and apply model fitting to global tectonic zones with the two models. The two models are compared in aspect of their computation and goodness-of-fit.

In computation aspect, the EM-type (Expectation-Maximization) algorithm introduced by Dempster *et al.*, (1977) is used. Veen and Schoenberg (2008) proposed EM-type algorithms to find MLEs of ETAS model parameters, and one of the algorithms is implemented by using Java programming for model fitting in this chapter. The EM scheme is widely used in algorithm computing and optimization. It is more robust comparing to Newton-Raphson type procedures (Veen, 2006; Veen and Schoenberg, 2008). Since EM-type algorithms do not guarantee a global extremum solution, the program includes a remedial step to find global extremum solution within a reasonable range of seismic parameters. While computation with all parameter values varying does not guarantee convergence, especially for very small dataset or extremely long and narrow regions, this remedial solution fixes one parameter's value and uses an alternative procedure to find the other parameters' MLEs.

This chapter is organized as follows. Tectonic zones of Bird (2003) are briefly described in Section 4.2 for zone descriptions. In Section 4.2, we also describe the earthquake catalogs analyzed in this study. In Section 4.3, two models of Ogata (1998) are presented. Section 4.4 provides the computational methods of EM-type algorithm of Veen and Schoenberg (2008) with mathematical details

given. In Section 4.5, we provide the computation results of catalogs of various time windows and compare them. Moreover, methods and results of goodness-of-fit are presented in this section. Section 4.6 gives a conclusion with discussions on possible future work to extend global seismic analysis.

4.2 Seismic Data and Tectonic Zones with Computation Aspects

Bird (2003) categorized the globe into five zones. Each zone is a collection of complex polygons on the Earth's surface whose locations and sizes are based on the PB2002 plate boundary set of Bird (2003) and the plate-boundary seismicity study of Bird and Kagan (2004), respectively. The Appendix in Kagan *et al.* (2010) provides the details on the zones' partition rules. The descriptions of the four major zones are summarized in Chu *et al.* (2011) and given below.

1. Active continent (including continental parts of all orogens of PB2002, plus continental plate boundaries of PB2002).
2. Slow-spreading ridges (oceanic crust, spreading rate $<$40 mm/y, including transforms).
3. Fast-spreading ridges (oceanic crust, spreading rate $\geqslant$40 mm/y, including transforms).
4. Trench (including incipient subduction, and earthquakes in outer rise or upper plate).

The zones are not divided based on the depths of the earthquakes because these depths are not very accurately recorded in global catalogs. Figure 4.1a displays the zones with world map. All regions that are not part of these four zones are grouped into zone 0.

The zone data are from http://bemlar.ism.ac.jp/wiki/index.php/Bird's_Zones. The data consist of longitude and latitude of a grid on the earth surface. A number 0, 1, 2, 3 or 4 is used to indicate the zone where the grid resides. Each grid is 0.1 degree by 0.1 degree in area (approximately 111 km$\times$111 km=12,321 km^2). The Java program uses the data with global map data (CIA World DataBank II, https://www.evl.uic.edu/pape/data/WDB/) to plot Figure 4.1a. Table 4.1 provides each zone's area with percentage of area with respect to the entire global area.

The seismic data used in this work are retrieved from the PDE (Preliminary Determination of Epicenters) database of the United States Geological Survey (2008). The time window of events used in this work is from January 1, 2000 to December 31, 2006. Following Bird *et al.* (2002), the data analysis in this article

limits to only shallow events of depth $\leqslant$70 km, and only events with moment magnitude $\geqslant$5.0 are considered. Such catalogs are near completeness due to the moment magnitude's cumulative distribution function (survivor function) being nearly linear on logarithmic scale (Chu *et al.*, 2011). Besides time and magnitude, other variables used in the model are longitude and latitude. Figures 4.1a–4.1f depict the delineations of events in zones 1, 2, 3, 4 and 0, all in time window 2000–2006.

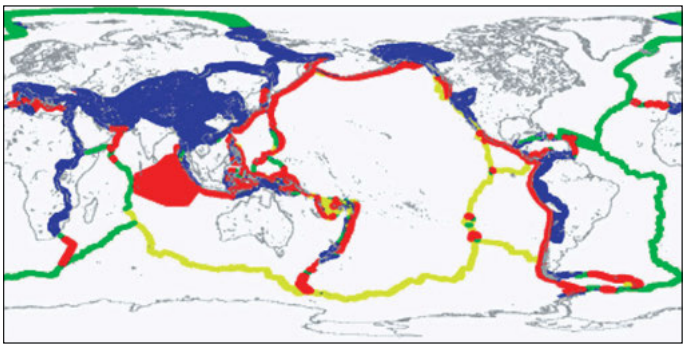

(a)

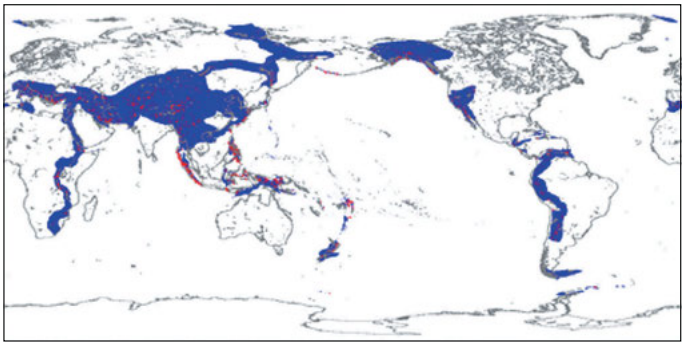

(b)

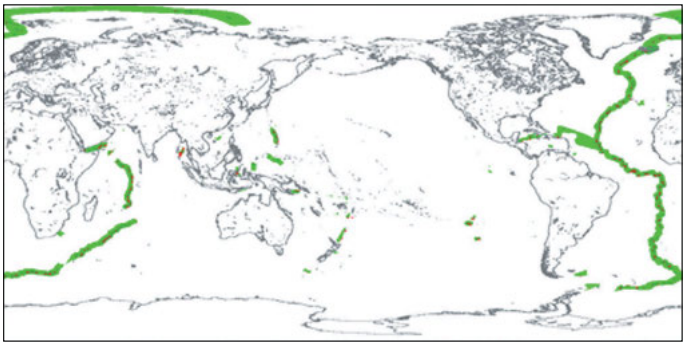

(c)

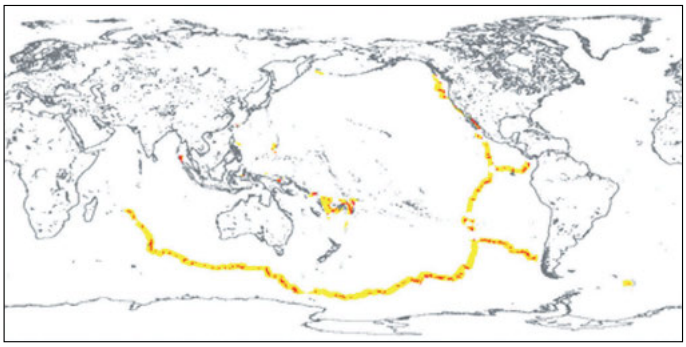

(d)

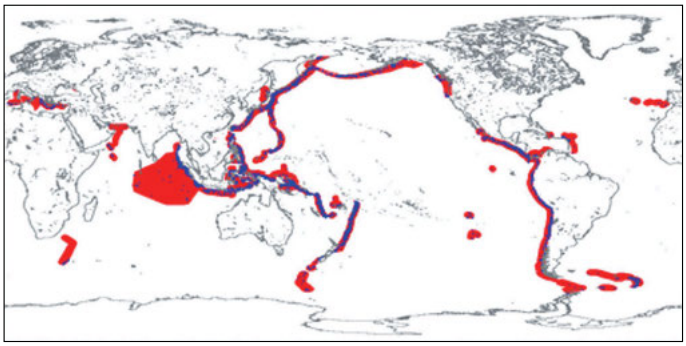

(e)

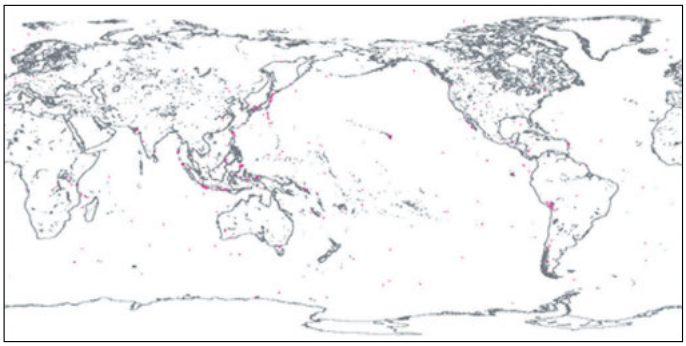

(f)

Fig. 4.1 **(a)** Global Tectonic Zones. Zones 1, 2, 3, 4, and 0 are represented in blue, green, yellow, red, and white, respectively. **(b)** Zone 1's events with depth $\leqslant$70 km and magnitude $\geqslant$5.0. Time window is 2000–2006. Blue regions indicate zone 1. Red points indicate events. **(c)** Zone 2's events with depth $\leqslant$70 km and magnitude $\geqslant$5.0. Time window is 2000–2006. Green regions indicate zone 2. Red points indicate events. **(d)** Zone 3's events with depth $\leqslant$70 km and magnitude $\geqslant$5.0. Time window is 2000–2006. Yellow regions indicate zone 3. Red points indicate events. **(e)** Zone 4's events with depth $\leqslant$70 km and magnitude $\geqslant$5.0. Time window is 2000–2006. Red regions indicate zone 4. Blue points indicate events. **(f)** Zone 0's events with depth $\leqslant$70 km and magnitude $\geqslant$5.0. Time window is 2000–2006. Red points indicate events. Events are not clustered, with no significant pattern comparing with the other zones.

Table 4.1 Number and proportion of each zone in time window 2000–2006 with restrictions of minimum depth 70 km and magnitude cutoff 5.0. Each zone's area is provided by Chu *et al.* (2011). Total area is the entire global surface area.

Zone	Area ($\times 10^7$ km^2)	Proportion of area	Number of events	Percentage of events	Average intensity (Number of events per 10^7 km^2)
1	3.36	6.58%	1444	16.0%	430
2	1.58	3.09%	773	8.53%	489
3	0.844	1.65%	652	7.20%	774
4	1.52	2.98%	5811	64.2%	3823
0	43.8	85.8%	372	4.11%	9
Total	51.0	100%	9119	100%	179

Note that in Chu *et al.* (2011), the time window of 34 years (from January 1, 1973 to December 31, 2006) is used to investigate the zones' seismic nature, but this chapter uses a shorter time window of seven year (from January 1, 2000 to December 31, 2006). This chapter's primary goal is comparison between the two models used in computation and seismicity interpretation. Seven years of seismic data are adequate for this purpose.

As shown in Table 4.2, in the time window 2000–2006, the total number of global events is 9119; zones 1, 2, 3, 4 and 0 have 1444, 773, 652, 5811 and 372 events, respectively. The actual seismicity rate in space (number of events per 10^7 km^2) is given in Table 4.2. It can be seen that zone 4 has the highest seismicity rate with 3823 events per 10^7 km^2 in 2000–2006. Zones 1, 2, 3 and 0 have 430, 489, 774 and 9 events per 10^7 km^2 in 2000–2006, respectively. Since zone 0 has few events, and zone 0 does not generally include seismic active regions, it is excluded from model comparison.

To show comparisons in computing time, the complete data of 2000–2006 are grouped into the following seven groups, with time windows of one through seven years.

(1) 2000–2000: Jan. 1, 2000–Dec. 31, 2000. (1235 global events)
(2) 2000–2001: Jan. 1, 2000–Dec. 31, 2001. (2373 global events)
(3) 2000–2002: Jan. 1, 2000–Dec. 31, 2002. (3466 global events)
(4) 2000–2003: Jan. 1, 2000–Dec. 31, 2003. (4581 global events)
(5) 2000–2004: Jan. 1, 2000–Dec. 31, 2004. (5994 global events)
(6) 2000–2005: Jan. 1, 2000–Dec. 31, 2005. (7575 global events)
(7) 2000–2006: Jan. 1, 2000–Dec. 31, 2006. (9119 global events)

Such time windows are chosen so that most of the catalogs are relatively small and do not cause computing burden. From each of the seven time windows, zones 1, 2, 3, and 4's sub-catalogs are fitted into two models for a comparison in computing time. Table 4.2 shows the size of each sub-catalog.

Table 4.2 Performance comparison (tolerance is 0.01). N denotes catalog size. The number of iterations for a catalog analyzed using Models (A) and (B) is shown in each cell. The figures in parentheses are time taken to find the MLEs, in seconds. If iteration number 1000 is shown, it means the convergence is not completed and may need more iterations, or it may never converge. An alternative grid method is used to find the MLEs. All are run with the same set of initial values.

	1	2	3	4
2000–2000	$N = 172$ A:36(11.71) B:48(14.96)	$N = 99$ A:78(8.68) B:1000(101.31)	$N = 67$ A:29(2.2) B:1000(63.51)	$N = 848$ A:47(277.68) B:57(353.34)
2000–2001	$N = 311$ A:20(17.48) B:27(24.07)	$N = 191$ A:93(36.2) B:1000(314.31)	$N = 146$ A:55(13.34) B:1000(185.51)	$N = 1614$ A:48(1022.87) B:60(1327.77)
2000–2002	$N = 481$ A:25(50.00) B:31(58.05)	$N = 280$ A:89(67.62) B:1000(612.88)	$N = 226$ A:1000(369.45) B:1000(412.49)	$N = 2323$ A:48(2013.29) B:58(2128.96)
2000–2003	$N = 651$ A:33(121.95) B:47(147.59)	$N = 384$ A:63(98.58) B:1000(1152.43)	$N = 304$ A:1000(634.62) B:1000(753.35)	$N = 3046$ A:50(3217.49) B:62(4351.35)
2000–2004	$N = 911$ A:21(148.23) B:30(193.34)	$N = 528$ A:42(107.04) B:57(171.27)	$N = 400$ A:1000(1072.35) B:1000(1298.85)	$N = 3902$ A:47(5957.41) B:59(6171.12)
2000–2005	$N = 1260$ A:25(340.78) B:31(373.21)	$N = 632$ A:40(114.49) B:54(217.19)	$N = 563$ A:1000(2087.95) B:1000(2312.39)	$N = 4799$ A:45(8024.01) B:55(8793.78)
2000–2006	$N = 1444$ A:25(423.41) B:32(498.96)	$N = 773$ A:44(213.34) B:55(239.99)	$N = 719$ A:1000(3888.11) B:1000(3931.51)	$N = 5811$ A:46(10584.13) B:54(13162.17)

4.3 Models

The ETAS model is a type of Hawkes point process model and is also called branching or self-exciting point process. For a temporal Hawkes process with only the time of events considered, the conditional intensity rate at time t, given history information H_t of all events prior to time t, has the form:

$$\lambda(t|H_t) = \mu + \Sigma_{i:t_i<t} g(t - t_i) \tag{4.1}$$

where $\mu > 0$ denotes the background rate. Background rate indicates number of events per unit time. Background events are the events treated as always existing and not being triggered by previous events. $\Sigma_{i:t_i<t} g(t - t_i)$ is the model's triggering part. $g(t - t_i) \geqslant 0$ is the triggering function dictating the aftershock activity rate associated with a prior event with time t_i. In other words, triggered events are those triggered by previous seismic activity. Note that whether

an event is a background event or triggered event is not observed, and the discretion is stochasticly determined by model fitting. Also note that the ETAS model allows assignments where a triggered event has larger magnitude than its parent event. Additionally, $g(u)du < 1$ in order to ensure stationarity (Hawkes, 1971). Models described as (4.1) are called epidemic by Ogata (1988): an earthquake can produce aftershocks like offspring, and the aftershocks produce their aftershocks, and so on.

An example of triggering functions is the time-magnitude ETAS model of Ogata (1988), which has magnitude-dependent triggering function:

$$g(t - t_i; m_i) = \frac{K_0}{(t - t_i + c)^p} \mathrm{e}^{\alpha(m_i - M_0)} \tag{4.2}$$

where α is a parameter describing the influence of magnitude; smaller α indicates more swarm type seismic activity, and larger α indicates pronounced difference between large and small events in activity. $K_0 > 0$ is a normalizing constant governing the expected number of direct aftershocks triggered by earthquake i. m_i denotes the magnitude of earthquake i. Events with magnitude less than the lower cutoff M_0 are excluded in the data analysis. The parameters c and p are related to temporal decay of aftershock activity. c indicates temporal decay in clustering as an event moves further from the mainshock. The term $K_0/(t - t_i + c)^p$ describing the temporal distribution of aftershocks is known as the modified Omori-Utsu law (Utsu *et al.*, 1995).

Ogata (1998) extended the temporal ETAS model (4.1) to describe the space-time-magnitude distribution of earthquake occurrences by introducing circular or elliptical spatial functions into the triggering function; two forms of the conditional rate proposed in Ogata (1998) are presented below. Model (A) is:

$$\lambda(t, x, y|H_t) = \mu + \Sigma_{i:t_i<t} g(t - t_i, x - x_i, y - y_i, m_i) \tag{4.3}$$

where

$$g(t - t_i, x - x_i, y - y_i, m_i) = K_0(t - t_i + c)^{-p} \frac{e^{\alpha(m_i - M_0)}}{[(x - x_i)^2 + (y - y_i)^2 + d]^q} \tag{4.4}$$

Parameters d and q are related to spatial decay of aftershock activity. d indicates the scale of spatial decay in aftershocks generation. Larger d indicates more gradual spatial decay in clustering as an event moves further from the mainshock. The parameter q governs the spatial distribution of aftershocks. Smaller q corresponds to longer range decay while larger q indicates shorter range decay.

Model (B) has the same form of $\lambda(t, x, y|H_t)$ but with a different triggering function:

$$g(t-t_i, x-x_i, y-y_i, m_i) = K_0(t-t_i+c)^{-p} \left[\frac{(x - x_i)^2 + (y - y_i)^2}{e^{\alpha(m_i - m_t)}} + d \right]^{-q} \tag{4.5}$$

In the case of spatially inhomogeneous background rate, μ may be written as $\mu(x, y)$ and treated as a location-dependent function (Ogata, 1998). In this chapter, homogeneous models are considered, and μ is treated as a constant, since our discussion primarily focuses on comparing Models (A) and (B) and the differences are best characterized by triggering behaviors. Moreover, since we use the zone partition of Birds (2003), there is no knowledge supporting further heterogeneous dissection based on the zone partition. Methods and implementation of inhomogeneous models will be discussed further in Section 4.6.

In local catalogs, square of distance is generally calculated by squared epicentral distance in the Cartesian plane: $(x - x_i)^2 + (y - y_i)^2$ as in equations (4.4) and (4.5). For global seismicity the curvature of the Earth surface is considered, and the term is not calculated by $(x - x_i)^2 + (y - y_i)^2$ but replaced with the squared great circle distance between (x, y) and (x_i, y_i). It should also be noted that zone areas are calculated by approximation. While a more accurate method using spherical triangles may be used, the difference between actual area and approximation is negligible for a rectangular area of 0.1 degree by 0.1 degree.

4.4 Methods

The log-likelihood function of the ETAS model is:

$$\log L(\theta) = \Sigma_i \log \lambda(t, x, y|\mathcal{H}_t) - \int_0^T \int_{y_0}^{y_1} \int_{x_0}^{x_1} \lambda(t, x_i, y_i|\mathcal{H}_t) dx dy dt \qquad (4.6)$$

The parameters in the ETAS model may be estimated by maximizing the log-likelihood function, where the true parameter vector $\theta = (\alpha, c, d, K_0, p, q, \mu)$. The MLE estimator defined as in Veen (2006):

$$\widehat{\theta} = \arg\max_\theta L(\theta)$$

is the MLE and would be recorded as the result in computation.

The expectation-maximization (EM) algorithm consists of an expectation step (E-step) where the expectation of the likelihood given the unobserved variables is computed and a maximization step (M-step) where the parameters maximizing the expected likelihood computed in the E-step are found. The above steps are iterated until a certain tolerance is attained. In the EM-type estimation procedure proposed by Veen and Schoenberg (2008), the branching structure dictating which earthquake triggered which aftershocks are the unobserved part and is estimated in each E-step. This view of the ETAS model is called "stochastic reconstruction" by Zhuang *et al.* (2002, 2004).

We use θ to denote the parameter vector, X to denote the observed data, Y to denote the missing data. X consists of the observed data t_i, x_i, y_i and

m_i. The missing part Y contains the information of which events trigger which events. Background events have indicator $u_i = 0$ and triggered events have indicator $u_i \neq 0$. In our study, $L_c(\theta; X, Y)$ is the complete log-likelihood function, respectively, provided in the subsections 4.4.1 and 4.4.2 for models (A) and (B). We first provide generic EM steps:

Input: X and θ^0, the initial value of θ.

E-step: Compute the expectation of the log-likelihood function of Y given the observed data X and current θ^n.

M-step: With X and Y, Find θ^{n+1} as the solution of the complete log-likelihood function $L_c(\theta)$ by MLE.

E-step and M-step are iteratively computed until a tolerance is attained.

4.4.1 Algorithm to Implement Model (A)

In this subsection, we explain the algorithm of Veen and Schoenberg (2008) in details. To start the EM procedure, one determines homogeneous polygons in space that contains the events. If more than one homogeneous polygons are considered, the software has the flexibility to handle multiple homogeneous polygons. For any cell i, $i = 1$ to k, we have:

$$\nu_k = \mu_k \cdot (\text{area of cell } k) \cdot (\text{length of time window})$$

In our zone analysis, only one polygon is considered for each zone.

The complete log-likelihood, by assuming the complete information of what events are background or triggered events, and what events trigger what events, is given by equation (4.7), where n_k is the actual number of background events. For simplicity of notations, we let $\omega = p - 1, \rho = q - 1, T_i = t_i - t_{u_i}, D_i^2 = [(x_i - x_{u_i})^2 + (y_i - y_{u_i})^2]$, and $E_i = \mathrm{e}^{\alpha(m_i - M_0)}$.

$$\begin{aligned} L_c(\theta) = &\sum\nolimits_{k=1}^{K}(-\log n_k - \nu_k + n_k \log \nu_k) + \sum\nolimits_i(-\log L_i! - G_i(\theta) \\ &+L_i \log G(\theta)) + \sum\nolimits_{i:u_i \neq 0}[\log\omega + \omega\log c + \log\rho + \rho\log d - \log\pi \\ &-(1+\omega)\log(T_i + c) - (1+\rho)(D_i^2 + d)] \end{aligned} \tag{4.7}$$

and $G_i(\theta)$ is the expectation of first generation (i.e. directed) aftershocks.

$$\begin{aligned} G_i(\theta) &= \int_0^\infty \int_{-\infty}^\infty \int_{-\infty}^\infty g(t - t_i, x - x_i, y - y_i, m_i)\mathrm{d}x\mathrm{d}y\mathrm{d}t \\ &= \pi K_0 \frac{c^{-\omega}}{\omega}\frac{d^{-\rho}}{\rho}E_i \end{aligned} \tag{4.8}$$

Equation (4.8) is obtained by employing the polar system, with square of distance $r^2 = x^2 + y^2, x = r\cos\theta$, and $y = r\sin\theta$, the spatial part of the integral is

$$I = \int_{-\infty}^{\infty}\int_{-\infty}^{\infty} \frac{1}{(x^2+y^2+d)^{1+\rho}}\mathrm{d}x\mathrm{d}y = 2\pi\int_{0}^{\infty}\int_{0}^{2\pi} \frac{1}{(r^2+d)^{1+\rho}}\mathrm{d}x\mathrm{d}y \quad (4.9)$$

To begin iteration, initial value of the background rate μ is set to be number of events/area/time window, and other parameters are set according to Veen and Schoenberg (2008) by finding the derivative of $L_c(\theta)$ with respect to all parameters. The derivatives are given in equations (4.9)–(4.15). To find extreme values, the derivative of $L_c(\theta)$ would be set to 0.

$$\frac{\partial L_c}{\partial \nu_k} = -1 + \frac{n_k}{\nu_k} = 0 \quad (4.10)$$

$$\frac{\partial L_c}{\partial K_0} = -\frac{1}{K_0}\sum\nolimits_i (G_i(\theta) - L_i) = 0 \quad (4.11)$$

Having $\sum_i(G_i(\theta) - L_i)$, yield an extremum of K_0, we set $\sum_i(G_i(\theta) - L_i) = 0$. This makes the second term of the equations (11) and (12) become 0.

The proceeding two equations are to obtain optimal values of c and ω.

$$\frac{\partial L_c}{\partial c} = \sum\nolimits_{i:u_i\neq 0}\left(\frac{\omega}{c} - \frac{1+\omega}{T_i + c}\right) + \frac{\omega}{c}\sum\nolimits_i (G_i(\theta) - L_i) = 0 \quad (4.12)$$

With $\frac{\partial G_i(\theta)}{\partial \omega} = -\left(\frac{1}{\omega} - \log c\right) G_i(\theta)$, we have

$$\frac{\partial L_c}{\partial \omega} = \sum\nolimits_{i:u_i\neq 0}\left[\frac{1}{\omega} + \log c - \log(T_i + c)\right] + \left(\frac{1}{\omega} - \log c\right)\sum\nolimits_i (G_i(\theta) - L_i) = 0 \quad (4.13)$$

We denote $L = \sum_i G_i(\theta)$ = number of first generation triggered events = $\sum_{i:u_i\neq 0} 1$. With input of initial values of c and ω, we have the following system to be solved iteratively for current c and ω. Current values of c and ω are used to calculate other parameters' current estimates.

$$\begin{cases} \dfrac{\omega}{c(1+\omega)} = \dfrac{1}{L}\displaystyle\sum_{i:u_i\neq 0}\frac{1}{(T_i + c)} \\ \dfrac{1}{\omega} + \log c = \dfrac{1}{L}\displaystyle\sum_{i:u_i\neq 0}\log(T_i + c) \end{cases}$$

Next, we provide the mathematical details to find d and ρ. For optimal values of d and ρ, we set their corresponding derivatives 0. The derivatives are shown in equations (4.13) and (4.14).

Similarly to c and ω, the current values of d and ρ are calculated in each iteration.

$$\frac{\partial L_c}{\partial d} = \sum\nolimits_{i:u_i\neq 0}\left(\frac{\rho}{d} - \frac{1+\rho}{D_i^2 + d}\right) + \frac{\rho}{d}\sum\nolimits_i (G_i(\theta) - L_i) = 0 \quad (4.14)$$

With $\frac{\partial G_i(\theta)}{\partial \rho} = -\left(\frac{1}{\rho} - \log d\right) G_i(\theta)$, we have

$$\frac{\partial L_c}{\partial \rho} = \sum\nolimits_{i:u_i \neq 0} \left[\frac{1}{\rho} + \log d - \log(D_i^2 + d)\right] + \left(\frac{1}{\rho} - \log d\right) \sum\nolimits_i (G_i(\theta) - L_i) = 0 \tag{4.15}$$

With $\sum_i (G_i(\theta) - L_i) = 0$ from equation (4.11), we have the system below to get current values of d and ρ:

$$\begin{cases} \dfrac{\rho}{d(1+\rho)} = \dfrac{1}{L} \displaystyle\sum_{i:u_i \neq 0} \dfrac{1}{(D_i^2 + d)} \\ \dfrac{1}{\rho} + \log d = \dfrac{1}{L} \displaystyle\sum_{i:u_i \neq 0} \log(D_i^2 + d) \end{cases}$$

Finally, we solve derivative equations (4.11) and (4.16) for values of α and K_0. Since only the second term of L_c has α,

$$\frac{\partial L_c}{\partial \alpha} = \sum\nolimits_i (M_0 - m_i)(G_i(\theta) - L_i) \tag{4.16}$$

In each iteration, it is estimated what events are background events and what are triggered to determine u_i, t_{u_i}, x_{u_i} and y_{u_i}. The information is carried to the next iteration.

4.4.2 Algorithm to Implement Model (B)

Model (B)'s computing setup are given below, with its background rate part ν_k and temporal part c and p identical to Model (A)'s computing setup.

The complete log-likelihood, by assuming the complete information of assignments of background and triggered events is given by equation (4.17), where n_k is the actual number of background events. $\omega = p-1, \rho = q-1, T_i = t_i - t_{u_i}, D_i^2 = [(x_i - x_{u_i})^2 + (y_i - y_{u_i})^2]$, and $E_i = \mathrm{e}^{\alpha(m_i - M_0)}$ for simplicity of notations.

$$\begin{aligned} L_c(\theta) = {} & \sum\nolimits_{k=1}^{K} (-\log n_k - \nu_k + n_k \log \nu_k) + \sum\nolimits_i (-\log L_i! - G_i(\theta) + L_i \log G(\theta)) \\ & + \sum\nolimits_{i:u_i \neq 0} \Bigg[\log \omega + \omega \log c + \log \rho + \rho \log d - \log \pi - (1+\omega) \log(T_i + c) \\ & - \alpha(m_i - M_0) - (1+\rho) \log\left(\frac{D_i^2}{E_i} + d\right) \Bigg] \end{aligned} \tag{4.17}$$

$L_c(\theta)$ of Model (B) has its first two terms identical to $L_c(\theta)$ of Model (A). $G_i(\theta)$ is the expectation of directed aftershocks. Model (B)'s $G_i(\theta)$, and calculation of $\frac{\partial L_c}{\partial \nu_k}$, $\frac{\partial L_c}{\partial K_0}\frac{\partial L_c}{\partial c}$, and $\frac{\partial L_c}{\partial \omega}$ is also identical to those of Model (A). For optimal

values of d and ρ, we set their corresponding derivatives 0. The derivatives are expressed in equations (4.18) and (4.19):

$$\frac{\partial L_c}{\partial d} = \sum\nolimits_{i:u_i\neq 0}\left[\frac{\rho}{d} - (1+\rho)\left(\frac{D_i^2}{E_i}+d\right)^{-1}\right] + \frac{\rho}{d}\sum\nolimits_i (G_i(\theta) - L_i) = 0 \tag{4.18}$$

$$\frac{\partial L_c}{\partial \rho} = \sum\nolimits_{i:u_i\neq 0}\left[\log d + \frac{1}{\rho} - \log\left(\frac{D_i^2}{E_i}+d\right)\right] + \left(\frac{1}{\rho} - \log d\right)\sum\nolimits_i (G_i(\theta) - L_i) = 0 \tag{4.19}$$

With $\sum_i (G_i(\theta) - L_i) = 0$ from equation (4.11), we have the system below to obtain current values of d and ρ:

$$\begin{cases} \dfrac{\rho}{d(1+\rho)} = \dfrac{1}{L}\displaystyle\sum_{i:u_i\neq 0}\left(\frac{D_i^2}{E_i}+d\right)^{-1} \\ \dfrac{1}{\rho} + \log d = \dfrac{1}{L}\displaystyle\sum_{i:u_i\neq 0}\log\left(\frac{D_i^2}{E_i}+d\right) \end{cases}$$

Lastly, we solve the derivative equations (4.11) and (4.20) of α and K_0.

$$\frac{\partial L_c}{\partial \alpha} = \sum\nolimits_i (M_0 - m_i)(G_i - L_i) + \sum\nolimits_{i:u_i\neq 0}(M_0 - m_i)\left\{1 - (1+\rho)\frac{D_i^2 E_i}{(D_i^2 E_i + d)}\right\} \tag{4.20}$$

Computation is repeated iteratively to estimate for MLEs of θ.

4.5 Results with a Discussion on Computation Implementation

The computation for catalogs in zones 1 and 4 converges within certain number of iterations. Undoubtedly, smaller catalogs should generally take less computing time. The actual computing time and iterations needed are shown in Table 4.2. Computing is done on a personal computer with 2.40 GHz processor. On a faster computer or a supercomputer, the speed would be faster. Catalogs of such sizes do not have issues of Java program's being out of memory, however, such problems are seen in this computer when catalog size is much bigger (around 10,000) or larger. Supercomputers with larger memory would be able to overcome the problem with computer memory. The increasing trends of time on catalog size of Models (A) and (B) are depicted in Figures 4.2a and 4.2b, respectively. It is seen that the trends appear somewhat exponential than linear.

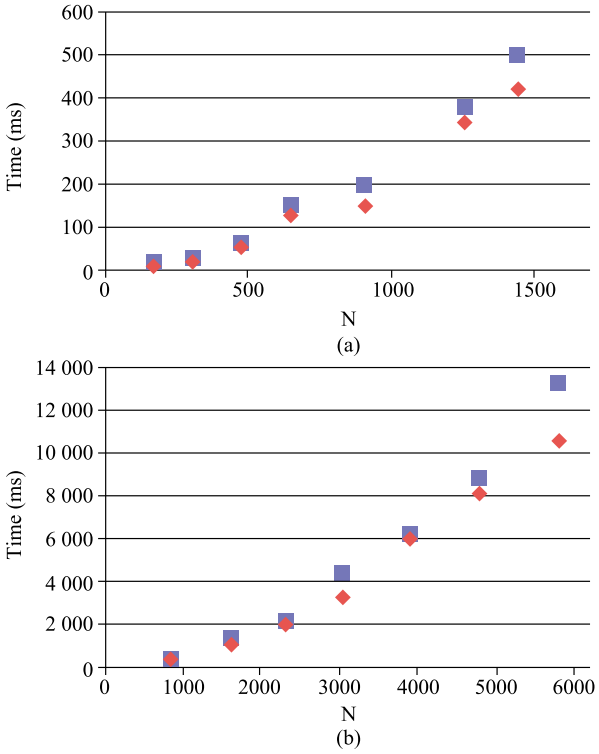

Fig. 4.2 **(a)** Increasing trend of computing time for Zone 1. Square points for model (A); rhombic points for model (B). For both models, the trend does not appear linear but appear somewhat exponential. **(b)** Increasing trend of computing time for Zone 4. Square points for model (A), rhombic points for model (B).

For the case of zone 2, it is seen that for groups 2000–2000, 2000–2001, 2000–2002, and 2000–2003, the number of iterations is indicated with 1000. The program setting uses a number as maximal number of iterations, for example, 1000 for this chapter's computations. If convergence is not achieved within 1000 iterations, the program stops. In groups 2000–2004 and beyond, zone 2's MLEs are obtained within small numbers of iterations. The maximal number of iterations may be reset in the program to another maximal iteration number determined by the user. When the maximal iteration number shows as the program stops, it means convergence is not attained and may need more iterations to achieve it, or it may never converge. In such situation, it is not recommended to run more iterations because convergence is often unlikely to reach due to the nature of the data or the shape of the region.

Despite the EM-type algorithm being relatively stable, optimization surface can be too flat for convergence to be reached (Veen and Schoenberg, 2008). Additionally, it is observed during computing process that long and narrow

regions tend to have non-convergent estimation comparing to regions closer to a circle or square in shape. It is also observed that different catalogs on the same region might have different convergence result; that is, it may converge or not, depending on the actually data. Such computing difficulty appears in both zones 2 and 3, but not in zones 1 and 4. Usually such computing difficulty occurs more often when the catalog size is small, like zone 2's smaller three catalogs, while the difficulty is not always correlated to catalog size. Table 4.2 shows that zone 2's computation eventually converges; but zone 3's computation never converges in any group. Sometimes the problem is solved by increasing the catalog size and changing time length or magnitude threshold. However, this solution may not always be possible. Often, a large size of catalog does not solve the convergence problem.

When such a computing issue occurs, the alternative solution is to fix a parameter by a constant and then estimate other parameters. The Java program fixes the parameter α with a chosen constant and estimates other parameters, and it then fixes another α value and the process iterates. The program does it systematically, using α values on the interval $0 < \alpha \leqslant 2.0$. The computing procedure may be set to use 0.1, 0.2, 0.3, $\cdots$, 2.0; that is, with an increment of 0.1. Once we find the parameter estimates that produce an MLE by checking the log-likelihood, for example, on $0.1 \leqslant \alpha \leqslant 0.2$, the computing procedure may be set to use 0.11, 0.12, 0.13, $\cdots$, 0.19, to find corresponding MLEs for the other parameters. It may be determined by the user on number of accurate digits desired, size of increment, and range of α. Such method is likely drawing "grids" in a seven-dimensional coordinate system with the parameters. The values of α is fixed in the computing procedure to local optimal values of other parameters. This method guarantees MLEs in the range studied, even taking more computing time. In the estimation, α is estimated to the hundredth digit and we have found $\alpha = 0.01$ for Model (A) and 0.18 for Model (B), as shown in Table 4.3, along with MLEs of other zones.

It should be pointed out that zone 4's estimates show two set of values in Table 4.3. Directly running the above-stated EM algorithm without the grid method has encountered being trapped in a local extremum, while using the grid method with increment 0.1 between 0 and 1 has approximately attained global MLE of α. Their parameter estimates and log-likelihood values are recorded in Table 4.3.

Two criteria are applied to compare the models' goodness of fit. The information gain (IG) is defined as (Kagan and Knopoff, 1977; Kagan, 1991):

$$I = \frac{L - L_0}{N}$$

where L is the logarithm of the likelihood for the ETAS model, L_0 is the logarithm of the likelihood for the stationary Poisson process, and N is the catalog size.

Table 4.3 Parameter estimates using the catalog 2000–2006. (A) and (B) are shown, with results of model (B) in Chu *et al.* (2011) that uses time window 1973–2006 for zones 1, 2, 3 and 1999–2006 for zone 4. Note that identical numbers do not mean they are actually identical but due to rounding. Two results of zone 4's using Model (B) is given: (B.1) provides the result of running EM algorithm directly and local MLE is obtained; (B.2) provides the result of running EM with grid method and global MLE is obtained, within the range $0 < \alpha \leqslant 1$.

Zone	Model (A) (2000–2006)	Model (B) (2000–2006)		Model (B) (Chu *et al.*, 2011)
1	$\alpha = 1.11$	$\alpha = 0.809$		$\alpha = 0.980$
	$c = 0.044$	$c = 0.0418$		$c = 0.0781$
	$d = 94.0$	$d = 71.9$		$d = 69.3$
	$K_0 = 0.322$	$K_0 = 0.316$		$K_0 = 0.539$
	$p = 1.25$	$p = 1.25$		$p = 1.19$
	$q = 1.80$	$q = 1.80$		$q = 1.91$
	$\mu = 8.13E-9$	$\mu = 8.11E-9$		$\mu = 7.63E-9$
2	$\alpha = 0.265$	$\alpha = 0.213$		$\alpha = 0.180$
	$c = 0.0156$	$c = 0.0157$		$c = 0.0319$
	$d = 176$	$d = 163$		$d = 227$
	$K_0 = 3.81$	$K_0 = 3.48$		$K_0 = 23.2$
	$p = 1.22$	$p = 1.22$		$p = 1.16$
	$q = 2.16$	$q = 2.14$		$q = 2.33$
	$\mu = 1.24E-8$	$\mu = 1.24E-8$		$\mu = 8.43E-9$
3	$\alpha = 0.01$	$\alpha = 0.18$		$\alpha = 0.324$
	$c = 0.0283$	$c = 0.0284$		$c = 0.0307$
	$d = 398$	$d = 369$		$d = 327$
	$K_0 = 279$	$K_0 = 219$		$K_0 = 77.6$
	$p = 1.23$	$p = 1.23$		$p = 1.15$
	$q = 2.60$	$q = 2.59$		$q = 2.49$
	$\mu = 2.08E-8$	$m = 2.08E-8$		$\mu = 1.56E-8$
4	$\alpha = 0.936$	B.1	B.2	$\alpha = 0.942$
	$c = 0.0419$	$\alpha = 0.535$	$\alpha = 0.80$	$c = 0.0408$
	$d = 208$	$c = 0.0389$	$c = 0.0387$	$d = 141$
	$K_0 = 1.87$	$d = 164$	$d = 147$	$K_0 = 1.33$
	$p = 1.25$	$K_0 = 1.89$	$K_0 = 1.40$	$p = 1.25$
	$q = 1.94$	$p = 1.25$	$p = 1.25$	$q = 1.95$
	$\mu = 6.26E-8$	$q = 1.95$	$q = 1.94$	$\mu = 6.17E-8$
		$\mu = 6.22E-8$	$\mu = 6.28E-8$;	
		$LL = -82169$	$LL = -82097$	

Poisson model assumes homogeneous background rate with no triggering behavior. A bigger IG means a non-Poisson model like Models (A) or (B) to fit the data better. Since the difference between ETAS and the stationary Poisson model is that the former is capable of modeling intense clustering behavior, higher values of IG generally signify increased clustering in the earthquake catalog. According to Table 4.4, Model (A) fits better in zone 1 while Model (B) fits better in zones 2, 3 and 4.

Table 4.4 Comparison of log-likelihoods. In each cell, the first number means actual log-likelihood, and the second number means information gain. Boldface indicates better fit.

Zone	Model (A)	Model (B)	Poisson
1	**−22410, 3.381**	−22423, 3.372	−27292
2	−12940, 2.028	**−12937, 2.031**	−14507
3	−11672, 1.982	**−11671, 1.984**	−13097
4	−82149, 2.579	**−82097, 2.589**	−97140

Table 4.5 Comparison of goodness of fit using AIC (2000–2006). Model (B) on 1073–2006 data is not presented because the sizes of the two global catalogs are different. Smaller AIC indicates better fit and they are emphasized with boldface.

Zone	Model (A)	Model (B)
1	**44834**	44861
2	25894	**25889**
3	23358	**23357**
4	164313	**164207**

Akaike's Information Criterion (AIC) (Akaike, 1974) is a widely used and convenient tool for model comparison. It is applied to compare the models:

$$\text{AIC} = -2\max(\log - \text{likelihood}) + 2(\text{number of adjustd parameters}).$$

Smaller values of AIC indicate better fit and a more desirable model. Table 4.5 shows that Model (A) fits better in zones 1, and model (B) fits better in zones 2, 3 and 4. Despite the more desirable model is chosen using the two criteria, the difference in AIC and IG is not very pronounced, and in some cases, the numbers are almost identical in two models. The goodness-of-fit comparison coincides between the two models.

In computation of model parameter estimates shown in Table 4.3, tolerance 0.01 is used. In each iteration, $\frac{|\text{currentvalue}-\text{previousvalue}|}{\text{previousvalue}}$ is checked to be less than 0.01 for each parameter as the stopping criterion. The tolerance 0.01 may be reset by the user; for example, a smaller number for better accuracy, or a larger tolerance for testing purpose.

Each parameter's estimate is presented in Table 4.5. Comparing Models (A) and (B), we observe that in zone 1, the values are similar between two models for all parameters except d and K_0. This shows that Models (A) and (B) provide very similar estimates for the same catalog. Similar phenomena appear in other zones. The estimates of parameters p, q and μ are less varying. Parameters d and K_0 appear to vary more widely. It should be noted that the variation of K_0 is pronounced due to flatness of the conditional intensity function, and large change in K_0 can correspond to small change in likelihood or models (Veen,

2006). In order to determine whether the estimates are close, we employ standard errors statistically. Wang *et al.* (2010) have fit exponential functions to estimate standard errors for parameters in Model (A). The functions are provided below with x denoting time window length. For time window 2000–2006, x is 7 years and the standard errors are calculated as follow:

$$\widehat{SE}_\alpha = 0.4321x^{-0.7122} + 0.01355 = 0.1216$$
$$\widehat{SE}_c = 0.00001969x^{-0.1759} + 0.000001671 = 1.565 \times 10^{-5}$$
$$\widehat{SE}_d = 2.145x^{-0.7807} + 0.3481 = 0.8176$$
$$\widehat{SE}_{K_0} = 0.002349x^{-0.3538} + 0.00001416 = 0.001194$$
$$\widehat{SE}_p = 0.1188x^{-0.4462} + 0.06351 = 0.1134$$
$$\widehat{SE}_q = 0.2669x^{-1.433} + 0.07212 = 0.08854$$
$$\widehat{SE}_\mu = 0.000006075x^{-0.1314} - 0.0000004229 = 4.281 \times 10^{-6}$$

If the MLEs of Model (A) with 2000–2006 time window are used as the base to compare with other time windows, the 95% confidence intervals (CIs) of the parameter are:

$$95\%CI_\alpha = 1.11 \pm t\widehat{SE}_\alpha = (0.8696, 1.356)$$
$$95\%CI_c = 0.0438 \pm t\widehat{SE}_\alpha = (0.04385, 0.04391)$$
$$95\%CI_d = 94.0 \pm t\widehat{SE}_\alpha = (92.33, 95.60)$$
$$95\%CI_{K_0} = 0.322 \pm t\widehat{SE}_\alpha = (0.3199, 0.3246)$$
$$95\%CI_p = 1.25 \pm t\widehat{SE}_\alpha = (1.024, 1.477)$$
$$95\%CI_q = 1.80 \pm t\widehat{SE}_\alpha = (1.620, 1.974)$$
$$95\%CI_\mu = 8.13 \times 10^{-9} \pm t\widehat{SE}_\alpha = (0, 8.5711 \times 10^{-6})$$

where t is the critical value of Student's t-distribution. $t \approx 2$ is used.

Table 4.6 consists of the parameter estimates of all seven time windows. It is revealed that some parameters have their estimates coincide with 2000–2006, and some parameters do not. For example, the estimates of α, p, and μ in all of the six time windows are within the corresponding 95% confidence interval; and none of the estimates of c, d, K_0 in all of six time windows are within the corresponding 95% confidence interval. Parameters d and K_0 usually fluctuate more in MLEs. Some of q's values are in the corresponding CI, and some are not. This indicates that MLEs may be statistically distinct on the regions with different time windows. Besides making comparison based on a single parameter, we also make comparison by viewing the models as a whole. If Model (A)'s values are used as the base, none of Model (B)'s α, c, d or K_0 is coincident with (A); some d values are coincident and some are not. Model (B)'s p is always in agreement with Model (A)'s p. It is reasonable because the two models share the same time part in the intensity function. Same phenomenon is observed for μ.

Table 4.6 MLEs $(\alpha, c, d, K_0, p, q, \mu)$ of Zone 1 for all seven time windows.

	Model (A)	Model (B)
2000–2000	(0.869, 0.0507, 169, 8.66, 1.30, 2.30, 9.34E-9)	(0.731, 0.0492, 126, 4.54, 1.30, 2.24, 9.35E-9)
2000–2001	(1.034, 0.0462, 121, 0.339, 1.26, 1.86, 8.93E-9)	(0.836, 0.0450, 82.6, 0.251, 1.26, 1.84, 8.98E-9)
2000–2002	(1.062, 0.0253, 142, 0.407, 1.24, 1.88, 8.72E-9)	(0.846, 0.0229, 99.0, 0.316, 1.24, 1.87, 8.73E-9)
2000–2003	(1.20, 0.0327, 164, 1.27, 1.23, 2.04, 8.64E-9)	(0.879, 0.0301, 122, 1.30, 1.23, 2.06, 8.64E-9)
2000–2004	(1.22, 0.0372, 106, 0.221, 1.22, 1.77, 8.36E-9)	(0.884, 0.0347, 77.6, 0.217, 1.25, 1.77, 8.33E-9)
2000–2005	(1.09, 0.0402, 91.9, 0.286, 1.26, 1.78, 8.26E-9)	(0.784, 0.0382, 70.5, 0.285, 1.26, 1.79, 8.23E-9)
2000–2006	(1.11, 0.0438, 94.0, 0.322, 1.25, 1.80, 8.13E-9)	(0.809, 0.0418, 71.9, 0.316, 1.25, 1.80, 8.11E-9)

We conclude that Models (A) and (B) produces coincident p, and μ, but are distinct in other parameters. This is reasonable because the two models share the same background and temporal functions, but different spacial functions. Although the spatially dependent parameters α, d and q have the same geophysical meanings in both models, they are different with regards to modeling and computation. One phenomenon observed is that, using the same model across different time windows, the parameters estimates of c, p, q and μ are comparably similar but estimates of α, d, and K_0 are not.

A question raised is "Do different regions in the same zone have the same model parameters?" To answer this question, analysis is done with Southern California data as an example, in time window January 1,2000 to December 31,2016, and moment magnitude cutoff used is $M_0 \geqslant 3.0$. The catalog size 4377 and the region in a rectangular region with -124 to -111 in longitude, and 30 to 39 in latitude are used. Models (A) and (B) are fit to the data and the MLEs are summarized in Table 4.7. Based on values of IG and AIC, we see that Model (A) fits slightly better than Model (B). In Figure 4.3, we depict the estimated conditional intensity computed using the two models and their difference. In Figures 4.3a and 4.3b, the estimated conditional intensity of Models (A) and (B) appear almost identical, but Figure 4.3c shows that the estimated conditional intensities in two models are indeed different. We also find that the difference in parameter estimates between global and Southern California data is more significant than that between the two models. Regional analysis versus global analysis can indeed have different results. One should be careful not to substitute global parameter estimates for local estimates. Computation of ETAS models is often sensitive regarding datasets used and spatial features. And bias may rise as an issue that is difficult to detect.

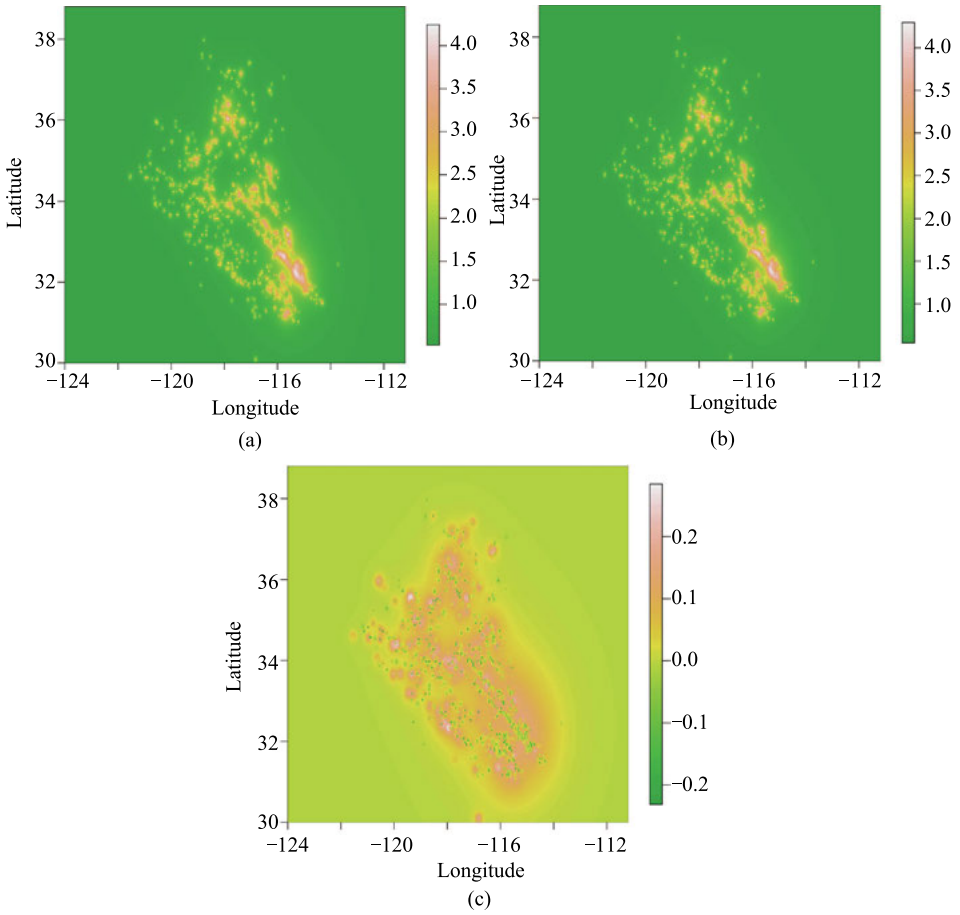

Fig. 4.3 **(a)** shows predicted intensity rate using Model (A); **(b)** shows predicted intensity rate using Model (B); and **(c)** shows difference of predicted intensity rate between the two models.

Table 4.7 MLEs $(\alpha, c, d, K_0, p, q, \mu)$ of Southern California (3500 events in time window from January 1, 2000 to February 20, 2011. $M_0 = 3.0$).

Model (A)	Model (B)
$(\alpha, c, d, K_0, p, q, \mu)$=(0.0816, 0.0232, 1.21E-4, 1.19E-4, 1.20, 1.45, 5.36E-4) IG=6.38 AIC=−2475.7	$(\alpha, c, d, K_0, p, q, \mu)$=(0.44, 0.0219, 8.870E-5, 1.26E-4, 1.20, 1.45, 5.55E-4) IG=6.37 AIC=−2367.16

4.6 Conclusion

This study's result shows that for all global tectonic zones, Model (A) performs somewhat better than Model (B) in computing effort. Model (A) takes less iterations loops than model (B) by very small number; and each loop takes less time in general. The amount of time difference may be due to the computation part of additional coding requirement of Model (B), which may be noticeable for large datasets. Despite the difference in computation time for Model (A) and Model (B) being small and negligible when the catalog size is small, the difference between the two models can be very noticeable when the catalog size is large. Furthermore, it is more likely for Model (B) to run into a "out of memory" problem. In terms of goodness of fit, Model (A) performs slightly better than Model (B) for zone 1 while the situation is reverse for zones 2, 3 and 4: Model (B) performs better. Nevertheless, the difference between the two models is small. The difference between using the same model, model (B) on two different catalogs 2000–2006 and 1973–2006, is yet more noticeable.

This chapter treats the background intensity rate as homogeneous. If one is to implement a heterogeneous background rate model, one may dissect a zone into several subzones and apply homogeneous model to each subzone (Veen, 2006). One may also apply the Delauney tessellation method (Ogata, 2011, 2003), but it might lead a complex for global tectonic zones. In addition, while it is reasonable to assume triggering behaviors to happen between zones, our models do not include it for modeling simplicity. Among all of the models mentioned above, which one fits the global data better is still a question. The issues of heterogeneity and inter-zone triggering are our future work to extend understanding of global seismicity.

It is also found in our computing procedure that the MLE results from long-narrow spatial shapes appear to be more difficult to manipulate than in a region with shapes closer to a circle or square. Would the same data in zone 2 or 3 have different result if the zone's shape is different? How are geographical shapes and MLE related to each other? These questions are not yet answered well, but they are interesting in our future research on this topic.

Acknowledgements

Part of this work was carried out under SCEC/NSF Grant No. 10162 and 129569, and Grant-in-Aid No. 20240027 for Scientific Research (A) from the Ministry of Education, Science, Sports and Culture, Japan. I also thank Dr. Jiancang Zhuang and Dr. Yong-Gang Li for helpful discussions.

References

Akaike, H. (1974). A new look at the statistical model identification. IEEE Transactions on Automatic Control, AC-19, 716–723.

Anonymous (1988). Digital Relief of the Earth, Data Announcement [CD-ROM], 88-MGG-02, Natl. Geophys. Data Cent., Boulder, Colo.

Bird, P. (2003). An updated digital model of plate boundaries. Geochemistry Geophysics Geosystems, 4(3), 1027, doi:10.1029/2001GC000252.

Bird, P. and Y.Y. Kagan (2004). Plate-tectonic analysis of shallow seismicity: Apparent boundary width, beta, corner magnitude, coupled lithosphere thickness, and coupling in seven tectonic settings. Bull. Seismol. Soc. Amer., 94(6), 2380–2399.

Bird, P., Y.Y. Kagan, and D.D. Jackson (2002). Plate tectonics and earthquake potential of spreading ridges and oceanic transform faults. In: Plate Boundary Zones. AGU Geodynamics Series Monograph Volume 20, edited by Stein S. and J. T. Freymueller, 203–218, doi: 10/1029/030GD12.

Chu, A., F.P. Scheoenberg, P. Bird, Jackson, D.D. Jackson, and Y.Y. Kagan (2011). Comparison of ETAS parameter estimates across different global tectonic zones. Bull. Seismol. Soc. Ameri., 101(5), 2323–2339.

Daley, D. and D. Vere-Jones (2003). An Introduction to the Theory of Point Processes, 2nd ed., Springer, New York.

Dempster, A., N. Laird, and D. Rubin (1977). Maximum likelihood from incomplete data via the EM algorithm. Journal of the Royal Statistical Society, Series B, 39(1), 1–38.

Gutenberg, B. and C.-F. Richter (1944). Frequency of earthquake in California. Bull. Seismol. Soc. Amer., 34, 185–188.

Hawkes, A.G. (1971). Point spectra of some mutually exciting point processes. Journal of the Royal Statistical Society, Series B, 33(3), 438–443

Kagan, Y.Y. (1991). Likelihood analysis of earthquake catalogues. Geophys. J. Int., 106(1),135–148.

Kagan, Y.Y., P. Bird, and D.D. Jackson (2010). Earthquake patterns in diverse tectonic zones of the globe. Pure Appl. Geoph., 167(6/7), doi: 10.1007/s00024-010-0075-3.

Kagan, Y., and L. Knopo (1977). Earthquake risk prediction as a stochastic process. Phys. Earth Planet. Inter., 14, 97–108.

Ogata, Y. (1988). Statistical models for earthquake occurrences and residual analysis for point processes. Journal of the American Statistical Association, 83, 9–27.

Ogata, Y. (1998). Space-time point process models for earthquake occurrences. Annals of the Institute of Statistical Mathematics, 50, 379–402.

Ogata, Y. and K. Katsura (1993). Analysis of temporal and spatial heterogeneity of magnitude frequency distribution inferred from earthquake catalogs. Geophys. J. Int., 113,727–738.

Ogata, Y., K. Katsura, and M. Tanemura (2003). Modelling heterogeneous space-time occurrences of earthquakes and its residual analysis. Applied Statistics, 52(4):499–509, 2003.

Ogata Y., and J. Zhuang (2006). Space time ETAS models and an improved extension. Tectonophysics, 413(1-2), 13–23.

Ogata, Y. (2011). Significant improvements of the space-time ETAS model for forecasting of accurate baseline seismicity. Earth Planets Space, 63, 217–229.

Ripley, B.D. (1976). The second-order analysis of stationary point processes. J. Appl. Probab., 13, 255–266.

Southern California Earthquake Data Center (SCEDC) (2016). California Institute of Technology, http://scedc.caltech.edu/.

Schoenberg, F.P. (2003). Multi-dimensional residual analysis of point process models for earthquake occurrences. JASA, 98(464), 789–795.

Schoenberg, F.P., A. Chu, and A. Veen (2010). On the relationship between lower magnitude thresholds and bias in ETAS parameter estimates. J. Geophys. Res., 115, B04309, doi:10.1029/2009JB006387.

U.S. Geological Survey. (2008). Preliminary determination of epicenters (PDE) US Department of the Interior, National Earthquake Information Center, http://neic.usgs.gov/neis/epic/epic global.html.

Utsu, T. (1961). A statistical study on the occurrence of aftershocks. Geoph. Magazine, 30, 521–605.

Utsu, T. (1970). Aftershocks and earthquake statistics (II) — Further investigation of aftershocks and other earthquake sequences based on a new classi_cation of earthquake sequences. J. Fac. Sci. Hokkaido Univ., Ser.VII, 3, 197–266.

Utsu, T., Y. Ogata, and R.S. Matsu'ura (1995). The centenary of the Omori formula for a decay law of aftershock activity. Journal of Physics of the Earth, 43, 1–33.

Veen, A. (2006). Some methods of assessing and estimating point processes models for earthquake occurrences. PhD thesis, University of California, Los Angeles.

Veen, A. and F.P. Schoenberg (2005). Assessing spatial point process models for California earthquakes using weighted K-functions: analysis of California earthquakes. In: Case Studies in Spatial Point Process Models, edited by Baddeley, A., P. Gregori, J. Mateu, R. Stoica, and D. Stoyan (eds.). Springer-Verlag, New York, 293–306.

Veen, A. and F. Schoenberg (2008). Estimation of space-time branching process models in seismology using an EM-type algorithm. Journal of the American Statistical Association, 103(482), 614–624.

Wang, Q., F.P. Schoenberg, and D.D. Jackson (2010). Standard errors of parameter estimates in the ETAS model. Bull. Seismol. Soc. Amer., 100(5A), 1989–2001.

Zhuang, J., Y. Ogata, and D. Vere-Jones (2002). Stochastic declustering of space-time earthquake occurrences. Journal of the American Statistical Association, 97(458), 369–380.

Zhuang, J., Y. Ogata, and D. Vere-Jones (2004). Analyzing earthquake clustering features by using stochastic reconstruction. J. Geophys. Res., 109, B05301.

Zhuang J., Y. Ogata, and D. Vere-Jones (2005). Diagnostic analysis of space-time branching processes for earthquakes. In: Case Studies in Spatial Point Process Models, edited by Baddeley A., Gregori P., Mateu J., Stoica R. and Stoyan D. Springer-Verlag, New York, 275–290.

Author Information

Annie Chu
Department of Mathematics, Woodbury University
7500 N. Glenoaks Boulevard, Burbank CA 91504, USA
E-mail: aannchu@gmail.com

Chapter 5

Distribution of Earthquake-Triggered Landslides across Landscapes: Towards Understanding Erosional Agency and Cascading Hazards

Gen Li, A. Joshua West, Alexander L. Densmore, Zhangdong Jin, Fei Zhang, Jin Wang, and Robert G. Hilton

In mountainous regions, earthquake-triggered landslides are a critical geohazard, a major agent of erosion, and a powerful driver of the carbon cycle. How landslides are distributed across landscapes provides key information for hazard management and for better understanding of orogenic evolution and cycling of carbon. In this chapter, we study the distribution of landslides caused by the 2008 M_w7.9 Wenchuan earthquake at the eastern margin of the Tibetan Plateau in the context of recent advances in understanding landslide spatial patterns. We have previously produced a Wenchuan landslide inventory by mapping landslides from remote sensing images. Combining this landslide inventory map with analysis of digital topography, regional geology, and ground motion data, we explore the controlling factors of the Wenchuan earthquake-triggered landslides. We study the locations of the Wenchuan landslides relative to river networks to evaluate how and to what extent landslides supply sediment to rivers. We examine the hillslope aspects of landslides and discuss how the preferred facing directions reveal information about earthquake source, seismic ground motion, and rupture propagation. We evaluate the distribution of landslides from hillslope tops to bases and discuss the implications for long-term evolution of hillslope morphology. Assuming that the Wenchuan seismogenic fault was a linear energy source, we can successfully model the pattern of Wenchuan landslides by adapting a functional form of the law of seismic wave attenuation which accounts for both geometric spreading and quality decay. In conjunction with models predicting total volumes of earthquake-triggered landslides, this approach has promise

https://doi.org/10.1515/9783110560329-170

for predicting the magnitude and pattern of landslides caused by earthquakes based on known characteristics of the seismogenic faults and the seismotectonic, topographic, and geological setting.

Key words: Wenchuan earthquake, earthquake-triggered landslides, landslide pattern and modeling, erosional agency and cascading hazards, surface landscape, fluvial network, fault characteristics, seismic wave attenuation equation.

5.1 Introduction

5.1.1 Earthquake-Triggered Landslides as Hazards and Erosional Agents

In tectonically active mountain ranges, shallow and large earthquakes can induce widespread landsliding due to strong ground motion and seismic wave propagation (Keefer, 1984; Jibson *et al.*, 1993; Keefer, 1994; Harp and Jibson, 1996; Guzzetti *et al.*, 2009). Earthquake-triggered landslides are a critical seismic hazard, not only causing severe loss of life and immediate damage to infrastructure (Swiss Re, 2000; Petley, 2012), but also leading to prolonged and widespread secondary impacts like channel aggradation and flooding—known as "cascading hazards" (Korup *et al.*, 2004; Glade and Crozier, 2005; Wang *et al.*, 2015). Earthquake-triggered landslides also represent an important erosional agent, converting rocks to clastic sediment and supplying large volumes of erodible materials to rivers (Pearce and Watson, 1986; Keefer *et al.*, 1994; Hovius *et al.*, 1997; Montgomery and Brandon, 2002; Larsen *et al.*, 2010; Howarth *et al.*, 2012; Egholm *et al.*, 2013). Riverine export of landslide materials means mass loss from mountains, which could counteract coseismic rock uplift (Hovius *et al.*, 2011; Parker *et al.*, 2011; Li *et al.*, 2014; Marc *et al.*, 2016a). Over longer timescales of multiple earthquake cycles (10 s of kyr to Myr), earthquake-triggered landslides contribute significantly to the erosional budget at orogenic scales, and are capable of producing erosional fluxes comparable to those measured from cosmogenic nuclides and low-temperature chronometers (Li *et al.*, 2017). Landslides provide the sediment that acts as effective tools shaping stream bedform and landforms as well (Sklar and Dietrich, 2004; Yanites *et al.*, 2010; Egholm *et al.*, 2013). Landslides also work as a powerful driver of the carbon cycle, harvesting organic carbon from vegetation, soil and bedrock (Garwood *et al.*, 1979; Hilton *et al.*, 2011; Wang *et al.*, 2016), as well as creating fresh mineral surface for chemical weathering (Gabet, 2007; Jin *et al.*, 2016; Emberson *et al.*, 2016).

To evaluate the role of earthquake-triggered landslides in hazard generation, erosional dynamics, mountain belt evolution, and the carbon cycle, it is critical

to understand the spatial pattern of landslides. Many studies have focused on empirical observations using landslide inventories mapped from remotely-sensed images, and have explored how landslides are distributed across gradients of topography and seismic shaking, and among different climatic and geologic conditions (Harp and Jibson, 1996; Meunier *et al.*, 2007; Meunier *et al.*, 2008; Gorum *et al.*, 2011; Xu *et al.*, 2014; Li *et al.*, 2016; Huang *et al.*, 2017; Roback *et al.*, 2018). Other studies have focused on modeling the magnitude (e.g., area or volume) and pattern of earthquake-triggered landslides either using an empirical approach (e.g., fitting landslide data using different functions) or a forward approach based on engineering mechanics (e.g., Newmark analysis) or earthquake physics (Keefer, 1994; Jibson *et al.*, 2000; Malamud *et al.*, 2004; Jibson *et al.*, 2006; Gallen *et al.*, 2015; Gallen *et al.*, 2017; Marc *et al.*, 2016b). Most studies have identified a linkage between landslide spatial pattern, seismic shaking, and seismic wave propagation (Harp and Jibson, 1996; Dadson *et al.*, 2004; Meunier *et al.*, 2007; Li *et al.*, 2016). This linkage provides the possibility for using landslide pattern to invert for fault rupture properties and information about energy propagation during earthquakes (e.g., Meunier *et al.*, 2013). Many studies have also shown that hillslope gradient and properties of hillslope material modulate landslide occurrence during earthquakes (Jibson *et al.*, 2006; Gallen *et al.*, 2015; Marc *et al.*, 2016b; Roback *et al.*, 2018; Gallen *et al.*, 2017). Thus, combining landslide pattern, topography, and seismic conditions can help to constrain properties of hillslope materials, such as rock strength (Gallen *et al.*, 2015). Conversely, known seismic conditions, topography, and rock strength can be combined to quickly predict landslide occurrence and produce rapid response landslide hazard maps following large earthquakes (e.g., Kritikos *et al.*, 2015; Gallen *et al.*, 2017; Robinson *et al.*, 2017).

Empirical studies have examined patterns of earthquake-triggered landslides from scales of fault zones to individual hillslopes. At fault zone scales, for most earthquake-triggered landslide inventories, landslide areal density ($P_{Als}\%$, the percentage of area impacted by landsliding per unit landscape area) scales with peak ground accelerations (PGA) and decays away from the epicenter. At hillslope scales, topographic amplifications of seismic shaking modulate how landslides are distributed from hillslope ridges to valley bottoms as well as their preferred facing directions (Meunier *et al.*, 2008). These hillslope-scale landslide patterns are indicative of the dominance of seismic triggers versus climatic triggers (Densmore and Hovius, 2000; Meunier *et al.*, 2008). How landslides are distributed across hillslopes also contributes to the extent to which landslides are connected to fluvial networks, a key factor expected to influence post-earthquake sediment transport (Dadson *et al.*, 2004; Huang and Montgomery, 2014; Li *et al.*, 2016). With this background in mind, this contribution focuses on the spatial patterns of landslides triggered by the 2008 Wenchuan earthquake.

5.1.2 Landslides Triggered by the 2008 Wenchuan Earthquake

On May 12th, 2008, the M_w7.9 Wenchuan earthquake occurred in the Longmen Shan mountain range at the eastern margin of the Tibetan Plateau (Burchfiel *et al.*, 2008; Hubbard and Shaw, 2009). Characterized by an unexpectedly high magnitude and long return time, the Wenchuan earthquake ruptured the Yingxiu-Beichuan and Pengguan faults with a combination of thrust and dextral strike-slip deformation. The earthquake also induced massive landsliding in the steep Longmen Shan mountains, over dramatic gradients of topography, seismic shaking, and climate, and among a variety of lithologic units. Many studies have produced Wenchuan landslide inventory maps and examined patterns of the Wenchuan landslides in the context of regional environmental conditions. Huang and Li (2009) reported preliminary observations of the Wenchuan earthquake-triggered landslides, finding that most landslides were close to the ruptured fault and on the hanging wall. Dai *et al.* (2011) mapped over 56,000 landslides using aerial photos and satellite images, identified major landslide types by combining field observations and interpretation of images, and discussed landslide areal and point density in the context of distance to the fault rupture, elevation, slope, PGA, seismic intensity, and lithology. Gorum *et al.* (2011) mapped ∼60,000 landslides using both pre-earthquake and post-earthquake images, reported landslide areal and point density variations versus distance to fault rupture, co-seismic slip, and lithology, and derived empirical relations to describe the landslide pattern with distance from the fault rupture. Parker *et al.* (2011) mapped $> 70,000$ landslides by combining automated algorithms and a series of topographic filters and visual screening. They estimated the Wenchuan landslide volume using empirical landslide area-volume scaling relations and found that, if landslide debris is evacuated by rivers over the earthquake cycle, the landslide-induced erosion could counteract the rock uplift caused by the Wenchuan earthquake, thus raising an intriguing question of "earthquake mass balance", i.e., whether earthquakes build or destroy mountainous topography. Xu *et al.* (2011) examined the effects of locked fault segments where most co-seismic moment was likely released and the locations of landslides relative to the seismic energy source. They identified a "back slope effect", whereby hillslopes facing the energy source were less susceptible to landsliding in several valleys. Fan *et al.* (2012) systematically studied 828 Wenchuan earthquake-triggered landslide dams, estimated their size distribution and storage capacity, and discussed the implications for the post-earthquake sediment budget. Xu *et al.* (2014) updated the landslide inventory of Dai *et al.* (2011), reported a landslide inventory map with 197,481 landslide polygons, and identified primary controls on the Wenchuan landslides from seismic-related parameters (e.g., PGA and seismic intensity) by adopting a bivariate statistical analysis. Yuan *et al.* (2013) focused on the relation between

the Wenchuan landslide pattern and seismic parameters (PGA and distance to the hypocenter) and fitted the Wenchuan data to a landslide pattern model by assuming a point energy source following the functional form of seismic wave attenuation (Meunier *et al.*, 2007). Li *et al.* (2014) mapped landslides using semi-automated algorithms and manual segregation of amalgamated landslide features, and examined the Wenchuan landslide inventory in the context of a generalized model of earthquake mass balance; following this work, Li *et al.* (2016) combined the landslide inventory map and analysis of digital topography to quantify the connectivity between earthquake-triggered landslides and the regional fluvial network. Gorum and Carranza (2015) explored controls on the patterns of landslides from fault-types and suggested that landslides associated with thrust slip occur over a wider zone, further away from the fault trace, compared to strike-slip deformation. While most studies have focused on the co-seismic landsliding, several studies have also looked into post-seismic landsliding caused by rainfall and reactivation of the co-seismic landslide debris in the Wenchuan epicentral region (e.g., Tang *et al.*, 2011; Zhang *et al.*, 2014).

In this contribution, we review previous studies of earthquake-triggered landslides associated with Wenchuan and other earthquakes, and conduct new analysis to explore how the Wenchuan landslides are distributed across the Longmen Shan range. Specifically, previous Wenchuan studies have not fully considered the effect of the background landscape on the observed characteristics of landslides (Meunier *et al.*, 2008; Huang *et al.*, 2017). For example, if landslides randomly sample a landscape, the topographic characteristics of landslides should reproduce the characteristics of the landscape rather than reveal information about other controlling mechanisms. To correct for such an effect, we normalize the statistical distribution of any metric of interest (e.g., hillslope gradient) of the landslide inventory over the distribution of this metric of the background landscape. Combining the Wenchuan landslide inventory map reported by Li *et al.* (2014) with analysis of digital topography, we identify the preferred elevation, slope and lithologic units where the coseismic landslides were located relative to the background landscape. We investigate the relations between landslides and seismic shaking and model the Wenchuan landslide pattern at orogenic scales by adopting a model of seismic energy release. We estimate the average geometric profiles of hillslopes in the Longmen Shan region, quantify how Wenchuan landslides were located relative to hillslope ridges and river channels, and discuss the implications for landslide triggers and landslide-channel connectivity. We also track the preferred facing directions of landslides along the Yingxiu-Beichuan fault rupture to examine the linkage between landslide aspects and the characteristics of earthquake source, ground motion, and energy propagation.

5.2 Settings

5.2.1 Topography, Hydrology and Climate

With > 5 km of relief over a 50 km horizontal distance from the Sichuan Basin, the Longmen Shan mountains range marks the steepest margin of the Tibetan Plateau (Fig. 5.1) (Densmore *et al.*, 2007; Burchfiel *et al.*, 2008). Landscape relief and steepness peak at the mountain front and gradually decrease westward toward the Tibetan Plateau. Several major tributaries of the Yangtze River, including the Min Jiang, Fu Jiang and Tuo Jiang, drain the Longmen Shan mountains to the Sichuan Basin (Liu-Zeng *et al.*, 2011). The regional climate is dominated by the East Asian monsoon, with over 70% of rainfall occurring during the wet season from June to September. Average annual rainfall is around 1100 mm/yr at the margin and decreases to ∼600 mm/yr toward the plateau (Liu-Zeng *et al.*, 2011 and references therein). The regional climatic pattern is largely controlled by the high, steep mountainous topography which works as a barrier to moisture or causes heating of the atmosphere (Molnar *et al.*, 2010). The orographic rainfall and steep topography lead to intensive denudation of the mountain front, ∼0.3-0.5 mm/yr determined before the Wenchuan earthquake (Liu-Zeng *et al.*, 2011). After the Wenchuan earthquake, the seismically induced landslides supplied large volumes of clastic sediment to the rivers and greatly enhanced local denudation rates as high as 1–1.2 mm/yr integrated over four years following the earthquake (Wang *et al.*, 2015; Li *et al.*, 2017).

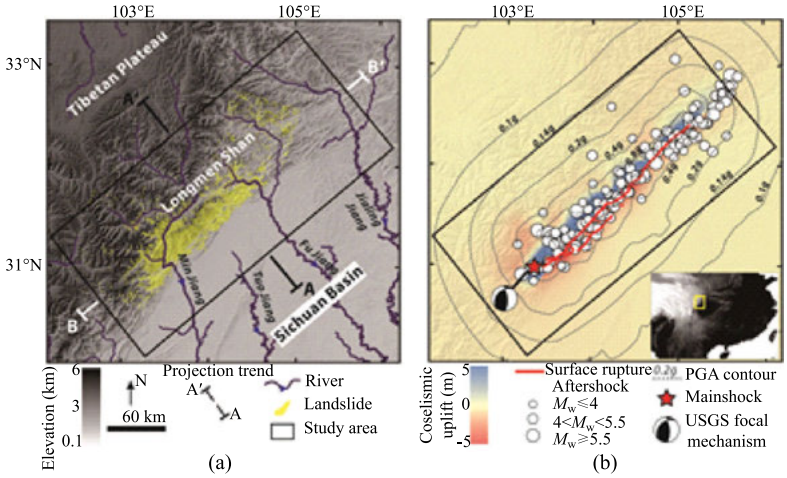

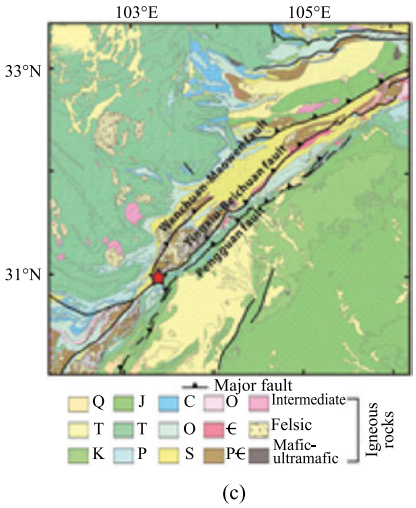

Fig. 5.1 Maps of the topography **(a)**, seismological parameters **(b)** and lithologic units **(c)** of the Longmen Shan range where the Wenchuan earthquake and associated landsliding occurred. In panel (a), A–A' and B–B' are projection trends perpendicular and parallel to the fault strike, respectively, and the rectangular box delineates the study area where topographic metrics are calculated. The inset in panel (b) indicates the geographic location of the study area in the context of East Asia. Panel (c) shows major lithological units and faults of the Longmen Shan range, including Proterozoic (pЄ) basement consisting of granitoids and metamorphic rocks, Paleozoic (Є: Cambrian, O: Ordovician, S: Silurian, D: Devonian, C: Carboniferous, and P: Permian) and Mesozoic (T: Triassic, J: Jurassic, and K: Cretaceous) passive margin and foreland sedimentary sequences, and Cenozoic (Q: Quaternary) sediment, modified from a $1:2,500,000$ geological map (China Geological Survey, 2004).

5.2.2 Geology and Tectonics

The Longmen Shan is underlain by Proterozoic basement granitoid and high-grade metamorphic rocks, a Paleozoic passive margin sediment sequence of metamorphic sediment and granitic intrusion, and a Mesozoic foreland basin sediment sequence consisting of marine and clastic sediment, and limited exposure of Cenozoic sediment (Figure 1; Li *et al.*, 2003; Densmore *et al.*, 2007; Burchfiel *et al.*, 2008). Cenozoic deformation in the Longmen Shan is superimposed on a Mesozoic orogeny (Burchfiel *et al.*, 2008). River profile analysis and low temperature thermochronometry suggest high uplift and exhumation rates (0.5–1 km/Myr), respectively, during the late Cenozoic (Kirby *et al.*, 2003; Kirby *et al.*, 2008; Tian *et al.*, 2013). The high, steep topography of the Longmen Shan range has stimulated heated debates on different geodynamic models of plateau margin mountain building and on the relative importance of ductile lower crustal flow versus brittle faulting in the upper crust (Royden *et al.*, 1997; Clark and Royden,

2000; Tapponnier *et al.*, 2001; Hubbard and Shaw, 2009). The Longmen Shan is bounded by a fault system composed of three major faults: the Wenchuan-Maowen fault, the Yingxiu-Beichuan fault and the Pengguan fault (Chen and Wilson, 1996; Densmore *et al.*, 2007; Liu-Zeng *et al.*, 2009; Xu *et al.*, 2009). The Wenchuan earthquake nucleated in the southern part of the Longmen Shan, rupturing the Yingxiu-Beichuan and Pengguan faults and propagating ∼270 km to the northeast. The co-seismic moment release varied significantly along the fault rupture but was concentrated in the Yingxiu and Beichuan regions (Xu *et al.*, 2009; Shen *et al.*, 2009). Fault displacement was mainly in the form of dextral-thrust slip in the southwestern part of the rupture and changed to dextral strike slip towards the northeast (Liu-Zeng *et al.*, 2009). Paleoseismology and geodetic studies suggest a relatively long return time (500–4000 years) for Wenchuan-like events in the Longmen Shan region (Densmore *et al.*, 2007; Liu-Zeng *et al.*, 2009; Shen *et al.*, 2009; Thompson *et al.*, 2015; Lin *et al.*, 2016).

5.3 Materials and Methodology

We analyzed the Wenchuan earthquake-triggered landslide inventory reported in Li *et al.* (2014) in the context of the digital topography of the Longmen Shan mountains. We used the SRTM 90 digital elevation model (DEM, resolution ∼87 m) from the Consultative Group for International Agricultural Research (CGIAR), with regional void filled using reinterpolation algorithms and other data products including local data and SRTM 30 data (Jarvis *et al.*, 2008). Seismological data, including aftershock sequences and peak ground accelerations, was taken from the USGS Earthquake Hazard program (2008). Analysis of the digital topography and the landslide inventory was conducted in the ArcGIS platform.

Based on our analyses, we consider how the Wenchuan landslides are distributed in directions perpendicular to and parallel to the fault trend, in different topographic and lithologic conditions, and relative to the fluvial network. We evaluate controls from seismic processes on the pattern of the Wenchuan landslides. We examine the relations between landslide areal density and ground motion, whether the Wenchuan landslides can be explained using a simplified model based on seismic energy propagation, and the imprint of a seismic trigger on landsliding at hillslope scales.

5.4 Distribution of Wenchuan Earthquake-Triggered Landslides across the Longmen Shan

In this section, we report the spatial patterns of the Wenchuan earthquake-triggered landslides in directions perpendicular and parallel to the fault trend. We explore the statistical distributions of the topographic and lithologic attributes of the landslides, accounting for the variations of the background topography and non-uniform distribution of lithologic units across the landscape. Finally, we compare different methods for quantifying the locations of the landslides relative to the fluvial network to better constrain how landslides might be expected to influence post-earthquake sediment dynamics.

5.4.1 Variations of Landslide Pattern Perpendicular to the Fault Trend

We plot total landslide areas in 5 km-wide increments paralle and perpendicular to the Longmenshan fault trend (Fig. 5.2). Because both seismic shaking and topography show greatest gradients perpendicular to the fault trend (Figs. 5.1a and 5.1b), we would expect that plotting landslide data along this trend would capture the most significant variations of landslide occurrence. Indeed, perpendicular to the fault trend, we observe the highest amount of landslide area at the Longmen Shan mountain front, on the hanging wall and coinciding with the location of the epicenter. Landslide area decays sharply towards the Sichuan Basin and the Tibetan Plateau (Fig. 5.2a). This variation normal to the fault trend is quite similar to other cases, including the 1993 M_{w}6.9/6.7 Finisterre, the 1994 M_{w}6.7 Northridge, and the 1999 M_{w}7.6 Chi-Chi earthquakes, with landslides clustering at mountain fronts and decaying towards both the foreland and hinterland (Meunier *et al.*, 2007). This is expected because fault-bounded mountain fronts generally have steeper topographic gradients and experience most intensive shaking, whereas the foreland and hinterland are characterized by gentler topographic gradients and lower seismic activity (Meunier *et al.*, 2007; Gallen *et al.*, 2015; Roback *et al.*, 2018). Orographically-enhanced precipitation among mountain fronts may also promote landsliding by modulating rock strength (Gallen *et al.*, 2015).

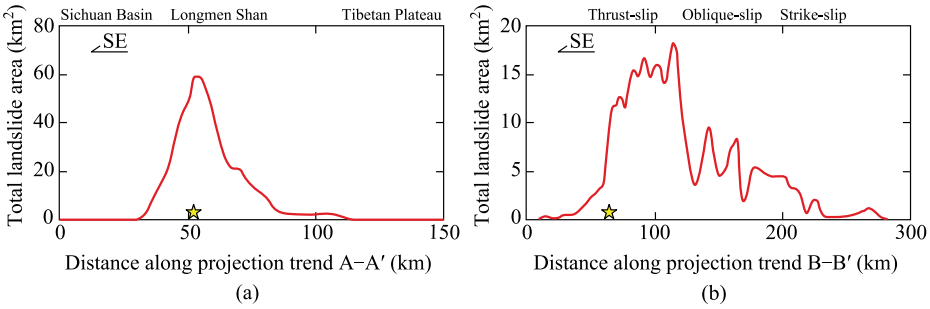

Fig. 5.2 Distribution of Wenchuan earthquake-triggered landslides in directions **(a)** perpendicular to and **(b)** parallel to the fault strike, along the A–A' and B–B' trends, respectively, in Figure 5.1. The total landslide area is calculated as the sum of areas of the landslides in 5 km-wide increments. Stars indicate the epicenter.

5.4.2 Variations of Landslide Pattern along the Fault Trend

The complex fault slip pattern makes the Wenchuan case a good opportunity to examine fault type controls on landsliding. Several studies have shown that, for the same initial stress conditions, thrust faults produce much stronger ground motion compared to normal and strike-slip faults (Oglesby and Dai, 2002; Gubachian *et al.*, 2014). Thus, we would expect to see some relationship between slip orientation in the earthquake and landslide occurrence. We show that there are quite significant variations in Wenchuan earthquake-triggered landslide area parallel to the fault trend (Fig. 5.2b), and the landslide area decreases from the southeast towards the northeast. The maximum landslide area is located near the southwestern end of the rupture, although offset by ∼40 km from the epicenter (Fig. 5.2b). Whereas there are no dramatic gradients in topography along the fault trend (Figs. 5.1a and 5.1b), the along-trend variations in landsliding seem to coincide with changes in the fault slip orientation from oblique dextral-thrust slip domains in the southwest towards strike-slip in the northeast. Gorum and Carranza (2015) conducted a more comprehensive analysis of the along-strike variations of the Wenchuan landslides, showing that more and larger landslides occurred on the oblique thrust-slip segment and that, when accounting for fault types, the landslide spatial pattern could be better predicted as a function of distance to fault than without considering of fault types. The effects of slip orientation on landsliding thus provide additional constraints in modeling landsliding occurrence in multi-fault type settings like Wenchuan.

5.4.3 Distribution of Landslides with Respect to Topographic Metrics and Lithology

We plot the distribution of Wenchuan landslides by number as a function of topographic metrics (gradient and elevation) and lithology (Fig. 5.3). Because the studied landscape does not necessarily have a uniform distribution of topographic gradient, elevation and lithology, we also derive the distribution of the studied metrics for all landscape cells as the background condition. We then normalize the distribution of the metrics for the Wenchuan landslides over the background landscape distribution, and obtaine a background-corrected distribution of landsliding susceptibility over the landscape (e.g., Meunier *et al.*, 2008; Clark *et al.*, 2016; Huang *et al.*, 2017).

The topographic gradients of all landslides and the studied landscape both show unimodal and slightly right-skewed distributions, with modal gradients of $\sim 30^\circ$ and $\sim 38^\circ$ for the landscape and all landslides, respectively (Fig. 5.3a). Note that 30° is thought to be a threshold topographic gradient in the study area (Ouimet *et al.*, 2009). When corrected for the background landscape, the Wenchuan landslides are found to preferentially occur at much steeper hillslopes, which is consistent with the Newmark sliding model: with other environmental factors set, steeper gradients would have a lower factor of safety and are more prone to fail (Jibson, 2007; Gallen *et al.*, 2015). The Wenchuan landsliding susceptibility also increases monotonically with increasing gradient, underlining the importance of hillslope steepness in setting landslide occurrence.

For elevation, the Wenchuan landslides show a unimodal left-skewed distribution, quite distinct from the underlying landscape (Fig. 5.3b). The modal elevation of the landslides is around 1.5 km, roughly corresponding to the elevation of the Longmen Shan mountain front (Fig. 5.3c). When corrected for the elevation distribution of the background landscape, the Wenchuan landslides preferentially occur at elevations of around 2–3 km (Fig. 5.3b). Notably, this elevation range corresponds to the region identified as a ready-to-fail, threshold landscape where mean hillslope gradients approach the angle of repose (Fig. 5.3c) and are insensitive to increasing erosion rates (Ouimet *et al.*, 2009). Thus our analyses suggest that, during the Wenchuan earthquake, although the mountain front experienced the most intensive seismic shaking and landsliding, the region of highest landslide susceptibility was located at slightly higher elevations of 2–3 km. This may indicate where a threshold topographic gradient is reached, with steeper hillslopes that were more prone to fail (Fig. 5.3a). Across different rock types, we find that most landslides occurred in sandstone, limestone, mylonite, and marble (Fig. 5.3d). When accounting for the distribution of lithologic units across the landscape, marble and mylonite units were most prone to landsliding (Fig. 5.3d). Better understanding the roles of rock type requires

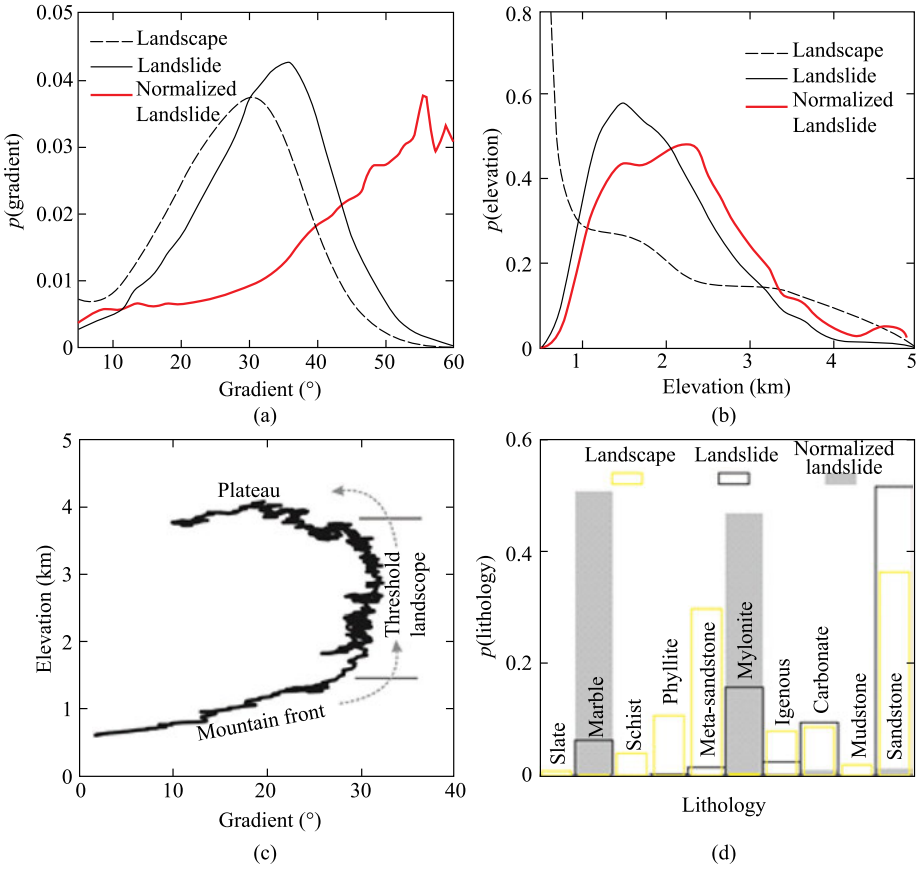

Fig. 5.3 Distribution of Wenchuan earthquake-triggered landslides by number as a function of **(a)** topographic gradient, **(b)** elevation, and **(d)** lithology. Panel **(c)** shows the relationship between elevation and gradient. In panels (a) and (b), the dashed and solid curves indicate the probability density of the studied metrics of the landscape and landslides, respectively, and the red thick curves represent the probability density of landslide occurrence normalized by the distribution of the studied metrics across the landscape, a measure of landslide susceptibility. In panel (c), the elevation and gradient data are calculated as the means within 87 m-wide DEM strips along the A–A' trend, from the Sichuan Basin to the Longmen Shan range and the Tibetan Plateau. In panel (d), the yellow and black bars show the probability distributions of lithology of the landscape and landslides, respectively, and the grey bars show the probability distribution of landslides across lithologic units normalized by the distribution of lithologic units across the landscape.

further exploration of the coupling between lithology, rock strength, and other landscape properties, as well as the spatial coincidence between lithologic units, seismic shaking, topography, and climate (e.g., Luo *et al.*, 2008; Chen *et al.*, 2011; Gallen *et al.*, 2015).

5.4.4 Landslide Locations Relative to the Fluvial Network

Fluvial landscapes are typically composed of two geomorphic domains: streams and hillslopes. Landslides directly connected to fluvial stream networks may more easily deliver sediment to streams, whereas landslides located on hillslopes may be less effective at transferring sediment. Thus, the locations of landslides relative to fluvial stream networks should provide a key constraint on the potential effect of landslide debris on sediment transport after earthquakes. Several studies have explored the extent to which landslides connect to fluvial streams (Dadson *et al.*, 2004; Meunier *et al.*, 2008; Hilton *et al.*, 2011; Hovius *et al.*, 2011; Li *et al.*, 2016; Roback *et al.*, 2018). Li *et al.* (2016) evaluated the fluvial connectivity of Wenchuan landslides using a raster-based approach. Here, we compare this prior approach with a vector-based calculation to evaluate the landslide-stream connectivity for the Wenchuan earthquake (Fig. 5.4). In both cases, to delineate streams, we determine a cutoff upstream contributing area (A_0) using the scaling relation between topographic gradient (S) and upstream contributing area (A) (Fig. 5.4b) (e.g., Montgomery, 2001). For the raster-based approach, we compare the maximum upstream contributing area for a given landslide ($A_{\max}$) to A_0. If $A_{\max}$ is greater than A_0, then the landslide is assigned as "stream-connected" (Dadson *et al.*, 2004, Li *et al.*, 2016). We estimate that, for the Wenchuan case, ~16% of the total landslide population is connected to the fluvial streams (Fig. 5.4a), but those landslides are larger than average in both area and volume and represent ~43% of the total landslide volume (Fig. 5.4c). For the vector-based approach, we delineate the ridge lines as the boundaries of each small watershed defined by the fluvial streams and calculate the normalized distances to ridges and streams for all landslides (Fig. 5.4f). For a given landslide, the normalized distance to stream (D_{nstream}) is defined as the ratio of the distance of the lowest point within the landslide polygon to the hill-

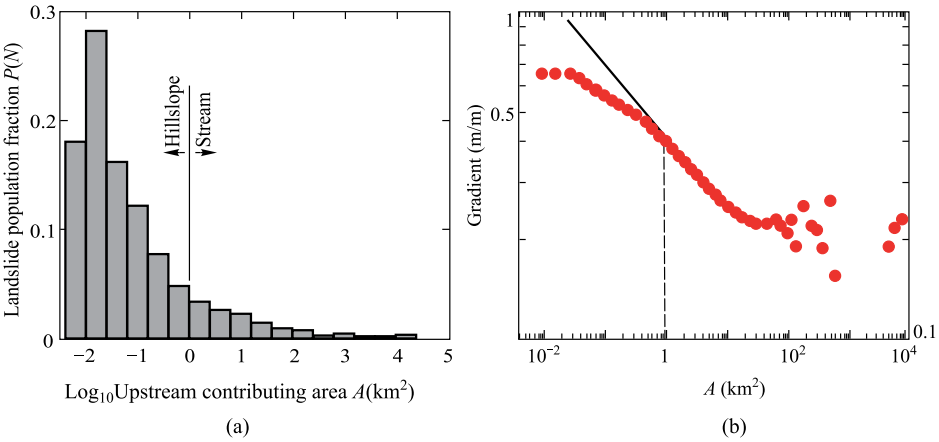

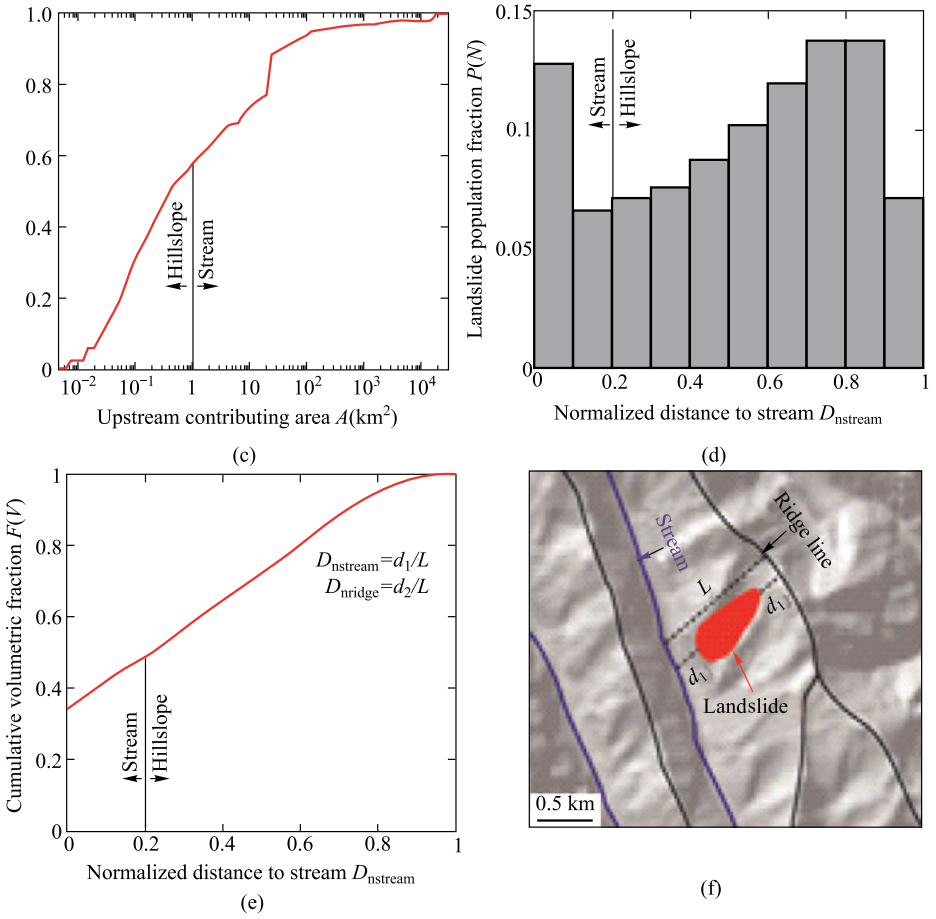

Fig. 5.4 The connectivity between Wenchuan earthquake-triggered landslides and the fluvial network is evaluated using a raster-based approach (panels a, b, c) and a vector-based approach (d, e, f). **(a)** Landslide population fraction $p(N)$ versus upstream contributing area, with the vertical line indicating the cutoff area for fluvial streams. **(b)** A typical relationship between upstream contributing area (A) and mean topographic gradient (S) of each A bin ($\delta \log_{10} A = 0.1$) in a Longmen Shan catchment (Dujiang); the transition in the S-A relationship marks the cutoff area for fluvial streams (Montgomery, 2001; Dadson *et al.*, 2004; Li *et al.*, 2016) and is marked by a vertical dashed line. **(c)** Cumulative distribution of landslide volume $F(V)$ versus A; the vertical line indicates the cutoff A between hillslope and fluvial stream domains. **(d)** Landslide population fraction $p(N)$ versus normalized distance to stream or hillslope base (D_{nstream}), with the vertical line indicating the assumed cutoff distance between stream and hillslope domains. **(e)** Cumulative distribution of landslide volume $F(V)$ versus D_{nstream}; the vertical line indicates the assumed cutoff distance between hillslope and fluvial stream domains. **(f)** A schematic diagram showing the definitions of D_{nstream} (the Euclidean distance between the lowest point of a landslide to a stream d_1, normalized by the hillslope length revealed as the planar straight line distance L) and D_{nridge} (normalized distance to hillsope ridge, the Euclidean distance between the highest point of a landslide to a stream d_2, normalized by L).

slope base (stream) over the total length of the hillslope (L), and similarly the normalized distance to ridge (D_{nridge}) is based on the highest point within the landslide polygon and the located hillslope's ridge (Densmore and Hovius, 2000; Meunier *et al.*, 2008; Huang and Montgomery, 2014). For computational simplicity, we calculate the distance as the Euclidean distance. Choosing $D_{\mathrm{nstream}} = 0.2$ as a cutoff for "stream-connected" (Meunier *et al.*, 2008; Hovius *et al.*, 2011), this second approach reveals that ∼19% of the landslide population and ∼46% of the total landslide volume are connected to the fluvial streams, consistent with the first approach and validating our estimate of the Wenchuan landslide-stream connectivity. A vector-based approach was also adopted by Roback *et al.* (2018) to evaluate landslide-stream connectivity following the 2015 Gorkha M_{w}7.8 earthquake, yielding similar results to a raster-based approach for that event as well.

Using the first approach (i.e., the raster method comparing A_0 and $A_{\max}$), we have previously conducted a detailed analysis of the Wenchuan landslide-stream connectivity considering controlling factors and influence on sediment transport (see analysis and discussion in Li *et al.*, 2016). This study identified primary controls on connectivity from seismic shaking and fault type, and secondary modulations from topography and lithology. More intensive shaking triggered larger-sized landslides, which are more likely to reach hillslope bases and connect to streams. Regions with higher drainage density also have higher landslide-stream connectivity as more streams are available. Lithologic units likely affect connectivity due to both different drainage densities and different capacities to generate larger-sized landslides. Another interesting finding is that the Wenchuan landslide-stream connectivity seems not to influence post-earthquake transport of fine landslide sediment, perhaps because this material can easily mobilize over hillslopes via diffusive transport processes. As a result, even those landslides not immediately connected to fluvial channels can supply fine-grained material to rivers. In contrast, we expect that connectivity may have a more profound influence on the export of coarser materials (grain size > 0.25 mm), which compose ∼90% of the total landslide material (Wang *et al.*, 2015; Li *et al.*, 2016). These effects could be modulated by mobilization of coarse-grained material in rainfall-induced debris flows in the months to years following the earthquake. Data to evaluate these effects and test the hypothesized roles for connectivity in transport of coarse-grained landslide debris remain lacking but will be important to predicting the cascading hazards associated with sedimentation in the wake of large earthquakes.

5.5 Seismic Controls on the Pattern of the Wenchuan Earthquake-Triggered Landslides

In this section, we evaluate how the spatial pattern of Wenchuan earthquake-triggered landslides relates to the seismic trigger. We examine potential controls on landsliding from seismic shaking and seismic energy propagation across spatial scales from the rupture zone to hillslopes.

5.5.1 PGA versus Landslide Areal Density

The most significant gradients of seismic shaking and ground motion are observed perpendicular to the fault trend (Figs. 5.1a and 5.1b). Following other studies (e.g., Meunier *et al.*, 2007), we plot the areal density of landslides, P_{Als}, against the mean peak ground acceleration (PGA) in 5 km-wide increments perpendicular to the fault trend. We find a clear separation between landslides occurring on the hanging wall versus on the footwall, and the landslide data on the hanging wall and the footwall can be fitted separately (Fig. 5.5a). For data points with $P_{Als} > 0.1\%$, the regression line for the hanging wall data has a similar slope to the regression line for the footwall data but a much smaller intercept at the x-axis, representing lower threshold accelerations to initiate landsliding (Fig. 5.5a). We suggest that, in the Wenchuan region, under similar seismic shaking, hillslopes located on the hanging wall seem to be more prone to landsliding as compared to the footwall, but once a threshold acceleration is reached, the landsliding response to enhanced shaking (i.e., the slope of the regression line on Figure 5a, also termed *landscape sensitivity* in Marc *et al.*, 2016b) seems to be similar. Another interesting observation is that, at very high PGA values (the two red points in Fig. 5.5a), the landslide areal density in the hanging wall seems to saturate as PGA increases (Fig. 5.5a), which may reveal the saturation effect of ground motion for high magnitude events as indicated by Boore and Atkinson (2008) and Marc *et al.* (2016b).

We next compare the Wenchuan P_{Als}-PGA relations to those from other earthquakes compiled by Meunier *et al.* (2007) (Fig. 5.5b). Note that Meunier *et al.* (2007) derived P_{Als}-PGA relations using both horizontal and vertical components of the ground motion data. Though we do not have the horizontal and vertical PGA data from Wenchuan, our results still provide several insights into the P_{Als}-PGA relations. First, the Wenchuan case captures a greater range of variations in P_{Als} (up to near 8%) and PGA (0.2–0.7g), helping to constrain the relations between P_{Als} and PGA under much stronger seismic shaking conditions. Second, the Wenchuan case clearly shows the different trends between

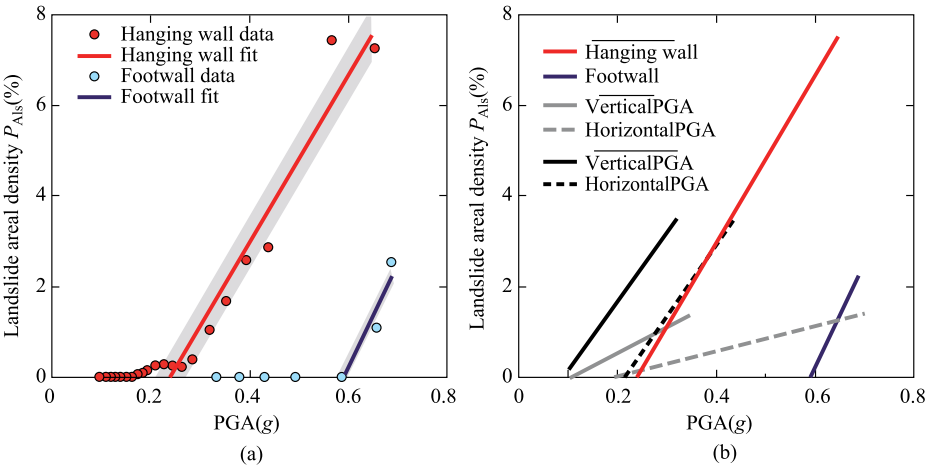

Fig. 5.5 Relationships between landslide areal density (P_{Als}) and mean peak ground acceleration (PGA) for **(a)** the Wenchuan earthquake and for **(b)** other earthquakes. P_{Als} and mean PGA are calculated in 5 km wide increments along the A–A' trend, perpendicular to fault strike. In panel (a), the red and blue lines are least-squares linear fits for the hanging wall and footwall data with $P_{Als} > 0.1\%$, respectively, and the grey shaded areas indicate ±1 s.d. uncertainties (residual errors). In panel (b), data for the Chi-Chi and Northridge earthquakes are from Meunier *et al.* (2007).

hanging wall and footwall. Third, the landsliding sensitivity to PGA, indicated by the slope of the regression line, is quite similar for the Wenchuan and the Northridge cases, and substantially greater than the sensitivity shown in the Chi-Chi earthquake (Fig. 5.5b). This difference may be partially caused by the characteristics of seismic wave propagation as discussed in Section 5.5.2 below.

5.5.2 Modeling of Landslide Pattern using a Simplified Seismic Wave Attenuation Equation

Earthquake-triggered landsliding records the surface geomorphic response to seismic energy propagation. Following this line of thought, Meunier *et al.* (2007) adopted a classical model describing seismic wave attenuation to predict the spatial pattern of earthquake-triggered landslides:

$$P_{Als} = P_{A0}\frac{R_0}{R}\exp\left(-\frac{R-R_0}{\beta}\right) \tag{5.1}$$

where P_{Als} is landslide areal density (%), R_0 is the mean asperity depth, R is the distance to the source, and P_{A0} and β are scaling factors. β is a spatial decay factor, with higher values meaning more widely spread landsliding. Equation

5.1 accounts for both geometric spreading (via the R^{-1} term) and quality decay (via the exponential term, which depends upon β). Using this model, Meunier *et al.* (2007) successfully reproduced patterns of landslides caused by the Chi-Chi, Northridge, and Finisterre earthquakes. Note that for those earthquakes, the seismic energy sources were approximated as point sources—a reasonable assumption since the ratio of length to width for those faults was close to one and those fault planes can be approximated as squares. This point source assumption may not be appropriate for the Wenchuan earthquake, which had a rupture length to width ratio of $\sim 5:1$. Thus, we assume a linear energy source rather than a point source. We then calculate the corresponding distance to the seismic energy source and fit the landslide data using Equation 5.1, treating P_{A0} and β as fitting parameters (Fig. 5.6a). We find that the simplified linear energy source model can be used to successfully reproduce the pattern of Wenchuan landslides, and that the hanging wall and footwall data show distinct trends. When compared to other cases (Fig. 5.6b), the trends of the Wenchuan case are similar to the trends of the Finisterre and the Northridge events, whereas the Chi-Chi case shows a near-horizontal trend, indicating a purely geometric spreading control on the pattern of landsliding with no quality decay during wave propagation (Meunier *et al.*, 2007). Because PGA varies as a function of R, the decay pattern of those landslides away from seismic energy sources thus controls the slope of the PGA-PAls relations (Fig. 5.5).

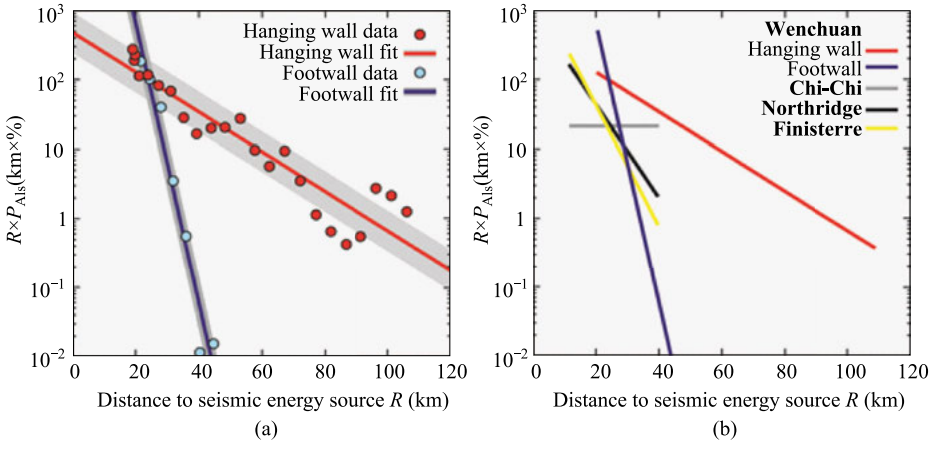

Fig. 5.6 The product of landslide areal density and distance to seismic energy source R versus R for **(a)** the Wenchuan earthquake and **(b)** other earthquakes, to validate the application of a seismic wave propagation model to predict earthquake-triggered landslide pattern. In panel (a), the red and blue lines are least-squares linear fits ($\log_{10}(R \times P_{Als})$ versus R) for hanging wall and footwall data, respectively, and the grey shaded areas indicate ±1 s.d. uncertainties (residual errors). In panel (b), Wenchuan results are compared to data for the other earthquakes compiled by Meunier *et al.* (2007). The Wenchuan landslide P_{Als} values are calculated in 5 km-wide increments along the A–A' trend perpendicular to fault strike.

5.5.3 Landslide "Clustering" as Signatures of a Seismic Trigger

Previous studies have proposed that the distribution of landslides from hillslope top to base could reveal information about the dominant landsliding-triggering mechanism (Densmore and Hovius, 2000; Meunier *et al.*, 2008). Meunier *et al.* (2008) conducted geophysical simulations of seismic wave propagation across variable topographic conditions, and found that during earthquakes geometric discontinuities such as hillslope ridges and inner gorge knick points could amplify seismic shaking and thus should experience more landsliding (i.e., landslide "clustering", Fig. 5.7a). In contrast, rainfall-triggered landslides should be distributed more evenly across hillslopes due to the lack of such seismic amplification effects (Fig. 5.7b). This theory has successfully explained the patterns of landslides triggered by the Chi-Chi, Finisterre, and Northridge earthquakes (Meunier *et al.*, 2008).

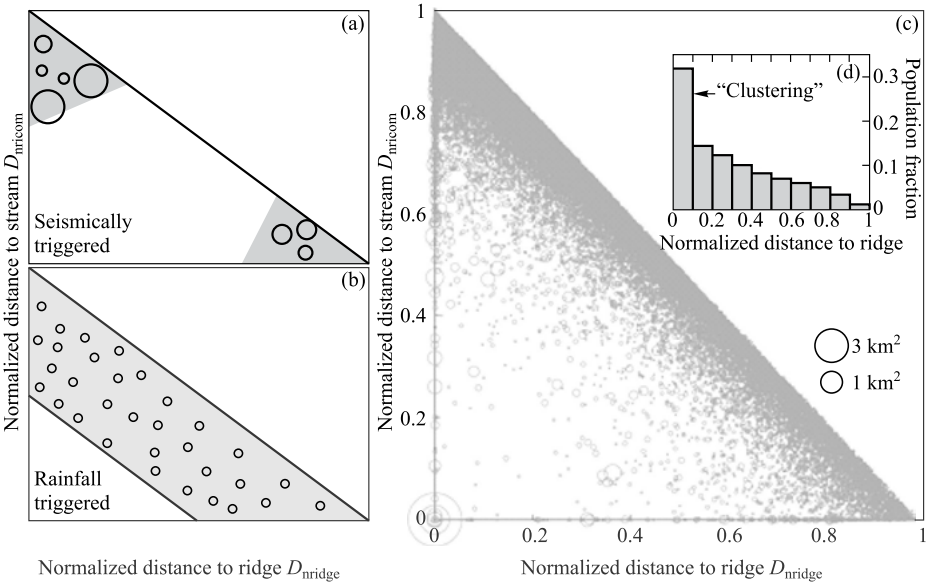

Fig. 5.7 Schematic diagrams of the distribution of landslides induced by seismic and rainfall triggers across hillslopes in D_{nridge}-$D_{nstream}$ space (panels a and b; adapted from Meunier *et al.*, 2008) and data from the Wenchuan earthquake (panels c and d). **(a)** Seismically triggered landslides cluster at hillslope ridges or bases due to amplification effects (Densmore and Hovius, 2000; Meunier *et al.*, 2008). **(b)** Rainfall-triggered landslides are distributed more evenly from hillslope tops to bases. **(c)** Distribution of the Wenchuan landslides in D_{nridge}-D_{nstream} space, with symbol size proportional to landslide area. **(d)** The Wenchuan landslide population fraction versus D_{nridge}, showing a strong clustering near ridges, consistent with a seismic trigger.

In the Wenchuan case, we find a "single clustering" pattern, i.e., most Wenchuan landslides initiate near ridges, thus reflecting the expected seismic triggering signal (Figs. 5.7c and 5.7d). This pattern may also help to explain the morphology of the hillslopes in the study area (Figs. 5.8a and 5.8b). For each topographic cell, we calculate the local gradient and the normalized distances to ridges and streams (i.e., D_{nridge} and D_{nstream}, respectively) (Meunier *et al.*, 2008). We plot the mean topographic gradient as a function of D_{nstream} (Fig. 5.8a) and convert the gradient-D_{nstream} relation to a composite or average hillslope profile (Fig. 5.8b, D_{nstream} versus normalized height). This hillslope profile should represent the typical hillslope shape in the Longmen Shan area. The profile consists of near-planar hillslopes without any evidence of widespread inner gorges, suggesting topographic amplification of seismic shaking at ridge crests is the dominant

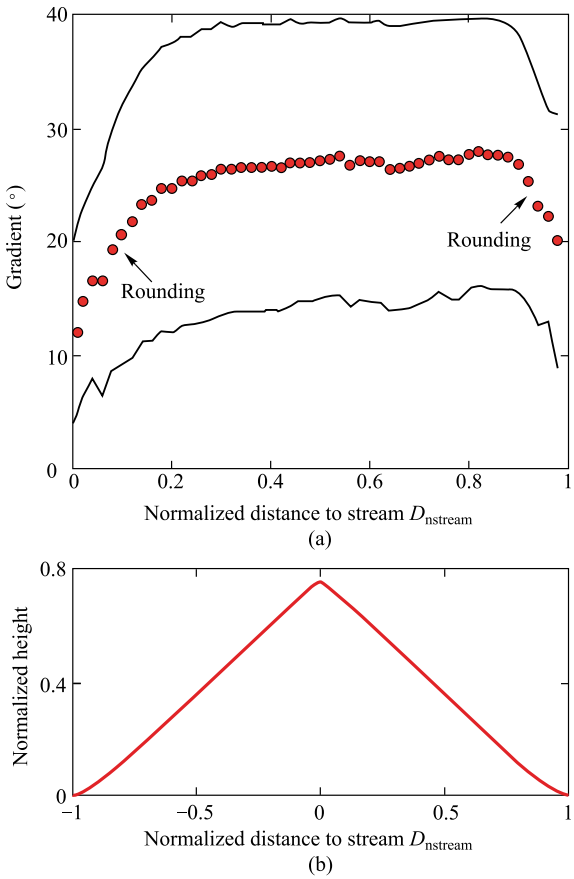

Fig. 5.8 Local topographic gradient versus **(a)** D_{nstream} and **(b)** the resulting composite or average hillslope profile in the study area. In panel (a), the red dots are the mean gradient in each D_{nstream} bin ($\Delta D_{\mathrm{nstream}} = 0.02$), and the solid lines are the uncertainty boundaries defined by one standard deviation.

influence on hillslope form. The uppermost and lowermost parts of the hillslopes seem to have shallower local gradients (Fig. 5.8b), perhaps caused by the erosional rounding due to the clustered seismic landsliding near the ridges (as shown in Fig. 5.7c and d) and by the deposition of landslide debris near the bases.

5.5.4 Landslide Preferred Aspect Variation and Relevance to Fault Slip Type

The preferred aspect, or hillslope facing directions, of earthquake-triggered landslides are thought to be indicative of seismic conditions. Hillslopes facing away from seismic energy sources are typically more susceptible to landsliding as compared to those directly facing the energy sources (Fig. 5.9) (Meunier *et al.*, 2008).

Considering the complex characteristics of the energy source and the rupture process of the Wenchuan earthquake, we track the variations of landslide aspect along the fault trend by dividing the study area into six segments (Figs. 5.10a–g). Interestingly, we find that most of the Wenchuan landslides were preferentially located on hillslopes facing southeast when normalized by the distribution of aspects of all topographic cells in the study area (Figs. 5.10b–f), opposite to the direction (northwest) that would experience more landsliding in theory if triggered by seismic wave propagation (Meunier *et al.*, 2008). This preferred facing direction is the same as the direction of the motion of the hanging wall of the fault's thrust portion (Liu-Zeng *et al.*, 2009), likely implying a more important role of the directivity of ground motion rather than the relative position of seismic energy sources with respect to topography for triggering landsliding.

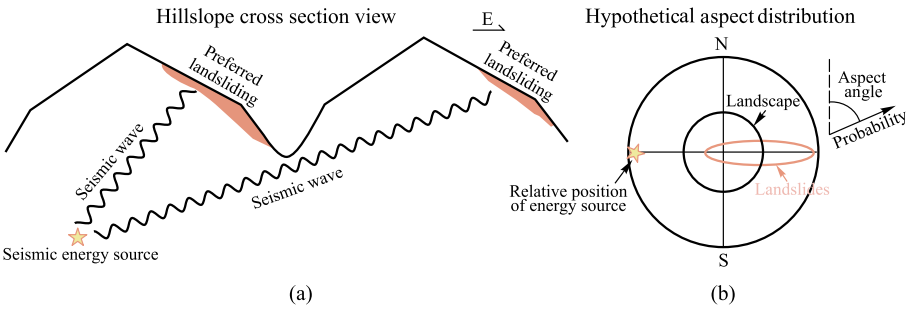

Fig. 5.9 Schematic diagrams illustrating the expected effect of aspect on earthquake-triggered landslides and the corresponding distribution of landslide aspects across landscapes. **(a)** Landslides are often preferentially located on hillslopes facing away from the seismic energy source due to asymmetric amplification of ground motion, as shown by Meunier *et al.* (2008). **(b)** Distribution of landslide aspects (normalized by the distribution of aspects of all hillslopes in the studied landscape) corresponding to the scenario in panel (a).

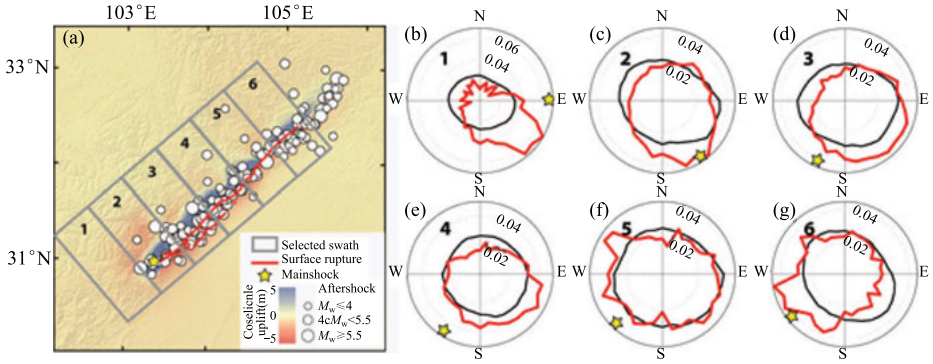

Fig. 5.10 Variability in preferred hillslope aspect directions of the Wenchuan earthquake-triggered landslides along fault strike. **(a)** Map view of co-seismic uplift, mainshock location (star), major aftershocks (circles) and surface rupture (red line), and locations of the six swath profiles. **(b)** to **(g)** Landslide aspect distributions (red curves, corrected for landscape aspect distribution) and landscape aspect distributions (grey curves) for each numbered swath. Data are grouped in 10° bins; the stars indicate the relative locations of the epicenter.

This pattern may also be caused by the fact that hillslopes facing in the landsliding-preferred direction have more favorable climatic conditions (e.g., precipitation) and vegetation cover for weathering and regolith development, so they may be more prone to fail during shaking. Another interesting observation is that the landslides in swath six (Fig. 5.10g) preferentially face southwest, which is hard to explain by climatic factors (favoring hillslopes with a southeast aspect), seismic energy propagation (favoring landslides with a northwest aspect), or ground motion (favoring hillslopes with a northeast aspect). We tentatively interpret this pattern as influenced by the clustered aftershock sequences on the eastern side of swath six (Fig. 5.10a), which could induce landslides preferentially located on hillslopes facing away from those aftershock energy sources, i.e., southwest. Our observations point to the need for further studies examining the effects of seismic processes, climatic conditions and rock strength in setting landsliding aspects.

5.6 Conclusions, Implications and Future Directions

The distribution of landslides across landscapes provides valuable information for hazard management and prediction, for understanding how tectonic fault systems control erosion and the biogeochemical cycles of essential nutrient elements,

and for evaluating orogenic erosion and evolution over tectonic timescales. Our observations from the Wenchuan earthquake validate several theories and hypotheses related to earthquake-triggered landsliding and shed new light on the importance of source characteristics. Specifically, we find significant variations of landslide occurrence both perpendicular to and parallel the seismogenic fault strike, likely due to variations in the gradients of seismic shaking and changes in fault slip modes, respectively. The Wenchuan earthquake-triggered landslides are preferentially located on the steepest hillslopes and in elevation zones dominated by threshold landscapes. As in the 1999 M_w7.6 Chi-Chi earthquake, only 10%–20% of the total landslide population is connected to the fluvial stream network, but those stream-connected landslides are larger and represent 40%–50% of the total landslide volume. We use two independent approaches (raster-based and vector-based) to estimate landslide-stream connectivity and obtain consistent results. We find good correlations between landslide areal density and seismic shaking across the Longmen Shan range, confirming a first-order control on landslide occurrence from seismic shaking. Assuming that the Wenchuan earthquake was a linear energy source, we demonstrate that the co-seismic landslide pattern can be modeled using a classical model of seismic wave propagation, characterized by a geometric spreading factor and a quality decay factor.

At hillslope scales, the Wenchuan landslides show a strong clustering near ridges, consistent with previous findings of amplifications of seismic shaking at ridges and consequently enhanced landsliding. The clustering of landslides near ridges and the deposition of landslide debris near streams may explain the rounding of the hillslope tops and bases in the study area (e.g., Korup *et al.*, 2007). Most Wenchuan landslides preferentially face southeast, similar to the direction of the horizontal ground motion of the thrust-slip part of the hanging wall but facing the seismic energy source, pointing to a more important role of ground motion and to other possible factors like climatic conditions rather than seismic wave propagation in setting landslide aspects.

While patterns observed in Wenchuan appear consistent in this case, several other recent and well-studied continental earthquakes, there are some notable exceptions. For example, the maximum landslide occurrence triggered by the 2015 M_w7.8 Gorkha earthquake did not overlap with the area of peak PGA (Roback *et al.*, 2018). The Gorkha earthquake was also characterized by large aftershocks (up to M_w7.2) that occurred far from the mainshock epicenter. Those aftershocks may be a major contributor to the seismic moment release to the local surface landscape, and may consequently contribute significantly to landsliding (e.g., Williams *et al.*, 2017). Altogether, these observations raise further questions about the roles of long-term tectonic and climatic conditions and aftershock sequences in landsliding during earthquakes. Moreover, long-term tectonic and climatic conditions largely determine another critical but less well constrained component: the bedrock fracture system, via modulations of tectonic stress and

surface processes (e.g., chemical weathering). The bedrock fracture system exerts a primary control on hillslope-scale rock strength and thus on susceptibility to landsliding. Recent advances in modeling bedrock fracture systems using topography (St. Clair *et al.*, 2015; Moon *et al.*, 2017) provide a promising tool to investigate how the subsurface structures of hillslopes affect landsliding. Overall, the spatial pattern of earthquake-triggered landslides in landscapes provides key information to validate hypotheses and to calibrate models. Our observations highlight the importance of earthquake source characteristics and fault rupture patterns, which could be better described in statistically-based models. Hillslope-scale metrics (e.g., landslide-channel connectivity, clustering pattern, and aspect) could be applied to evaluate model performance as well. In conjunction with other models predicting the total volume of earthquake-triggered landslides (e.g., Keefer, 1994; Malamud *et al.*, 2004; Marc *et al.*, 2016b), understanding of and efforts to predict the landsliding patterns would also allow better incorporation of landsliding processes into landscape evolution models (e.g., Bellugi *et al.*, 2015), as well as better prediction of landsliding hazards both during earthquake events and in their aftermath as sediment is delivered to river systems.

Acknowledgements

This work was supported by U.S. National Science Foundation (NSF-EAR/GLD grant 1053504 to A.J.W.) and the Chinese Academy of Sciences (YIS fellowship grant 2011Y2ZA04 to A.J.W.). Gen Li was supported by a USC Dornsife College merit fellowship and a GSA graduate research grant. We thank Niels Hovius, Patrick Meunier, Odin Marc, Marin Clark, Sean Gallen, and Dimitrios Zekkos for helpful discussions. We thank Chong Xu for proofreading and insightful comments. This work benefited from the workshop "Geomorphic workshops of large earthquakes" at Durham University in May 2014. Yong-Gang Li is thanked for editorial handling.

References

Bellugi, D., D.G. Milledge, W.E. Dietrich, J.A. McKean, J.T. Perron, E.B. Sudderth, and B. Kazian (2015). A spectral clustering search algorithm for predicting shallow landslide size and location, Journal of Geophysical Research: Earth Surface, 120 (2), 300–324.

Burchfiel, B.C., L.H. Royden, R.D. van der Hilst, B.H. Hager, Z. Chen, R.W. King, C. Li, J. Lü, H. Yao, and E. Kirby (2008). A geological and geophysical context for the Wenchuan earthquake of 12 May 2008, Sichuan, People's Republic of China. GSA Today, 18 (7), 5.

Chen, H., G.W. Lin, M.H. Lu, T.Y. Shih, M.J. Horng, S.J. Wu, and B. Chuang (2011). Effects of topography, lithology, rainfall and earthquake on landslide and sediment discharge in mountain catchments of southeastern Taiwan. Geomorphology, 133(3–4), 132–142.

Chen, S. and C. J. L. Wilson (1996). Emplacement of the Longmen Shan Thrust-Nappe Belt along the eastern margin of the Tibetan Plateau. Journal of Structural Geology, 18, 413–430.

China Geological Survey (2004). China Geological Base Map and Instructions (1 : 2, 500, 000), edited by K. Huang. SinoMaps Press, Beijing.

Clark, M.K. and L.H. Royden (2000). Topographic ooze: Building the eastern margin of Tibet by lower crustal flow. Geology, 28(8), 703–706.

Clark, K. E., A.J. West, R.G. Hilton, G.P. Asner, C.A. Quesada, M.R. Silman, S.S. Saatchi, W. Farfan-Rios, R.E. Martin, A.B. Horwath, K. Halladay, M. New, and Y. Malhi (2016). Storm-triggered landslides in the Peruvian Andes and implications for topography, carbon cycles and biodiversity. Earth Surface Dynamics, 4(1), 47–70.

Dadson, S.J., N. Hovius, H. Chen, W. B. Dade, J.C. Lin, M.L. Hsu, C.W. Lin, M.J. Horng, T.C. Chen, J. Milliman, C. P. Stark (2004). Earthquake-triggered increase in sediment delivery from an active mountain belt. Geology, 32(8), 733–736.

Dai, F. C., C. Xu, X. Yao, L. Xu, X. B. Tu, and Q. M. Gong (2011). Spatial distribution of landslides trig-gered by the 2008 M_s8.0 Wenchuan earthquake, China. J Asian Earth Sci, 40(4), 883–895.

Densmore, A. L. and N. Hovius (2000). Topographic fingerprints of bedrock landslides. Geology, 28(4), 371–374.

Densmore, A. L., M.A. Ellis, Y. Li, R.J. Zhou, G.S. Hancock, and N. Richardson (2007). Active tectonics of the Beichuan and Pengguan faults at the eastern margin of the Tibetan Plateau. Tectonics, 26(4), TC4005.

Egholm, D.L., M.F. Knudsen, and M. Sandiford (2013). Lifespan of mountain ranges scaled by feed-backs between landsliding and erosion by rivers. Nature, 498(7455), 475–478.

Emberson, R., N. Hovius, A. Galy, and O. Marc (2016). Chemical weathering in active mountain belts controlled by stochastic bedrock landsliding. Nature Geoscience, 9(1), 42–45.

Fan, X.M., C.J. van Westen, O. Korup, T. Gorum, Q. Xu, F.C. Dai, R.Q. Huang and G.H. Wang (2012). Transient water and sediment storage of the decaying landslide dams induced by the 2008 Wenchuan earthquake, China. Geomorphology, 171, 58–68.

Gabet, E.J. (2007). A theoretical model coupling chemical weathering and physical erosion in landslide-dominated landscapes. Earth and Planetary Science Letters, 264(1–2), 259–265.

Gabuchian, V., A.J. Rosakis, N. Lapusta, and D.D. Oglesby (2014). Experimental investigation of strong ground motion due to thrust fault earthquakes. Journal of Geophysical Research: Solid Earth, 119(2), 1316–1336.

Gallen, S.F., M.K. Clark and J.W. Godt (2015). Coseismic landslides reveal near-surface rock strength in a high-relief, tectonically active setting. Geology, 43(1), 11–14.

Gallen, S.F., M.K. Clark, J.W. Godt, K. Roback, and N.A. Niemi. (2017). Application and evaluation of a rapid response earthquake-triggered landslide model to the 25 April 2015 M_w7.8 Gorkha earthquake, Nepal. Tectonophysics, 714–715, 173–187.

Garwood, N.C., D.P. Janos, and N. Brokaw (1979). Earthquake-caused landslides: A major disturbance to tropical forests. Science, 205(4410), 997–999.

Glade, T. and M.J. Crozier (2005). The nature of landslide hazard impact. In: Landslide Hazard and Risk, edited by Glade, T., M.G. Anderson, and M.J. Crozier. John Wiley & Sons, Ltd, 41–74.

Gorum, T., and E.J. M. Carranza (2015). Control of style-of-faulting on spatial pattern of earth-quake-triggered landslides. Int. J. Environ. Sci. Technol., 12(10), 1–24.

Gorum, T., X.M. Fan, C.J. van Westen, R.Q. Huang, Q. Xu, C. Tang, and G.H. Wang (2011). Distribu-tion pattern of earthquake-induced landslides triggered by the 12 May 2008 Wenchuan earthquake. Geomorphology, 133(3–4), 152–167.

Guzzetti, F., F. Ardizzone, M. Cardinali, M. Rossi, and D. Valigi (2009). Landslide volumes and landslide mobilization rates in Umbria, central Italy. Earth and Planetary Science Letters, 279(3–4), 222–229.

Harp, E.L., and R.W. Jibson (1996). Landslides triggered by the 1994 Northridge, California, earthquake. Bulletin of the Seismological Society of America, 86(1B), S319–S332.

Hovius, N., C.P. Stark, and P.A. Allen (1997). Sediment flux from a mountain belt derived by landslide mapping. Geology, 25(3), 231–234.

Hilton, R.G., P. Meunier, N. Hovius, P.J. Bellingham, and A. Galy (2011). Landslide impact on organic carbon cycling in a temperate montane forest. Earth Surface Processes and Landforms, 36, 1670–1679.

Hovius, N., P. Meunier, L. Ching-Weei, C. Hongey, C. Yue-Gau, S. Dadson, H. Ming-Jame, and M. Lines (2011). Prolonged seismically induced erosion and the mass balance of a large earthquake. Earth and Planetary Science Letters, 304(3–4), 347–355.

Howarth, J.D., S.J. Fitzsimons, R.J. Norris, and G.E. Jacobsen (2012). Lake sediments record cycles of sediment flux driven by large earthquakes on the Alpine fault, New Zealand. Geology, 40(12), 1091–1094.

Huang, A.Y.L. and D.R. Montgomery (2014). Topographic locations and size of earthquake- and typhoon-generated landslides, Tachia River, Taiwan. Earth Surface Processes and Landforms, 39(3), 414–418.

Huang, J.C., J.D. Milliman, T.Y. Lee, Y.C. Chen, J.F. Lee, C.C. Liu, J.C. Lin, and S.J. Kao (2017). Terrain attributes of earthquake- and rainstorm-induced landslides in orogenic mountain Belt, Taiwan. Earth Surface Processes and Landforms.

Hubbard, J. and J.H. Shaw (2009). Uplift of the Longmen Shan and Tibetan Plateau, and the 2008 Wenchuan ($M = 7.9$) earthquake. Nature, 458(7235), 194–197.

Jarvis, A., H.I. Reuter, A. Nelson, E. Guevara (2008). Hole-filled SRTM for the globe Version 4, available from the CGIAR-CSI SRTM 90 m Database. http://srtm.csi.cgiar.org.

Jibson, R.W. and D.K. Keefer (1993). Analysis of the seismic origin of landslides: Examples from the New Madrid seismic zone. Geol. Soc. Am. Bull., 105(4), 521–536.

Jin, Z., A.J. West, F. Zhang, Z. An, R.G. Hilton, J. Yu, J. Wang, G. Li, L. Deng, and X. Wang (2016). Seismically enhanced solute fluxes in the Yangtze River headwaters following the A.D. 2008 Wenchuan earthquake. Geology, 44(1), 47–50.

Keefer, D. K. (1984). Landslides caused by earthquakes. Geol. Soc. Am. Bull., 95(4), 406–421.

Keefer, D.K. (1994). The importance of earthquake-induced landslides to long-term slope erosion and slope-failure hazards in seismically active regions. Geomorphology, 10(1–4), 265–284.

Kirby, E., K.X. Whipple, W. Tang, and Z. Chen (2003). Distribution of active rock uplift along the eastern margin of the Tibetan Plateau: Inferences from bedrock channel longitudinal profiles. Journal of Geophysical Research: Solid Earth, 108, 2217.

Kirby, E., K. Whipple, and N. Harkins (2008). Topography reveals seismic hazard. Nature Geoscience, 1(8), 485–487.

Korup, O., M.J. McSaveney, and T.R.H. Davies (2004). Sediment generation and delivery from large historic landslides in the Southern Alps, New Zealand. Geomorphology, 61(1–2), 189–207.

Korup, O., J.J. Clague, R.L. Hermanns, K. Hewitt, A.L. Strom, and J.T. Weidinger (2007). Giant land-slides, topography, and erosion. Earth and Planetary Science Letters, 261(3–4), 578–589.

Kritikos, T., T.R. Robinson, and T.R.H. Davies (2015), Regional coseismic landslide hazard assessment without historical landslide inventories: A new approach. Journal of Geophysical Research: Earth Surface, 120(4), 711–729.

Larsen, I.J., D.R. Montgomery, and O. Korup (2010). Landslide erosion controlled by hillslope material. Nat. Geosci., 3(4), 247–251.

Li, G., A.J. West, A.L. Densmore, Z. Jin, R.N. Parker, and R.G. Hilton (2014). Seismic mountain building: Landslides associated with the 2008 Wenchuan earthquake in the context of a generalized model for earthquake volume balance, Geochemistry. Geophysics, Geosystems, 15(4), 833–844.

Li, G., A.J. West, A.L. Densmore, D.E. Hammond, Z. Jin, F. Zhang, J. Wang, and R.G. Hilton (2016). Connectivity of earthquake-triggered landslides with the fluvial network: Implications for landslide sediment transport after the 2008 Wenchuan earthquake. Journal of Geophysical Research: Earth Surface, 121(4), 703–724.

Li, G., A.J. West, A.L. Densmore, Z. Jin, F. Zhang, J. Wang, M. Clark, and R.G. Hilton (2017). Earthquakes drive focused denudation along a tectonically active mountain front, Earth and Planetary Science Letters, 472, 253–265.

Li, Y, P.A. Allen, A.L. Densmore, and X. Qiang (2003). Evolution of the Longmen Shan Foreland Basin (Western Sichuan, China) during the Late Triassic Indosinian Orogeny. Basin Research, 15(1), 117–138.

Lin, A., B. Yan, and G. Rao (2016). Millennium recurrence interval of morphogenic earthquakes on the Qingchuan fault, northeastern segment of the Longmen Shan Thrust Belt, China. Journal of Seismology, 20(2), 535–553.

Liu-Zeng, J., L. Wen, M. Oskin, and L.S. Zeng (2011). Focused modern denudation of the Longmen Shan margin, eastern Tibetan Plateau. Geochemistry Geophysics Geosystems, 12, Q1107.

Liu-Zeng, J., Z. Zhang, L. Wen, P. Tapponnier, J. Sun, X. Xing, G. Hu, Q. Xu, L. Zeng, L. Ding, C. Ji, K.W. Hudnut and J. van der Woer (2009). Co-seismic ruptures of the 12 May 2008, M_s8.0 Wenchuan earthquake, Sichuan: East-west crustal shortening on oblique, parallel thrusts along the eastern edge of Tibet. Earth and Planetary Science Letters, 286(3–4), 355–370.

Luo, W. and T. Stepinski (2008). Identification of geologic contrasts from landscape dissection pattern: An application to the Cascade Range, Oregon, USA. Geomorphology, 99(1–4), 90–98.

Malamud, B.D., D.L. Turcotte, F. Guzzetti, and P. Reichenbach (2004). Landslides, earthquakes, and erosion. Earth and Planetary Science Letters, 229(1–2), 45–59.

Marc, O., N. Hovius, and P. Meunier (2016a). The mass balance of earthquakes and earthquake sequences. Geophysical Research Letters, 43(8), 3708–3716.

Marc, O., N. Hovius, P. Meunier, T. Gorum, and T. Uchida (2016b). A seismologically consistent expression for the total area and volume of earthquake-triggered landsliding. Journal of Geophysical Research: Earth Surface, 121(4), 2015JF003732.

Meunier, P., N. Hovius, and A. J. Haines (2007). Regional patterns of earthquake-triggered landslides and their relation to ground motion, Geophysical Research Letters, 34, L20408, doi: 10.1029/2007GL031337.

Meunier, P., N. Hovius, and A.J. Haines (2008). Topographic site effects and the location of earthquake induced landslides. Earth and Planetary Science Letters, 275(3–4), 221–232.

Meunier, P., T. Uchida, and N. Hovius (2013). Landslide patterns reveal the sources of large earthquakes. Earth and Planetary Science Letters, 363, 27–33.

Molnar, P., W.R. Boos, and D.S. Battisti (2010). Orographic controls on climate and paleoclimate of Asia: Thermal and mechanical roles for the Tibetan Plateau. Annual Review of Earth and Planetary Sciences, 38(1), 77–102.

Montgomery, D.R. (2001). Slope distributions, threshold hillslopes, and steady-state topography. American Journal of Science, 301(4–5), 432–454.

Montgomery, D.R. and M.T. Brandon (2002). Topographic controls on erosion rates in tectonically active mountain ranges. Earth and Planetary Science Letters, 201(3–4), 481–489.

Moon, S., J.T. Perron, S.J. Martel, W.S. Holbrook, and J. St. Clair (2017). A model of three-dimensional topographic stresses with implications for bedrock fractures, surface processes, and landscape evolution. Journal of Geophysical Research: Earth Surface, 122(4), 823–846.

Oglesby, D.D. and S.M. Day (2002). Stochastic fault stress: Implications for fault dynamics and ground motion. Bulletin of the Seismological Society of America, 92(8), 3006–3021.

Ouimet, W. B., K. X. Whipple, and D. E. Granger (2009), Beyond threshold hillslopes: Channel adjust-ment to base-level fall in tectonically active mountain ranges. Geology, 37(7), 579–582.

Parker, R.N., A.L. Densmore, N.J. Rosser, M. de Michele, Y. Li, R.Q. Huang, S. Whadcoat, and D.N. Petley (2011). Mass wasting triggered by the 2008 Wenchuan earthquake is greater than orogenic growth. Nat. Geosci., 4(7), 449–452.

Pearce, A.J. and A.J. Watson (1986). Effects of earthquake-induced landslides on sediment budget and transport over a 50-yr period. Geology, 14(1), 52–55.

Petley, D. (2012). Global patterns of loss of life from landslides. Geology, 40(10), 927–930.

Roback, K., M. Clark, A.J. West, D. Zekkos, G. Li, S.F. Gallen, D. Champlain, J. Godt (2018). The size, distribution, and mobility of landslides caused by the 2015 M_w7.8 Gorkha earthquake, Nepal. Geomorphology, 301, 121–138.

Robinson, T.R., N.J. Rosser, A.L. Densmore, J.G. Williams, M.E. Kincey, J. Benjamin, and H.J.A. Bell (2017). Rapid post-earthquake modelling of coseismic landsliding intensity and distribution for emergency response decision support. Natural Hazards and Earth System Sciences, 171, 1521–1540.

Royden, L.H., B.C. Burchfiel, R.W. King, E. Wang, Z. Chen, F. Shen, and Y. Liu (1997). Surface Deformation and Lower Crustal Flow in Eastern Tibet. Science, 276(5313), 788–790.

Sklar, L.S., and W.E. Dietrich (2004). A mechanistic model for river incision into bedrock by saltating bed load. Water Resource Research, 40(6), 1–21.

St. Clair, J.,S. Moon, W.S. Holbrook, J.T. Perron, C.S. Riebe, S.J. Martel, B. Carr, C. Harman, K. Singha, and D.D. Richter (2015). Geophysical imaging reveals topographic stress control of bedrock weathering. Science, 350(6260), 534–538.

Shen, Z.K., J.B. Sun, P.Z. Zhang, Y.G. Wan, M. Wang, R. Burgmann, Y.H. Zeng, W.J. Gan, H. Liao, and Q.L. Wang (2009). Slip maxima at fault junctions and rupturing of barriers during the 2008 Wenchuan earthquake. Nat. Geosci., 2(10), 718–724.

Swiss Re (2000). Random Occurrence or Predictable Disaster? New Models in Earthquake Probability Assessment. Swiss Re, Zurich.

Tang, C., J. Zhu, X. Qi, and J. Ding (2011). Landslides induced by the Wenchuan earthquake and the subsequent strong rainfall event: A case study in the Beichuan area of China. Engineering Geology, 122(1–2), 22–33.

Tapponnier, P., X. Zhiqin, F. Roger, B. Meyer, N. Arnaud, G. Wittlinger, and J. Yang (2001). Oblique Stepwise Rise and Growth of the Tibet Plateau. Science, 294(5547), 1671–1677.

Thompson, T.B., A. Plesch, J.H. Shaw, and B.J. Meade (2015). Rapid slip-deficit rates at the eastern margin of the Tibetan Plateau prior to the 2008 M_w7.9 Wenchuan earthquake. Geophysical Research Letters, 42(6), 1677–1684.

Tian, Y., B.P. Kohn, A.J.W. Gleadow, and S. Hu (2013). Constructing the Longmen Shan eastern Tibetan Plateau margin: Insights from low-temperature thermochronology. Tectonics, 32(3), 576–592.

USGS Earthquake Hazard Program (2008). 2008 May 12 06:28:01 UTC. http://earthquake.usgs.gov/earthquakes.

Wang, J., Z. Jin, R.G. Hilton, F. Zhang, A.L. Densmore, G. Li, and A.J. West (2015). Controls on fluvial evacuation of sediment from earthquake-triggered landslides. Geology, 43(2), 115–118.

Wang, J., Z. Jin, R. G. Hilton, F. Zhang, G. Li, A.L. Densmore, D.R. Grocke, X. Xu, and A.J. West (2016). Earthquake-triggered increase in biospheric carbon export from a mountain belt. Geology, 44(9), 414–417.

West, A.J., R. Hetzel, G. Li, Z. Jin, F. Zhang, R.G. Hilton, and A.L. Densmore (2014). Dilution of ^{10}Be in detrital quartz by earthquake-induced landslides: Implications for determining denudation rates and potential to provide insights into landslide sediment dynamics. Earth and Planetary Science Letters, 396(0), 143–153.

Williams, J. G., N. J. Rosser, M. E. Kincey, J. Benjamin, K. J. Oven, A. L. Densmore, D. G. Milledge, and T. R. Robinson (2017). Satellite-based emergency mapping: Landslides triggered by the 2015 Nepal earthquake. Natural Hazards and Earth System Sciences Discussion, in review.

Xu, C., X. Xu, X. Yao, and F. Dai (2014). Three (nearly) complete inventories of landslides triggered by the May 12, 2008 Wenchuan M_w7.9 earthquake of China and their spatial distribution statistical analysis. Landslides, 11(3), 441–461.

Xu, Q., S. Zhang, and W. Li (2011). Spatial distribution of large-scale landslides induced by the $5 \cdot 12$ Wenchuan Earthquake. J. Mt. Sci., 8(2), 246.

Xu, X., X. Wen, G. Yu, G. Chen, Y. Klinger, J. Hubbard, and J. Shaw (2009). Coseismic reverse- and oblique-slip surface faulting generated by the 2008 M_w7.9 Wenchuan earthquake, China. Geology, 37(6), 515–518.

Yanites, B.J., G.E. Tucker, K.J. Mueller, and Y.G. Chen (2010). How rivers react to large earthquakes: Evidence from central Taiwan. Geology, 38(7), 639–642.

Yuan, R.M., Q.H. Deng, D. Cunningham, C. Xu, X.W. Xu, and C.P. Chang (2013). Density distribution of landslides triggered by the 2008 Wenchuan earthquake and their relationships to peak ground acceleration. Bulletin of the Seismological Society of America, 103(4), 2344–2355.

Zhang, S., L. M. Zhang, and T. Glade (2014). Characteristics of earthquake- and rain-induced landslides near the epicenter of Wenchuan earthquake. Engineering Geology, 175, 58–73.

Authors Information

Gen Li and A. Joshua West
Department of Earth Sciences, University of Southern California,
Los Angeles, California 90089-0740, USA.
E-mail: genli@usc.edu; ligengeo@gmail.com

Alexander L. Densmore and Robert G. Hilton
Institute of Hazard, Risk and Resilience and Department of Geography,
Durham University
Durham, DH1 3LE, UK

Zhangdong Jin, Fei Zhang, and Jin Wang
State Key Laboratory of Loess and Quaternary Geology,
Institute of Earth Environment, Chinese Academy of Sciences,
Xi'an, 710075, China

Chapter 6
A Review on Numerical Models for Coal and Gas Outbursts

Yucang Wang and Sheng Xue

An outburst of coal and gas is an event where coal or rocks are suddenly ejected from an advancing face to the excavation area, together with the emission of large amount of gas. Coal and gas outbursts have resulted in much loss of lives of numerous miners and equipment all over the world. However, despite extensive research efforts over more than 150 years, the fundamental mechanism causing coal and gas outbursts still remains unknown. Numerical simulations provide a means to study this complex phenomenon. In this chapter, the most outburst models which have been proposed in the past two or three decades are briefly reviewed. We then investigate the most important factors controlling the occurrence of outbursts, and discuss what a reliable numerical model should include in order to reproduce the realistic behaviors of outbursts. We point out that some important mechanisms are missing in the existing models. Finally, we propose a new model strategy which couples Discrete Element Method and Lattice Boltzmann Method. The new model includes more basic mechanisms and influencing factors. The preliminary results are promising.

Key words: Coal and gas outbursts, mechanisms, numerical models.

6.1 Introduction

An outburst of coal and gas is the rapid release of a large quantity of coal or rocks, together with the emission of huge amount of gas, into the working face in underground coal mines. The unexpected and violent nature of outbursts poses great threats to the lives of miners, facilities and production of coal. With

https://doi.org/10.1515/9783110560329-201

an increase in depth of coal mining, outburst intensity and frequency tend to increase. Therefore in recent decades, the subject of outbursts has been a focus of interest in major coal producing countries, particularly in China where some coal mines extract coal seams of greater than 1000 m depth.

These disasters have forced mining engineers and researchers all over the world to develop practical procedures to reduce the impacts of outbursts to a minimum level and to develop a deep understanding of the complex phenomena. In the past 150 years, considerable investigations relating to outburst mechanisms and techniques have been carried out which mainly fell into two main categories. The first one is development of practical mining methods, safety procedures and improvement of equipment to reduce or eliminate the effect of outbursts particularly on mine workers. It has been realised that the most effective way to reduce the risk of outbursts is through prediction, prevention and control. Effective gas drainage programmes, better management of outburst prone zones, strict regulations and vigilance and extensive researches have contributed to improvements in outburst prevention. Some practical techniques such as gas drainage and distressing techniques have been developed (Yuan *et al.*, 2011).

On the other hand, however, it is widely accepted that the reliable methods to mitigate risks of outbursts must be based not only on years of practical experiences in mines, but also on basic scientific researches which could lead to a better understanding of the mechanism of outbursts and the contributing factors. As a consequence, an enormous amount of energy has been directed in this field in many counties. Hypothesis and theoretical models have been proposed to explain the outburst phenomenon.

However, despite extensive research efforts over more than 150 years, the fundamental mechanism causing coal and gas outbursts still remains unknown. The difficulties of understanding such phenomena can be attributed to many factors, such as diverse geological structures, anisotropic and heterogeneous nature of coal properties, gas content, stress and the method of mining. Investigations of outbursts are also hindered by a lack of field data due to difficulties in direct observation of such catastrophic events.

Current knowledge about outbursts mostly comes from field observations and laboratory studies. Field observations can provide all sorts of data to develop practical methodologies and help to understand the role of geology in outbursts. Observations of sites where outbursts occur can help us to identify the mechanism and the influencing factors of an outburst. Post-occurrence survey is great helpful to determine the size and violence of an outburst. In-situ measurements of stress level and gas pressure or gas content also make great contribution to outburst prevention. The disadvantage of this method is that the first-hand observation of the whole process for an outburst is very rare due to its violent and dangerous nature.

Laboratory studies provide opportunities to test the hypothesis and study the relation between outbursts and various factors. These experiments include the laboratory modelling of outburst occurrence, and studies of the basic phenomena related to outbursts, such as fracturing of coal, desorbing and diffusion properties of coal. Since 1950s, laboratory studies have been carried out to understand the phenomenon of outbursts (Ignatieff, 1954, Famin, 1959; Kuroiwa and Tashiro, 1960). More extensive laboratory tests (Bodziony *et al.*, 1989; Lama and Bodziony, 1998; Butt, 1999; Sobczyk, 2011; Skoczylas, 2012; Tu *et al.*,2016) have been done recently using the advanced equipment to capture some basic elements of an outburst such as pressure, temperature and velocity of gas. One of the limitations of laboratory tests is that it is very difficult to accurately control a large number of factors and conditions such that they resemble those of the real outbursts. Also it is not easy to control initial and boundary conditions.

Apart from field observations and laboratory experiments, theoretical analysis is also used in outburst researches. Some attempts have been made to find the analytical solution for the process of an outburst (Ding *et al.*, 1989; Zheng *et al.*, 1993, Senjuntichai and Rajapakse, 1993, Chan *et al.*, 1993). Based on some simplified assumptions, these approaches have concentrated on the derivation of solutions for the evolution of certain quantities such as the fluid pressure and stress for some mathematically tractable problems. Although the analytical approaches can provide very useful insights into significance of some important parameters, its application is limited to problems with simple geometry and boundary conditions that can be represented mathematically by partial differential equations.

The rapid advance of computer technology has offered another opportunity: numerical simulations. In recent years, computer modelling emerges as a new and powerful tool to study the process of outbursts. Using computer model, all the relevant data are accessible and variables and conditions are completely controllable. Also it is not limited by geometrical and boundary conditions. A numerical model permits certain factors to be switch on and off so that their effects on outbursts can be studied. In this way a model can be used to predict what would be the likely mechanism for outburst occurrence with the known insitu data and to identify the critical factors for outburst control and management purpose.

Some attempts have been made to numerically model the process of an outburst. However, these models are still over simplistic. While most of these models include the mechanisms of deformation of the solid, desorption of gas and Darcy flow of the fluid, some mechanisms that play an important role, such as the fracturing and fragmentation of the solid, are is either ignored or modelled with continuum mechanics, which cannot naturally model the discrete nature of solid fragmentation and movement. Therefore, there is no single numerical model that can accurately simulate the entire process of an outburst, and none

of the models has been successful in developing quantitative measures to predict and prevent outbursts in practice.

In this chapter, outburst models which have been proposed in the past two or three decades are briefly reviewed. We then review the most important factors controlling the occurrence of outbursts, and analyse what a reliable numerical model should include in order to reproduce the realistic behaviours of outbursts. Based on these analyses, we developed a new outburst model to simulate the entire process of an outburst. It includes the most recognized effecting factors of outbursts. The new model couples two well-developed numerical approaches: the discrete element method (DEM) and the lattice Boltzmann method (LBM). The former explicitly models the deformation, fracture and fragmentation of the solid, while the later models fluid flow. A 2-D example to simulate the process of an outburst is presented to demonstrate the potential capability of the coupled model.

6.2 Mechanisms of Outbursts and Influencing Factors

6.2.1 Mechanisms of Outbursts

Mechanism of coal and gas outbursts explains the reasons, conditions and progress of initiation, development, termination of outbursts. Any hypothesis seeking to explain and describe the mechanism of outbursts must explain the events leading up to and during the outbursts, therefore account not only for the initiation of the outburst but also for the ejection and transport of coals and rocks for a considerable distance from the outburst cavity. Various hypotheses have been suggested to explain the mechanism of an outburst. Most existing mechanism models fall into the four flowing major categories.

6.2.1.1 Early theories in which gas plays the dominant role

Taylor (1852–1853) first noticed the close relationship between sudden emission of gases in coal mines and outbursts. Halbaum (1899–1900) proposed a theory in which gas pressure plays the dominant role. Rowan (1911–1912) proposed his concept in which the cause of outbursts is the presence of "pocket" of highly pulverised coal in which gas present in cracks under high pressure. Graham

(1916–1917) first considered the mechanism of accumulation of gas in coal and sorption (solubility) of CH_4, CO_2, N_2 and H_2 at different percentages. Briggs (1920–1921), Ruff (1930) and Bykov (1936) also believed that the most common and direct factor that initiate an outburst is the free gas present in the coal seam.

6.2.1.2 The concept in which stress plays a dominant role

Loiret and Laligant (1923) first pointed out that the effects of mechanical forces, or rock stress, are independent of the gas pressure. Stresses in rock play a major role on the occurrence of outbursts directly or indirectly. Caulfield (1931) presented the opinion that the main cause of outbursts and rock bursts are stresses. Pechuk (1933) supported the idea that outbursts are the result of liberation of potential energy accumulated in rock during the process of tectonic movement. Gas that is liberated during the crushing of coal is only secondary. Budryk (1951) put outbursts in a sub category of rock bursts, based on the observation of that both these phenomena have common characteristics. Josse (1957) thought that an outburst is initiated as a result of bursting of the strong elastic roof rocks, and gas performs the function of carrier of fractured coal along the excavation. Rozantsev (1959) confirmed that the role of rock stress as an initiating factor of an outburst.

6.2.1.3 Modern ideas based on multi-factor mechanism

Nekrasovski (1951) identified for the first time that outbursts are not caused by a single factor, but rather by a multiple of factors acting together. He also pointed out that gravity plays a very important role in steep seams. Khodot (1951) proposed that an outburst is caused by potential energy stored in coal seam and internal energy of gas. Khristianovich (1953) combined the concept of stress, strength, and gas. Skochinski (1954) believed that outbursts occur as a result of mutual interaction of the flowing factors: rock stress, the gas present in the coal, physical and mechanical properties of the coal seam and gravitational force of coal. Hargraves (1958) supported the idea that an outburst is caused by multiplicity of factors. Hanes, Lama and shepherd (1983) stated that both stress and gas play a role in the occurrence of outbursts, but one may be more dominant than the other depending on the local conditions.

6.2.1.4 Thermodynamic and other mechanisms

Belov (1931) explained outbursts as a thermodynamic phenomenon, as the process where the mechanical energy of rock changes into heat and dry distillation of coal occurs. Ettinger (1979) pointed out that treating coal, sorbed with gas, as a mechanical system is not enough in understanding the physical and chemical processes that happen in a coal seam as a result of disturbances in its thermodynamic equilibrium. The gas-coal system formed over the whole geological history is in a metastable state so that transition to a different state must be accompanied by emission of energy in the form of heat and work. Thermodynamic description has also been proposed by Jagiello *et al.* (1992). In this description, liberation of gas, upon entering a coal seam, is connected to a decrease in temperature of the system. As result of the work performed by the gas, the internal energy of the system decrease. The gas contained in the coal has some store of work, which can be used in an outburst process.

Other mechanisms of outbursts include the following two theories. First, Jiang *et al.* (Jiang *et al.*, 1995; Jiang, 1998) proposed spherical shell destabilization hypothesis, in which rock stress first crushes the coal, and generates cracks inside the coal seam, forming spherical shell shaped coal layers. Coal releases gas to the fractured zones, accumulating high-pressure gas, which further expands the cracks and finally the spherical shell shaped coal layers destabilize, fracture and are thrown into the excavation. The re-distribution of stress further fractures the coal close to the face, developing into a continuous outburst process. The second, Guan *et al.* (2009) hypothesized that the mechanism of outbursts is similar to magma fragmentation during explosive volcanic eruptions. According to them, an outburst is caused by high gas pressure inside coal but low ambient pressure on it, breaking coal into pieces and releasing the high-pressure gas in a shock wave. Coal outburst may be regarded as another type of gas-driven eruption. More detailed reviews on the mechanisms of outbursts can be found in Famer and Pooley (1967), Shepherd (1981), Hyman (1987), Beamish and Crosdale (1998), Lama and Bodziony (1998) and Guan *et al.* (2009).

6.2.2 Factors Influencing Outbursts

Now it is generally accepted that changes in stress and reservoir pressure during mining cause the deformation and failure of coal and the interaction between coal and gas in a seam manifests itself to a dynamic type of failure or outburst, and that the occurrence and development of an outburst is the result of combined effects of stress redistribution, coal gassiness and physical mechanical properties of coal. For an outburst to occur coal must be deformed and failed under an

effective stress and gas in coal must be able to desorb rapidly from the coal and eject the failed coal into a mining opening instantaneously (Lama and Bodziony, 1998; Li, 2001; Cao *et al.*, 2003; Aguado and Nicieza, 2007; Yuan *et al.*, 2011; Torano *et al.*, 2012).

Further studies on the nature of this phenomena by different researchers have been focused on the factors that contribute to an outburst rather than the mechanism. Different investigators may recognized different factors, depending on the detailed mining conditions. Cis (1958, 1965) stated the following six factors that contribute to an outburst: geological disturbances, such as faults, contact zones of coal with volcanic and deformation of coal; static and dynamic stresses due to excavations; gas pressure in the coal seam; gravity; sudden exposure of the coal seam; part of the excavation that forms narrow angle. Hargraves (1958) recognized the flowing contributing factors: presence of gas in the seam; local faulting and crushing of coal; tectonic stress; contortions of seam, and variation in thickness; steep dip of the seam; intrusion of the seam by dykes; low moisture content of coal; coal with low permeability; working conditions which do not allow satisfactory escape of sorbed gas. Williams and Rogis (1980) emphasised the importance of coal rank and geological features.

The most important factors that influence the occurrence of outbursts are summarised as (Shepherd *et al.*, 1981; Singh, 1984; Lama and Bodziony, 1998; Cao *et al.*, 2001; Lama and Saghafi, 2002; Cao *et al.*, 2003):

- Gassiness of the coal seam (gas content and pressure);
- Geological factors (the depth of occurrence, angle of dip, thickness of the seam, folds, fracturing, faults, shear zones, changes in seam thickness and magmatic intrusions);
- Properties of the coal (permeability and diffusivity, Sorption/desorption properties, strength and rank of coal);
- Stress conditions.

Effects of these factors can be reflected by the fact that the coal seam is liable to an outburst mostly under the following conditions:

- Higher the gas content or pressure;
- The existence of more complex geological factors, such as folds, fracturing, faults, dykes, shear zones, changes in seam thickness, magmatic intrusions and mylonite zones;
- Deeper mining depth;
- Steeper inclined seam or higher angle of dip;
- Thicker seam;
- Lower strength of coal seam;
- The less permeable the coal seam;
- Higher diffusivity coefficients;
- Higher desorption rate of gas;

- Higher coal rank;
- Higher stress level.

Besides, it is noticed that the factors can effects each other, for example, coal permeability is effected by stress level and presence of joints, cleats and fractures; stress level is effected by geological structures and mining depth; The rate of release of gas from the coal particles (gas desorption rate) is overwhelmingly influenced by the size of coal particles or degree of coal fragmentation; coal strength may be influenced by gas pressure. Therefore these factors influence the occurrence of outbursts in a very complicated way.

6.2.3 The Ingredients Should Be Included in a Reliable Outburst Model

It has proven to be difficult to develop a generalised numerical model to simulate the entire process of outburst. Based on the analysis of influencing factors and mechanisms in the previous section, we think the necessary ingredients of a good outburst model should include the following basic ingredients:

6.2.3.1 Deformation of coal

The capability of deformation of coals under mechanical forces and gas pressure determines the stress transfer inside the coal seams. The advance of mining, collapse of one part of the coal seam and gas pressure changes induce stress change close to the work face. This stress change is transferred inside the coal seams and is extremely important to generate the fracturing of coal in the future.

6.2.3.2 Fracture and fragmentation of coal

The most essential part of an outburst process is fracturing of coal under mechanical stress and gas pressure. Without the breakage of coals an outbursts cannot manifest itself. The fracture mechanisms should include tensile fracturing and shear fracturing. Fragmentation of coals happens when the coal particles are transported to excavation areas by gas flow. It is caused by a series of complicated interactions such as gas pressure changes during the gas desorption and collisions between coal particles and between coal particles and walls.

6.2.3.3 Gas adsorption/desorption

In case of pressure changes or changes in other conditions, the adsorbed gas desorbs to cleats or interface. Desorption of gas from the coal surface occurs at a much faster rate than the diffusion of the gas through the coal matrix.

6.2.3.4 Gas diffusion or Darcy flow in coal seams

Generally two types of gas flow take places inside the coal seams. The coal matrix consists of a micro-porous system through which gas diffuses to the fractures. Diffusion flow occurs whenever a difference in concentration of molecules of a given gas occurs, and can be described mathematically by Fick's first law of diffusion. Another kind of gas flow is laminar flow in the fractures. The laminar flow in the fracture network is and driven by pressure difference and follows Darcy's Law.

6.2.3.5 Free flow of gas

The free flow of gas mainly plays in role in transporting the broken coal particles outside the cavern. However, the coal particle keep desorbing gas in the transportation process, and this complicated flow patterns of mixture of solids and gas determine the pile of coals. Even in the earlier stage of an outburst, the transportation of broken coals outside of the cavern is very important since some researcher suggested that the fracturing of coals during an outburst occurs in a layer-by-layer fashion. In this case, the quick throw of one broken layer is a necessary condition for the next layer to desorb and break.

6.2.3.6 Coupling between gas and solid coal

An outburst process involves the motions and interaction of solids and fluids. The solid coal fracturing is influenced by the gas pressure, the broken coal particles are driven by the gas flow, and desorption of gas from coals provides source for gas flow, and the motion of solids provide a moving boundary conditions. This kind of two-way interaction between solids and fluids should not be neglected.

6.2.3.7 Geological structures (faults, shear zones)

As discussed in the previous section, the existence of more complex geological factors, such as folds, fracturing, faults, and shear zones have a strong effects on the occurrence of an outburst. While sometimes it is difficult to detect these structures, it is relatively easy to test the effects of these factors on the outburst process using the computer modelling. Therefore it is desirable for the new numerical model to implement these factors. In fact, fracturing, faults, and shear zones can be taken into account relatively easily if a model can include explicitly the mechanism of fracture, frictional sliding and frequent contacts.

6.2.3.8 Permeability change due to stress change or fracture

Because of the geometry of the cleat structures, the permeability of coal is generally anisotropic, and is stress dependent. Mostly it is believed that when the confining stress is increasing, the cleats tend to close, reducing the permeability. When there is a fresh fracture, or the existing fracture aperture is growing, the permeability increases. This kind of evolution of the permeability of gassy coal need to be considered in the computer model.

6.3 Numerical Models for Coal and Gas Outbursts

6.3.1 Existing Numerical Models of Outbursts

In the past two or three decades, numerical models of coal and gas outbursts have been developed and used to simulate the process of an outburst. The major models are listed below.

6.3.1.1 Litwiniszyn's phase transformation model

Litwiniszyn (1985, 1986) proposed a model which was based on the assumption of the gas existing in a condensed state within the coal. The model considered the structure of a porous rock medium including solid, condensed liquid and

gaseous substance. He also assumed that when a shock wave passed through the coal, a phase transformation occurs from a liquid to a gaseous phase. This sudden creation of gas causes stress gradients and the skeleton of the medium to be destroyed and an outburst initiated. However he did not pointed out how the shock wave was originated and obviously the desorption mechanism is a better candidate responsible for the sudden release of gas than the phase transformation.

6.3.1.2 Paterson's structural failure model

In Paterson's model (Paterson, 1986), the flow of ideal gas in homogeneous isotropic coal was studied. When gas is released from coal there are body forces on the coal. An outburst is assumed as the structural failure of coal due to high pressure gradients resulting from these body forces, and tensile strength was used as a criterion of failure. A non-linear finite element code has been used to analyse the stress-strain behaviour. It is observed in the simple simulations that large tensile stresses occur near the face of the seam, as a result of the gas pressure gradients. It was suggested from this simple model that the way to avoid outbursts is to avoid high pressure gradients at the mine face. The model included mechanisms of the gas desorption and diffusion but still was over simplistic.

6.3.1.3 Barron and Kullmann's boundary element model

Barron and Kullmann (1990) used a boundary element code to model non-coal outbursts. In their model, an outburst was treated as a series of instantaneous static events, caused by the failure of rock due to excessive pore fluid (gas) pressure. If the effective stress exceeds the tensile strength of the rock, the rock shatters completely, and if the shear strength is exceeded, the rock remains in place, but is fractured, allowing the gas to escape and producing a gas pressure gradient. The gas desorption mechanism was missing and no gas flow in the model existed since gas pressures within the coal were of hydrostatic nature.

6.3.1.4 Otuonye and Sheng's gas flow model

Otuonye and Sheng (1994) simulated the gas flow in airway during an instantaneous outburst of coal and gas. The fluid-dynamic process that occur after an

outburst are computed by the numerical integration of Navier-Stokes equations based on finite difference scheme. The model showed that when an outburst is initiated, a shock wave may be created and propagate into an airway and a rarefaction wave may be created and propagates into the coal seam in the outburst zone. This model is mostly focus on the post-initiation simulation.

6.3.1.5 Odintsev's fracture mechanics model

Odintsev (1997) proposed a concept model based on fracture mechanics. In the model, the coal was viewed as a solution of methane, and the dissolved methane was considered to be the principle motive force involving changes that lead to failure of the coal in the seam. Then a sudden outburst is a result of instability in the state of the methane/coal system when the seam is subjected to human activity. This model was also too simple in the sense that the most mechanisms of outbursts are missing.

6.3.1.6 Valliappan and Zhang's energy balance model

Valliappan and Zhang (1999) developed a model for methane gas migration in coal seams, in which the coupling among gas flow, deformation of solid coal and effect of diffusion of adsorbed methane gas from solid matrix to micro-pores has been considered.

The formulations above are incorporated in the finite element analysis. The results showed that under low gas pressure, most of released gas energy is contributed by desorption. Under high gas pressure, the contribution from gas expansion is significantly higher than that from desorption. The energy of high pressure gas within the coal is an important source for a coal and gas outburst to occur.

6.3.1.7 Xu's finite element model

Xu *et al.* (2006) studied outbursts using a simple finite element model. The code coupled gas flow and the deformation and failure of solid and also incorporated small scale variability in modulus and strength of the coal to model heterogeneity. Rather than the Langmuir adsorption law, an empirical relation, depending on the square root of pressure, was used to describe the gas stored in the coal. The

disadvantage of the model is that the treatment of fracture and fragmentation of coal is not realistic due to the continuous nature of the model.

6.3.1.8 Choi and Wold's damage mechanics model

Choi and Wold (2002, 2004) and Wold *et al.* (1999, 2008) proposed a new model which tries to simulate the whole process of an outburst. In the model, the failure of the coal seam was modelled using plasticity theory with softening mechanism and coal fragmentation is based on the continuum damage mechanics. In the early stage of coal ejection from the face, the dense flow of coal and gas was treated as two super-imposing continua and the interaction between them was represented by interfacial exchange terms in the momentum equations. This model considered the effects of particle sizes on the rate of the mass transfer, and also the effects of geological factors (such as dykes and faults) indirectly.

6.3.1.9 Chen's mechanistic model

In Chen's paper (Chen, 2011), the model combines fracture mechanics, gas dynamics and rock mechanics was proposed. It included three important elements: the highly fractured zone ahead of the coalface; a high pressure gas flow through the fractured zone; and a flow-induced failure of the coal. The highly fractured zone ahead of the working coalface was simplified as a group of parallel fracture channels perpendicular to the coalface. When the fractured zone length is smaller than the critical length, the flow through the fractured zone becomes choked. Then the gas pressure gradient at the exit of the fractured zone will be infinitely large, creating an extremely large effective tensile stress near the coalface, and inducing domino effect of an explosive and catastrophic outburst. This model also explained precursors of outbursts such as the increased noise level and dropped gas temperature.

6.3.1.10 Xue's FLAC-COMET coupling model

Xue *et al.* (2011, 2014) developed a coupled model to link two commercial software, Flac3D, a widely used software designed for rock and soil mechanics simulation, and Comet3, a reservoir software designed to model gas-bearing

coalbed. The unique attractive feature of the coupled model is that the two models are widely used, tested and widely accepted by the community of geomechanics and coal mining. The model also included stress-induce permeability changes, deformation of the coal seam under the effective pressure gas desorption and gas flow in the porous media. It is suitable to model the early stage of an outburst or initiation of an outburst since no explicit mechanisms of fracture and fragmentation of coal was included.

6.3.2 Comments on the Current Models and Necessity to Develop a New Model

Compared with the necessary mechanisms listed in the previous section, we have the following conclusions for the most existing numerical models of coal and gas outbursts.

- No model considers the two-way coupling of free gas flow and the motion of solid particles, that is, gas has a drag force to the solid coal and coal acts as a boundary for gas flow. This mechanism is responsible for the fracture of the coal seam in the early stage of outbursts and the ejection of coal in the later stage.
- No model except Choi and Wold's model (Choi and Wold, 2002, 2004; Wold *et al.*, 1999, 2008) takes into account the geological structures such as faults, dykes, shear zones. Choi and Wold's model simply viewed a fault zone as high permeability and low strength area, and dyke as low permeability and high stress area. In fact, the geological structures may have a multi- and complicated effects on the occurrence of an outburst, for example, the existence of a fault means the fragmentation degree of the coal seam which effects not only the permeability, stress state and strength, but the rate of desorption of gas. Also different kinds of faults may have different influences. A simplified treatment of the fault may not be enough.
- All of the existing outburst models are based on the continuum mechanics. However continuum based models are not suitable to simulate whole fracture process, especially the fragmentation of the coal seam and ejection of coal particles as granular materials.

6.4 The Suitable Candidates: DEM for Fracture and LBM for Fluid Flow

6.4.1 Basic Idea of DEM and LBM Coupling

Based on the researches above, the complete outburst model which includes most of the necessary and important mechanisms and can model the whole process of an outburst, does not exist yet, and a two-way coupled code of solid and fluid is much needed. The fast developing in the supercomputer capability and different numerical methods in the past three decades have made it possible to consider more mechanisms detailed in Section 6.2.3. Two well developed methods, discrete element method (DEM) and lattice Boltzmann method (LBM), have emerged as powerful tools in exploring a broad range of problems and may be used to model outbursts.

The basic idea of DEM is to model solids as an assemblage of discrete particles interacting with one another (Cundall and Strack, 1979). Some DEM model allow the bonds between particles to break, explicitly modelling microscopic fracturing events (Wang *et al.*, 2000; Wang *et al.*, 2006; Wang, 2009; Wang and Alonso-Marroquin, 2009; Wang and Mora, 2008, 2009; Wang *et al.*, 2012a; Wang and Guo, 2016). Due to the unique discrete nature of DEM, many problems which are highly dynamic with large deformations and a large number of frequently changing contacts can be modelled naturally and easily. Compared with the continuum based models, DEM is more suitable to simulate dynamic fracture under high stress, fragmentation of solid.

In recent years, the LBM has made brilliant progress as a new method in numerical modelling of fluid dynamics (Chen and Doolen, 1998). Lattice Boltzmann Model has the advantages of easily coding, paralleling and easily handing the complex boundary conditions. Also the mechanisms of adsorption/desorption, gas diffusion or Darcy flow in the coal seam should also be easily included. In contrast to the conventional computational fluid dynamics (CFD) techniques that solve macroscopic Navier-Stokes equations, the LBM is built on a mesoscopic scale in which the fluid is described by a group of discrete particles that propagate along a regular lattice and collide with each other.

We proposed a new outburst model based on coupling of DEM and LBM. DEM is used to model the deformation and fracturing of solids, while LBM models fluid flow. Figure 6.1 shows the sketch of the new model. The small square grids are nodes of LBM from which fluid flow is modelled. The particles are DEM particles which can be bonded, and the bonds break when the forces exceed certain threshold. Each particle represents a part of porous material inside which gas can fill the micro-pores.

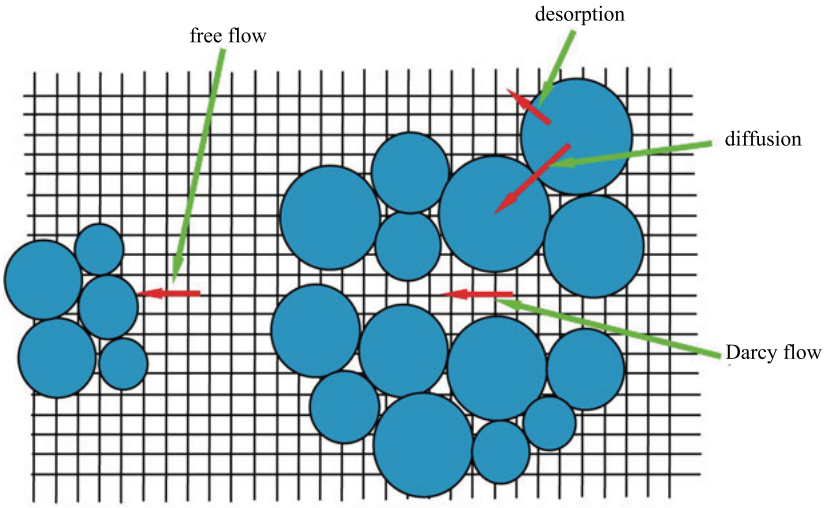

Fig. 6.1 A new outburst coupling DEM-LBM. Particles in DEM regraded as are porous material, and grids in LBM are regular square grids. The arrows represent different fluid flow.

Gas diffusion occurs between touching particles, depending on the difference of concentration between two particles and diffusion coefficient. Gas flow in the crack channel is dominant by Darcy flow, which can be modelled within the LBM framework. At the interface of solids and fluid, desorption occurs by releasing gas from the porous solid into the fluid domain, which can be describe using the Langmuir adsorption isotherms. Fluid flow in the open area is free flow. Coupling between DEM and LBM is taken into account by considering the dragging force from fluid to solids, and moving boundary of particles to the fluid and momentum exchange between them.

A completely coupled code of solid and fluid are based on the two widely used open source codes: ESyS-Particle and OpenLB (Wang *et al.*, 2012b, 2014; Xue *et al.*, 2015). Figure 6.2 shows the relationship between the basic ingredients and the two codes. The two-way coupling between DEM and LBM was realized by data exchange, and finally the two codes were combined into one united code with the united input, data flow, output, MPI calls and visualization tool. Detailed introduction of DEM and LBM model, and the coupling of the two codes can be found in published literatures (Wang *et al.*, 2012b, 2014; Xue *et al.*, 2015).

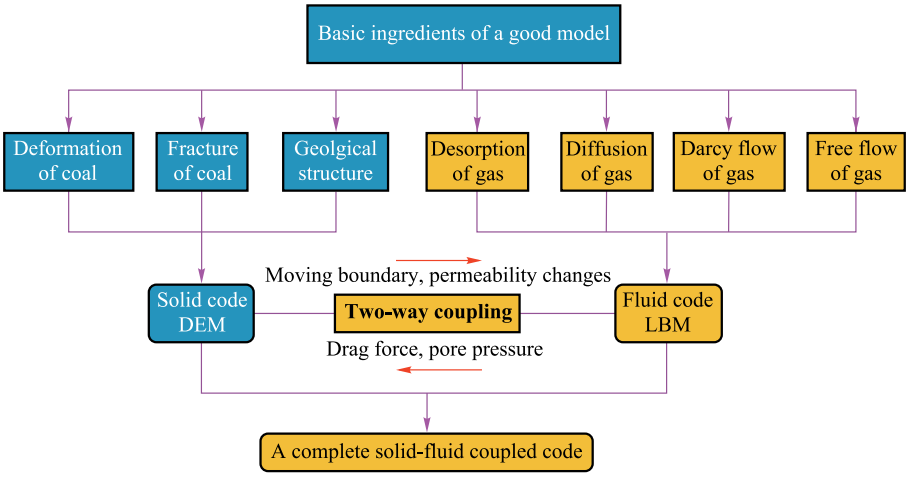

Fig. 6.2 The structure of DEM-LBM coupling code. Dark (blue) colour means DEM model and light (orange) colour represents LBM model.

6.4.2 Preliminary Results

A small outburst simulation is carried out. The model consists of 15 418 equal-sized particles and 1200×1200 fluid grids. Constant confining conditions are applied at left, right, top and bottom boundaries. The soft and fragile middle part, sandwiched by a harder and stronger rock, models a coal seam. The initial state of the model is shown in Figures 6.3a and 6.3b. Excavation starts from left side with constant speed by removing the dark grey part. Two supporting walls (horizontally dashed lines) are placed after the excavation, growing and following the moving excavation wall (vertical dashed line) at the right end. The simulation results are presented below.

Figures 6.3c, d, e, f show the particle motion, gas concentration and fluid velocity at two different time steps. In the early stage of excavation without fracturing events occurring, desorption of gas is mainly limited to the exposed surface. Lower concentration at the surface (the floor and the roof) is observed due to desorption (Fig. 6.3c). The concentration changes in the inner particles are caused by diffusion process. Once fractures occur at the excavation surface, desorption process speeds up since there are more solid surfaces exposed to the fluid. After 20,000 time steps the whole system of particle and fluid evolves by itself, and eventually the fractured coals are ejected from the face under exertion force of fluid and a cave with a small mouth and big inside void is formed, which is widely observed after the occurrence of an outburst in coal mines. The particles from the bursted coal have the lowest gas concentration (represented by blue colour) because they are totally exposed and have larger

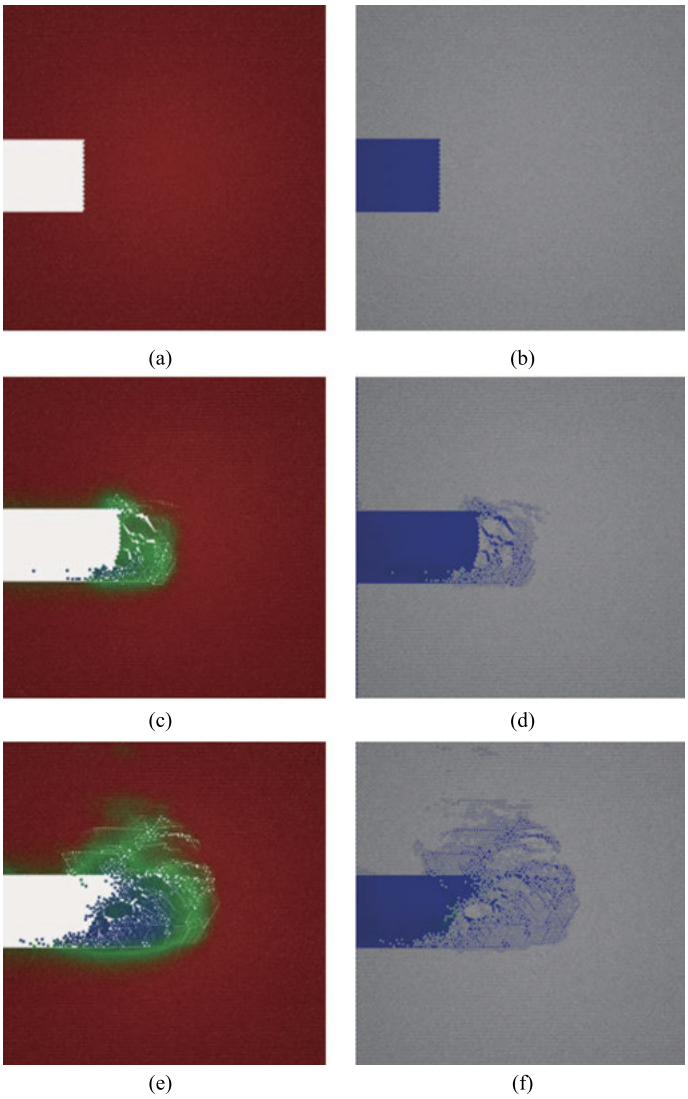

Fig. 6.3 Initial state of the model (time step = 0). **(a)** gas concentration; **(b)** fluid velocity. Initiation of an outburst (time step = 30, 000). **(c)** gas concentration; **(d)** fluid velocity. Developing of an outburst (time step = 50, 000). **(e)** gas concentration; **(f)** fluid velocity.

surface areas, therefore continue gas desorption while moving away from the face (Fig. 6.3e) . High fluid velocity can be seen at the front of the fractured coals (Fig. 6.3f), indicating that more gas are desorbed. This gas, in return, can help deliver and throw the fragile coal particles out of the bursted area. This example shows that the coupled model is encouraging as the entire process of an outburst is well reproduced.

6.5 Conclusion

An outburst of coal and gas is still a major hazard in underground coal mining. The fundamental mechanism of coal and gas outbursts remains unknown although great efforts have been done in the past. Currently it is generally accepted that an outburst occurs when certain conditions of stress, coal gassiness and physical mechanical properties of coal are met. There are many factors influencing the occurrence of an outburst. The most important ones are gas content, rate of gas desorption, coal strength, stress level and some geological structures.

Apart from in-situ investigations, the laboratory tests and analytical studies, the use of numerical simulations can provide useful insights on outbursts. A reliable numerical model permits certain factors to be varied such that their effect on outbursts can be studied. Carefully studying the assumption, the ingredients, advantages and disadvantages of each model is helpful to propose a new and advanced outburst model. Based on the literature review of the mechanisms and numerical models of outbursts, we concluded that the existing numerical model of outbursts are over simplistic, and only include certain factors or mechanisms. Some important mechanisms, such as the fracture and fragmentation of the solid and two-way solid-fluid coupling, are either ignored or not modelled explicitly and properly. Therefore current existing models only capture some aspects of outbursts and cannot explaining all of the phenomena and process leading to an outburst. We further pointed out that in order to build a complete and reliable numerical model, one needs to have a good understanding of the basic mechanism and the major influencing factors of outbursts, and understanding of what the basic ingredients a model should include to reproduce certain features. An over simplistic model with some important features missing cannot generate the meaningful results.

In order to accurately simulate the whole process of an outburst, a numerical model should include several interactive processes of different characteristics and may require different approaches in numerical modelling. These processes and interactions include coal deformation and failure, coal fracture and fragmentation, gas desorption, mass transfer between adsorbed gas and free gas, flow of gas and water within coal cleats, gas dynamics and transport of failed and fragmented coal.

Finally we presented our coupled DEM-LBM model developed to simulate the entire process of an outburst. DEM models the deformation, failure and fragmentation of solid coal, while LBM models the flow of fluid. These two methods are coupled in a two-way fashion, i.e., the solid part provides a moving boundary condition to fluid and transfer momentum to the fluid, while the fluid exerts a dragging force upon the solid. Gas desorption from coal occurs at the solid-fluid boundary, and gas diffusion is implemented in the solid code where

particles are assumed to be porous. A 2-D example to simulate the process of an outburst using the new model is presented, which gives a promising result and demonstrates the potential and capability of the coupled model.

References

Aguado, M.B.D. and C.G. Nicieza (2007). Control and prevention of gas outbursts in coal mines, Riosa–Olloniego coalfield, Spain. Int. J. Coal Geol., 69: 253–266.

Barron, K. and D. Kullmann (1990). Modelling of outburst at #26 Colliery, Glace Bay, nova Scotia, Part 2, Proposed outburst mechanism and model. Mining Science and Tech., 2: 261–268.

Beamish, B.B. and P.J. Crosdale (1998). Instantaneous outbursts in underground coal mines: An overview and association with coal type. International Journal of Coal Geology, 35: 27–55.

Belov, V.I. (1931). New explanation of sudden outbursts of methane. Gornyi Zhurnal, 6: 46–47 (in Russian).

Bodziony, J., A. Nelicki, and J. Topolnicki (1989). Results of laboratory investigations of gas and coal out-bursts. Archives of Mining Sciences, 94: 581–591.

Briggs, H. (1920-1921). Characteristics of outbursts of gas in mines. Trans. Instn. Min. Engrs, 61: 119–146.

Budryk, W. (1951). Emission of gas in mines. In: Wentylaya Kpoaln Part I. Przewietrzanie Wyrobrzk, Katowice, 54–61 (in Polish).

Bykov, L. N. (1936). Theory and basic principle of mining of seams liable to outbursts. NTI (in Russian).

Butt, S.D. (1999). Development of an apparatus to study the gas permeability and acoustic emission characteristics of an outburst-prone sandstone as a function of stress. Int. J. Rock Mech. Min. Sci., 8: 1079–1085.

Cao, Y.X., D.D. He, and D.C. Glick (2001). Coal and gas outbursts in footwalls of reverse faults. Int. J. Coal Geol., 48: 47–63.

Cao Y.X., A. Davis, R.X. Liu, X.W. Liu, and Y.G. Zhang (2003). The influence of tectonic deformation on some geochemical properties of coals: A possible indicator of outburst potential. Int. J. Coal. Geol., 53: 69–79.

Caulfield, B. (1931). Discussion of the paper by G.S. Rice on "Introductory notes on origin of instantaneous outbursts of gas". Trans. Am. Inst. Min. Met. Engrs., 94: 102–136.

Chan, D.Y.C., B.D. Hughes, and L. Paterson (1993). Transient gas flow around boreholes. Transport in Porous Media, 10: 137–1352.

Chen, K.P. (2011). A new mechanistic model for prediction of instantaneous coal outbursts—Dedicated to the memory of Prof. Daniel D. Joseph. International Journal of Coal Geology, 87: 72–79.

Chen, S. and G. Doolen (1998). Lattice Boltzmann method for fluid flows. Annu. Rev. Fluid Mech., 30: 329–364.

Choi, X.S.K. and M.B. Wold (2002). Numerical modelling of outburst mechanisms and the role of mixed gas desorption. ACARP Report C9023, Australia.

Choi, X.S.K. and M.B. Wold (2004). Study of the mechanisms of coal and gas outburst using a new numerical modelling approach, 2004 Coal operator's Conference.

Cis, J. (1958). Outbursts of gas and rock and rock bursts due to dynamic loading of strata. Przeglad Gorniczy, 12: 663–670 (in Polish).

Cis, J. (1965). Gas and rock outbursts in the Lower Silesian Coal Basin, Materialy z Prac Komisji dla Spraw Zagrozen Wyrmtami Gazow i SkalZ, eszyt 2, Warsaw, 59–73 (in Polish).

Cundall, P.A. and O. Strack (1979). A discrete element model for granular assemblies. Geotechnique, 29: 47–65.

Ding, Y.L., B.S. Yu, Y.S. Ding, S.Q. Qu, Q.M. Tan, and Z.M. Zheng (1989). The continuing failure mechanism of coal under effect of Darcy flow of methane gas. Science in China, A6: 582–589 (in Chinese).

Ettinger, I.L. (1979). Swelling stress in the gas-coal system as an energy source in the development of gas outbursts. Trans. From Russian, Soviet Mining Science, 15: 78–87.

Famin, L. B. (1959). Instantaneous outburst of coal and gas in a laboratory experiment. In: Problemy rudnichnoi aerologii. Gosgortekhizdat, Moscow (in Russian).

Farmer, I. W. and F.D. Pooley (1967). A hypothesis to explain the occurrence of outbursts in coal, based on a study of west Wales outburst coal. International Journal of Rock Mechanics & Mining Sciences, 4: 189–193.

Guan, P., H.Y. Wang, and Y.X. Zhang (2009). Mechanism of instantaneous coal outbursts. Geology, 37: 915–918.

Graham, J. I. (1916–1917). The permeability of coal to air or gas, and the solubilities of different gases in coal—Part I. Trans. of The Inst. of Mining Engrs., LII, 338–347.

Halbaum, H. W. (1899–1900). Discussion of J. Gerrard's paper "Instantaneous outbursts". Trans. Inst. Min. Engrs., XVIII: 258–265.

Hanes, J., R.D. Lama, and J. Shepherd (1983). Research into the phenomenon of outbursts of coal and gas. 5th Int. Cong. Rock mechanics, Melbourne, ISRM, E79–E85.

Hargraves, A. J. (1958). Instantaneous outbursts of coal and gas. Proc. AusIMM, 186: 21–72.

Hargraves, A.J. (1980). A review of instantaneous outburst data. Proc. The Occurrence, Prediction and Control of Outbursts in Coal Mines. The Aust. Inst. Min. Metall., Melbourne, 1–18.

Hyman, D. M. (1987). A review of the mechanisms of gas outburst in coal. U.S. Department of the Interior, Bureau of Mines, Information Circular 9155, NTIS PB88-231717, 1–16.

Ignatieff, A. (1954). Outbursts in coal seams. The Canadian Mining & Metallurgical Bulletin, 109: 143–149.

Jagiello, J., M. Lason, A. Nodzenski (1992). Thermodynamic description of the process of gas liberation from a coal bed. Fuel, 71: 431–435.

Jiang, C.L. and Q.X. Yu (1995). The hypothesis of spherical shell destabilization as the mechanism of coal and gas outbursts. Coal Safety, 16: 17–25 (in Chinese).

Jiang, C.L. (1998). The prediction model and indices of outbursts of coal and gas. J China Univ Min Technol, 27(4): 373–376.

Josse, J. (1957). Mining of seams liable to instantaneous outbursts of gas. Annales des Mines de Belgique, 9: 923–934 (in French).

Khristianovich, S. A. (1953) Distribution of gas pressure close to an advancing coal face Izv. AN USSR Otd. Tekhn. Nauk, 12: 1673–1678 (in Russian).

Khodot, V.V. (1951). The mechanism of sudden outbursts. Ugol, 12: 6–11 (in Russian).

Kuroiwa, T. and T. Tashiro (1960). Experimental study on coal pulverisation and gas emission in a moment of outbursts of gas and coal. Journal of Japanese Mining, 76: 227–233 (in Japanese).

Lama, R.D. and J. Bodziony (1998). Management of outburst in underground coal mines. International Journal of Coal Geology, 35: 83–115.

Lama, R.D. and A. Saghafi (2002). Overview of gas outburst and unusual emissions. 2002 Coal Operators' Conference.

Li, H. (2001). Major and minor structural features of a bedding shear zone along a coal seam and related gas outburst, Pingdingshan coalfield, northern China. Int. J. Coal Geol., 35: 83–115.

Litwiniszyn, J. (1985). A model for initiation of gas outburst. International Journal of Rock Mechanics, Mining Sciences & Geomechanics Abstract, 22: 39–46.

Litwiniszyn, J. (1986). Remarks concerning sudden rock-and-gas mass outburst, Mining Science and Technology, 3: 243–253.

Loiret, J. and G. Laligant (1923). General Report: Review of facts and observations; Regulations for mines with outbursts. Translated by Bergrat Gropp, as Manuscript Printed, 24 (in German).

Nekrasovski, Y.E. (1951). Mining of coal seams liable to outbursts of gas and coal. Ugletekhizdat, Moscow (in Russian).

Otuonye, F. and J. Sheng (1994). A numerical simulation of gas flow during coal/gas outbursts. Geotechnical and Geological Engineering, 12: 15–34.

Odintsev, V. N. (1997). Sudden outburst of coal and gas—failure of natural coal as a solution of methane in a solid substance. Journal of Mining Science, 33: 508–516.

Paterson, L. (1986). A model for outbursts in coal. Journal of Rock Mechanics & Mining Sciences & Geomechanics, 23: 327–332.

Pechuk, M. (1933). Results of inducer shotfiring in "Krasnyiprofintern" Colliery. Ugol, 95 (in Russian).

Rowan, H. (1911-1912). An outburst of coal and fie-damp at Valleyfield Colliery, Newmills, Fife, Trans. Inst. M. E., XLII: 50–52.

Rozantsev, E.S. (1959). Comments on the paper by L.N. Bykov "On the theory and practice of control of sudden outbursts of gas and coal in mines". Ugol, 3: 54–55 (in Russian).

Ruff, O. (1930). Cause of occurrence of gas in coal mines. Zeitschrift fur angewandte Chemie, Berlin, 43: 1038–1046 (in German).

Senjuntichai, T. and P.K.N.D. Rajapakse (1993). Transient response of a circular cavity in a poroelastic medium. International Journal for Numerical and Analytical Methods in Geomechanics, 17: 357–383.

Shepherd, J., L.K. Rixon, and L. Griffiths (1981). Outbursts and geological structures in coal mines: A review. Int. J. Rock Mech. Min. Sci. Geomech. Abstr., 18: 267–283.

Singh, J.G. (1984). A mechanism of outburst of coal and gas. Mining Science and Technology, 1: 269–273.

Skochinski, A.A. (1954). Modem concepts on the nature of sudden outbursts of gas and coal and control techniques. Ugol, 7: 4–10 (in Russian).

Skoczylas, N. (2012). Laboratory study of the phenomenon of methane and coal outburst. Int. J. Rock Mech. Min. Sci., 10: 102–107.

Sobczyk, J. (2011). The influence of sorption processes on gas stresses leading to the coal and gas outburst in the laboratory conditions. Fuel, 3: 1018–1023.

Taylor, T. J. (1852-1853). Proofs of subsistence of the firedamp at coal mines in a state of high tension in situ. Trans. N. England Inst. Min. Engrs, I: 275–299.

Torano J., S. Torno, E. Alvarez and P. Riesgo (2012). Application outburst risk indices in the underground coal mines by sublevel caving. Int. J. Rock Mech. Min. Sci., 50: 94–101.

Tu, Q.Y., Y.P. Cheng, P.K. Guo, J.Y. Jiang, L. Wang, and R. Zhang (2016). Experimental study of coal and gas outbursts related to gas-enriched areas. Rock Mech. Rock Eng., 9: 3769–3781.

Valliappan, S. W. and Zhang (1999). Role of gas energy during coal outbursts. International Journal for Numerical Methods in Engineering, 44: 875–895.

Wang, Y.C. (2009). A new algorithm to model the dynamics of 3-D bonded rigid bodies with rotations. Acta Geotechnica, 4: 117–127.

Wang, Y.C. and F. Alonso-Marroquin (2009). A new Discrete Element Model: particle rotation and parameter calibration. Granular Matter, 11: 331–343.

Wang, Y.C. and P. Mora (2009). ESyS_Particle: A new 3-D discrete element model with single particle rotation. In: Advances in Geocomputing, eds by Xing, H.L. Springer, 183–228.

Wang, Y.C. and P. Mora (2008). Elastic properties of regular lattices. J. Mech. Phys. Solids, 56: 3459–3474.

Wang, Y.C. and W.W. Guo (2016). Reproducing the realistic compressive-tensile strength ratio of rocks using discrete element model. In: Rock Anisotropy, Fracture and Earthquake Assessment, edited by Li, Y.G., Higher Education Press, Beijing.

Wang, Y.C., S. Abe, S. Latham, and P. Mora (2006). Implementation of particle-scale rotation in the 3D Lattice Solid Model. Pure Appl. Geophys., 163: 1769–1785.

Wang, Y.C., S. Xue, and J. Xie (2012a). Discrete element method and its applications in earthquake and rock fracture modeling. In: Imaging, Modeling and Assimilation in Seismology, edited by Li, Y.G., Higher Education Press, Beijing; De Gruyter, Berlin, 235–262.

Wang, Y.C., S. Xue, S., and J. Xie (2012b). A fully coupled solid and fluid model for simulating coal and gas outbursts with DEM and LBM. AGH Journal of Mining and Geoengineering, 36: 377–384.

Wang, Y.C., S. Xue, S., and J. Xie (2014). Two-way Coupling of solid-fluid: Discrete Element Model and Lattice Boltzmann Model. In: Seismic Imaging, Fault Damage and Heal, edited by Li, Y.G., Higher Education Press, Beijing, 143–172.

Wang, Y.C., X.C. Yin, F.J. Ke, M.F. Xia, and K.Y. Peng (2000). Numerical Simulation of rock failure and earthquake process on mesoscopic scale. Pure Appl. Geophys., 157: 1905–1928.

Williams, R. J. and J. Rogis (1980). An analysis of the geological factors leading to outburst-prone Conditions at Collinsville, Queensland. Symp. on Occurrence, Prediction & Control of Outbursts in Coal Mines, Brisbane, Qld., Australia, Sept., 99–110.

Wold, M.B. and X.S.K. Choi (1999). Outburst mechanisms: Coupled fluid flow-geomechanical modelling of mine development. ACARP Report C6024, Australia.

Wold, M.B., L.D. Connell, and X.S.K. Choi (2008). The role of spatial variability in coal seam parameters on gas outburst behaviour during coal mining. Int. J. Coal Geol.,75: 1–14.

Xu, T., C.A. Tang, T.H. Yang, W.C. Zhu, and J. Liu (2006). Numerical investigation of coal and gas outbursts in underground collieries. International Journal of Rock Mechanics & Mining Sciences, 43: 905–919.

Xue, S., Y.C. Wang, J. Xie, and G. Wang (2011). A coupled approach to simulate initiation of outbursts of coal and gas: model development. Int. J. Coal Geol., 86: 222–230.

Xue, S., L. Yuan, Y.C. Wang, and J. Xie (2014). Numerical analyses of the major factors affecting the initiation of outbursts of coal and gas. Rock Mech. Rock Eng., 47: 1505–1510.

Xue, S., L. Yuan, J.F. Wang, Y.C. Wang, and J. Xie (2015). A coupled DEM and LBM model for simulation of outbursts of coal and gas. Int. J. Coal Sci. Technol., doi: 10.1007/s40789-015-0063-4.

Yuan, L., S. Xue, and J. Xie (2011). Study and application of gas content to prediction of coal and gas outburst. Coal Sci, Technol., 39: 47–51.

Zheng, Z.M., L. Chen, Y.S. Ding (1993). Constant velocity movement of 1-D outburst surface of fracture. Science in China, A23: 377–384 (in Chinese).

Authors Information

Yucang Wang
School of Engineering and Technology, Central Queensland University,
Bruce Hwy, North Rockhampton QLD 4702, Australia
E-mail: y.wang2@cqu.edu.au

Sheng Xue
School of Energy and safety, Anhui University of Science and Technology,
Huainan, China

Chapter 7

International Consultation on the Likelihood of Earthquakes: Two Cases in 2008 after the Wenchuan Earthquake

Zhongliang Wu

After the May 12, 2008, Wenchuan earthquake, aftershock activity became a threat to the relief and reconstruction process, which was further emphasized because in the region of west Sichuan there had been quite a few landslide lakes caused by the mainshock. While organizing domestic work on the estimation of aftershock hazard, China Earthquake Administration (CEA) invited several experts from abroad for discussions on the aftershock sequence. At approximately the same time, a paper by a Russian group, indicating that there would be an earthquake with magnitude 6.5∼7 near Beijing around August, 2008, caused much concern, due to the sensitivity of the place and time (in the sense of not only the Wenchuan earthquake but also the 2008 Beijing Olympic Games). Dealing with this forecast, six experts from different countries were invited by the CEA to review the paper. The present Chapter summarizes the two cases by archiving the key messages arising from the international communication, providing a unique set of materials both for the study of earthquake forecasting and for the history of seismology.

Key words: The 2008 Wenchuan earthquake, aftershock sequence, Beijing Olympic Games, evaluation of earthquake forecast.

https://doi.org/10.1515/9783110560329-225

7.1 Forecasting the Aftershock Hazard Following the May 12, 2008, Wenchuan Earthquake: the International Component

Estimation of the likelihood of strong aftershocks, including their duration, place, maximum size, and expected rate, plays an important role in assisting the response to destructive earthquakes. Such estimation is theoretically feasible based on the physical predictability of aftershock sequence (e.g., Reasenberg and Jones, 1989; 1994; Tahir *et al.*, 2012). On May 21, just nine days after the May 12, 2008 Wenchuan earthquake in southwest China (Chen and Booth, 2011), the National Expert Committee on the Wenchuan Earthquake was established by the State Council of China. In the National Expert Committee, several working groups set up, focusing on different urgent issues from landslide disasters to reconstruction plans. I served as the vice chairman of the aftershock working group with chairman Guomin Zhang from China Earthquake Administration (CEA). On May 25, I wrote the following e-mail to express gratitude to our colleagues of the Commission on Geophysical Risk and Sustainability (called GeoRisk Commission, or GRC briefly) of the International Union of Geodesy and Geophysics (IUGG) for their kind words and offers to help:

> *Now what I need urgently is the methods and results of the forecast of strong aftershocks which have been a great threat to the relief and reconstruction process because in that region there have been quite a few landslide lakes. Any suggestion about this topic is welcome, and please contact me directly (and urgently) if there is any suggestion coming out from GeoRisk.*

I noted specially:

> *Please note that when we discuss forecast we are meaning in a general sense. For example, how long will the aftershock sequence last, and what will be the magnitude of the largest aftershock.*

Beyond the general comments on the Wenchuan earthquake and the physics of aftershocks, the following provides only the "predictive information" in the communication, subjected to test the real case of aftershock activity of the 2008 Wenchuan earthquake.

7.1.1 Estimate Based on Coulomb Failure Stress (CFS) Changes

As early as May 24, 2008, Jian Lin of Woods Hole Oceanographic Institution wrote:

> *I am pretty certain that the Wenchuan quake has had important impact on the stress changes on faults in nearby regions. However, because this quake is of complex source mechanism rather than being a pure thrust fault, it is very important that we consider the source complexity carefully during the Coulomb stress modeling. Even for a pure thrust fault, it can induce large Coulomb stress changes on nearby strike-slip faults, as illustrated in Fig.4b (page 5) in the Lin & Stein (JGR, 2004), which I am enclosing a copy and is also downloadable from the following site: http://quake.usgs.gov/research/deformation/modeling/papers/2004/Lin_Stein_JGR_2004.pdf, which I am enclosing a copy and is also downloadable from the following site:http://quake.usgs.gov/research/deformation/modeling/papers/2004/Lin_Stein_JGR_2004.pdf.*

Actually this is a 'trigger' of my message sent to the GeoRisk Commissioners. At the same time, a study on aftershock tendency was conducted by Chinese institutions, organized by the Department for Earthquake Monitoring and Forecast of the CEA, and facilitated by the China Earthquake Networks Center (CENC). CEA established an *ad hoc* working group on aftershocks, concentrating on the research work domestically conducted, and I served as the vice chairman. Both the results obtained in China (Jiang *et al.*, 2009) and those provided by colleagues from abroad confirmed and complemented each other. The logic for an international invitation was that since the aftershock problem is a major concern for rescue and relief actions, and the Wenchuan earthquake has caused widespread attention around the world, let's have the worldwide top-ranked experts to discuss this problem—a problem with urgent and critical priority.

On May 28, 2008, Walter Mooney (U.S. Geological Survey) wrote to the Chinese Embassy to USA and sent a copy to me:

> *I would like to draw your attention to the two attached scientific papers written by several of the world's leading seismologists, including two from the US Geological Survey, Dr. Ross Stein and Dr. Tom Parsons*[1]*. These papers present calculations of the change in stress in the crust of western China following the May 12, 2008, Wenchuan earthquake.*

1 Refer to the papers of Parsons *et al.* (2008) and Toda *et al.* (2008).

The paper by Toda and others, completed on May 22, 2008, correctly showed that there was increased stress (shown in RED on the color plot) at the northeast end of the fault. The destructive magnitude 6.0 aftershock occurred at this location on May 25, 2008, which seems to confirm the value of this calculation. There is also an increase in stress to the southwest of the fault. This means the faults in these regions are now more stressed.

On the other hand, the main fault trace that moved on May 12, 2008, is now more relaxed, and has less stress. A similar important study has been completed by USGS seismologists Tom Parsons and his colleague Chen Ji, and I also forward that report to you. Please consult this paper to learn their main conclusions, as I will not repeat them all here.

I have already forwarded both of these two important scientific papers to 50 scientific colleagues in China, including leading scientists at the CEA. My Chinese colleagues at the CEA are very knowledgeable, and are fully aware of these kinds of stress-change calculations. Perhaps they have already obtained similar results. However, as scientists, it is very useful to compare our results.

Indeed it is the case that Chinese seismologists also calculated the Coulomb failure stress (CFS) change caused by the mainshock, which was published later (*see* Jiang *et al.*, 2009).

7.1.2 Analysis of Seismicity and Estimate of Aftershock Probability

7.1.2.1 Analysis Based on the Gutenberg-Richter Law and the Omori Law

On May 25, 2008, Walter Mooney forwarded the message of Lucile Jones (USGS) to us:

*This aftershock sequence, at least as recorded by USGS-NEIC, is well behaved. With two weeks of data and 97 aftershocks, the b-value appears stable with a value of 1.05. The sequence is decaying in a well-behaved way with a p-value of 0.97+/−*0.1. *The a-value (as defined in Reasenberg and Jones, 1989) is* −2.15.

Taking these parameters and turning them into rates and probabilities, we expect about 10 more aftershocks of at least M5.0 in the next 30 days. In the same time period (30 days starting from 12.5 days after the mainshock), the probability of at least one M6.0 is 70%, the

probability of a M6.5 or greater is 30%, and the probability of a M7 or greater is 7%.

In general, this is an overall rather small aftershock sequence — for this size of mainshock. The "a-value" implies an overall rate 1/4 the average for California mainshocks. This a-value is the same we saw for Loma Prieta. Thus it seems likely there could be another magnitude 6, but a magnitude 7 is very unlikely. We believe (but do not yet have rigorous statistics to support) that a low a-value in the near-field aftershocks extends to the distant triggering as well and that would imply that the risk of a triggered earthquake in Xi'an or even farther east is unlikely.

On May 28, 2008, Mooney wrote again:

I spoke with Dr. Lucy Jones today at the USGS Menlo Park. She and Egill Hauksson have used your aftershock catalog to calculate time-dependent aftershock probabilities (Gerstenberger et al., Nature, 2005). Their results are consistent with their previous aftershock probability estimates, which I sent you about two days ago. In general, this aftershock sequence is relatively weak, with no aftershock that follows Bath's Law, that is, 1.2 magnitude units less than the mainshock (a magnitude 6.7 or 6.8 event). In their previous estimate, they gave a 7% probability for a magntude 7 aftershock. (using the method of Reasenberg and Jones, 1989).

7.1.2.2 Estimating the Duration of the Strong Aftershock Sequence

On May 26, 2008, Harsh Gupta, of the National Geophysical Research Institute (NGRI) of Hyderabad, India, wrote:

You have raised an extremely important question about how long the aftershocks would continue and what would be the largest aftershock's magnitude. I am not aware of any definite way of determining it. However, we can make some intelligent guesses by examining earlier earthquakes of similar size in the same region. Plotting of decay of aftershock activity of the past events and determining 'p' value may be helpful.

The 1950 M8.7 India-China border earthquake (not very far away from the May 12, 2008 earthquake) had after shocks occurring for more than 2 years, and the largest aftershock was M∼8! You may like to put some one to look at the past earthquakes, as you have a reasonably good catalogue of Chinese earthquakes. An important issue would be to re-examine earthquake magnitudes and the locations.

On June 23, 2008, Gupta wrote again:

Please refer to our discussions on the question as to how long the aftershocks of the Sichuan earthquake of May 12, 2008 would continue.

We have carried out preliminary studies of the 'p' values from the available data of the aftershocks for the May 12 earthquake and some other recent and historical earthquake sequences. As $M \geqslant 5$ aftershocks can be locally damaging, particularly in a region where the previous earthquakes have weakened the structures, we estimate that such aftershocks could occur for about 7 months after the main event, i.e. till January 2009. We have sent a short note on the same to the Geological Society of India.

7.1.2.3 Analysis Based on the SSE Algorithm

On May 26, 2008, V. Kossobokov, International Institute of Mathematical Geophysics and Earthquake Prediction, Moscow, Russia, wrote:

Eager to help with urgent analysis of what is going on in the region from the viewpoint of earthquake recurrences: You may recollect that pattern recognition studies by Inessa Vorobieva has led to so-called SSE algorithm dated back to 1992 (see the description http://www.mitp.ru/sse/SSE-Alg.html and early refs therein), which logic is in line with the Harsh's comment and suggestions[2]. The statistics of the on-going test of SSE confirm its high efficiency in predicting subsequent event of magnitude M-1 or larger (M being the magnitude of the earthquake in question). At the moment Inessa accumulates the data on the Wenchuan earthquake aftershocks required for a knowledgeable statement on the likelihood of subsequent strong earthquake (with magnitude 6.9 or larger) in the region.

2 See the last section of the comments of Harsh Gupta.

On June 23, 2008, Kossobokov wrote again:

> *According to SSE algorithm applied to the aftershock sequence (I.A. Vorobieva, personal communication): Due to pattern recognition criteria NO MAGNITUDE 6.9 or larger event is expected to follow the 2008 Wenchuan (Sichuan, China) earthquake in the circle of 450 km radius centered at the epicenter of the 12 May 2008 main shock and in time interval up to 10 Nov 2009. Note that in the forward testing mode to-date such a diagnosis made with SSE was confirmed in 13 out of 14 cases.*

7.1.2.4 ETAS Model-based Analysis and Estimate of Aftershock Probabilities

The epidemic-type aftershock sequence (ETAS) model (e.g., Zhuang and Ogata, 2006) was also used to characterize the aftershock sequence. Some estimate of the aftershock hazard was made based on the ETAS model. For example, on May 30, 2008, Jiancang Zhuang (Institute of Mathematics and Statistics, Japan) provided the analysis as follow:

Here are the probability forecasts for the 18th day after the mainshock:

Expected #	Prob.		Waiting time	Quantile				
				1%	5%	50%	95%	99%
$M \geqslant 4.0$	2.17	0.89	0.44	0.004	0.022	0.298	1.296	1.934
$M \geqslant 4.5$	1.03	0.64	0.89	0.010	0.048	0.605	2.655	4.061
$M \geqslant 5.0$	0.36	0.30	2.40	0.024	0.125	1.677	7.472	11.92
$M \geqslant 5.5$	0.12	0.11	6.53	0.058	0.339	4.306	20.08	32.89
$M \geqslant 6.0$	0.07	0.07	10.01	0.087	0.460	6.466	31.15	49.15

This analysis lasted for some time. The whole aftershock zone is basically consistent with the rupture zone of the mainshock, which can be divided into two parts: the north part, and the south part. On June 5, 2008, by analyzing the aftershock activity, Zhuang detected a slow slip in the south, and estimated that slow slip in the south might trigger the aftershocks in the north.

7.1.3 Actual Data on Aftershocks

Table 7.1 shows the actual data from the Wenchuan aftershock sequence with magnitude larger than 5.5 determined by the local seismic network. Table 7.2 shows a comparison of some descriptive estimates and the actual data shown in Table 7.1.

Table 7.1 The Wenchuan earthquake sequence (above M_S5.5). The data come from the China Earthquake Networks Center (CENC), courtesy of Li Li.

No.	Date	Origin Time (Local)	Lat.	Lon.	M_S
1	2008-5-12	14:28:04	31.0	103.4	8.0 (the mainshock)
2	2008-5-12	14:36:39	31.3	103.6	5.8
3	2008-5-12	14:43:14	31.3	103.7	6.0
4	2008-5-12	19:11:00	31.3	103.4	6.0
5	2008-5-13	04:08:49	31.4	103.8	5.6
6	2008-5-13	15:07:07	31.0	103.2	6.1
7	2008-5-14	10:54:36	31.3	103.4	5.6
8	2008-5-16	13:25:46	31.4	103.2	5.9
9	2008-5-18	01:08:25	32.3	104.9	6.0
10	2008-5-25	16:21:49	32.6	105.3	6.4 (the largest aftershock)
11	2008-5-27	16:37:51	32.8	105.6	5.7
12	2008-7-24	03:54:44	32.8	105.5	5.6
13	2008-7-24	15:09:29	32.8	105.5	6.0
14	2008-8-01	16:32:42	32.1	104.7	6.1
15	2008-8-05	17:49:16	32.8	105.5	6.1
16	2008-9-12	01:38:59	33.0	105.6	5.7
17	2009-6-30	02:03:50	31.5	104.0	5.8
18	2011-11-1	05:58:15	32.6	105.2	5.6

Probabilities based on the calculated CFS changes, even using the Dieterich (1994) formula, are still hard to be quantified and also hard to compare with actual aftershock data (Parsons *et al.*, 2012). Therefore, the comparison shown in Table 7.2 does not include the CFS-related estimates. The same issue exists for the ETAS model-based estimate of the probabilities. Table 7.2 mainly summarizes the analysis results based on the study of seismicity. Based on the present knowledge of aftershocks, it is possible to make some estimate of the maximum size, rate, duration, and location of strong aftershocks. However, how to use and interpret the pieces of information properly in response to earthquakes is still a challenge subject and is beyond the scope of this chapter.

Table 7.2 Comparison of estimate of aftershock hazard with real situation.

No.	Descriptive estimate and date	Real aftershock situation
1	There could be another magnitude $M6$, but a magnitude $M7$ was very unlikely (May 25, 2008)	There were 3 aftershocks over magnitude $M6$ occurred afterwards (2008/7/24 $M6.0$; 2008/8/01 $M6.1$; 2008/8/05 $M6.1$)
2	The risk of a triggered earthquake in Xi'an or even farther east was unlikely (May 25, 2008)	No earthquake larger than $M5.5$ occurred in Xi'an or farther east
3	No magnitude $M \geqslant 6.9$ event was expected to follow the 2008 Wenchuan earthquake in a circle of 450 km radius centered at the epicenter of the 12 May 2008 mainshock and in time interval up to 10 Nov 2009 (June 23, 2008)	Maximum magnitude of the aftershocks, after June, 2008, was $M6.1$
4	Slow slip in the south (identified by the ETAS-model fitting) might trigger the aftershocks in the north (June 5, 2008)	From July to September, 2008, all the aftershocks larger than $M5.5$ occurred in the north part of the aftershock zone
5	Such aftershocks could occur for about 7 months after the main event, i.e. till January 2009 (June 23, 2008)	From May 12 to December 31, 2008, 68 aftershocks over $M5.0$ occurred; From January 1, 2009 to December 31, 2011, 13 aftershocks over $M5.0$ occurred.

7.1.4 Additional Communications

Besides the experts mentioned in the text above, contribution to this endeavor was also provided by G. F. Panza who gave useful comments (on May 13, 2008) on the geodynamics of the Wenchuan earthquake, Peter Bormann who provided the fast estimate of the energy release of the Wenchuan mainshock (on May 22, 2008) indicating a high stress drop, E. R. Enghahl and E. Bergman who provided (on May 23, 2008) the EHB re-location of the Wenchuan aftershock sequence, X. D. Song (on May 28, 2008) who provided important references[3] for the aftershock analysis, N. Hirata who provided the ETAS analysis result of the Wenchuan aftershock series (on June 4, 2008), and Y. Kontar who gave useful comments on the properties and physics of aftershocks (replying my e-mail on May 25, 2008). J. Derr provided the information about the reported pre-shock anomaly (on May 23, 2008); L. Knopoff gave useful comments (on June 6, 2008) on the pre-shock seismicity; Alik Ismail-Zadeh facilitated the discussion within the GeoRisk Commission.

3 The provided references are Reasenberg and Jones (1989, 1994).

7.2 Review of the Paper Associated with the Forecast of a Strong Earthquake in Beijing for August 2008

7.2.1 The Forecast and Evaluation

In discussion on the Wenchuan aftershocks, R. Singh wrote on May 27, 2008 to warn:

> *If I understood correctly, people living in the epicentral region are very much afraid and scared from the scientists/other people who are busy in giving false forecasts, during such critical time number of such people/groups increase significantly. We must resolve that such groups should not do anything, if they make such efforts they must inform the Government agencies, in case of China, one must inform CEA.*

Indeed, his concern is realistic.

In May of 2008, while busy working on the Wenchuan aftershocks, we were requested by the Department for Earthquake Monitoring and Prediction of the CEA to review the paper "Fundamental Peculiarities of the Entropy Model of Energy Processes in Seismic Areas and Earthquake Prediction" (by Sibgatulin, V. G., Peretokin, S. A., Khlebopros, R. G., to be published in *Earth Science Frontiers*), in which it was indicated that there would be an earthquake with magnitude M6.5–7 near Beijing around August, 2008 (see Figure 7.1). The words of forecast were eliminated by the editor in the proof-reading stage, considering the sensitivity of the place and time of this predicted earthquake to public as the 2008 Beijing Olympic Games was approaching. Nevertheless the forecast provided by the Russian Scientists caused much concern within the CEA, especially in the social atmosphere after the disastrous Wenchuan earthquake.

Responding to this request, we invited six experts outside China working on earthquake predictabilities to review the paper. They are H. Gupta (India), V. Kossobokov (Russia), G. F. Panza (Italy), D. Rhoades (New Zealand), J. Rundle (USA), and A. Zavyalov (Russia). We got prompt and constructive responses from all of them.

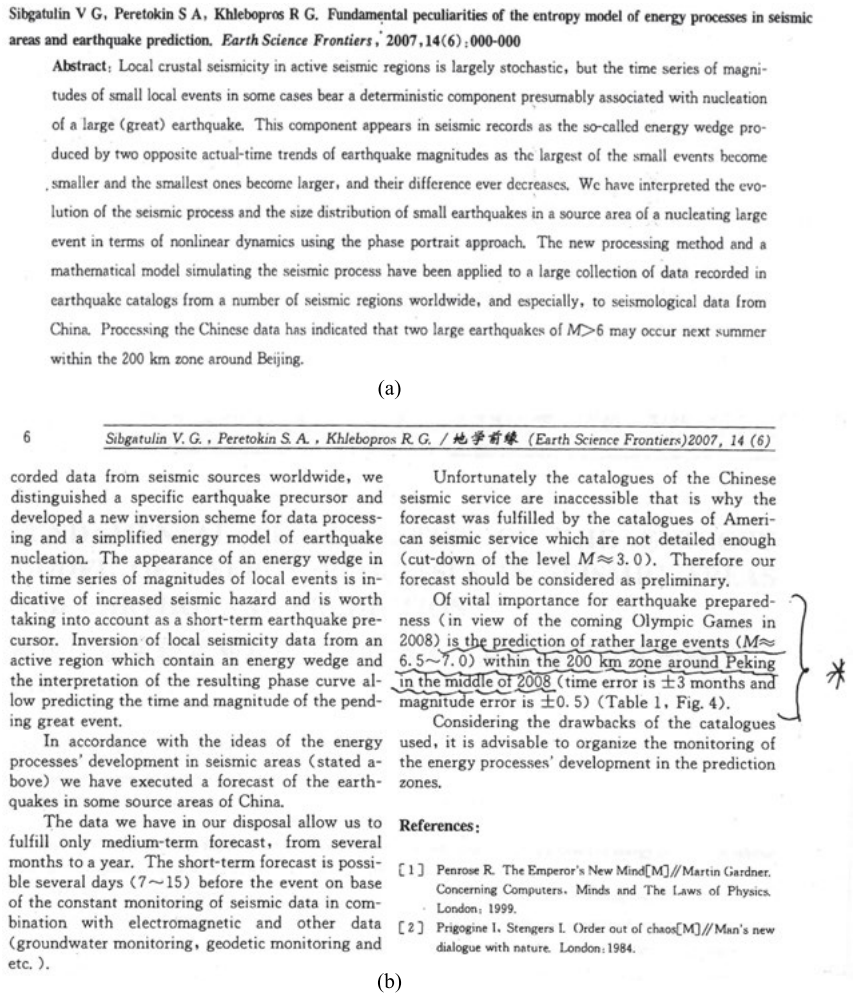

Sibgatulin V G, Peretokin S A, Khlebopros R G. Fundamental peculiarities of the entropy model of energy processes in seismic areas and earthquake prediction. *Earth Science Frontiers*, 2007, 14(6): 000-000

Abstract: Local crustal seismicity in active seismic regions is largely stochastic, but the time series of magnitudes of small local events in some cases bear a deterministic component presumably associated with nucleation of a large (great) earthquake. This component appears in seismic records as the so-called energy wedge produced by two opposite actual-time trends of earthquake magnitudes as the largest of the small events become smaller and the smallest ones become larger, and their difference ever decreases. We have interpreted the evolution of the seismic process and the size distribution of small earthquakes in a source area of a nucleating large event in terms of nonlinear dynamics using the phase portrait approach. The new processing method and a mathematical model simulating the seismic process have been applied to a large collection of data recorded in earthquake catalogs from a number of seismic regions worldwide, and especially, to seismological data from China. Processing the Chinese data has indicated that two large earthquakes of $M>6$ may occur next summer within the 200 km zone around Beijing.

(a)

corded data from seismic sources worldwide, we distinguished a specific earthquake precursor and developed a new inversion scheme for data processing and a simplified energy model of earthquake nucleation. The appearance of an energy wedge in the time series of magnitudes of local events is indicative of increased seismic hazard and is worth taking into account as a short-term earthquake precursor. Inversion of local seismicity data from an active region which contain an energy wedge and the interpretation of the resulting phase curve allow predicting the time and magnitude of the pending great event.

In accordance with the ideas of the energy processes' development in seismic areas (stated above) we have executed a forecast of the earthquakes in some source areas of China.

The data we have in our disposal allow us to fulfill only medium-term forecast, from several months to a year. The short-term forecast is possible several days (7～15) before the event on base of the constant monitoring of seismic data in combination with electromagnetic and other data (groundwater monitoring, geodetic monitoring and etc.).

Unfortunately the catalogues of the Chinese seismic service are inaccessible that is why the forecast was fulfilled by the catalogues of American seismic service which are not detailed enough (cut-down of the level $M \approx 3.0$). Therefore our forecast should be considered as preliminary.

Of vital importance for earthquake preparedness (in view of the coming Olympic Games in 2008) is the prediction of rather large events ($M \approx 6.5 \sim 7.0$) within the 200 km zone around Peking in the middle of 2008 (time error is ±3 months and magnitude error is ±0.5) (Table 1, Fig. 4). *

Considering the drawbacks of the catalogues used, it is advisable to organize the monitoring of the energy processes' development in the prediction zones.

References:

[1] Penrose R. The Emperor's New Mind[M]//Martin Gardner. Concerning Computers, Minds and The Laws of Physics. London: 1999.

[2] Prigogine I, Stengers I. Order out of chaos[M]//Man's new dialogue with nature. London: 1984.

(b)

Fig. 7.1 The Russian Forecast: **(a)** Part of the first page of the proof of their paper. The last sentence was eliminated by the copy editor when the paper got published. **(b)** Part of the last page of the proof. The sentence underlined was eliminated by the copy editor when the paper got published.

7.2.2 Review Comments

The following are the comments from all the reviewers, with minor editing of the typos.

7.2.2.1 Reviewer A

What follows is a set of short comments, pointing to a general weakness of the whole paper.

The idea may be worth a systematic testing, but what is in the written paper is far from being scientifically reliable and reproducible. A clear description of the procedure is missing. For example: The construction of fig. 2 is done after the occurrence of the 4 considered events. What is the Diameter within which earthquakes are analyzed? What is the center of each circle? If the location of the impending earthquake is not known (prediction) how are the circles distributed in space? How many false alarms, i.e. how many large events have been not preceded by the wedge? In summary I give very little value to the document you sent me.

In conclusion I renew the idea of an Earthquake Prediction Evaluation Council, involving, at least in its early stage, representatives from CEA, MITPAN, UNITS/DST and ICTP. Let me know your opinion.

7.2.2.2 Reviewer B

I read the paper today and I have several comments.

1. It is difficult to understand the method they are using – the "instructions" are vague.

2. There are many sentences discussing irreversible thermodynamics using terminology from Prigogine's work, such as entropy and energy flux. There is what looks like an equation of state (figure 3) with what looks like a hysteresis loop, but there is no indication how this was computed.

3. It is not clear how the seismic "energy levels" are defined, since it is not possible to observe energy directly (except radiated energy).

4. It is asserted on page 223 that various magnitude M earthquakes are associated with prediction distances D, but I do not know where these data came from?

In order to compute the type of "wedge" that is apparently plotted in figure 2, I would think the area of the seismicity considered would be a critical part of the computation. This means that such figures might be defined after the earthquake occurred, but it seems unlikely, based on what I see in the paper, that such "wedges" could be computed in advance of the main shock. If they have been computed, where was this information published?

In summary, the information in this paper does not allow a full understanding of the method, there is no evidence that the "wedge" can be computed in advance of the earthquake by an independent means, and the theoretical basis using ideas of entropy and energy flux is not well substantiated other than by speculation.

7.2.2.3 Reviewer C

It is too vague. One could work out the statistical probability of an M6 earthquake to occur within 200 km radius of Beijing in one year time window based on the historical catalogue of earthquakes.

Reviewer C also recommends that the comments of another reviewer will be important.

7.2.2.4 Reviewer D

I fully agree on the issue that the prediction in question is too vague and, as can be judged from the documents attached to your E-mail, can be statistically inconsistent. The Prediction.PDF has parts of the original submission that is omitted (Refs to Table 1 and Fig. 4 in proof-page6.JPG) . . .although it provides in full a rather general conceptual model that might seem plausible or even attractive. . .

The four, presumably, best examples given in Fig.2 raise a number of questions since there is no indication of the area but a point (perhaps, some estimate of epicenter location), magnitude cutoffs are rather small suggesting usage of data below the threshold of catalog completeness, magnitude of the 2004 Parkfield earthquake is wrong in the figure caption, and, finally, the M7.0+ event on 09 October 1994 is the aftershock of the great 04 October 1994 M8.0+ Shikotan earthquake. Being a projection of magnitude extremes (minima and maxima), which accuracy is in common to be about 0.3, the prediction of time has a huge uncertainty. . .

In my opinion, the prediction marked with an asterisk on proof-page6.JPG is most likely scientifically groundless. Yes, you can provide me with the materials (if any) for a review in more details as well as give my name to the agencies, which asked you for such a review.

7.2.2.5 Reviewer E

This paper concerns the seismicity patterns of small earthquakes that occur during the preparation process of a large earthquake. It proposes that an "energy wedge", in which the largest of the small events becomes smaller and the smallest ones become larger, occurs as a medium-term precursor of large earthquakes. The phenomenon is justified on theoretical grounds related to nonlinear thermodynamics, and is said to be supported by an analysis of worldwide earthquake catalogues.

However the description of the recognition of the energy wedge given in this paper is sketchy, and apparently has not been published anywhere else. The few anecdotal examples of the phenomenon presented are also rather sketchy. For example: There is no scale on the time axis in the four examples shown in Figure 2, so we cannot see whether there is any regularity in the length of the "preparation time". It is not stated what limits on earthquake location are represented by the plots. The drawing of the triangles that represent the energy wedges appears to be informal, and depends on the location and time ranges of the selected data. It is not clear that there exists any well-defined method to recognize the energy wedge in advance of the earthquake's occurrence. If such a well-defined method existed, it would be possible to calculate the "success rate" – the proportion of earthquakes above a given magnitude threshold which are preceded by such an energy wedge – and the "false alarm rate" – the proportion of apparent energy wedges which are not followed by earthquakes. The latter would allow a probability to be placed on the occurrence of an earthquake following the observation of an apparent energy wedge. No indication of the success rates or false alarm rate is given, so that it is impossible to get any idea from this paper as to how well this proposed method of earthquake prediction might work. If these rates are known to the authors, it is surprising that they would not mention them in this paper. The fact that a few anecdotal examples of the phenomenon can be presented does not lend any credence to the proposal. Experience with other proposed precursory seismicity patterns shows that it is always possible to find a few examples that conform to any proposed pattern, whether the pattern is an actual earthquake precursor or not.

In summary, no information given in this paper demonstrates that the interesting ideas discussed here are practically usual for earthquake prediction. It appears that much more research is needed first to define the method unequivocally, and then to test it systematically both retrospectively and prospectively, before it should be taken seriously as

a useful prediction method. The original version of the paper apparently contained a forecast of two large earthquakes within 200 km of Beijing in mid 2008. In my opinion, the editors did the right thing in removing the forecast from the paper. The authors admitted that their analysis was based on an inadequate catalogue of the area. But even if they had used the best available Chinese data, the forecast would have no scientific standing because of the deficiencies mentioned above.

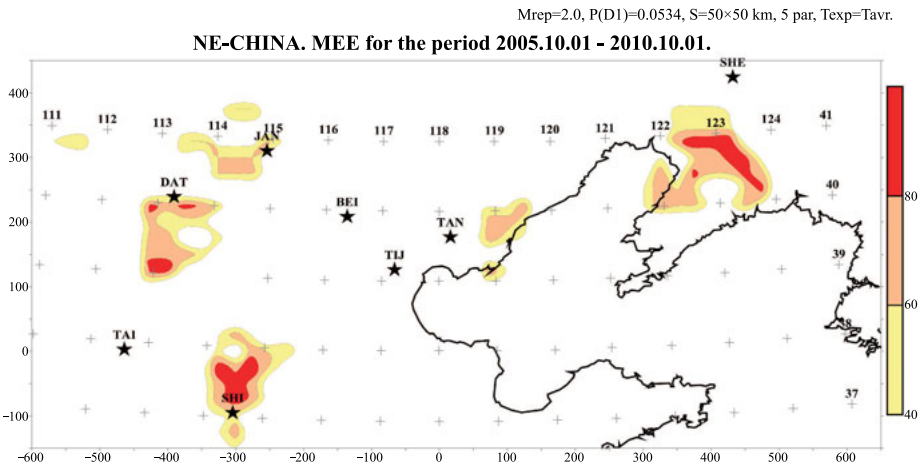

Fig. 7.2 Attached map of Reviewer F.

7.2.2.6 Reviewer F

I fully agree that it is impossible to evaluate an accuracy and reliability of the prediction made by authors of the paper. There are only very general reasonings about seismic process from the stochastic and chaotic point of view.

In attached file[4] *I send you the Map of Expected Earthquakes (MEE) which was compiled during my last visit to Beijing in December 2005. I was working in the Institute of Earthquake Science CEA and they have this map. Maybe it will be interesting for you. The MEE is the map of conditional probability of strong ($M >= 5.5$) occurrence during the time of prediction. The short description of MEE algorithm is in the second attached file. You see that there are no alarm areas 150–200 km around Beijing until the end of 2010.*

4 See Figure 7.2

7.2.3 Test against the Real Situation

From the review comments shown in Section 7.2.2, it seemed that all the reviewers were not supporting the arguments in the paper issued by the group of Russian Scientists. Eventually, the forecast was turned down. The fact is that there was NO earthquake over magnitude $M5$ around Beijing in August, 2008. Therefore, the evaluation which was completed in May, 2008, reached a correct conclusion.

7.3 Concluding Remarks and Discussion

This chapter summarizes two evaluation exercises that took place after the May 12, 2008, Wenchuan earthquake. The estimation of strong aftershock likelihood, and the evaluation of the forecast of a strong earthquake, both incuded an international component. Three issuses associated with these two cases seem noteworthy:

(1) The estimate of the aftershock hazard and the evaluation of an earthquake forecast provide important cases to make full use of the present knowledge about the predictability of earthquakes for the seismic safety of the society.

(2) In study and testing of earthquake forecasts, real forward forecasting plays a crucial role (e.g., Mulargia, 1997). In principle, such a forward requirement should include not only the forecast itself but also the evaluation, since both the forecast and the evaluation will be testified afterwards against the real seismic activity.

(3) Earthquake science, as well as its application to the reduction of seismic disaster risk, needs international collaboration. Remarkably, this was the first time for the Chinese seismological community to organize an international consultation concerning a real earthquake situation, although as early as in the 1990s Chinese seismological agencies had invited some foreign scientists to attend the Annual Consultation on the Likelihood of Earthquakes (Wu, 1997). Note that in history, there were quite a few lessons about the cross-border forecasting of earthquakes (e.g., Olson et al., 1989). The two cases show that invitation-based consultation, as a complement to ongoing domestic studies, may help in the reduction of earthquake disasters, without negative social effects.

In this sense, these two cases might be interesting not only in the history of (Chinese) seismology but also in the study of earthquake forecasting. The author of this chapter witnessed and recorded the whole process of such an endeavor. This chapter is thus a personal retrospective, to some extent being equivalent to an oral history.

Acknowledgements

Thanks to Ke Li and Shi Che, Director and Deputy of the Department for Earthquake Monitoring and Forecast, CEA, in 2008, and Prof. Guomin Zhang, Chairman of the aftershock working group of the National Expert Committee, for authorization and endorsement of the organization of the international consultations, and to Prof. Yong-Gang Li the editor of this book for kind invitation and helps to improve the manuscript.

References

Chen Y. and D.C. Booth (2011). The Wenchuan Earthquake of 2008: Anatomy of a Disaster. Science Press in cooperation with Springer.

Dieterich, J.H. (1994). A constitutive law for rate of earthquake production and its application to earthquake clustering. J. Geophys. Res., 99, 2601–2618.

Gerstenberger M.C., S. Wiemer, L.M Jones, and P.A. Reasenberg (2005). Real-time forecasts of tomorrow's earthquakes in California. Nature, 435, 328–331.

Jiang C.S., Y. Zheng, and L.Q. Zhou (2009). Aftershock sequence. Science Report on the Wenchuan Magnitue 8.0 Earthquake. Beijing, Seismological Press, 130–169 (in Chinese).

Lin J. and R.S. Stein (2004). Stress triggering in thrust and subduction earthquakes and stress interaction between the southern San Andreas and nearby thrust and strike-slip faults. J. Geophys. Res., 109 (B02303), doi:10.1029/2003JB002607.

Mulargia, F. (1997). Retrospective validation of the time association of precursors. Geophys. J. Int., 131, 500–504.

Olson R.S., B. Podesta, and J.M. Nigg (1989). The Politics of Earthquake Prediction. Princeton, NJ, Princeton University Press.

Parsons T., C. Ji, and E. Kirby (2008). Stress changes from the 2008 Wenchuan earthquake and increased hazard in the Sichuan basin. Nature, 454, 509–510.

Parsons T., Y. Ogata, J. Zhuang, and E.L. Geist (2012). Evaluation of static stress change forecasting with prospective and blind tests. Geophys. J. Int., 188, 1425–1440. doi: 10.1111/j.1365-246X.2011.05343.x.

Reasenberg P.A. and L.M. Jones (1989). Earthquake hazard after a mainshock in California. Science, 243, 1173–1176

Reasenberg P.A. and L.M. Jones (1994). Earthquake aftershocks: update. Science, 265: 1251–1252.

Tahir M., J.R.Grasso, and D. Amorèse (2012). The largest aftershock: How strong, how far away, how delayed? Geophys. Res. Lett., 39(4), L04301. doi: 10.1029/2011 GL050604.

Toda S., J. Lin, M. Meghraoui, and R.S. Stein (2008). 12 May 2008 $M = 7.9$ Wenchuan, China, earthquake calculated to increase failure stress and seismicity rate on three major fault systems. Geophys. Res. Lett., 35, L17305, doi:10.1029/2008GL034903.

Vorobieva I.A. and G.F. Panza (1993). Prediction of the occurrence of related strong earthquakes in Italy. Pure Appl. Geophys., 141, 25–41.

Wu, F.T. (1997). The annual earthquake prediction conference in China (National consultative meeting on seismic tendency). Pure Appl. Geophys., 149, 249–264.

Zhuang J. and Y. Ogata (2006). Properties of the probability distribution associated with the largest event in an earthquake cluster and their implications to foreshocks. Physical Review E, 73, 046134, doi: 10.1103/PhysRevE.73.046134.

Author Information

Zhongliang Wu
Institute of Geophysics, China Earthquake Administration,
Beijing, 100081, China
E-mail: wuzl@cea-igp.ac.cn